

Aus der Herzchirurgischen Klinik und Poliklinik  
der Ludwig-Maximilians Universität München

Direktor: Prof. Dr. med. Christian Hagl

## **Kardiovaskuläres Tissue Engineering**

-

## **Möglichkeiten, Limitationen und Innovationen**

*Kumulative Habilitationsschrift*

Vorgelegt von

Dr. med. Kay Nikolaus Florian Thierfelder

2022



Meinem Vater gewidmet.



## Inhaltsverzeichnis

1	Kontext der Habilitationsarbeit.....	7
1.1	Tissue Engineering .....	7
1.2	Forschungsansätze.....	7
1.2.1	In-vitro Tissue Engineering .....	7
1.2.2	In-situ Tissue Engineering / Synthetische Scaffolds.....	8
1.2.3	In-situ Tissue Engineering / Dezellularisation.....	8
1.3	Aktueller Stand der Technik des kardiovaskulären Tissue Engineerings .....	9
1.4	Anforderungen an medizinische Implantate .....	10
2	Wissenschaftliche Zielsetzung.....	12
3	Eigene Forschungsarbeiten .....	13
3.1	In-vitro Tissue Engineering.....	13
3.1.1	Bioreaktoren und Konditionierung.....	13
3.1.2	Synthetische und biologische Scaffolds im in-vitro Tissue Engineering .....	15
3.1.3	Möglichkeiten und Limitationen des klassischen Tissue Engineering .....	17
3.2	Dezellularisation .....	20
3.2.1	Biologische Varianz und Materialauswahl.....	20
3.2.2	Prozessierungsmethoden für biologische Materialien .....	22
3.2.3	Einflussfaktoren der Dezellularisation.....	25
3.3	Innovationen und neue Lösungsansätze.....	32
3.3.1	Eine alternative Zellquelle .....	32
3.3.2	Neuartige Qualitätssicherung im Tissue Engineering .....	34
3.3.3	Standardisierung und Kostenreduktion.....	36
3.3.4	Hydrogele als alternative Scaffolds .....	38
3.3.5	Tissue Engineering 2.0 – Elektrosponning und 3D-Druck .....	41
4	Diskussion.....	44
4.1	Rahmenbedingungen der Implantatherstellung.....	44
4.2	Sicherheitsrelevante und regulatorische Aspekte .....	47
4.3	Einsatz tissue-engineerter Implantate .....	48
4.4	Zusammenfassung .....	49

5	Schlussfolgerung und Ausblick .....	50
6	Quellenverzeichnis .....	52
7	Originalarbeiten .....	64
7.1	Use of a special bioreactor for the cultivation of a new flexible polyurethane scaffold for aortic valve tissue engineering (Aleksieva et al., 2012).....	64
7.2	In vitro comparison of novel polyurethane aortic valves and homografts after seeding and conditioning (Thierfelder et al., 2013).....	76
7.3	Is TAVI of living tissue engineered valves feasible? An in-vitro evaluation utilizing a decellularized and re-seeded biohybrid valve (Koenig et al., 2016).....	83
7.4	Mapping of Bovine Pericardium to Enable a Standardized Acquirement of Material for Medical Implants (Stieglmeier et al., 2021) .....	83
7.5	Pericardial tissue for cardiovascular application: an in-vitro evaluation of established and advanced production processes (Grefen et al., 2018) .....	95
7.6	Tissue-engineering acellular scaffolds – The significant influence of physical and procedural decellularization factors (Starnecker et al., 2018).....	95
7.7	Successful decellularization of thick-walled tissue: Highlighting pitfalls and the need for a multifactorial approach (Koenig et al., 2019).....	95
7.8	The cardiotomy reservoir – a preliminary evaluation of a new cell source for cardiovascular tissue engineering (von Nathusius et al., 2017) .....	103
7.9	Noninvasive analysis of synthetic and decellularized scaffolds for heart valve tissue engineering (Haller et al., 2013).....	103
7.10	Customized 3D-Printed Bioreactors for Decellularization – High Efficiency and Quality on a Budget (Grab et al., 2021) .....	112
7.11	Tuning Tissue Ingrowth into Proangiogenic Hydrogels via Dual Modality Degradation (Chokoza et al., 2019).....	126
7.12	Combining 3D-Printing and Electrospinning to Manufacture Biomimetic Heart Valve Leaflets (Freystetter et al., 2022) .....	126
8	Danksagung .....	127

## Abbildungsverzeichnis

Abbildung 1: Einfluss unterschiedlicher Konditionierungsverfahren .....	14
Abbildung 2: Immunhistochemische Färbungen zellbesiedelter Polyurethanscaffolds und Homografts .....	16
Abbildung 3: Einfluss von Konditionierung, Implantationssimulation und Re-Perfusion auf zellbesiedelte Scaffolds .....	19
Abbildung 4: Kartierung von Dicken und Faserausrichtungen an nativem, bovinem Perikard.....	21
Abbildung 5: Dezellularisierte, sterilisierte und zellbesiedelte Perikarde.....	24
Abbildung 6: Histologischer Nachweis unzureichender Dezellularisierung an porzinen Aorten .....	30
Abbildung 7: Quantitativer DNA- und GAG-Nachweis in porzinen Aorten .....	31
Abbildung 8: Isolation und TE-Anwendung von Fibroblasten und Endothelzellen aus dem Kardiotomiereservoir .....	33
Abbildung 9: $\mu$ -CT-Aufnahmen einer tissue-engineerten Herzklappenprothese.....	35
Abbildung 10: 3D-gedruckte Bioreaktoren zur Dezellularisierung von Perikarden und Aorten .....	37
Abbildung 11: Mehrschichtiges Polyurethanscaffold mit definierter Faserausrichtung.....	43

## Tabellenverzeichnis

Tabelle 1: DNA-Mengen und mechanische Belastbarkeiten nativer und dezellularisierter Perikarde .	22
Tabelle 2: Vergleich von Dicken, DNA-Gehalt und maximalen Belastbarkeiten dezellularisierter und fixierter Perikarde .....	25
Tabelle 3: Auswirkung physikalischer und prozeduraler Faktoren auf den DZ-Erfolg.....	28
Tabelle 4: DNA-Reduktion durch die 3D-gedruckten Bioreaktoren .....	38
Tabelle 5: Soll-Anforderungen und gegebene Eigenschaften tissue-engineerter Implantate .....	50

## Abkürzungsverzeichnis

<b>Abkürzung</b>	<b>Begriff</b>	<b>Ggf. Bedeutung / Funktion</b>
bFGF	Basic fibroblast growth factor	Wachstumsfaktor
CAD	Computer-aided design	Computergestütztes Konstruieren
CFD	Computational Fluid Dynamics	Computerbasierte Strömungsanalyse
DAPI	4',6-Diamidin-2-phenylindol	Fluoreszenzfarbstoff
DC	Natriumdesoxycholat	Detergens
DNA	Desoxyribonukleinsäure	Erbinformationstragendes Makromolekül
DNAse	Desoxyribonuklease	DNA-spaltendes Enzym
DS	Natriumdodecylsulfat	Detergens
DZ	Dezellularisation	Entfernung alle Zellbestandteile
EZM	Extrazellulärmatrix	Grundgerüst eines Gewebes
FDM	Fused Deposition Modeling	3D-Druckverfahren
GAG	Glykosaminoglykane	EZM-Bestandteil
HUVEC	Human umbilical vein endothelial cell	Endothelzellen der Nabelschnurvene
H&E	Hämatoxylin-Eosin	Histologische Färbung
PBS	Phosphatgepufferte Saline	Isotonische Salzlösung
PEG	Polyethylenglykol	Polymer zur Herstellung von Hydrogelen
PLA	Polylactic acid / Polymilchsäure	Polymer / 3D-Druckmaterial
TAVI	Transcatheter Aortic Valve Implantation	Minimalinvasive Aortenklappenimplantation
TE	Tissue Engineering	Gewebezüchtung
VEGF	Vascular endothelial growth factor	Wachstumsfaktor
vWF	von Willebrandt Faktor	Endothelzellspezifisches Antigen
μ-CT	μ-Computertomographie	Hochauflösendes Bildgebungsverfahren

Alle verwendeten Einheiten entsprechen dem SI-System und werden hier nicht gesondert aufgeführt.

# 1 Kontext der Habilitationsarbeit

## 1.1 Tissue Engineering

So gut wie alle klinisch verfügbaren konventionellen medizinischen Implantate wurden einzig und primär entwickelt die Funktion erkrankter Organe oder Gewebe zu ersetzen. So kommt es, dass viele von ihnen mit bestimmten sekundären Nachteilen behaftet sind. Am Beispiel künstlicher Herzklappen aufgezeigt, ist dies die begrenzte Haltbarkeit biologischer Prothesen, beziehungsweise die Antikoagulationsindikation mechanischer Substitute (Bloomfield, 2002). Das sogenannte Tissue Engineering (TE) versucht nun, mittels eines ganzheitlichen Ansatzes, Implantate nicht nur eine bestimmte Funktion übernehmen zu lassen, sondern das jeweils erkrankte Organ oder Gewebe mit einer möglichst originalgetreuen funktionalen und lebenden Nachbildung zu ersetzen. Erstmals im Jahr 1993 durch die Wissenschaftler Robert Langer und Joseph Vacanti umschrieben (Langer and Vacanti, 1993) ist dieses Forschungsgebiet noch relativ jung und kann in unterschiedliche Ansätze unterteilt werden.

## 1.2 Forschungsansätze

### 1.2.1 In-vitro Tissue Engineering

Auch als „klassischer“ Ansatz bezeichnet, versucht in-vitro TE die komplette Nachbildung und anschließende Implantation lebender und funktionsfähiger Gewebe oder Organe. Üblicherweise werden dafür spezifische, meist künstlich hergestellte Gerüstmaterialien, sog. „Scaffolds“, zur Struktur- und Formgebung des späteren Implantates verwendet. Diese können dabei biologischen (z.B. Fibrin (Jockenhoevel et al., 2001)) oder synthetischen (z.B. Polyurethan (Choi et al., 2008)) Ursprungs sein und je nach Art und Herkunft mit Hilfe unterschiedlicher Verfahren in die benötigte Form gebracht werden. Sehr oft werden dafür Elektrospinningtechniken (Vaz et al., 2005) oder Gussverfahren (Moreira et al., 2014) angewendet und man orientiert sich üblicherweise am histologischen Aufbau, sowie an der anatomischen Form des zu ersetzenden Gewebes oder Organs.

Nach der Scaffoldherstellung werden die Trägermaterialien mit gewebetypischen Zellen besiedelt. So kommen zur Herstellung von vaskulären Strukturen beispielsweise Endothelzellen zum Einsatz (Hinderer et al., 2014), beim Knorpelersatz hingegen Chondrozyten (Cao et al., 1997), bei der Herstellung von Hautersatz Fibroblasten (van den Bogaerd et al., 2002) und für das Leber-TE werden Hepatozyten verwendet (Mirdamadi et al., 2020). Die jeweiligen Zelltypen können als adulte Zellen isoliert (Scheuer, 2012) oder in Form von (induzierten) Stammzellen (Hilfiker et al., 2011) verwendet

werden. Zu beachten sind dabei jedoch immer mögliche spätere immunologische Probleme im Sinne einer Implantat- bzw Transplantatabstoßung bei unpassenden Spender-Empfänger-Kombinationen.

Nachdem die Scaffolds mit Zellen besiedelt wurden, findet vor Implantation üblicherweise eine Konditionierung der Konstrukte in sog. Bioreaktoren statt. Mit Hilfe physiologischer Reize (z.B. mechanische Belastung oder elektrische Stimulation (Jin et al., 2015b)) versucht man dabei eine „Reifung“ und Adaptation an spätere Belastungen zu erreichen, so dass es nicht zu einem Implantatversagen durch Überbeanspruchung kommt. Die fertigen zellbesiedelten und konditionierten Scaffolds können dann mit Hilfe der jeweils üblichen Methoden implantiert werden.

### 1.2.2 In-situ Tissue Engineering / Synthetische Scaffolds

Beim in-situ TE hingegen verfolgt man einen regenerativen Ansatz und es sollen azelluläre Scaffolds implantiert werden, so dass anschließend die Zellbesiedelung und Funktionalisierung der Implantate durch den Körper selbst erfolgt. Der künstlich hergestellte Scaffold kann dabei wie beim „klassischen“ TE der Formgebung des späteren Gewebes dienen und wird meist sogar mit den gleichen oder ähnlichen Verfahren hergestellt (Voorneveld et al., 2017). Ein weiterer Ansatz des in-situ TE ist die Verwendung von Hydrogelen als Scaffolds (Gomez-Florit et al., 2020). Um später in-vivo eine schnelle und funktionale Zellbesiedelung durch den Körper zu erreichen, kann es sinnvoll sein, den Scaffold im Rahmen der Produktion noch bestimmten Modifikationen zu unterziehen. Dabei können beispielsweise Aminosäuresequenzen kovalent gebunden (Hersel et al., 2003), Wachstumsfaktoren in das Scaffold inkorporiert (Davies et al., 2012) oder aber das gesamte Gerüst in ein Gel eingebettet werden (Gualandi et al., 2016). Nach Durchführung der Modifikationen kann der azelluläre Scaffold implantiert werden.

### 1.2.3 In-situ Tissue Engineering / Dezellularisation

Dem Dezellularisations-(DZ)Ansatz liegt der Gedanke zugrunde, dass die Implantation (zellfreier) extrazellulärer Matrices die ideale Grundlage zur re-Zellularisierung und Wiederherstellung der Funktionalität eines Gewebes oder Organs ist (VeDepo et al., 2017). Bei der Implantation dezellularisierter Materialien kann man daher auch von in-situ TE sprechen. Die biologischen Rohmaterialien können entweder humanen (Wilson et al., 2015) oder tierischen (Hashimoto et al., 2015) Ursprungs sein, wobei durch die (im Idealfall) vollständige Entfernung von Antigenen im DZ-Prozess keine immunologischen Reaktionen nach Implantation auftreten sollten.

Zur DZ wird üblicherweise auf biologische (z.B. Desoxyribonukleasen; DNAsen), physikalische (z.B. Fluss, Ultraschall und Aggregatswechsel) und chemische (z.B. Detergentien) Methoden zurückgegriffen

(Crapo et al., 2011). Methodische Anpassungen, wie beispielsweise zyklische Expositionen können die Effektivität erhöhen und den DZ-Prozess verkürzen. Entscheidend ist jedoch immer, dass ein Gleichgewicht zwischen effektiver Zellentfernung und Schonung der Extrazellulärmatrix (EZM) gefunden wird, da sonst nach Implantation inflammatorische Prozesse hervorgerufen werden können (Naso and Gandaglia, 2017). Zum Nachweis des DZ-Erfolges und im Rahmen der Qualitätssicherung sollten vor Implantation der Gewebe üblicherweise histologische und molekularbiologische Methoden Anwendung finden (Gupta and Mishra).

### 1.3 Aktueller Stand der Technik des kardiovaskulären Tissue Engineerings

Bereits seit der Entstehung des TE-Ansatzes und bei der Definition des Begriffs durch Langer und Vacanti lag auch ein Einsatzfokus im Bereich der kardiovaskulären Medizin (Langer and Vacanti, 1993, Zund et al., 1997, Fuchs et al., 2001). So sind über die Jahre unzählige Ideen generiert, eine Vielzahl an Studien durchgeführt und letztendlich zahlreiche Publikationen im Bereich des kardiovaskulären TE veröffentlicht worden. Im November 2021 sind mit Hilfe der Suchmaschine „PubMed Central“ beispielsweise über 64.000 wissenschaftliche Artikel unter dem Begriff „Cardiovascular Tissue Engineering“ abrufbar. Bei genauer Betrachtung findet man zu allen drei o.g. Forschungsansätzen Ergebnisse sowohl aus der Grundlagenforschung als auch aus dem in-vivo Einsatz (Xue et al., 2017).

Unterschiedlichste Scaffolds die nach dem „klassischen“ in-vitro Verfahren hergestellt wurden, konnten bereits in verschiedenen tierexperimentellen Studien überzeugen (Emmert et al., 2012, Sodian et al., 2000). Auch das in-situ TE synthetischer Scaffolds konnte im Tiermodell vielversprechende Ergebnisse in unterschiedlichen Studien bereits für einen mittelfristigen (bis 12 Monate) Intervall zeigen (Kluin et al., 2017, Weber et al., 2013).

Als einziger der genannten Ansätze werden dezellularisierte Implantate im Bereich der Herzchirurgie bereits seit einigen Jahren beispielsweise in Form von Herzklappen und Rekonstruktionspatchen klinisch eingesetzt. Dabei sind bis zum heutigen Zeitpunkt jedoch kontroverse Ergebnisse dokumentiert worden. So wurde neben vielversprechenden „midterm“ (bis 3 Jahre) in-vivo Ergebnissen (da Costa et al., 2010), ebenso vom schnellen Versagen (Implantatversagen nach 2 Jahren: 60,2 % (95 % CI: 50,1 – 69,6)) xenogener Implantate (Perri et al., 2012) berichtet.

Resümierend lässt sich also feststellen, dass nach inzwischen jahrzehntelanger Forschung noch kein TE-Ansatz soweit überzeugen konnte, dass es zu einem verbreiteten klinischen Einsatz kommt.



## 1.4 Anforderungen an medizinische Implantate

Im Entwicklungsprozess von Medizinprodukten ist es unerlässlich, bereits von Beginn an die Trias „Herstellung, Zertifizierung und Anwendung“ zu berücksichtigen, da hier verschiedene beteiligte Parteien – der Hersteller, die „benannte Stelle“ zur Zulassung (z.B. TÜV oder Dekra), der klinische Anwender (= Arzt) und der Patient – mit unterschiedlichen oder ggf. kollidierenden Interessen eine Rolle spielen. Dies gilt auch für alle tissue-engineerten Implantate mit dem Ziel einer (späteren) klinischen Anwendung im Menschen.

Für den Hersteller stehen bei der Entwicklung eines Medizinproduktes meist ökonomische Aspekte an primärer Stelle. So sind auf der einen Seite die Kosten, welche durch Rohstoffe, Arbeitszeit (Komplexität des Herstellungsprozesses + regulatorische und administrative Tätigkeiten) und Infrastruktur bedingt werden zu verzeichnen. Für ein rentables Erzeugnis dürfen diese Kosten die erzielbaren Einnahmen auf der anderen Seite nicht längerfristig übersteigen. Die Erlöse (= Preis des Produktes) können durch den Markt, Vergleichsprodukte und den Innovationsgehalt des neuen Medizinproduktes beeinflusst werden. Eine Firma wird unter den Rahmenbedingungen einer freien Marktwirtschaft immer daran interessiert sein, einen Gewinn durch die Entwicklung und Vermarktung neuer Produkte zu generieren.

Dem gegenüber steht die „benannte Stelle“, welche vom Gesetzgeber dazu verpflichtet ist, das Produkt im Zulassungsprozess und auch nach stattgehabter Zertifizierung in Intervallen unter Berücksichtigung der regulatorischen Rahmenbedingungen zu prüfen. Bei (tissue-engineerten) kardiovaskulären Implantaten ist so gut wie immer davon auszugehen, dass diese als Hochrisikoprodukt (= „Klasse III“ Medizinprodukt) eingestuft werden, da sie meist im „direkten Kontakt zum Herz oder dem zentralen Kreislaufsystem“ Anwendung finden (Europ.Rat“, 2020). Damit einher gehen hohe regulatorische Anforderungen, zur Gewährleistung der klinischen Sicherheit und des unbedenklichen Einsatzes des jeweiligen Produktes. Hier sind neben der Bereitstellung umfassender in-vitro Daten und der Durchführung klinischer Studien ggf. auch Gegenüberstellungen zu vergleichbaren Produkten durchzuführen. Ziel des gesamten Zulassungsprozesses ist dabei immer, dass nur wirksame und sichere Produkte von gleichbleibend hoher Qualität in den Verkehr kommen.

Abschließend müssen bei der Entwicklung eines Medizinproduktes die späteren Interessen des Anwenders und selbstverständlich auch des Nutzers (= Patient) berücksichtigt werden. Diese sind durch den Rahmen der regulatorischen Anforderungen bereits grundlegend vertreten (z.B. Patientensicherheit), erstrecken sich darüber hinaus jedoch auch auf Aspekte wie Nutzer-/Anwenderfreundlichkeit oder Alleinstellungsmerkmale eines Medizinproduktes.

Alle genannten Bedingungen und Interessen können den Prozess von der Idee über die Entwicklung und Vermarktung bis hin zur Anwendung eines Medizinproduktes beeinflussen oder sogar stoppen. Es

ist also anzunehmen, dass Gründe für den bisher ausbleibenden klinischen Einsatz und Erfolg tissue-engineerter Implantate an einer oder mehreren Stellen dieses Prozesses zu verorten sind.

## 2 Wissenschaftliche Zielsetzung

Im Rahmen des vorliegenden Habilitationsprojektes soll untersucht werden, ob Implantate im Sinne der vorgestellten TE-Ansätze (in-vitro und in-situ) herzustellen sind und welche möglichen Gründe deren Einsatz in der kardiovaskulären Medizin bisher verhindert haben. Durch die Berücksichtigung von Rahmenbedingungen der Implantatherstellung, regulatorischen Aspekten sowie den Bedürfnissen des klinischen Anwenders und des Nutzers wird angestrebt, eine möglichst umfassende Bewertung durchzuführen. Die klinische Erprobung soll nicht Bestandteil dieser Arbeit sein.

Im Zuge der Evaluation sollen mit Hilfe der genannten TE-Methoden unterschiedliche Scaffolds hergestellt und getestet werden. Bei der Herstellung „klassischer“ tissue-engineerter Implantate wird dabei auch eine Bewertung unterschiedlicher Zellträger und -typen sowie des gesamten Produktionsablaufs einfließen. Ferner werden zur Beurteilung von DZ-Prozessen Untersuchungen zu einzelnen DZ-Faktoren ebenso wie zu den Analysemethoden in der Qualitätssicherung angestrebt. In diesem Zusammenhang wird es ebenso notwendig sein, Ursachen für möglicherweise unzureichende DZ-Ergebnisse im biologischen Rohmaterial zu suchen. Abschließend sollen mögliche Hürden in der (klinischen) Anwendung der tissue-engineerten Materialien/Implantate sowie Verbesserungen und Lösungsansätze aufgezeigt werden.

Zusammenfassend findet eine Bewertung der TE-Ansätze mit Empfehlung eines Vorgehens und dem Aufzeigen möglicher Perspektiven statt.

## 3 Eigene Forschungsarbeiten

### 3.1 In-vitro Tissue Engineering

#### 3.1.1 Bioreaktoren und Konditionierung

*“Use of a special bioreactor for the cultivation of a new flexible polyurethane scaffold for aortic valve tissue engineering” (Aleksieva et al., 2012)*

Autoren: Aleksieva G., Hollweck T., **Thierfelder N.**, Haas U., König F., Fano C., Dauner M., Wintermantel E., Reichart B., Schmitz C., Akra B.

Insbesondere im in-vitro TE kommen vielfach Bioreaktoren zur Präkonditionierung der Gewebe-Zell-Konstrukte vor Implantation zum Einsatz. Während dieser, meist Tage bis Wochen dauernden Phase werden die späteren Implantate unterschiedlichen Reizen (z.B. mechanische Belastung oder elektrische Impulse) ausgesetzt (Jin et al., 2015a). Üblicherweise wird die Intensität der Reize über den Zeitraum gesteigert, so dass eine Adaptation an physiologische Bedingungen stattfinden kann, damit es nach der Implantation zu keinem frühzeitigen Implantatversagen kommt. Da Herzklappen im Körper extremen mechanischen Bedingungen ausgesetzt sind, erscheint es sinnvoll, tissue-engineerte Herzklappenprothesen im Herstellungsprozess auch einem Konditionierungsschritt zu unterziehen.

Zur Überprüfung dieser These sollte daher im Rahmen einer in-vitro Studie der Effekt einer pulsatilen Präkonditionierung mittels eines neuartigen Bioreaktors auf tissue-engineerte Herzklappenprothesen untersucht werden.

Zunächst sind vliesartige Herzklappengerüste (n = 10) im Elektrosponningverfahren hergestellt und in einem zweischrittigen Verfahren mit humanen Fibroblasten und Endothelzellen besiedelt ( $1,5 \times 10^6$  Zellen/cm<sup>2</sup>) worden. Die Zellen konnten zuvor in einem enzymatischen Verfahren aus Reststücken der Vena saphena magna nach aortokoronaren Bypass-Operationen isoliert und anschließend kultiviert werden. Die Herzklappen wurden nach der Zellbesiedelung entweder einer statischen Kultur- (6 Tage) oder einer dynamischen Konditionierungsphase zugeführt. Während der dynamischen Inkubation sind die Herzklappen in einem Bioreaktor für 3 Tage mit 750 ml/min und für 2 Tage mit 1100 ml/min mit Zellkulturmedium (Viskosität:  $0,738 \pm 0,078$  mPas) pulsatil durchströmt worden. Im Rahmen der Versuchsauswertung wurde die Oberflächenbeschaffenheit und -integrität mit rasterelektronenmikroskopischen Aufnahmen untersucht. Immunhistochemische Färbungen gegen VE-Cadherin, Connexin-43, Fibronectin und Collagen IV sind zum Nachweis von Komponenten der EZM herangezogen worden. Die Auswirkung der Flusskonditionierung auf die Regulation inflammatorischer

Prozesse (IL-1a, IL-6, IL-8, MCP-1, VCAM) wurde anhand von Genexpressionsänderungen über mRNA-Quantifizierung mittels reverser Transkription und rt-PCR nachgewiesen.

In der Versuchsauswertung zeigte sich, dass die faserigen Herzklappengerüste erfolgreich mit Fibroblasten und Endothelzellen besiedelt werden konnten. Sowohl die statisch kultivierten als auch die dynamisch-pulsatil konditionierten Herzklappen offenbarten einen konfluenten Zellüberzug, wobei eine Zellausrichtung in Flussrichtung bei den perfundierten Proben zu erkennen war (s. Abbildung 1). Die immunhistochemischen Färbungen offenbarten die Bildung einer EZM für beide Versuchsschemata, jedoch mit deutlich stärkerer Ausprägung nach pulsatiler Konditionierung. Im Rahmen der Genexpressionsanalyse wurde der vorteilhafte Effekt der Endothelzellbeschichtung durch eine Reduktion der pro-inflammatorischen Zytokine IL-6 (statisch: -66 %; dynamisch: -95 %) und MCP-1 (statisch: -71 %; dynamisch: -56 %) deutlich. Ein positiver Effekt der Konditionierungsphase zeigte sich in einer signifikanten Herabregulation (-59 %;  $p \leq 0,05$ ) des stark pro-inflammatorisch wirkenden Zytokins IL-6. Es konnte gleichzeitig jedoch eine Hochregulation von IL-8 durch die Endothelzellbesiedelung (statisch: +868 %; dynamisch: +123 %) und Konditionierung (+37 %) beobachtet werden. Diesem Zytokin wird neben der Beeinflussung pro-inflammatorischer Prozesse auch eine wichtige Rolle in der Angiogenese zugeschrieben (Simonini et al., 2000).

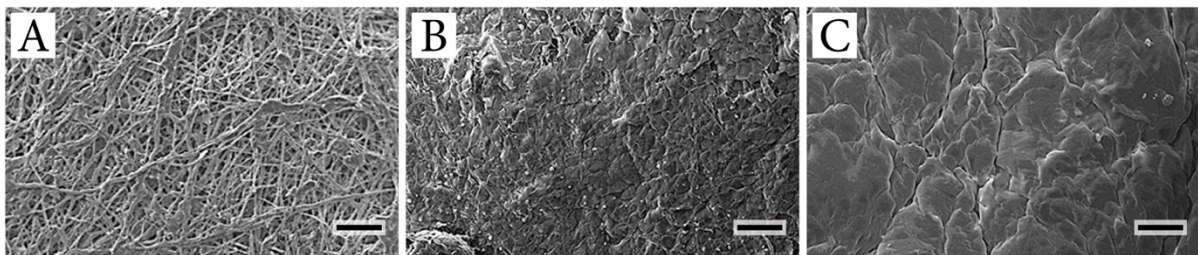


**Abbildung 1: Einfluss unterschiedlicher Konditionierungsverfahren**

*In rasterelektronenmikroskopischen Aufnahmen zeigen sich am nativen Polyurethanscaffold unausgerichtete Fasern (A); Nach sequenzieller Beschichtung mit Fibroblasten und Endothelzellen stellt sich nach 6-tägiger statischer Konditionierung ein konfluenten Zellüberzug dar (B); Nach pulsatiler Perfusion der zellularisierten Scaffolds ist zusätzlich eine strömungsabhängige Zellausrichtung (vertikal ausgerichtet) zu erkennen (C); Maßstabsbalken = 100  $\mu$ m*

Die vorliegende in-vitro Studie konnten den Vorteil einer Präkonditionierung von tissue-engineerten Herzklappen durch die verstärkte Bildung einer EZM und die Strömungsausrichtung von Endothelzellen klar belegen. Die molekulargenetische Auswertung offenbarte den positiven Einfluss der Konditionierungsphase auf (pro-)inflammatorische Prozesse und gibt den Hinweis, dass diese ausgedehnt werden sollte. Der neuentwickelte Bioreaktor stellt dabei ein wertvolles Werkzeug zur pulsatilen Konditionierung zellbesiedelter Herzklappenprothesen dar.

### 3.1.2 Synthetische und biologische Scaffolds im in-vitro Tissue Engineering

*“In vitro comparison of novel polyurethane aortic valves and homografts after seeding and conditioning” (Thierfelder et al., 2013)*

Autoren: **Thierfelder N.**, König F., Bombien R., Fano C., Reichart B., Wintermantel E., Schmitz C., Akra B.

*Hiermit wird explizit darauf hingewiesen, dass sich die im Folgenden vorgestellte Forschungsarbeit thematisch auf die Promotionsarbeit „In-vitro Vergleich von zellbesiedelten und konditionierten neu-entwickelten Polyurethanaortenklappen-prothesen und Homografts“ (Nikolaus Thierfelder, 2014) bezieht. Sie dient nicht der Erlangung der Habilitationsleistung, sondern wird aufgrund ihrer thematischen Relevanz und zum Verständnis des wissenschaftlichen Kontextes hier aufgeführt.*

Zur Herstellung tissue-engineerter Herzklappenprothesen können unterschiedliche form- und funktionsgebende Zellträger verwendet werden (Xue et al., 2017). Dabei wird entweder auf synthetische Matrizen oder auf Materialien biologischen Ursprungs zurückgegriffen (Jana et al., 2019a, Puperi et al., 2016, Hof et al., 2016). Synthetische Zellträger bieten in diesem Zusammenhang den Vorteil, dass sie wenigen Restriktionen in der geometrischen Ausgestaltung unterliegen und von Beginn an hohen mechanischen Belastungen widerstehen können (Saidy et al., 2019).

Im Rahmen einer in-vitro Studie sollte daher eine neuartige tissue-engineerte Polymerherzklappe mit Zellen besiedelt, unter Fluss konditioniert und mit einem biologischen Zellträger verglichen werden.

Zu Beginn der Studie sind humane Endothelzellen und Fibroblasten in einem mehrschrittigen, enzymatischen Verfahren aus Bypass-Gefäßen isoliert und kultiviert worden. Diese Gefäße sind als Restmaterial im Rahmen von herzchirurgischen Bypass-Operationen angefallen. Faserige, synthetische Herzklappengerüste ( $\varnothing$  24 mm; Materialstärke: 0,3 mm; n = 4) konnten mittels Elektrosprayingverfahren hergestellt und anschließend  $\gamma$ -sterilisiert werden. Als Vergleichsgruppe dienten kryokonservierte humane Aortenklappenhomografts ( $\varnothing$  27 mm; Lagerzeit:  $7,33 \pm 2,11$  Jahre; n = 4). Die Zellträger beider Versuchsgruppen sind in einem dynamischen Verfahren zunächst mit den gewonnenen Fibroblasten ( $92,11 \pm 11,08 \times 10^6$  Zellen) beschichtet, für 24 Stunden in eine statische Kultur überführt und abschließend für 5 Tage unter Fluss konditioniert worden. Die Konditionierungsphase wurde in einem speziellen Bioreaktor unter pulsatilen Bedingungen mit steigender Flussrate (750 -> 1100 ml/min) durchgeführt. Es folgte die Besiedelung mit Endothelzellen ( $96,48 \pm 8,05 \times 10^6$  Zellen) sowie eine analoge Ruhe- und Konditionierungsphase zum ersten

Studienteil. Zur Analyse sind Proben der Zellträger mittels Rasterelektronenmikroskopie, Immunhistochemie und rt-PCR ausgewertet worden.

Anhand der rasterelektronenmikroskopischen Aufnahmen konnte die erfolgreiche Zellularisierung beider Zellträger sowohl mit Fibroblasten als auch mit Endothelzellen nachgewiesen werden. Immunhistochemische Färbungen bestätigten dies anhand des Nachweises endothelzell- (CD31) und fibroblastenspezifischer (TE-7) Antigene (s. Abbildung 2). Ebenfalls immunhistochemisch konnte mittels zunehmender Anfärbung von Kollagen IV und Fibronectin über den zeitlichen Verlauf der Aufbau einer EZM in beiden Versuchsgruppen beobachtet werden. Die Abhängigkeit dieser Reaktion von der Konditionierung mit pulsatilem Fluss zeigte sich durch die verstärkte Ausprägung der EZM auf der flusszugewandten Seite. Als Indikator einer konfluenten und kompetenten Endothelzellschicht nach Flusseexposition diente der immunhistochemische Nachweis der Interzellulärproteine Connexin-43 und VE-Cadherin.

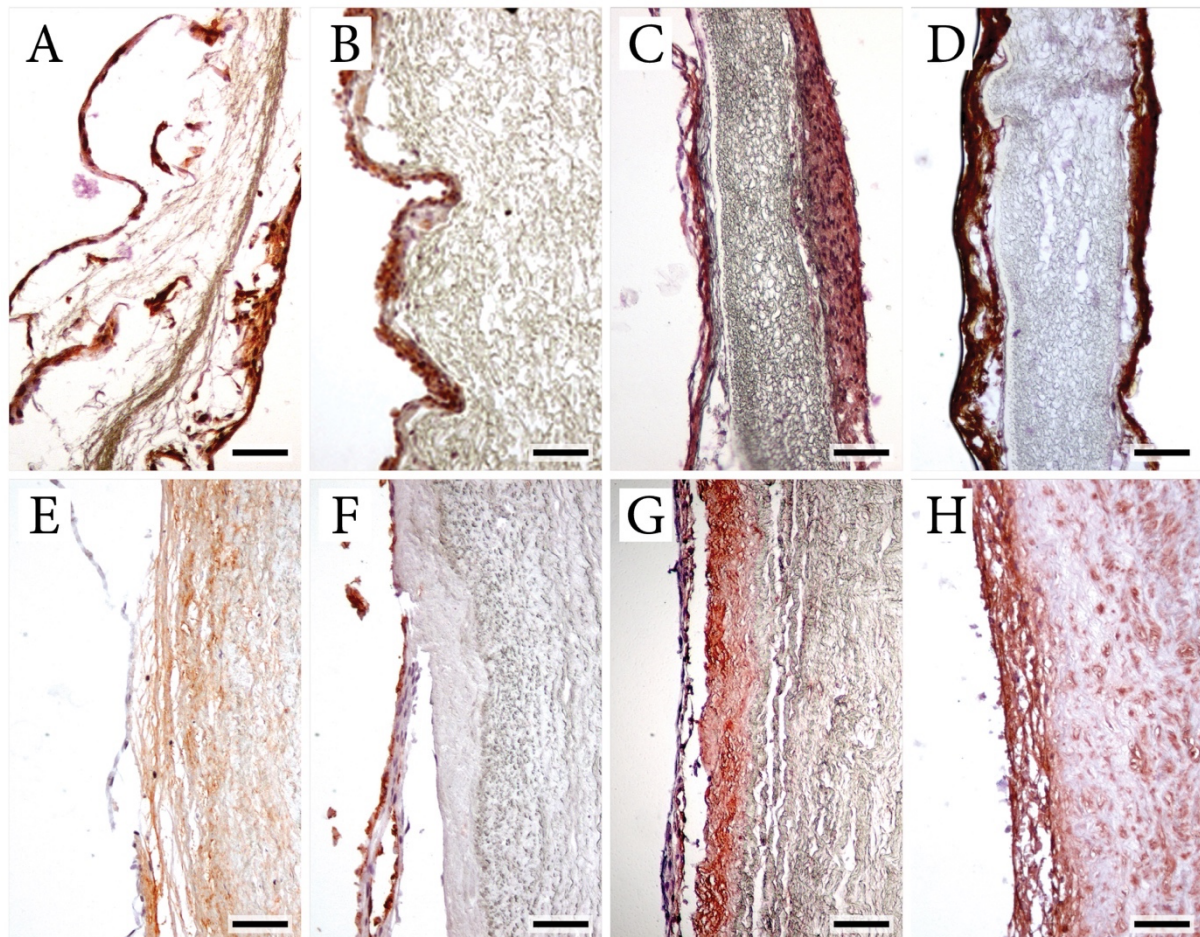


**Abbildung 2: Immunhistochemische Färbungen zellbesiedelter Polyurethanscaffolds und Homografts**

Die erfolgreiche Beschichtung mit Fibroblasten (A + E) und Endothelzellen (B + F) zeigte sich anhand positiver Färbung gegen TE-7 bzw. CD31; Der Aufbau einer EZM konnte anhand positiver Färbungen gegen Collagen IV (C + G) und Fibronectin (D + H) nachgewiesen werden; A – D: Polyurethanscaffold, E – H: Homograft; Kernfärbung mit Hämalaun, positive immunhistochemische Färbung durch rot-braune Bereiche dargestellt; Maßstabsbalken = 100  $\mu$ m



Die molekulargenetische Auswertung offenbarte eine deutliche Herabregulation des pro-inflammatorischen IL-6 (synthetischer Zellträger: -78,82 %; biologischer Zellträger: -97,42 %) durch die Endothelialisierung der tissue-engineerten Konstrukte in beiden Gruppen. Die Endothelialisierung bewirkte gleichzeitig jedoch auch auf dem synthetischen Zellträger eine signifikante Hochregulation der IL-8-Expression (+559,7 %).

Anhand vergleichbarer Ergebnisse mit der biologischen Referenzgruppe konnte im Rahmen dieser in-vitro Studie die Eignung des Polyurethanfasergerüsts zur Herstellung tissue-engineerter Herzklappenprothesen nachgewiesen werden. Sowohl eine gute Zellularisierbarkeit des synthetischen Materials als auch die Bildung einer ausgeprägten EZM während der pulsatilen Flusskonditionierung untermauerten dies.

### 3.1.3 Möglichkeiten und Limitationen des klassischen Tissue Engineering

*“Is TAVI of living tissue engineered valves feasible? An in-vitro evaluation utilizing a decellularized and re-seeded biohybrid valve”* (Koenig et al., 2016)

Autoren: König F.\*, Lee J.S.\*, Akra B., Dauner M., Winterwandel E., Hagl C., **Thierfelder N.**

Bei der Behandlung kardiovaskulärer Erkrankungen, insbesondere beim Herzklappenersatz, zeigt sich in den letzten Jahren ein klarer Trend weg von der chirurgischen Behandlung und hin zu minimalinvasiven oder interventionellen Therapieverfahren (Bourantas and Serruys, 2014, Rahhab et al., 2020). Neben dem Patientenwunsch spricht die geringere Komplikations- und Mortalitätsrate besonders bei einem alten und/oder multimorbiden Patientenkollektiv für die Durchführung der neuen Verfahren und wird daher in den aktuell gültigen Leitlinien für Risikopatienten empfohlen (Vahanian et al., 2012, Otto et al., 2017). Für den interventionellen Aortenklappenersatz (TAVI) können dabei aufgrund der Implantationsart nur biologische Substitute eingesetzt werden, welche, wie von konventionell-chirurgischen Prothesen bekannt, eine limitierte Lebensdauer aufweisen (Hoffmann et al., 2008). Im Gegensatz zu den avitalen, fixierten Geweben biologischer Herzklappenprothesen, welche zur Degeneration durch Kalzifizierung neigen, versprechen tissue-engineerte Materialien durch Regeneration und Wachstum eine verbesserte Therapieoption (Schoen and Levy, 2005, Fioretta et al., 2018).

Es wurde daher die Entwicklung und Evaluation einer neuartigen tissue-engineerten Herzklappenprothese zur minimalinvasiven Anwendung angestrebt.

Für die Studie sind biohybride Zellträger (n = 6) aus vliesartigem Polyurethangewebe und den Segeln humaner Aortenklappenhomografts ( $\varnothing 25,5 \pm 0,76$  mm) hergestellt und in Cobalt-Chrom-Stents ( $\varnothing 20$



mm) vernäht worden. Die Herzklappengerüste wurden zur DZ der biologischen Segel in einem nächsten Schritt für 24 Stunden mit Desoxycholsäure (DC; 0,5 %) und Dodecylsulfat (DS; 0,5 %) inkubiert und anschließend mehrfach gewaschen. Es folgten die zweischrittige Zellularisierung der Zellträger mit humanen Fibroblasten ( $45,23 \pm 1,55 \times 10^6$  Zellen) und Endothelzellen ( $38,24 \pm 14,91 \times 10^6$  Zellen), eine statische Ruhephase (6 Tage) sowie ein Konditionierungsschritt unter pulsatilem Perfusion (500 ml/min; 5 Tage). Zur Simulation einer TAVI-Implantation wurden die tissue-engineerten Herzklappenprothesen für 10 Minuten „gecrimpt“ ( $\varnothing$  10 mm), danach mittels Ballon dilatiert ( $\varnothing$  20 mm) und abschließend pulsatile durchströmt (1100 ml/min; 2 Tage). Rasterelektronenmikroskopische Aufnahmen, immunhistochemische Färbungen, Zellvitalitätsfärbung und eine Funktionsanalyse der Klappenprothesen dienten der Versuchsauswertung.

Elektronenmikroskopische Aufnahmen zeigten einen konfluenten Zellüberzug der Prothesen nach Zellbesiedelung und Konditionierungsphase (s. Abbildung 3). In der immunhistochemischen Auswertung bestätigte sich dies und es wurde ein zweischichtiger Überzug mit einer kompetenten, oberflächlichen Endothelzellschicht (positive Färbung gegen CD31 und Connexin-43) dargestellt. Insbesondere während der 5-tägigen Flusskonditionierung konnte anhand einer zunehmenden Anfärbung mittels spezifischer Antikörper (gegen Collagen IV und Fibronectin) der Aufbau einer EZM nachgewiesen werden. Nach der TAVI-Simulation zeigten sich elektronenmikroskopisch starke Schäden der Zellschicht, im Sinne von Löchern und Fissuren. Immunhistochemisch waren zu diesem Zeitpunkt zwar noch Fibroblasten und Endothelzellen nachweisbar, in der Quantifizierung mittels Vitalitätsmessung stellten sich jedoch stellenweise über die Hälfte der Zellen ( $50,5 \pm 17,7$  %) als abgestorben dar. Durch die anschließende pulsatile Perfusion sind die entstandenen Schäden noch deutlicher geworden und in einigen Bereichen zeigte sich gar keine Beschichtung des Zellträgers mehr, mutmaßlich durch Wegspülen abgestorbener Zellen verursacht. Eine immunhistochemisch gleichzeitig nachgewiesene und eindruckliche Zunahme von ICAM-Zelladhäsionsmolekülen in diesem Zeitraum ist ein deutliches Indiz für eine akute inflammatorische Reaktion. In der Funktionsanalyse nach der Implantationssimulation zeigten sich die tissue-engineerten Herzklappen mit einer adäquaten Öffnungs- und Schließbewegung sowie keinem Hinweis auf eine Insuffizienz.

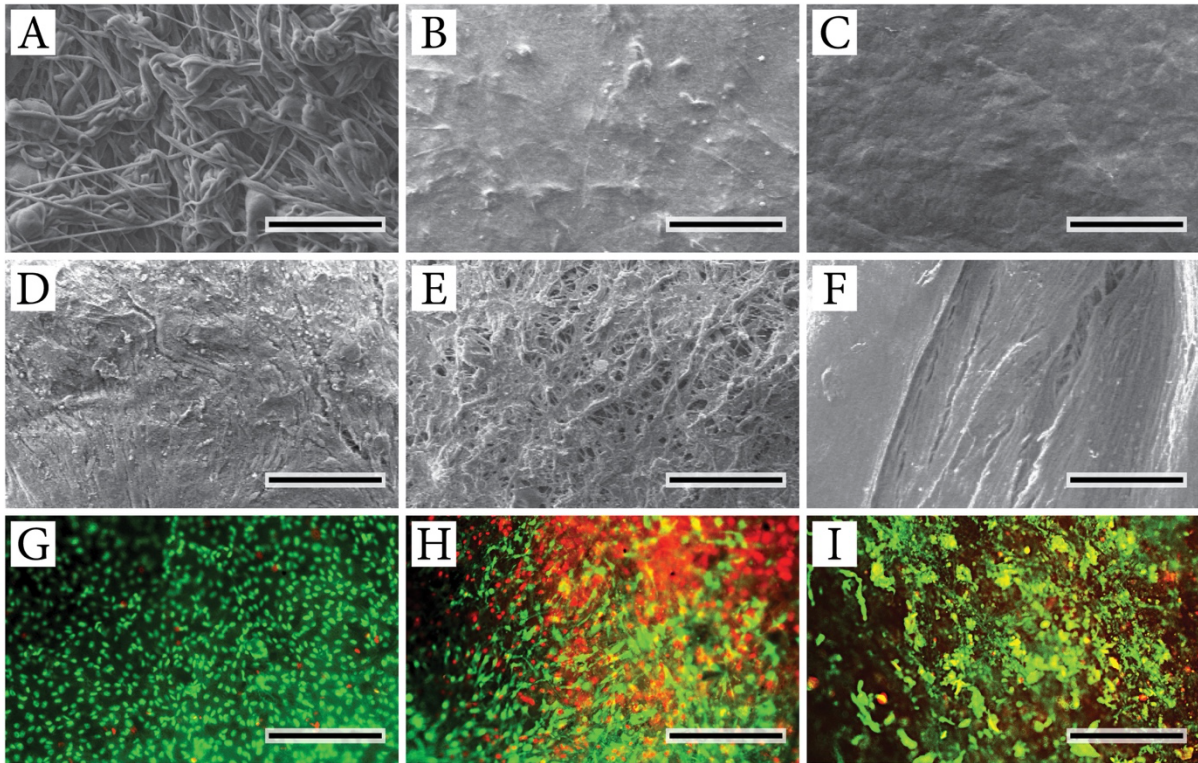


**Abbildung 3: Einfluss von Konditionierung, Implantationssimulation und Re-Perfusion auf zellbesiedelte Scaffolds**

Natives Polyurethanscaffold (A); Konfluente Zellschicht nach Fibroblasten und Endothelzellbeschichtung (B + G) und 5-tägiger pulsatiler Konditionierung (C). Nach „crimping“ und Ballondilatation zeigen sich deutliche Schäden an der Zellschicht (D + H), welche nach einer Re-Perfusionsphase, sichtbar durch die Freilegung des Zellträgers an Herzklappenwand (E + I) und -segel (F), weiter zunehmen; A – F: Rasterelektronenmikroskopische Aufnahmen, G – I: Vitalitätsfärbung (grün = lebende Zellen, rot = tote Zellen); Maßstabsbalken = 100  $\mu$ m

In der beschriebenen Studie konnte nachgewiesen werden, dass auch funktionale TAVI-Prothesen in einem tissue-engineering Ansatz hergestellt werden können. Die signifikante Schädigung der Zellbeschichtung und die Provokation einer ausgeprägten inflammatorischen Reaktion durch die Simulation einer Implantationsprozedur lassen die in-vivo Anwendung mit einem minimalinvasiven Verfahren jedoch fraglich erscheinen.

## 3.2 Dezellularisation

### 3.2.1 Biologische Varianz und Materialauswahl

*“Mapping of Bovine Pericardium to Enable a Standardized Acquirement of Material for Medical Implants”* (Stieglmeier et al., 2021)

Autoren: Stieglmeier F., Grab M., König F., Büch J., Hagl C., **Thierfelder N.**

Bovines Perikard wird seit vielen Jahren als Rohmaterial für unterschiedliche kardiovaskuläre Implantate verwendet und kommt damit im sog. Hochrisikobereich vom Medizinprodukten zum Einsatz (Li et al., 2011, Attia and Raja, 2021). Mit der Zulassung solcher Implantate gehen aufgrund ihres Einsatzbereichs hohe gesetzlicher Vorgaben und regulatorische Anforderungen einher (Byrne, 2019, Lauer et al., 2017). Umso erstaunlicher ist, dass in der Literaturrecherche nur sehr wenige und dazu noch verhältnismäßig alte Empfehlungen zur standardisierten Gewinnung des Rohmaterials zu finden sind (Braile et al., 1998, Simionescu et al., 1993, Sacks et al., 1994).

Ziel der Studie war es daher, bovines Perikard hinsichtlich seiner biomechanischen und histologischen Eigenschaften zu kartographieren, um idealerweise eine Handlungsempfehlung zur Gewinnung des Rohmaterials kardiovaskulärer Implantate zu generieren.

Im Rahmen der experimentellen in-vitro Studie ist natives und durch DZ prozessiertes Rinderperikard evaluiert worden. Als Vergleichsproben dienten kommerzielle, glutaraldehyd-fixierte Perikardpatche (Supple Peri-Guard; Synovis, St. Paul, USA) mit Zulassung zur kardiovaskulären Implantation. Als Versuchsmaterial sind frische Perikarde junger Bullen ( $\varnothing$  Alter:  $19,5 \pm 1,4$  Monate;  $n = 20$ ) eines lokalen Schlachtbetriebes verwendet worden. Diese wurden zunächst makroskopisch hinsichtlich ihrer Dicken (140 Messpunkte) und der vorherrschenden Faserausrichtung evaluiert. Auf Basis dieser Ergebnisse konzentrierte man sich im weiteren Verlauf auf die Untersuchung von fünf umgrenzten Arealen („A“ – „E“), welche entweder direkt weiteren Analysemethoden zugeführt oder davor einem DZ-Prozess unterzogen worden sind. Die Gewebe-DZ erfolgte in einem zyklischen Prozess mittels der Detergentien DC und DS (jew. 0,5 % in phosphatgepufferter Saline, PBS), gefolgt von Waschsritten und einer DNase-Inkubation (1 %; 30 U/ml). DNA-Messungen sowie histologische Färbungen mit Hämatoxylin-Eosin (H&E) und DAPI (4',6-Diamidin-2-phenylindol) dienen der Erfolgskontrolle nach DZ. Alle gewonnenen Proben wurden mechanischen Belastungsuntersuchungen, rasterelektronenmikroskopischen Aufnahmen und einer histologischen Aufarbeitung mit Färbungen nach Movat's Pentachrom- und Pikrosirius-Rot-Schema unterzogen. Zur Evaluation ihrer Langzeitbelastbarkeit sind die Proben zudem einer zyklischen, hydrodynamischen Belastung ( $9,5 \pm 0,5 \times 10^6$  Zyklen; 10,5 Tage) unter arteriellen Druckbedingungen (120 mmHg Spitzendruck) ausgesetzt worden.

In der Auswertung wurde deutlich, dass bovines Perikard bei vergleichbaren inter-individuellen Ergebnissen signifikante intra-perikardiale Unterschiede aufweist (s. Abbildung 4). Insbesondere die Dicke, die Faserausrichtung und die mechanische Belastbarkeit zeigten sowohl für das native als auch für das prozessierte Biomaterial nur in umschriebenen Arealen homogene Ergebnisse.

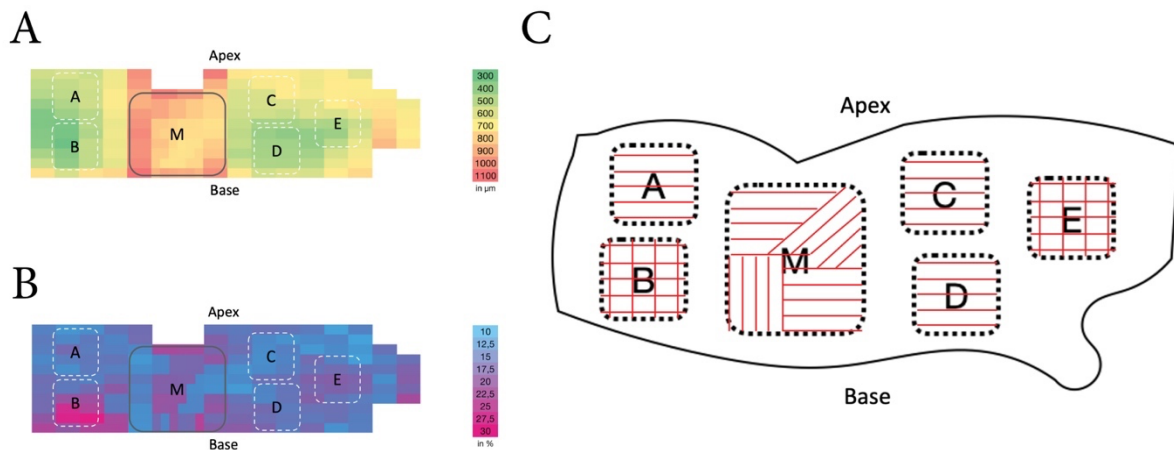


**Abbildung 4: Kartierung von Dicken und Faserausrichtungen an nativem, bovinem Perikard**

Es zeigen sich signifikante Dickenunterschiede (A) und interindividuelle Varianzen (Standardabweichungen einzelner Messpunkte; B) über die Perikarde. In der Faseranalyse (C) wurden unterschiedliche Bereiche mit ausgerichteten („A“, „C“ und „D“) und ungerichteten Fasern („B“ und „E“) detektiert.

Die histologische Aufarbeitung hingegen offenbarte keine relevanten lokalisationsbezogenen Unterschiede. Der Erfolg des DZ-Prozesses konnte durch die signifikante Reduktion des DNA-Gehaltes um 84 % ( $\bar{\varnothing}$  Nativ:  $72,14 \pm 34,63$  ng/mg Gewebe;  $\bar{\varnothing}$  DZ:  $11,59 \pm 4,39$  ng/mg Gewebe;  $p \leq 0,01$ ; s. Tabelle 1) und die Abwesenheit von Kernstrukturen in den histologischen Färbungen nachgewiesen werden. Im Rahmen der zyklischen Langzeitstestung kam es zu keinem „Implantatversagen“ und alle untersuchten Perikarde zeigten sich am Ende der Belastungssimulation intakt. Die dezellularisierten Proben erschienen makroskopisch jedoch etwas mürbe, was bei reduzierter mechanischer Belastbarkeit ( $F_{\max\text{-Belastungssimulation}}$ :  $19,3 \pm 10,44$  N vs.  $F_{\max\text{-DZ}}$ :  $26,84 \pm 17,73$  N; s. Tabelle 1) durch eine verminderte Dehnbarkeit (Belastungssimulation:  $36,6 \pm 13,3$  % vs. DZ:  $52,34 \pm 15,61$  %) quantifiziert werden konnte.

**Tabelle 1: DNA-Mengen und mechanische Belastbarkeiten nativer und dezellularisierter Perikarde**

DNA-Messungen (ng/mg Gewebe) der nativen und dezellularisierten Perikarde (DZ), sowie Erhebung der maximalen mechanischen Belastbarkeit (in N) in den 5 definierten Arealen („A“ – „E“). Angabe der Messungen als Mittelwerte  $\pm$  Standardabweichung. \* =  $p \leq 0,001$  im Vergleich zu den jeweiligen Nativwerten; † =  $p \leq 0,05$  im Vergleich zum Nativwert; # = signifikante Unterschiede ( $p \leq 0,05$ ) zwischen maximaler Längs- und Querbelastung der jeweiligen Gruppe.

Areal	DNA <sub>Nativ</sub> [ng/mg Gewebe]	DNA <sub>DZ</sub> [ng/mg Gewebe]	F <sub>max-Nativ</sub> [N]	F <sub>max-DZ</sub> [N]	F <sub>max-Belastung</sub> [N]
„A“	82,42 $\pm$ 49,59	12,37 $\pm$ 7,09*	23,82 $\pm$ 16 <sup>#</sup>	22,84 $\pm$ 15,71 <sup>#</sup>	17,85 $\pm$ 12,54
„B“	75,96 $\pm$ 28,15	10,76 $\pm$ 3,37*	31,85 $\pm$ 16,29	26,70 $\pm$ 10,51	16,57 $\pm$ 9,77
„C“	61,59 $\pm$ 30,52	11,09 $\pm$ 2,48*	26,36 $\pm$ 18,09 <sup>#</sup>	22,87 $\pm$ 18,41 <sup>#</sup>	17,62 $\pm$ 8,55
„D“	75,52 $\pm$ 31,39	11,54 $\pm$ 3,92*	40,98 $\pm$ 20,87	33,34 $\pm$ 20,59	15,58 $\pm$ 5,08
„E“	61,23 $\pm$ 24,39	12,16 $\pm$ 3,93*	30,06 $\pm$ 20,10	28,42 $\pm$ 20,13	28,86 $\pm$ 10,54
∅	72,14 $\pm$ 34,63	11,59 $\pm$ 4,39*	30,61 $\pm$ 19,15	26,84 $\pm$ 17,73	19,30 $\pm$ 10,44 <sup>†</sup>

Die durchgeführte Studie zeigte anhand signifikanter, intraperikardialer Unterschiede die Notwendigkeit einer sorgfältigen Materialelektion bei der Verwendung von bovinem Perikard. In Zusammenschau der Daten ist außerdem ersichtlich, dass die Berücksichtigung von histologischen Ergebnissen allein nicht ausreichend ist und das Hauptaugenmerk bei der Materialauswahl auf die mechanische Belastbarkeit gelegt werden sollte. Abschließend kann anhand aller gewonnenen Daten ein umschriebener Bereich, welcher sich auf den linken Ventrikel projiziert, zur Verwendung für kardiovaskuläre Implantate empfohlen werden.

### 3.2.2 Prozessierungsmethoden für biologische Materialien

*“Pericardial tissue for cardiovascular application: an in-vitro evaluation of established and advanced production processes”* (Grefen et al., 2018)

Autoren: Grefen L., König F., Grab M., Hagl C., **Thierfelder N.**

In der modernen kardiovaskulären Chirurgie hat sich der Einsatz von Perikard als Biomaterial zur Rekonstruktion oder als Gewebeersatz, beispielsweise bei Herzklappenerkrankungen, angeborenen Herzfehlern oder Gefäßdefekten, bewährt (Texakalidis et al., 2018, RJ et al., 2020, Li et al., 2020). Am häufigsten greift man dafür aufgrund seiner einfachen Verfügbarkeit und vorteilhafter biomechanischer Eigenschaften auf bovines Perikard zurück. Die Verwendung von Perikard anderer Spezies (z.B. equinen Ursprungs) lässt sich in der Literatur jedoch ebenso finden wie ein autologer

Einsatz beispielsweise bei der sogenannten Ozaki-Methode (Baird et al., 2020, Ellassal et al., 2021) oder bei der Rekonstruktion angeborener Herzfehler (RJ et al., 2020).

Zur Optimierung der Materialeigenschaften hinsichtlich der mechanischen Belastbarkeit (Aguiari et al., 2016, Yamashita et al., 2012), der Sterilisierung (Fidalgo et al., 2018, Walker et al., 2020) sowie zur Reduktion immunologischer Prozesse nach Implantation (Kim et al., 2016a) sind bereits eine Vielzahl an unterschiedlichen Behandlungsmethoden veröffentlicht worden und/oder im klinischen Einsatz. Aktuell werden dabei meist Fixierungslösungen (z.B. Glutaraldehyd) verwendet, aber auch Verfahren der Gewebe-DZ kommen neben chemischen Desinfektionslösungen immer häufiger zum Einsatz. Diese unterschiedlichen Verfahren zeigen individuelle Vor- und Nachteile, so dass eine direkte Gegenüberstellung der Ansätze untereinander unerlässlich ist.

Um einen umfassenden in-vitro Vergleich von unterschiedlichen Behandlungsmethoden bovinen Perikardes mittels Fixierung, DZ und Sterilisation zu erstellen, ist daher eine experimentelle Studie durchgeführt worden.

Als Rohmaterial diente dabei Rinderperikard eines lokalen Schlachthofes, welches den unterschiedlichen Versuchsgruppen zugeteilt wurde (jew. n = 5). Diese sind entweder mittels Glutaraldehyd (0,1 %) für 48 Stunden fixiert (Versuchsgruppe „GA“) oder in einem mehrschrittigen, vorbeschriebenen Verfahren (0,5 % DC und 0,5 % DS in PBS) über 16 Stunden dezellularisiert worden. Das Protokoll sah mehrere Zyklen von Detergentien- und Ultraschalleexposition, sowie zum Abschluss eine Serie von repetitiven Waschschritten mit PBS vor. Nach Abschluss des DZ-Prozesses sind die Perikarde entweder einem Fixierungsprozess unter genannten Bedingungen (s.o.; Versuchsgruppe „DZ-GA“) oder einer chemischen Sterilisation (0,5 % Octenidin gefolgt von 0,1 % Peressigsäure; Versuchsgruppe „DZ“) für jeweils eine Stunde zugeführt worden. Als Vergleichsgruppen dienten kommerziell erhältliches (als Medizinprodukt zugelassenes) equines, dezellularisiertes Perikard (Kontrollgruppe „KEP“), sowie mit demselben Verfahren behandeltes bovines Perikard (Kontrollgruppe „KBP“).

Zur Evaluation sind mechanische Belastungsuntersuchungen, rasterelektronenmikroskopische Aufnahmen, eine photometrische DNA-Quantifikation und Sterilitätsnachweise durchgeführt worden. In der histologischen Aufarbeitung konnte die EZM durch H&E, Movat-Pentachrom- und Pikrosiriusfärbungen beurteilt, sowie residuelle DNA durch DAPI-Fluoreszenz nachgewiesen werden. Zur Bestimmung der Biokompatibilität sind ferner humane Endothelzellen gewonnen und für 72 Stunden auf die gewonnenen Biomaterialien gegeben worden ( $3 \times 10^4$  Zellen/cm<sup>2</sup>). Die Auswertung dieser Proben erfolgt analog zu den unbesiedelten Perikarden.

Im Vergleich zu den gewonnenen Nativproben zeigte keines der prozessierten Perikarde in der histologischen Aufarbeitung offensichtliche Veränderungen oder Degenerationen der EZM durch den



Behandlungsprozess. In den dezellularisierten Versuchsgruppen konnten keine Zellkerne mehr angefärbt werden, was sich in der photometrischen DNA-Quantifizierung bestätigen ließ (s. Tabelle 2). Die geringsten Konzentrationen an residueller DNA zeigte die equine Kontrollgruppe. Im Gegensatz dazu offenbarte die bovine Kontrollgruppe interessanterweise sowohl im histologischen als auch quantitativen Nachweis große Mengen an verbliebener DNA im Gewebe. Passend dazu zeigten sich die bovinen Kontrollperikarde mit einer im Vergleich zu den Perikarden der Versuchsgruppen deutlich dickeren Materialstärke. Hinsichtlich der mechanischen Belastbarkeit war insgesamt keine Korrelation zur Perikarddicke zu erkennen und es konnten zwischen den Messwerten der Versuchs-, Kontroll- sowie den Nativproben keine signifikanten Unterschiede erhoben werden. Einzig die glutaraldehydfixierten Perikarde imponierten mit einer signifikant erhöhten Maximalbelastbarkeit sowohl längs als auch quer zur vorherrschenden Faserrichtung, was bisherige Ergebnisse unterstützt (Yamashita et al., 2012). In den Sterilitätsuntersuchungen konnte bei keiner der dezellularisierten Proben nach 14 Tagen Inkubation mikrobielles Wachstum nachgewiesen werden. Eine unzureichende Sterilisation durch die Glutaraldehydexposition zeigte sich sowohl nach Inkubation im Nährmedium als auch durch eine rasterelektronenmikroskopisch nachgewiesene bakterielle Besiedelung einiger Perikarde. In den Biokompatibilitätsuntersuchungen war es bei keiner der glutaraldehydbehandelten Proben möglich adhärente, lebende Endothelzellen nachzuweisen, entweder aufgrund von Unsterilität oder Zytotoxizität der Behandlung. Auf allen nur dezellularisierten Materialien wurde eine adhärente Zellschicht detektiert (s. Abbildung 5).

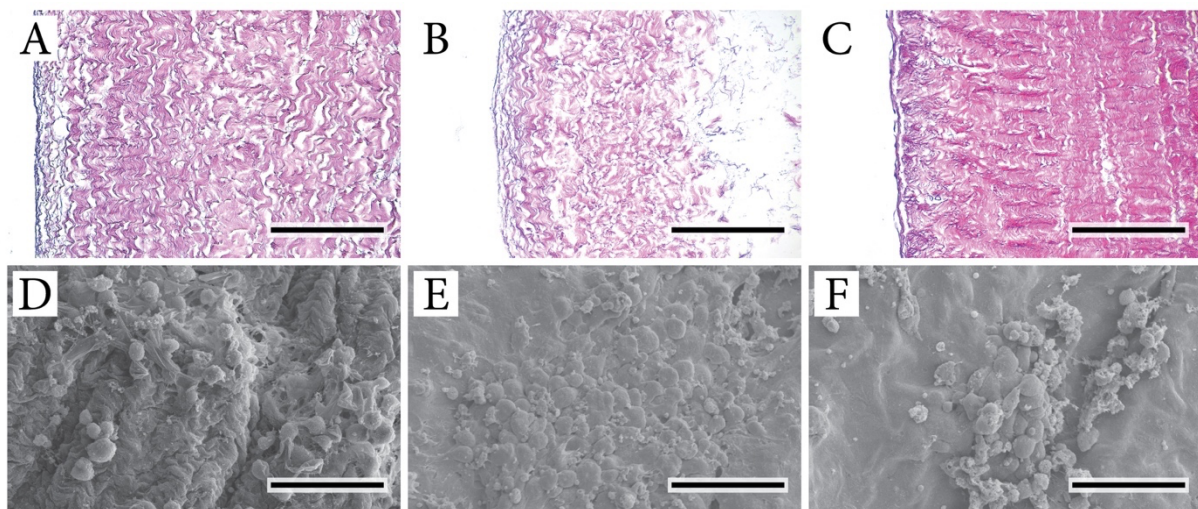


**Abbildung 5: Dezellularisierte, sterilisierte und zellbesiedelte Perikarde**

*Bovines Perikard der Versuchsgruppe (A + D), sowie das equine (B + E) und das bovine (C + F) Perikard der Kontrollgruppen zeigten nach Dezellularisierung und Sterilisation eine gute Zellularisierbarkeit. Es zeigte sich keine bakterielle Kontamination; A – C: H&E-Färbung, D – F: Elektronenmikroskopische Aufnahmen; Maßstabsbalken = 100 µm*

**Tabelle 2: Vergleich von Dicken, DNA-Gehalt und maximalen Belastbarkeiten dezellularisierter und fixierter Perikarde**

Es sind die Dicken, der DNA-Gehalt, sowie die maximale mechanische Belastbarkeit längs und quer zur Hauptfaserrichtung sowohl für native, fixierte („GA“) und dezellularisierte (sterilisiert: „DZ“ oder fixiert: „DZ-GA“) Perikarde als auch für equine („KEP“) und bovine („KBP“) Kontrollen gemessen worden. Angabe der Messungen als Mittelwerte  $\pm$  Standardabweichung. \* =  $p \leq 0,05$  im Vergleich zum jeweiligen Nativwert

Gruppe	Dicke [ $\mu\text{m}$ ]	DNA [ng/mg Gewebe]	F <sub>max-längs</sub> [N]	F <sub>max-quer</sub> [N]
Nativ	419,90 $\pm$ 84,77	85,19 $\pm$ 6,28	40,54 $\pm$ 3,30	33,70 $\pm$ 9,04
GA	258,53 $\pm$ 28,65	82,48 $\pm$ 6,12	73,78 $\pm$ 9,46*	67,66 $\pm$ 12,93*
DZ	451,10 $\pm$ 64,63	58,69 $\pm$ 4,06*	28,72 $\pm$ 3,80	11,96 $\pm$ 1,70
DZ-GA	374,01 $\pm$ 37,53	-	31,75 $\pm$ 10,55	15,20 $\pm$ 1,86
KBP	824,16 $\pm$ 159,50	70,60 $\pm$ 12,32	24,37 $\pm$ 3,10	25,24 $\pm$ 4,49
KEP	390,10 $\pm$ 38,95	38,51 $\pm$ 1,82	8,80 $\pm$ 1,14	4,54 $\pm$ 1,06

In Zusammenschau der experimentellen Ergebnisse konnte durch die Gewebe-DZ sowohl eine effektive Reduktion von zellulären Bestandteilen, insbesondere DNA, als auch eine bessere Biokompatibilität im Vergleich zur Glutaraldehydbehandlung erreicht werden. Kommerzielle equine, dezellularisierte Perikarde bestätigten diese Ergebnisse. Interessanterweise konnte in ebenso behandelten bovinen Perikarden der Kontrollgruppe keine effektive DZ erreicht werden, mutmaßlich zurückzuführen auf die deutlich höhere Materialdicke dieser Perikarde. Diese Beobachtung untermauernd, offenbarten sich bereits im gewonnenen Rohmaterial deutliche interperikardiale Unterschiede, was die Durchführung einer minutiösen Materialselektion und strengen Qualitätskontrolle in der Herstellung von perikardbasierten Implantaten zwingend notwendig erscheinen lässt.

### 3.2.3 Einflussfaktoren der Dezellularisation

*“Tissue-engineering acellular scaffolds – The significant influence of physical and procedural decellularization factors”* (Starnecker et al., 2018)

Autoren: Starnecker F., König F., Hagl C., **Thierfelder N.**

Im DZ-Prozess biologischer Gewebe kommt immer eine Kombination unterschiedlicher Methoden zum Einsatz (Boroumand et al., 2018). Diese beinhalten die Immersion oder Perfusion des Gewebes in, bzw. mit der DZ-Lösung, welche die chemischen (meist Detergentien) oder biologisch (z.B. DNase) aktiven



Substanzen enthält (Kawecki et al., 2017, Gilbert et al., 2006). Die Wirkung dieser Substanzen kann durch die Verwendung physikalischer Verfahren, wie Temperatur (Cheng et al., 2019) oder Ultraschall (Azhim et al., 2014) unterstützt werden. Es ist bekannt, dass zudem prozedurale Faktoren, wie beispielsweise repetitive Waschschritte, hinsichtlich der Biokompatibilität der generierten Materialien eine wichtige Rolle spielen (Cebotari et al., 2010).

Während der Einsatz unterschiedlichster Detergentien und die Auswirkung von biologischen Substanzen bereits vielfach systematisch untersucht wurden, sind über den Einfluss physikalischer und prozeduraler Faktoren auf die DZ-Effektivität bisher wenige Daten verfügbar.

Ziel der folgenden Studie war daher eine systematische Evaluation unterschiedlicher physikalischer und prozeduraler Einflussfaktoren auf die DZ porziner Aorten. Durch Protokollvariationen sollte die Auswirkung von Ultraschall, Immersionsregime und zyklischen Prozeduren untersucht werden.

Zur Versuchsdurchführung sind Segmente ( $n = 72$ ) der porzinen Aorta ascendens von einem lokalen Schlachtbetrieb bezogen und unterschiedlichen Versuchsgruppen zugeteilt worden. Die Gruppen wurden mittels einem von drei Immersionsregimen ( $G_C$ : Schüttelinkubation = Kontrollgruppe;  $G_1$ : Flussinkubation;  $G_2$ : Flussinkubation + Ultraschallexposition) entweder für 4 oder 8 Stunden kontinuierlich oder zyklisch behandelt (jeweils  $n = 6$ ). Zur Flusserzeugung ist eine handelsübliche Zentrifugalpumpe (10 l/min) eingesetzt worden und für die kontinuierliche Ultraschallexposition diente ein kommerzielles Ultraschallbad (120 W; 45 kHz). Als Detergentien kamen in dieser Studie DC (0,5 %) und DS (0,5 %) zu Einsatz. Alle Protokolle sind bei 37° C durchgeführt worden, wobei bei Ultraschalleinsatz aufgrund der generierten Abwärme eine aktive Kühlung eingesetzt werden musste. Gewaschen wurden die Materialien mit isotoner Natriumchloridlösung (0,9 %), bei den zyklischen Protokollen für jeweils 2 Stunden zwischen den DZ-Schritten und zum Abschluss aller Prozeduren jeweils zehnmal für 15 Minuten.

Zur Auswertung der Versuche sind die Proben einerseits histologisch aufgearbeitet und andererseits deren Topografie mittels Rasterelektronenmikroskopie untersucht worden. Nach der Anfertigung von Paraffinschnitten wurden diese entweder zur Darstellung der Zellkerne mittels H&E-Protokoll oder DAPI-Farbstoff angefärbt und zur Beurteilung der EZM mit den Übersichtsfärbungen Movats Pentrachrom oder Pikrosiriusrot behandelt. Zur Quantifizierung der DZ-Effektivität sind die Eindringtiefen der Detergentien im Querschnitt der Proben, ausgehend von deren Oberflächen (innen:  $ET_i$ ; außen:  $ET_a$ ) vermessen worden. Als Eindringtiefe ist dabei der zellfreie Bereich definiert worden, in dem keine DAPI-Fluoreszenz und keine Zellkerne in der H&E-Färbung mehr nachgewiesen werden konnten.

Basierend auf den Ergebnissen der genannten Versuchsgruppen ist im Anschluss ein weiteres Protokoll ( $G_3$ ) erstellt worden, um zu untersuchen, ob eine weitere Effektivitätssteigerung des DZ-Prozesses

durch Kombination der Methoden möglich ist. Dieses Protokoll beinhaltete eine leistungsfähigere Pumpe (20 l/min) für die DZ-Flüssigkeit, eine Ultraschallexposition von 30 Minuten zu Beginn jedes Inkubationsschrittes sowie die zyklische Exposition in den o.g. Detergentien (insg. 24 Stunden) und Natriumchlorid als Waschlösung. Als Material dienten wiederum porcine Aorten und die Auswertung ist analog zur bereits beschriebenen Methodik durchgeführt worden.

In der Auswertung zeigten sich sowohl erhebliche Unterschiede in der DZ-Effektivität der einzelnen Versuchsgruppen (s. Tabelle 3) als auch im Vergleich der DZ-Eindringtiefen von der luminalen Oberfläche zur Außenseite der Aortenstücke (außen  $61.3 \pm 6.5$  % höhere Eindringtiefe;  $p \leq 0,001$ ). Mittels physikalischer Modifikation der DZ-Protokolle ließ sich im Vergleich zur Kontrollgruppe durch die Flussinkubation ( $G_1$ : + 19 %;  $p \leq 0,05$ ) und mittels Ultraschall ( $G_2$ : + 49 %;  $p \leq 0,001$ ) jeweils eine signifikante Effizienzsteigerung der DZ erzielen. Die Änderung des Protokolls in eine zyklische Inkubation bei gleicher Dauer resultierte ebenfalls in einer signifikanten Steigerung der DZ-Effizienz ( $G_1$ : + 39 %,  $p \leq 0,001$ ;  $G_2$ : + 17 %,  $p \leq 0,01$ ;  $G_c$ : + 43 %,  $p \leq 0,001$ ). Durch die Kombination der unterschiedlichen Einflussfaktoren, d.h. Flussinkubation, Ultraschall und zyklische Behandlung, ließ sich die Effektivität sogar um maximal 74 % ( $p \leq 0,001$ ) steigern. Durch Verlängerung der Behandlungszeiten von 4 auf 8 Stunden erhöhten sich die gemessenen Eindringtiefen bei allen Versuchsproben. Insgesamt bestätigten sich dabei alle effizienzsteigernden Effekte ebenfalls durch signifikante Zunahmen der Eindringtiefen. Mittels spezifische Modifikation ( $G_3$ ) konnte die DZ-Effektivität um weitere 46 % ( $p \leq 0,001$ ) erhöht werden. In allen Versuchsproben deckten sich die Messergebnisse hinsichtlich der Eindringtiefen zwischen DAPI- und H&E-Färbung.

**Tabelle 3: Auswirkung physikalischer und prozeduraler Faktoren auf den DZ-Erfolg**

Quantitativer Vergleich der Auswirkung von Flussinkubation ( $G_1$ ), Ultraschall ( $G_2$ ), zyklischen Prozeduren („zyk.“) und Prozessdauer auf die DZ-Effektivität. In der Vergleichsgruppe ( $G_c$ ) ist ein konventionelles Immersionsverfahren durchgeführt worden. Alle Angaben sind als Mittelwerte  $\pm$  Standardabweichung in  $\mu\text{m}$  dargestellt und sind die Distanzen von der Innen- bzw. Außenoberfläche der Aorten (im Querschnitt gemessen) innerhalb derer kein DAPI-Signal detektiert werden konnte. \* =  $p \leq 0,05$  im Vergleich zu den jeweiligen Werten der Vergleichsgruppe; # =  $p \leq 0,05$  beim Einsatz zyklischer Inkubation; † =  $p \leq 0,05$  bei Verdopplung der Inkubationszeit.

Gruppe		4 Stunden	4 Stunden zyk.	8 Stunden	8 Stunden zyk.
		[ $\mu\text{m}$ ]	[ $\mu\text{m}$ ]	[ $\mu\text{m}$ ]	[ $\mu\text{m}$ ]
Außen (ET <sub>a</sub> )	$G_c$	213,1 $\pm$ 24,1	304,7 $\pm$ 18,1 <sup>#</sup>	452,6 $\pm$ 58,3 <sup>†</sup>	547,6 $\pm$ 91,9 <sup>#†</sup>
	$G_1$	253,2 $\pm$ 28,1 <sup>*</sup>	351,0 $\pm$ 33,4 <sup>#</sup>	514,3 $\pm$ 28,2 <sup>*†</sup>	493,7 $\pm$ 43,8 <sup>†</sup>
	$G_2$	317,1 $\pm$ 17,4 <sup>*</sup>	370,3 $\pm$ 32,8 <sup>#</sup>	519,6 $\pm$ 27,7 <sup>*†</sup>	600,4 $\pm$ 41,2 <sup>#†</sup>
Innen (ET <sub>i</sub> )	$G_c$	159,3 $\pm$ 33,2	180,0 $\pm$ 21,4	231,3 $\pm$ 67,2 <sup>†</sup>	341,8 $\pm$ 43,2 <sup>#†</sup>
	$G_1$	186,9 $\pm$ 15,4	179,1 $\pm$ 35,1	270,6 $\pm$ 106,6	370,6 $\pm$ 14,8 <sup>#†</sup>
	$G_2$	178,6 $\pm$ 60,8	244,1 $\pm$ 22,6 <sup>#</sup>	307,6 $\pm$ 82,9 <sup>†</sup>	384,5 $\pm$ 38,1 <sup>#†</sup>

Nach allen durchgeführten DZ-Prozeduren konnte anhand der histologischen Übersichtsfärbungen der Erhalt des mehrschichtigen Aufbaus der Aortenwände nachgewiesen werden. Die Struktur der Aortenwände erschien im Querschnitt nach der DZ an der Oberfläche etwas aufgelockert. Am ehesten war dies auf das Auswaschen der zellulären Bestandteile zurückzuführen. Insgesamt zeigten sich dabei aber sowohl kollagene als auch elastische Fasern in ihrer mikroskopischen Erscheinung unverändert. Mit Hilfe elektronenmikroskopischer Aufnahmen konnte die Freilegung der Faserstruktur der EZM durch die Behandlungen dargestellt werden. Relevante Schädigungen der sichtbaren Fasern waren jedoch nach keiner der beschriebenen DZ-Methoden erkennbar.

Anhand dieser systematischen Studie konnte nachgewiesen werden, dass sowohl physikalische als auch prozedurale Faktoren einen signifikanten Einfluss auf DZ-Prozeduren haben. So können durch den Einsatz von Ultraschall, zyklischen Prozeduren und aktiver Perfusion biologische Gewebe effektiver dezellularisiert werden.

*“Successful decellularization of thick-walled tissue: Highlighting pitfalls and the need for a multifactorial approach”* (Koenig et al., 2019)

Autoren: König F., Kilzer M., Hagl C., **Thierfelder N.**

Die erfolgreiche DZ biologischer Gewebe geht immer mit einer schwierigen Balance zwischen effektiver Zellentfernung und möglicher Schädigung der EZM einher. Um die Bestandteile der Zellen aus dem Gewebe zu entfernen, werden diese mittels eines Lösungsmittels, oft angereichert mit Detergentien, ausgewaschen (Guruswamy Damodaran and Vermette, 2018). Insbesondere bei dickeren, bindegewebsreichen und wenig vaskularisierten Materialien gestaltet sich deren Durchdringung mit dem DZ-Medium jedoch schwierig (González-Andrades et al., 2015). Im Kontext des kardiovaskulären TE sei hier insbesondere das Gewebe der Aortenwand genannt, welches einen hohen Anteil an kollagenen und elastischen Fasern zeigt, was eine schonende und effektive DZ herausfordernd macht (Sierad et al., 2015).

Es wurde daher angestrebt, einen multifaktoriellen Ansatz zur effektiven und schonenden DZ von Aortengewebe zu entwickeln.

Im Rahmen der in-vitro Studie sind porcine Aorten (n = 20) eines lokalen Schlachtbetriebes zufällig einer von drei Versuchsgruppen zugeordnet worden. Diese sind in unterschiedlich langen ( $G_1 = 24$  h,  $G_2 = 48$  h und  $G_3 = 72$  h), zyklischen Verfahren mittels den Detergentien DC und DS (jew. 0,5 % in PBS) unter Fluss und Ultraschallexposition dezellularisiert worden. Es folgten mehrere Waschschriffe mit isotoner Natriumchloridlösung (0,9 %), sowie Inkubationen mit DNase (30 U/ml; 24 h) und  $\alpha$ -Galaktosidase (0,1 U/ml; 24 h). Zur Quantifizierung der DZ-Effektivität wurden im Anschluss DAPI- und H&E-Färbung durchgeführt, sowie die residuelle DNA-Menge photometrisch bestimmt. Mittels Movat's Pentachrom- und Pirkrosirius-Rot-Färbung konnte die Integrität der EZM evaluiert werden. Eine immunhistochemische Färbung gegen  $\alpha$ -Gal-Epitope (Galactose-alpha-1,3-galactose), die Messung des Glykoaminoglykananteils der Gewebe und rasterelektronenmikroskopische Aufnahmen komplettierten die Versuchsauswertung.

Nach Abschluss der Versuche konnten bereits nach 24 Stunden in den meisten Aorten histologisch keine residuellen Zellen mehr nachgewiesen werden, einige Proben zeigten jedoch auch nach 48 Stunden noch verbliebene Zellreste in der DAPI-Färbung an. Erst nach 72 Stunden ließen sich in den Versuchsproben mit keiner der verwendeten Methoden mehr relevante Mengen an DNA nachweisen. Es zeigte sich, dass nur durch eine multifaktorielle Auswertung der Proben verlässliche Resultate erhoben werden konnten, da beispielsweise in der H&E-Färbung oft bereits keine Zellkerne mehr erkennbar waren, während sich diese in der DAPI-Färbung klar darstellten (s. Abbildung 6).

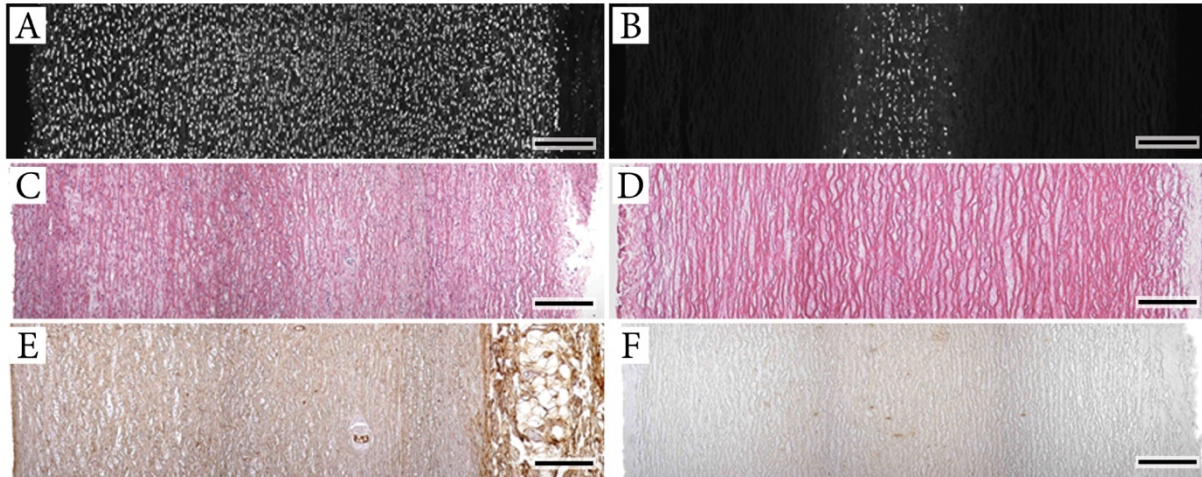


**Abbildung 6: Histologischer Nachweis unzureichender Dezellularisierung an porcinen Aorten**

Die histologischen Färbungen von nativen Aorten zeigen eine homogene Zellkernverteilung (A + C) und den Nachweis von  $\alpha$ -Gal-Epitopen (E); Nach 24-stündiger DZ und DNase-Behandlung ( $G_1$ ) stellen sich in der DAPI-Färbung (B) noch deutliche DNA-Reste dar, diese sind mittels H&E-Färbung nicht mehr zu detektieren (D); Auch nach 72-stündiger DZ ( $G_3$ ) sind noch  $\alpha$ -Gal-Epitope nachweisbar, insbesondere in der Vasa vasorum der porcinen Aorten (F); A + B: DAPI-Fluoreszenzfärbung, C + D: H&E-Färbung, E + F: Immunhistochemische Färbung gegen  $\alpha$ -Gal-Epitope (braun); Maßstabsbalken = 100  $\mu$ m

Auch die, eigentlich als sehr sensitive Methode bekannte, photometrische DNA-Quantifizierung scheiterte daran, einzelne verbliebene Zellen oder DNA-Reste verlässlich zu detektieren (DNA-Gehalt in ng/mg Gewebe:  $G_1$ :  $38,07 \pm 18,24$ ;  $G_2$ :  $31,53 \pm 27,49$ ;  $G_3$ :  $27,43 \pm 18,53$ ; Nativ:  $453,39 \pm 83,96$ ; s. Abbildung 7). Hier zeigte sich auch der signifikante Einfluss der DNase-Exposition ( $366,13 \pm 102,51$  vs.  $38,07 \pm 18,24$  ng/mg Gewebe nach 24 Stunden DZ;  $p \leq 0,05$ ). Insgesamt stellte sich die entwickelte DZ-Methode für alle Versuchsgruppen als schonende dar, da anhand der histologischen Übersichtsfärbungen und den rasterelektronenmikroskopischen Aufnahmen visuell keine Schädigung der Gewebe festgestellt werden konnte. Ein primär signifikanter Verlust von Glykosaminoglykanen (GAG) durch die DZ nahm jedoch auch bei längerer Behandlung in keinem relevanten Ausmaß zu (Im Vergleich zu Nativ:  $G_1$ :  $-48,63 \pm 37,7$  %;  $G_2$ :  $-56,38 \pm 18,12$  %;  $G_3$ :  $-50,01 \pm 37,44$  %; s. Abbildung 7). Die Inkubation mit  $\alpha$ -Galaktosidase erwies sich als effektiv und konnte das Antigen insbesondere bei längeren DZ-Dauern stark reduzieren. Insbesondere im Bereich der Vasa vasorum der porcinen Aorten waren jedoch in allen Versuchsgruppen residuelle  $\alpha$ -Gal-Epitope nachweisbar.

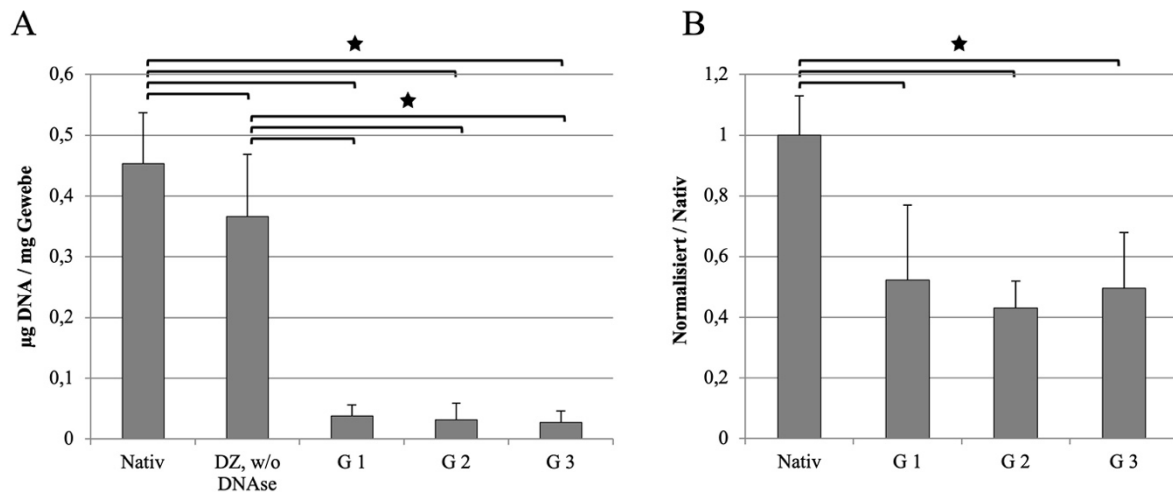


**Abbildung 7: Quantitativer DNA- und GAG-Nachweis in porzinen Aorten**

Photometrische DNA-Quantifikation (A) der Nativproben, sowie nach 24-stündiger DZ ohne DNase (DZ, w/o DNase) und nach jeweils 24 (G1), 48 (G2) und 72 Stunden (G3) mit DNase-Inkubation; Kolorimetrische GAG-Messung (B) der Versuchsgruppen G<sub>1-3</sub>; \* =  $p \leq 0,001$ .

Durch die entwickelten multifaktoriellen Protokolle war somit eine zuverlässige und EZM-schonende DZ von porzinen Aorten in einem Zeitraum von 72 Stunden reproduzierbar möglich. Da sich jedoch die vollständige Entfernung der immunologisch hoch-relevanten  $\alpha$ -Gal-Epitope als schwierig gestaltete, sollte über die Verwendung von Gewebe von knock-out Tieren nachgedacht werden (Wilczek et al., 2015), um inflammatorische Reaktionen zu reduzieren. Hohe biologische Varianzen und mangelnde Sensitivität mancher Auswertungsmethoden zeigen die Notwendigkeit einer umfangreichen Qualitätssicherung bei der Herstellung dezellularisierter Implantate auf.

### 3.3 Innovationen und neue Lösungsansätze

#### 3.3.1 Eine alternative Zellquelle

*“The cardiotomy reservoir – a preliminary evaluation of a new cell source for cardiovascular tissue engineering”* (Nathusius et al., 2018)

Autoren: von Nathusius S., König F., Sodian R., Born F., Hagl C., **Thierfelder N.**

Neben einem adäquaten Zellträger müssen im „klassischen“, bzw. in-vitro TE auch entsprechende Zellen eingesetzt werden (Chaudhuri et al., 2017). Diese können aus einer Vielzahl an Quellen gewonnen werden und sind mit unterschiedlichsten Vor- und Nachteilen behaftet. So bieten embryonale Stammzellen eine nahezu universelle Differenzierbarkeit, zeigen jedoch ein gewisses Entartungspotential und werden darüber hinaus gelegentlich ethisch-moralisch kontrovers diskutiert (Volarevic et al., 2018). In vielen Ländern ist ihre Gewinnung und Verwendung daher verboten oder stark eingeschränkt. Postembryonale Stammzellen, zu denen adulte und induzierte Stammzellen gezählt werden, unterliegen weniger ethischen Bedenken und können daher unter geringeren ethischen Restriktionen verwendet werden (Ohnuki and Takahashi, 2015). Sie sind jedoch in ihrer Differenzierbarkeit eingeschränkt. Adulte, ausdifferenzierte Zellen, die zu den somatischen Zellen gehören, stellen die dritte Zellgruppe dar. Sie sind durch ihre Differenzierung in einen bestimmten Zelltypus für ein bestimmtes Gewebe und entsprechende Funktionen spezifisch (Jana et al., 2016). Meist kommen sie in großer Anzahl vor und sind ohne Restriktionen einsetzbar, was sie für die Verwendung im TE auszeichnet. Im Bereich des kardiovaskulären TE kommen vielfach adulte, differenzierte Zellen zum Einsatz (A. M. Schnell, 2001). Diese müssen jedoch durch einen extra Eingriff gewonnen werden oder als Ausschuss bei geplanten Operationen (z.B. Gefäßreste bei aortokoronaren Bypass-Operationen) anfallen.

Ziel einer experimentellen Studie war daher zu evaluieren, ob Endothelzellen und Fibroblasten zur Verwendung im kardiovaskulären TE auch im Rahmen der extrakorporalen Zirkulation einer herzchirurgischen Operation gewonnen werden können.

Die experimentelle Studie wurde im Zusammenhang mit konventionellen, offenen herzchirurgischen Operationen durchgeführt. Dabei sind bei 10 Patienten 20 ml heparinisiertes Vollblut im letzten Drittel der Operation aus der extrakorporalen Zirkulation entnommen und nach Beendigung der OP die Kardiotomiereservoirs der Herz-Lungen-Maschinen verwendet worden. Aus dem Kardiotomiereservoirs wurden nach Ende der Operationen die enthaltenen Filter herausgetrennt und diese entweder direkt in eine Petrischale mit Zellkulturmedium gegeben oder die Zellen mittels Waschung und Dichtegradientenzentrifugation daraus isoliert. In mehreren Schritten sind die

Bestandteile des Vollblutes durch Zentrifugation voneinander getrennt und das Zellpellet mononukleärer Zellen gewaschen worden. Nach der Kultivierung fand die Identifikation der Zellen und die Evaluation zur Eignung im kardiovaskulären TE statt. Zur Typisierung wurden die Zellmorphologie beurteilt und immunhistologische, bzw Immunfluoreszenz-Färbungen gegen CD31, von Willebrand-Faktor (vWF; endothelzellspezifisch) und TE-7 (fibroblastenspezifisch), sowie SMC-Myosin und VE-Cadherin angefertigt. Mit Hilfe von Tetrazoliumassays (WST-1) konnten Vitalität und Wachstumsraten der einzelnen Zellkulturen evaluiert werden. Durch eine zweizeitige Besiedelung von faserigen Polyurethanscaffolds mit den gewonnenen Zellen ( $7,5 \times 10^5$  Zellen/cm<sup>2</sup>) wurde abschließend deren Eignung für den Einsatz im TE untersucht. Nach 14 Tagen statischer Kultivierung sind die zellularisierten Konstrukte Rasterelektronenmikroskopie sowie Immunfluoreszenz- und Vitalitätsfärbung unterzogen worden.

Mittels der durchgeführten Isolationsmethoden war es möglich, Fibroblasten (n = 7 / 10) und Endothelzellen (n = 3 / 10) aus der Herz-Lungen-Maschine zu gewinnen. Anhand von entsprechenden immunzytologischen Färbungen und ihrer typischen Morphologie (Endothelzellen = Pflastersteinrelief, Fibroblasten = spindelförmig) konnten die Zellen identifiziert werden (s. Abbildung 8).

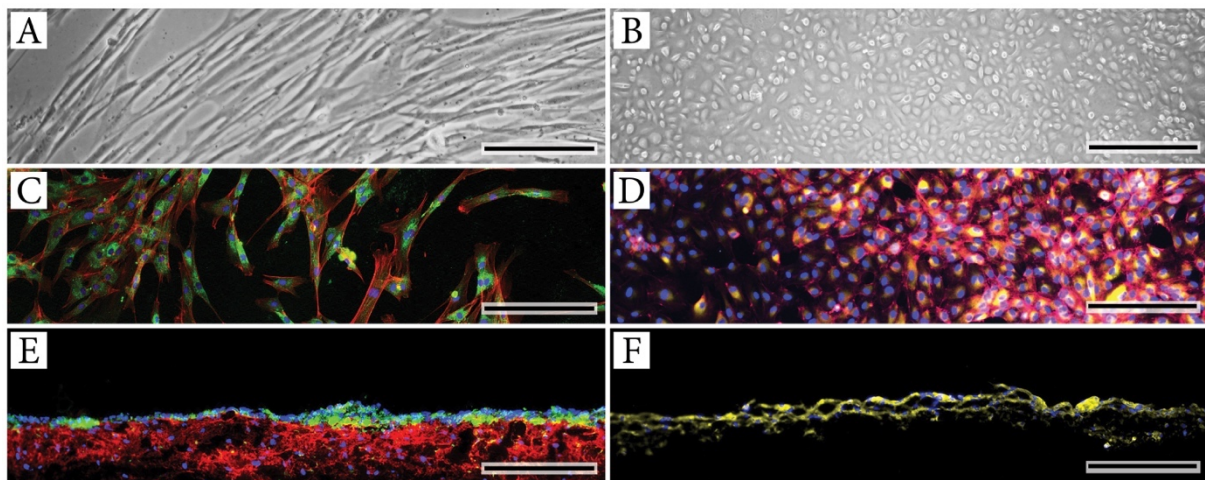


**Abbildung 8: Isolation und TE-Anwendung von Fibroblasten und Endothelzellen aus dem Kardiotomiereservoir**

Aus den Kardiotomiereservoirs ließen sich erfolgreich Fibroblasten (A + C) und Endothelzellen (B + D) isolieren. Diese konnten konfluent auf ein Polyurethanscaffold gesiedelt (E) und der Aufbau einer EZM nachgewiesen werden (F). A + B: Hellfeldmikroskopie (Phasenkontrast); C – F: Immunfluoreszenzfärbungen (blau = Zellkerne, grün<sub>C</sub> = TE-7, grün<sub>E</sub> = Endothelzellen, gelb<sub>D</sub> = vWF, gelb<sub>F</sub> = Kollagen IV, rot<sub>C+D</sub> = Aktin, rot<sub>E</sub> = Fibroblasten); Maßstabsbalken: A + B = 100 µm, C – F = 200 µm

Proliferationsuntersuchungen zeigten hohe Wachstumsraten, welche nicht mit klinischen Daten (EuroScore II:  $1,7 \pm 1,1$  %) und Patientencharakteristika (z.B. Alter:  $66,7 \pm 10,1$  Jahre; Bypasszeit:  $129,3 \pm 38,4$  Minuten) zu korrelieren waren. In der elektronenmikroskopischen Untersuchung konnten konfluente Zellschichten auf den besiedelten Polymerscaffolds nachgewiesen werden. Diese korrelierten in den Immunfluoreszenzfärbung mit einem zweischichtigen Zellüberzug aus den



genannten Endothelzellen und Fibroblasten. Die Vitalitätsfärbung zeigte dabei einen Anteil lebender Zellen von  $88,9 \pm 9,9$  %. Zusätzlich wurde anhand weiterer positiver Färbungen gegen Kollagen IV, Laminin und Fibronectin der Aufbau einer intakten EZM bestätigt.

Es konnte somit eindeutig nachgewiesen werden, dass die extrakorporale Zirkulation im Rahmen von herzchirurgischen Eingriffen zur Zellgewinnung genutzt werden kann. Diese Zellen eignen sich für den Einsatz im kardiovaskulären TE und könnten insbesondere in der mehrstufigen Therapie von komplexen, angeborenen Herzfehlern Anwendung finden. Hier bietet sich die Gewinnung in der Initialoperation an, um anschließend mit Hilfe der isolierten Zellen ein tissue-engineertes Konstrukt zu erstellen und dieses in einer weiteren oder der finalen Korrekturoperation einzusetzen.

### 3.3.2 Neuartige Qualitätssicherung im Tissue Engineering

*“Noninvasive analysis of synthetic and decellularized scaffolds for heart valve tissue engineering”*

(Haller et al., 2013)

Autoren: Haller N., Hollweck T., **Thierfelder N.**, Schulte J., Hausherr J.M., Dauner M., Akra B.

Medizinprodukte, und damit auch tissue-engineerte Implantate, unterliegen höchsten Qualitätsstandards, was sich in klar definierten Produktionsprozessen und strengen, genormten Qualitätssicherungsmaßnahmen widerspiegelt (Yano et al., 2018, Galgon, 2016). Diese Maßnahmen beinhalten neben einer lückenlosen Dokumentation der Prozesse meist auch nicht-invasive Prüfungen (z.B. Geometrie oder Ramanspektroskopie) und können bei invasiven Messungen (z.B. Maximalkraftbestimmung, Histologie oder zytologische Untersuchungen) bis zur Zerstörung einzelner Produkte gehen (Zuncheddu et al., 2021). Da beim in-vitro TE einzelne, individualisierte Implantate in langwierigen und teuren Produktionsverfahren hergestellt werden, erscheint es nicht sinnvoll, diese invasiven oder gar zerstörenden Prüfmethode zu unterziehen.

Im Rahmen einer in-vitro Studie sollte daher die Eignung von  $\mu$ -CT-Aufnahmen als neuartige Qualitätssicherungsmaßnahme im Herstellungsprozess von tissue-engineerten Herzklappenprothesen untersucht werden.

Als Herzklappengerüste dienten ein faseriges Polyurethanpolymer ( $\varnothing$  18 mm), ein humanes Aortenklappenhomograft ( $\varnothing$  19 mm) und eine kommerziell erhältliche, porcine Herzklappenprothese ( $\varnothing$  19 mm; Medtronic Freestyle®). Die biologischen Herzklappen sind zunächst einem DZ-Prozess (0,5 % DC + 0,5 % DS) unterzogen worden und im Anschluss, wie die synthetische Klappe, in einem zweistufigen Verfahren mit humanen Fibroblasten und Endothelzellen besiedelt worden ( $1,5 \times 10^6$

Zellen/cm<sup>2</sup>). Die Zellen wurden zuvor mittels enzymatischer Isolation aus Reststücken der Vena saphena magna nach aortokoronaren Bypass-Operationen gewonnen. Zur Auswertung sind unter sterilen Bedingungen native, dezellularisierte und zellbesiedelte Herzklappenprothesen in einem  $\mu$ -Computertomographen (120 kV; 150  $\mu$ A) durchleuchtet worden. Das Verfahren ermöglichte eine allgemeine räumliche Auflösung von 35  $\mu$ m mit einer Detailauflösung von 9  $\mu$ m in umschriebenen Bereichen. Zu Vergleichbarkeit mit etablierten Methoden wurden die Proben außerdem der invasiven und destruktiven (= Fixierung) Analyse mittels Rasterelektronenmikroskopie und immunhistochemischen Färbungen unterzogen.

Histologische Färbungen zeigten die Zellfreiheit der biologischen Herzklappenprothesen nach dem DZ-Schritt und konnten anhand der zelltypspezifischen, immunologischen Anfärbung von Endothelzellen und Fibroblasten eine erfolgreiche Re-Zellularisierung nachweisen. Dies wurde durch den Nachweis von konfluenten Zellschichten in elektronenmikroskopischen Aufnahmen zu diesem Zeitpunkt bestätigt. Im Rahmen der  $\mu$ -CT-Auswertung konnte bei der kommerziell erhältlichen Herzklappenprothese durch den DZ-Prozess eine Volumenabnahme von 0,5 %, gefolgt von einem Volumenanstieg von 8,6 % nach der Zellbesiedelung detektiert werden (s. Abbildung 9).

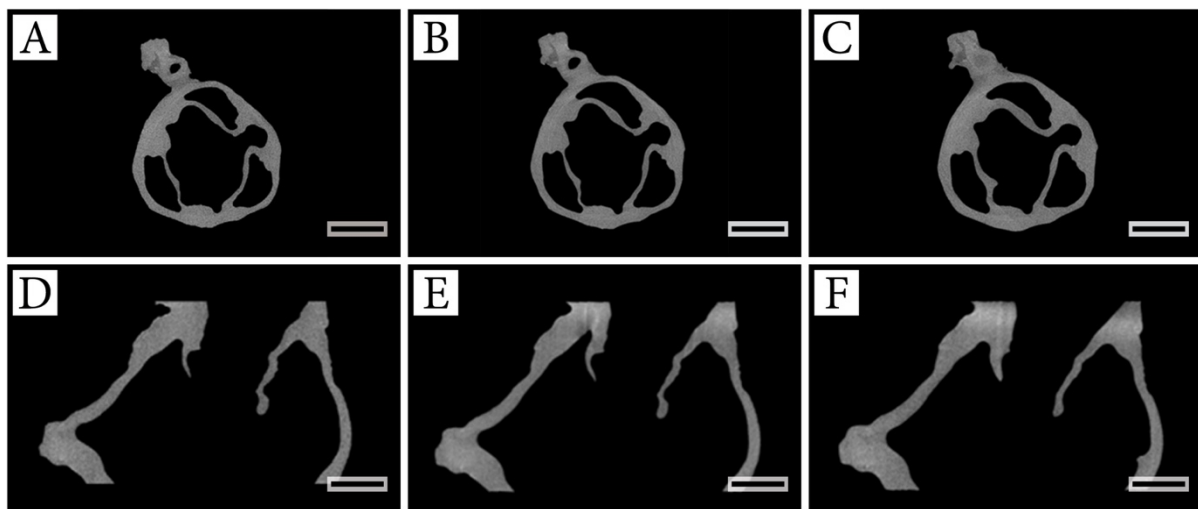


**Abbildung 9:  $\mu$ -CT-Aufnahmen einer tissue-engineerten Herzklappenprothese**

*Mit der nicht-invasiven Analysemethode können deutliche Dickenänderungen einer biologischen Herzklappenprothese (A + D) nach DZ (B + E) und insbesondere nach anschließender Zellbesiedelung (C + F) dargestellt werden. Im Bereich der mittleren Segel ist dies am eindrucklichsten nachzuvollziehen; Maßstabsbalken = 10 mm*

Dickenmessungen der Herzklappensegel bestätigten diese Daten (exemplarisch: nativ = 0,36 mm; dezellularisiert = 0,26 mm; re-zellularisiert = 0,63 mm), welche sich in der Untersuchung der humanen Homografts vergleichbar zeigten. Auch in der computertomografischen Untersuchung der Polymerherzklappen konnte die Zellbesiedelung eindeutig nachgewiesen und in den entsprechenden Bildern sogar visuell nachvollzogen werden. In der kumulativen Analyse wurde auf einem

Oberflächenanteil von 90 % der Herzklappe eine Dickenzunahme um 210 µm und mehr nachgewiesen, was als ein klarer Indikator für eine konfluente Zellschicht in diesen Bereichen zu werten ist.

Die erhobenen Daten zeigen die Möglichkeit, mittels µ-CT-Aufnahmen Zellbeschichtungen von tissue-engineerten Herzklappenprothesen nachzuweisen und bestätigen damit die Eignung dieser Analyseverfahren zur Qualitätssicherung anhand von Dicken- und Volumenänderungen.

### 3.3.3 Standardisierung und Kostenreduktion

*“Customized 3D-Printed Bioreactors for Decellularization – High Efficiency and Quality on a Budget”*  
(Grab et al., 2021)

Autoren: Grab M., Stieglmeier F., Emrich J., Grefen L., Leone A., König F., Hagl C., **Thierfelder N.**

Die DZ biologischer Gewebe zur Verwendung als medizinisches Implantat stellt sich meist als zeit- und arbeitsaufwändiger Prozess dar (He et al., 2017, Ghassemi et al., 2019, Gilpin et al., 2014). Insofern ist es folgerichtig, dass nach Möglichkeiten gesucht wird, diese Prozesse zu vereinheitlichen und zu automatisieren, meist unter der Zuhilfenahme von spezialisierten Bioreaktoren (Choudhury et al., 2020). Aufgrund der Fertigung von Bioreaktoren meist als Prototypen, selten in der Kleinserie, sind die Kosten beim Einsatz konventioneller maschinenbaulicher Verfahren (beispielhaft: drehen, bohren, fräsen und schleifen) sehr hoch.

Ziel der folgenden Studie war es daher, zwei kostengünstige Systeme zur DZ von Perikard und großlumigen Gefäßen zu konzipieren, mittels additiver Fertigung herzustellen und im Vergleich mit konventionellen DZ-Verfahren zu validieren. Weitere Anforderungen waren der Einsatz eines biokompatiblen Werkstoffes und die gleichzeitige Prozessierung von mindestens 5 Proben während eines DZ-Vorgangs.

Zunächst sind im CAD-Verfahren („Computer aided design“; Solidworks®) zwei kastenförmige Reaktoren konzipiert und deren Durchströmung mit Prozessflüssigkeit in einer CFD-Analyse („Computational fluid dynamics“; Ansys Workbench 2019 R2) analysiert worden (s. Abbildung 10). Hierbei lag der Fokus auf einer gleichförmigen Exposition der Biomaterialien gegenüber den DZ-Flüssigkeiten. Im Rahmen einer Materialanalyse wurden zudem Polymilchsäure (PLA; Ultimaker) und ein Silikonpolymer (AR-M2; Keyence) hinsichtlich ihrer Biokompatibilität, Kosten, Druckeigenschaften und Oberflächencharakteristik miteinander verglichen. Anhand der erhobenen Daten konnten präferierte Design-, Material- und Druckeigenschaften erhoben und die entworfenen Bioreaktoren im FDM-Verfahren („Fused deposition modeling“) aus PLA 3D-gedruckt (Ultimaker 3 extended) werden.

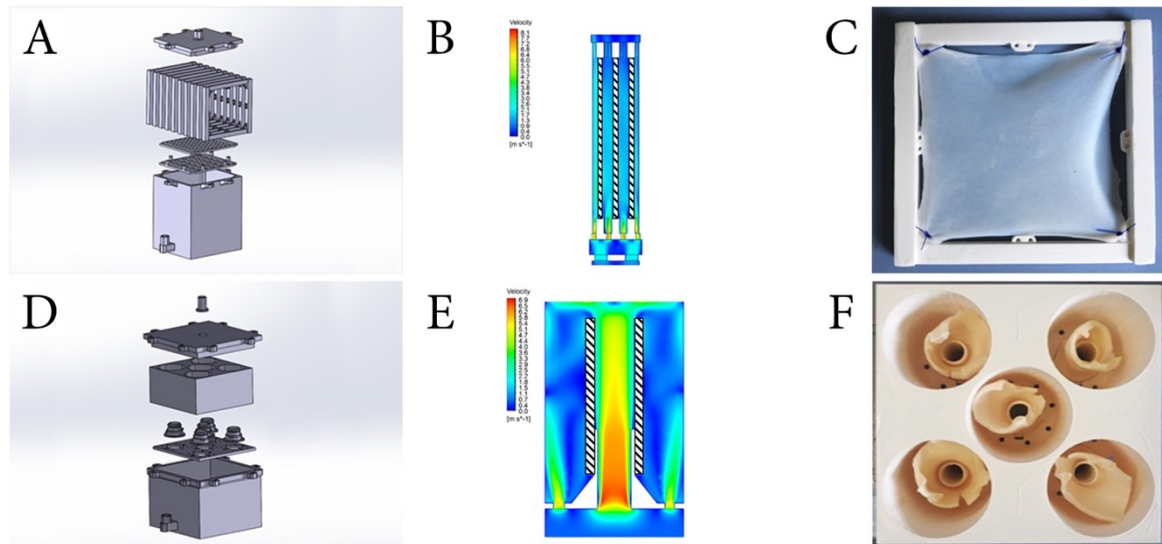


**Abbildung 10: 3D-gedruckte Bioreaktoren zur Dezellularisierung von Perikarden und Aorten**

Bioreaktoren zur DZ von Perikarden (A – C) und Aorten (D – F); Explosionszeichnung mit Darstellung aller Einzelbauteile der CAD-designten Bioreaktoren (A + D); Flusssimulation (CFD) zur Beurteilung der Exposition der Gewebe gegenüber der Prozessflüssigkeit (B + E); Probenhalterungen mit einem Perikard (C) bzw. fünf Aorten (F).

Abschließend sind zur in-vitro Validierung bovine Perikarde (n = 10) und porcine Aortenstücke (n = 10) in einem dynamischen Verfahren unter Detergentienexposition (0,5 % DC + 0,5 % DS) dezellularisiert worden. Die Probenevaluation wurde mittels Rasterelektronenmikroskopie, histologischen Färbungen, uniaxialen Zugversuchen und photometrischer DNA-Quantifizierung durchgeführt. Die Kontrollgruppe aus Perikard- und Aortenproben (jew. n = 10) ist mit einem konventionellen Immersionsverfahren behandelt worden.

Es war möglich, im CAD-Verfahren zwei unterschiedliche Bioreaktorsysteme mit einer DZ-Kapazität von 10 Perikarden, bzw. 5 Aortenstücken zu konzipieren. Durch den Einsatz perforierter Einstromplatten zeigten sich in der CFD-Analyse gerichtete und homogene Flussmuster entlang der Proben (Perikarde:  $1,784 \pm 0,064$  m/s; Aorten<sub>luminal</sub>:  $5,547 \pm 0,2$  m/s, Aorten<sub>extraluminal</sub>:  $0,540 \pm 0,152$  m/s). In der Materialanalyse konnten eine vergleichbare maximale Zugbelastbarkeit (PLA: 49,5 MPa; AR-M2: 40 – 55 MPa), eine höhere Zytotoxizität des Silikonpolymers nach 48 Stunden Inkubation (PLA:  $-10,7 \pm 8,9$  % Zellvitalität vs. AR-M2:  $-85,6 \pm 25,7$  % Zellvitalität) sowie signifikante Unterschiede hinsichtlich der Beschaffungskosten (PLA: 53,27 €/kg vs. AR-M2: 449,33 €/kg) erhoben werden. Die Materialien zeigten sich gegenüber der Exposition mit 70 %-igem Ethanol zur Desinfektion inert. Die Kosten des 3D-Druckmaterials betragen 20,13 € für den Bioreaktor zur Perikard-DZ (kum. Druckzeit: 87:50 Stunden), bzw. 22,07 € für das System zur Aortenprozessierung (kum. Druckzeit: 108:00 Stunden).

Die Validierung der Bioreaktorsysteme zeigte für beide Aufbauten eine hochsignifikante Reduktion der DNA-Menge (s. Tabelle 4) während der DZ (DNA-Gehalt in ng/mg Gewebe: in Perikard:  $135,2 \pm 62,7$  ->

6,35 ± 4,4; p ≤ 0,001; Aortenstücke: 217,6 ± 86,5 → 23,8 ± 4,2; p ≤ 0,001). In den Kontrollgruppen konnte für die DZ von Perikarden eine ähnliche und signifikante Reduktion (DNA: 1,5 ± 1,8 ng/mg Gewebe; p ≤ 0,001) erhoben werden, während im Aortengewebe kein relevanter Effekt deutlich wurde (DNA: 251,1 ± 86,4 ng/mg Gewebe). Die genannten Messwerte korrelierten mit der histologischen Aufarbeitung zum Nachweis von Nukleinsäure mittels DAPI-Färbung. In weiteren Färbungen (Pikrosirius Rot, H&E und Movat's Pentachrom) und rasterelektronenmikroskopischen Aufnahmen konnte kein schädigender Einfluss der DZ-Prozeduren auf die EZM der Biomaterialien nachgewiesen werden. Dies bestätigte sich durch vergleichbare Werte der unterschiedlichen Perikard- und Aortenversuchsgruppen in der maximalen mechanischen Belastbarkeit.

**Tabelle 4: DNA-Reduktion durch die 3D-gedruckten Bioreaktoren**

Messung der DNA-Menge in Aorten und Perikardgewebe vor und nach DZ mit den 3D-gedruckten Bioreaktoren (DZ-Bioreaktor) sowie mit Hilfe konventioneller Immersionstechnik (Kontrollgruppe). Angabe der Messungen als Mittelwerte ± Standardabweichung. \* = p ≤ 0,001

Versuchsgruppe	Perikard		Aorta	
	DNA <sub>Nativ</sub> [ng/mg Gewebe]	DNA <sub>DZ</sub> [ng/mg Gewebe]	DNA <sub>Nativ</sub> [ng/mg Gewebe]	DNA <sub>DZ</sub> [ng/mg Gewebe]
DZ-Bioreaktor	135,2 ± 62,7	6,35 ± 4,4*	217,6 ± 86,5	23,8 ± 4,2*
Kontrollgruppe	112,9 ± 47,8	1,5 ± 1,8*	236,7 ± 89,4	251,1 ± 86,4

In einem interdisziplinären Entwicklungs- und Validierungsansatz war es somit möglich, zwei kostengünstige und effiziente Bioreaktormodelle zur DZ von bovinem Perikard und porcinen Aortensegmenten herzustellen. Im Vergleich zu herkömmlichen Prozessierungsmethoden zeigten sich die neuentwickelten Systeme bei besserer Prozesskontrolle hinsichtlich ihrer Effektivität gleichwertig oder überlegen.

### 3.3.4 Hydrogele als alternative Scaffolds

*“Tuning Tissue Ingrowth into Proangiogenic Hydrogels via Dual Modality Degradation”* (Chokoza et al., 2019)

Autoren: Chokoza C., Gustafsson CA., Goetsch KP., Zilla P., **Thierfelder N.**, Pisano F., Mura M., Gnechi M., Bezuidenhout D., Davies NH.

Eine weitere große Gruppe von funktionellen Scaffolds zum Einsatz im (kardiovaskulären) TE stellen sog. Hydrogele dar (Gomez-Florit et al., 2020). Durch ihren strukturellen Aufbau aus langen, zum Teil verzweigten Polymeren mit hydrophilen Gruppen sind sie in der Lage, große Mengen an Wasser aufzunehmen und imitieren so morphologisch die EZM. Neben natürlichen Bestandteilen der EZM wie beispielsweise Hyaluronsäure (Chircov et al., 2018) oder Chondroitin (Yang et al., 2020), werden Hydrogele für das TE dafür auch auf Basis von Polyethylenglykol (PEG) hergestellt (Zhu, 2010).

Bei der Wahl eines entsprechenden Scaffolds für einen TE-Ansatz muss im Kontext der späteren Anwendung auch immer berücksichtigt werden, ob dieses biostabil oder abbaubar sein soll (Zhang and King, 2020, Jana et al., 2014). Die Abbaubarkeit der Materialien wird dabei durch die Degradationsrate bestimmt und hat im Allgemeinen Auswirkungen auf die Persistenz im Körper, beeinflusst im Speziellen aber auch die Infiltration von Zellen in das Material selbst.

Ziel einer experimentellen Studie war daher zu untersuchen, wie sich die Degradationsrate eines PEG-Hydrogels biochemisch steuern lässt und welche Auswirkungen dies in-vivo auf Gewebeeinfiltration und Neoangiogenese hat.

Hierfür sind zwei unterschiedliche biochemische Mechanismen gewählt worden: Der hydrolytische Abbau, welcher an bestimmten Acrylatgruppen stattfinden kann, sowie die Implementierung matrixmetalloproteinasespezifischer Peptid-Querverbindungen (Sequenz: GCREGPQGIWGQERCQ) zwischen den PEG-Molekülen zur proteolytischen Degradation. Über unterschiedliche Mischungsverhältnisse zweier PEG-Typen, eines mit Vinylsulfon- (PEG-VS; biostabil) das andere mit den genannten Acrylatgruppen (PEG-AC; hydrolytisch abbaubar) modifiziert, wurde angestrebt, die Geschwindigkeit der Materialdegradation zu steuern. Zur weiteren Modifikation und für ein optimiertes EZM-Mimikry sind an die Polymere definierte Polypeptide (Sequenz: GCGYGRGDSPG) und Heparin kovalent gebunden worden.

Für die Versuche sind 5 Gruppen mit jeweils unterschiedlichen Konzentrationen der PEG-AC- mit PEG-VS-Polymeren gemischt (PEG-AC<sub>100</sub>: 100/0; PEG-AC<sub>75</sub>: 75/25; PEG-AC<sub>50</sub>: 50/50; PEG-AC<sub>25</sub>: 25/75 und PEG-AC<sub>0</sub>: 0/100) und damit Hydrogele (4 % m/v) hergestellt worden. So lagen Hydrogele mit einer allgemeinen proteolytischen Abbaubarkeit vor, welche durch variierende PEG-AC-Konzentration zudem eine unterschiedliche Anzahl hydrolytischer Angriffspunkte boten. Zur in-vitro Charakterisierung der Gele wurden das Speichermodul, sowie der hydrolytische Abbau mittels Quantifizierung der Wasseraufnahme bestimmt. Ferner sind Endothelzellen aus Nabelschnüren (HUVEC) isoliert und Sphären dieser Zellen in den Hydrogelen eingeschlossen worden, um die Zellinfiltration in der Fluoreszenzmikroskopie quantifizieren zu können.

Im Rahmen einer Seitenstudie ist außerdem die Inkorporation von Wachstumsfaktoren (80 ng/μL VEGF = vascular endothelial growth factor; 80 ng/μL bFGF = basic fibroblast growth factor) in PEG-Hydrogele

(PEG-AC<sub>50</sub>-VEGF/bFGF) und deren Einfluss auf Zellwachstum und Neoangiogenese untersucht worden. Dafür wurde zunächst in-vitro die Wachstumsfaktorfreisetzung aus dem Hydrogel über einen Zeitraum von 28 Tagen mittels ELISA quantifiziert sowie deren Aktivität durch 72-Stündige Inkubation mit HUVECs und dermalen Fibroblasten im Zellproliferationsassay bestimmt.

Zur Durchführung von in-vivo Versuchen war es zum Handling notwendig, den Hydrogelen (PEG-AC<sub>0-100</sub> und PEG-AC<sub>50</sub>-VEGF-bFGF) durch Infiltration in poröse Polyurethanscheiben (Ø: 5,4 mm; Höhe: 1 mm; Porosität: 82 %; Porendurchmesser: 157 µm) mechanische Stabilität zu verleihen. Diese Scheiben konnten für maximal 28 Tage subkutan in männlichen Wistar-Ratten implantiert und anschließend histologisch (H&E, Pikrosirius-Rot-Färbung, sowie immunhistochemisch gegen endothelzellspezifisches CD31-Antigen) evaluiert werden.

Hinsichtlich ihrer mechanischen Eigenschaften, zeigten alle 5 Versuchsgruppen bei der Speichermodulmessung (Ø G': 1398 ± 171 Pa) keine signifikanten Unterschiede. Während die hydrolysevermittelte in-vitro Degradation bei beiden Versuchsgruppen mit den höchsten PEG-AC-Anteilen nach 10-12 Tagen (PEG-AC<sub>100</sub>) bzw. 16-18 Tagen (PEG-AC<sub>75</sub>) zum Zerfall des Materials führte, bewahrten alle anderen Materialien ihre strukturelle Integrität bis zum Ende des Messzeitraumes. In-vitro zeigte sich außerdem eine starke Korrelation (R<sup>2</sup>: 0,9) zwischen PEG-AC-Anteil und Zellinfiltration nach 5 Tagen Inkubation. Diese Abhängigkeit konnte durch die in-vivo Ergebnisse bestätigt werden, wo signifikante Unterschiede zwischen den Versuchsgruppen gemessen wurden und sowohl nach 14 als auch nach 28 Tage ein höherer PEG-AC-Anteil mit stärkerer Gewebsbildung und höheren Kollagenanteilen (maximal 39 ± 2 % bei PEG-AC<sub>100</sub>) assoziiert war. Für die Hydrogele mit Wachstumsfaktoren konnte in-vitro eine konstante Abgabe ebendieser gemessen und auch zu späten Freisetzungzeitpunkten (Tag 22-28) noch ein signifikanter Wachstumseffekt auf HUVEC (+27 % Wachstum; p ≤ 0,01) und Fibroblasten (+40 % Wachstum; p ≤ 0,01) festgestellt werden. Auch diese in-vitro Erkenntnisse sind durch die in-vivo Versuchsreihe untermauert worden und zeigten eine signifikant höhere Neoangiogeneserate (VEGF: +44 %; bFGF: +59 % und VEGF+bFGF: +55 %; p ≤ 0,05) in Anwesenheit von Wachstumsfaktoren.

In Zusammenschau der Ergebnisse lässt sich schlussfolgern, dass durch die Implementierung spezifischer hydrolytischer Angriffspunkte in PEG-Hydrogele deren Degradationsrate sowie Zell- und Gewebeeinfiltration gezielt steuerbar ist. Mittels biochemischer Modifikationen, beispielsweise durch die Inkorporation von Wachstumsfaktoren ist zudem eine signifikante Beeinflussung der Zellproliferation und der Neoangiogenese möglich. Die untersuchten PEG-Hydrogele bieten somit großes Potential zum Einsatz im kardiovaskulären TE, aber auch für andere regenerative Anwendungen.

### 3.3.5 Tissue Engineering 2.0 – Elektrosponning und 3D-Druck

*“Combining 3D-Printing and Electrospinning to Manufacture Biomimetic Heart Valve Leaflets”*

*Am 02.02.2022 zur Publikation angenommen, JOVE Journal*

Autoren: Freystetter B., Grab M., Grefen L., Bischof L., Isert L., Bezuidenhout D., Mela P., Hagl C.,  
**Thierfelder N.**

Eine Vielzahl an unterschiedlichen Produktionstechniken, wie Elektrosponning (Maurmann et al., 2018), DZ (Naso and Gandaglia, 2017) oder Gussverfahren (van Velthoven et al., 2020), werden heutzutage im kardiovaskulären TE zur Herstellung der benötigten Scaffolds eingesetzt. Fast ausschließlich verfolgt man dabei das Ziel, ein poröses, meist faseriges Gerüst mit einer Strukturgröße im Mikrometerbereich zu fertigen (Jana et al., 2014). Nachdem aufgrund von Limitierungen der Fertigungstechniken initial nur die Produktion homogener Scaffolds möglich war (Sodian et al., 2000), rückt nun mehr und mehr die Optimierung der Scaffoldarchitektur und die Herstellung von „designten“ Strukturen in den Fokus der Forschung (Chen et al., 2020, Chung et al., 2020). Berücksichtigt man diesbezüglich den mikroanatomischen und histologischen Aufbau einer gesunden menschlichen Herzklappe so wird deutlich, dass hier drei verschiedene Schichten mit variierender Faserausrichtung und jeweils spezifischen Funktionen nachzubilden sind (Buchanan and Sacks, 2014, Wiltz et al., 2013). Hierbei fällt insbesondere auf, dass die äußeren Schichten eine um 90° gedrehte Hauptausrichtung der Fasern der EZM aufweisen aber auch, dass die mittige Schicht ungeordnete Fasern zeigt und eine Dämpfungsfunktion innehat. Erste Studien beschreiben Versuche, den Aufbau menschlicher Aortenklappen zu imitieren, wobei es an dieser Stelle bisher nicht gelang, gleichzeitig den 3-dimensionalen anatomischen Aufbau der Herzklappensegel korrekt nachzubilden (Masoumi et al., 2014, Jana et al., 2019b).

Idealerweise sollte also bei der Herstellung eines tissue engineerten Herzklappensubstitutes nicht nur die Struktur der EZM mit ihrem spezifischen Faserverlauf nachgebildet, sondern auch die makroskopische, räumliche Konfiguration des menschlichen Originals berücksichtigt werden. Um dies zu erreichen, sind in einem neuartigen Verfahren die Fertigungstechniken 3D-Druck und Elektrosponning miteinander kombiniert und in einer Validierungsstudie hinsichtlich der Eignung für das kardiovaskuläre TE evaluiert worden.

Als Basis für das neuartige Fertigungsverfahren diente ein konventioneller Elektrosponningaufbau mit Rotationskollektor. Dieser wurde so modifiziert, dass neun einzelne und jeweils um 90° drehbare Negativformen (drei Negative auf drei 120° gekippten Oberflächen) von Herzklappensegeln aus leitfähiger PLA darauf befestigt werden konnten. Hinsichtlich der Herzklappensegelform kann mit dem



vorliegenden Versuchsaufbau prinzipiell eine Vielzahl an unterschiedlichen Geometrien genutzt werden – In der genannten Studie lehnte man sich an der Segelform einer biologischen Herzklappenprothese an. Als Material zur Herstellung der Scaffolds verwendete man biostabiles Polyurethan, welches mit Hilfe von Tetrahydrofuran und N,N-Dimethylformamid (1:1 + 15 % w/v Polyurethan) für den Elektrospinningprozess gelöst und bei 19,5 kV Spannung versponnen wurde. Im Herstellungsprozess ist der Kollektor zur Schaffung gerichteter Faser zunächst mit hoher Drehzahl (2000 U/min) rotiert worden, gefolgt von einer niedrigen Rotationsgeschwindigkeit (10 U/min) für die Erstellung der mittleren Schicht von ungerichteten Fasern. Zum Abschluss wurden die neun segelförmigen Negative um jeweils 90° gedreht und eine weitere Schicht mit ausgerichteten Fasern bei hoher Kollektordrehzahl (2000 U/min) aufgebracht. Vor dem Ablösen der Scaffolds von den Negativen ist eine Trocknung bei 40° C über Nacht durchgeführt worden. Während des gesamten Elektrospinningprozesses sollten als Umgebungsbedingungen 15-20 % relativer Luftfeuchtigkeit und eine Temperatur von 21-24° C herrschen.

Zur morphologischen Beurteilung der Scaffolds wurden elektronenmikroskopische Aufnahmen erstellt und diese hinsichtlich des allgemeinen Erscheinungsbildes sowie der Faserdurchmesser quantitativ ausgewertet. Uniaxiale Zugversuche zeigten die mechanische Belastbarkeit der gerichteten und unausgerichteten Fasern. Die Verwendung unterschiedlicher Fluoreszenzfarbstoffe (Fluorescein, Texas Red® und DAPI) in den verschiedenen Schichten der elektrogewebenen Herzklappensegel ist zur Darstellung der jeweiligen Faserverläufe mittels Fluoreszenzmikroskop genutzt worden.

Die benötigten Modifikationen eines bestehenden Elektrospinningaufbaus konnten in wenigen Tagen mit Hilfe eines konventionellen 3D-Druckes und Materialkosten von unter 30€ umgesetzt werden. Der umgerüstete Aufbau konnte im Anschluss problemlos genutzt und damit mehrschichtige elektrogewebene Scaffolds in 3-dimensionaler Herzklappensegelform mit spezifischen Faserausrichtungen hergestellt werden. In der elektronenmikroskopischen Evaluation zeigten sich homogene Polymerfasern mit einer durchschnittlichen Stärke von  $4,15 \pm 1,55 \mu\text{m}$ . Mit Hilfe der Fluoreszenzmikroskopie konnten die drei Schichten der Scaffolds dargestellt und deren unterschiedliche Faserausrichtung bestätigt werden (s. Abbildung 11). Während sich die Polymerfasern der beiden äußeren Schichten in ihrer Hauptausrichtung um 89° unterschieden, war in der mittleren Schicht ein ungerichtetes Ausrichtungsmuster zu detektieren. In den mechanischen Untersuchungen offenbarte sich ein hoch signifikanter Unterschied der Maximalspannung und Dehnbarkeit, abhängig von der Zugrichtung bei ausgerichteten Fasern ( $F_{\text{max-längs}}$ :  $12,26 \pm 2,59 \text{ N/mm}^2$ ;  $F_{\text{max-quer}}$ :  $3,86 \pm 1,08 \text{ N/mm}^2$ ;  $p \leq 0,001$ ). Lag keine Faserausrichtung vor, waren die mechanischen Eigenschaften in alle Belastungsrichtungen vergleichbar.

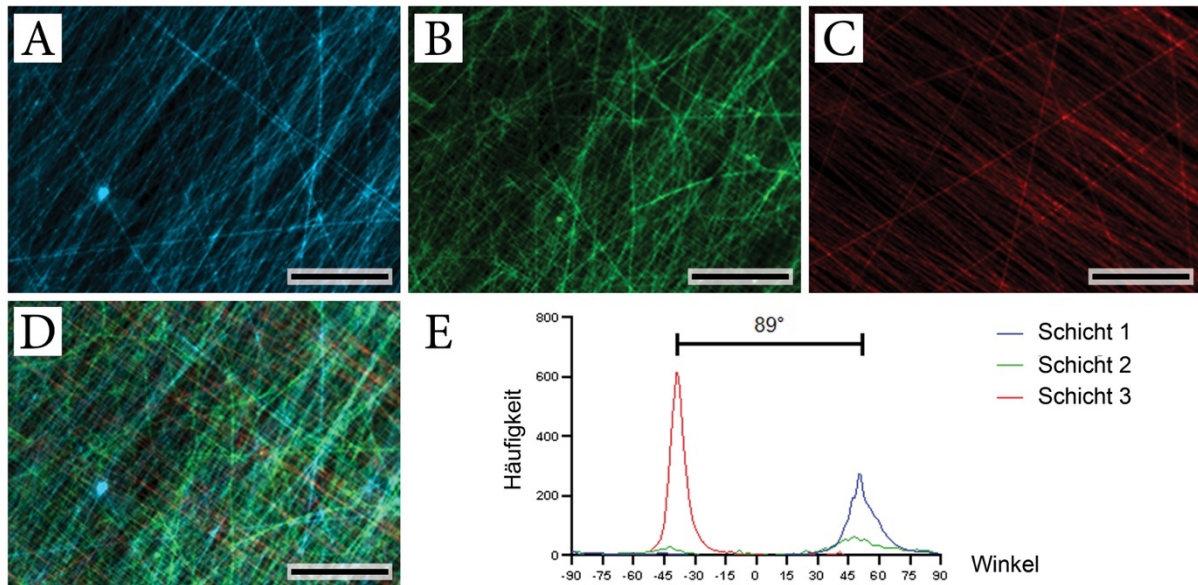


**Abbildung 11: Mehrschichtiges Polyurethanscaffold mit definierter Faserausrichtung**

Fluoreszenzmikroskopische Darstellungen der einzelnen Schichten (A – C) des 3-lagigen elektrogesponnenen Polyurethanscaffolds, sowie deren Fusionsdarstellung (D). In der quantitativen Auswertung der Faserausrichtung (E) zeigt sich, dass die äußeren Scaffoldschichten gerichtete Fasern ( $\Delta$  Hauptfaserausrichtung:  $89^\circ$ ) aufweisen. Die mittlere Schicht besteht hingegen aus ungeordneten Fasern.

Mit Hilfe dieses neuartigen Fertigungsverfahrens konnten erstmalig dreischichtige Aortenklappensegel mit spezifischen Faserausrichtungen und korrekter anatomischer Geometrie erstellt werden. Aufgrund des modularen Elektrospinnungsaufbaus ist es für weiteren Studien zudem möglich, sogar patientenspezifische Herzklappensegel oder Scaffolds für nicht-kardiovaskuläre Anwendungen einfach, schnell und kostengünstig zu implementieren.

## 4 Diskussion

Entsprechend der Zielsetzung dieses Habitationsprojektes war es möglich, verschiedene in-vitro und in-situ TE-Ansätze zur Herstellung unterschiedlicher kardiovaskulärer Implantate anzuwenden. Die durchgeführten Prozesse unterschieden sich hinsichtlich ihrer Dauer, der Komplexität, den möglichen Komplikationen und in ihren Kosten zum Teil erheblich. Gleichzeitig offenbarten sich aber auch zahlreiche Möglichkeiten, durch Innovationen eine Optimierung dieser Parameter durchzuführen. Im Folgenden sollen die erhobenen Vor- und Nachteile der TE-Ansätze erörtert und daraus mögliche Probleme und Hinderungsgründe für einen umfassenden klinischen Einsatz abgeleitet werden.

### 4.1 Rahmenbedingungen der Implantatherstellung

Bei der Entwicklung von Medizinprodukten ist es essenziell, in einer Machbarkeitsanalyse und ökonomischen Evaluation auch immer einzelne Aspekte der Produktion (u.a. Komplexität und Dauer), sowie die verwendeten Ressourcen zu berücksichtigen.

So war es im Rahmen der verschiedenen Studien dieses Habitationsprojektes möglich, tissue-engineerte Scaffolds auf Basis von biologischen Geweben (DZ von Perikard, Herzklappen und Gefäßen), synthetischen Polymeren (Polyurethan) und Hydrogelen (PEG-Basiert) herzustellen. Dies deckt sich mit den Erfahrungen aus anderen Studien, in denen diese Materialien auch zur Herstellung von regenerativen Implantaten genutzt werden konnten (Wang et al., 2017, Arefin et al., 2017, Heuschkel et al., 2019, Roosens et al., 2017, O'Connor Mooney et al., 2015). Alle verwendeten synthetischen Rohstoffe (u.a. Polymere, Detergentien, Wachstumsfaktoren) waren leicht und zeitnah verfügbar, zumeist über einschlägige Großhändler. Die porzinen und bovinen Materialien zur DZ wurden von einem lokalen Schlachthof bezogen. Es ist anzumerken, dass bei einem späteren kommerziellen klinischen Einsatz die Verwendung von hoch-reinen „medical grade“ und/oder „pharmaceutical grade“ Rohstoffen bedacht werden sollte. Außerdem ist die Verwendung von Rohstoffen aus der Nutztierschlachtung bei einer klinischen Anwendung kritisch zu evaluieren, um das Risiko von Zoonosen zu mindern und eine bessere Prozesskontrolle gewährleisten zu können.

Als größte Herausforderung bei der Rohstoffbeschaffung stellte sich die Zellgewinnung zur Durchführung der in-vitro TE-Ansätze heraus. Im Rahmen mehrerer Studien fanden humane Endothelzellen und Fibroblasten zur Fertigung der tissue-engineerten Implantate Anwendung (Thierfelder et al., 2013, Koenig et al., 2016, Aleksieva et al., 2012). In diesen Fällen sind Gefäßreste (V. saphena magna) bei aortokoronaren Bypass-Operationen als Abfall angefallen und die Zellen daraus

isoliert, kultiviert und später auf die Scaffolds gesiedelt worden. Bei einem therapeutischen Einsatz der genannten tissue-engineerten Implantate müsste jedoch für einen immunologisch unbedenklichen Einsatz, jeweils ein gesonderter Eingriff zur Zellgewinnung vom selben Patienten erfolgen. Die Verwendung alternativer Zellquellen und weniger invasiver Gewinnungsverfahren sollte daher evaluiert und angestrebt werden. In Übereinstimmung mit publizierten Daten (Yao et al., 2020, Mewhort et al., 2017) ist beispielsweise im Rahmen einer der durchgeführten Studien die erfolgreiche Gewinnung und der Einsatz von Nabelschnurzellen zur Scaffoldevaluation gezeigt worden (Chokoza et al., 2019). Ferner wäre die Gewinnung und Verwendung von Hautfibroblasten, welche mittels Biopsie gewonnen werden können, denkbar (Kisiel and Klar, 2019). Als mögliche weitere Alternative könnte sich im kardiovaskulären TE auch das Kardiotomiereservoir der Herz-Lungen-Maschine anbieten. Im Verlauf des Habilitationsprojektes war es erstmalig möglich ein Verfahren zur Zellisolation aus dem Kardiotomiereservoir zu entwickeln (Nathusius et al., 2018). Insbesondere bei bestimmten kongenitalen Vitien, welche mehrere Korrekturingriffe bedürfen, wäre diese Zellquelle eine interessante Alternative, da die Zellen in der Primäroperation gewonnen und das tissue-engineerte Implantat in einer Folgeoperation eingesetzt werden könnte.

Wie auch von anderen Studien bekannt (Paniagua Gutierrez et al., 2015, Kluin et al., 2017, Sodian et al., 2006), zeigte sich auch in allen hier dargestellten TE-Ansätzen, dass die Herstellung der regenerativen Implantate aus vielen konsekutiven Einzelschritten besteht. Beispielsweise sind bei manchen der durchgeführten DZ-Protokolle bis zu 35 zum Teil 24-stündige Einzelschritte notwendig (Koenig et al., 2019). Auch Modifikationen wie die Ultraschallexposition oder die Anwendung zyklischer Prozeduren, die zwar zur signifikanten Verbesserung der DZ beitragen, gestalten den Gesamtprozess meist aufwendiger (Starnecker et al., 2018). Die einzelnen Schritte sind zwar für sich betrachtet nicht sonderlich komplex, gestalten aber den Gesamtprozess sehr arbeitsintensiv. Hier wäre zur Optimierung der Einsatz von automatisierten DZ-Bioreaktoren, wie sie bereits bei manchen publizierten DZ-Protokollen (Khalpey et al., 2015) oder bei der Herstellung zellbesiedelter Implantate (Gorman et al., 2018) zum Einsatz kommen, denkbar.

Bioreaktoren finden im TE, insbesondere bei der Herstellung „lebender“ tissue-engineerter Implantate (in-vitro Ansatz) bereits vielfach Anwendung (Jin et al., 2015a). Der signifikante Nutzen spezifischer Bioreaktoren konnte auch im Rahmen dieser Habilitationsarbeit nachgewiesen werden (Aleksieva et al., 2012, Koenig et al., 2016, Thierfelder et al., 2013). Sie ermöglichen die Bereitstellung und Überwachung definierter Rahmenbedingungen, um das Gewebe an Fluss- und Scherkräfte adaptieren zu lassen. Dabei werden u.a. pro-inflammatorische Prozesse abgemildert, Endothelzellen richten sich in Strömungsrichtung aus und es wird eine EZM ausgebildet. Der Nachweis dieser Adaptationsprozesse steht in Einklang mit publizierten Daten anderer Forschungsgruppen (Jin et al., 2015b, Selden and Fuller, 2018). Es sollte jedoch bedacht werden, dass die Konzeption und der Bau solcher Bioreaktoren

in den meisten Fällen entsprechend ausgebildetes Personal (Ingenieure und Maschinenbauer) sowie den Zugang zu einem passenden Maschinenpark benötigen. Unter diesen Voraussetzungen sind dann – wie in dieser Arbeit vorgestellt (Grab et al., 2021) – computerbasierte Konstruktion und Simulation sowie die Produktion, auch mittels additiver Fertigung (3D-Druck) möglich (Gensler et al., 2020).

Ein weiterer großer Unterschied zwischen den unterschiedlichen TE-Ansätzen zeigte sich in den benötigten Produktionszeiten. So konnten die synthetischen Scaffolds der in-situ Strategie schneller als die biologischen hergestellt werden, gefolgt von den langen Produktionszeiten der mit Zellen besiedelten Implantate. Wie auch von anderen Studien berichtet, zieht sich hier der Produktionsprozess von Zellisolation, über Kultivierung, Scaffoldbesiedelung und Konditionierung meist über mehrere Wochen hin (Moreira et al., 2014, Hoerstrup et al., 2002). Allein der Besiedelungs- und Konditionierungsprozess der Studien des Habilitationsprojektes variierte zwischen 8 (Aleksieva et al., 2012), 14 (Thierfelder et al., 2013) und 19 (Koenig et al., 2016) Tagen. Hinzu kommt, dass eine genaue Prognose der Produktionsdauer aufgrund interindividueller Proliferationsraten der verwendeten Zellen unmöglich ist und somit eine relevante Limitation dieses Ansatzes darstellt. Eine verbesserte Vorhersagbarkeit oder die Optimierung der Prozessdauer erscheint zum aktuellen Zeitpunkt zudem schwierig. Ein praktikabler Einsatz wäre daher nur bei einigen, elektiv therapierbaren Krankheitsbildern, beispielsweise im Kinderherzchirurgischen Bereich denkbar.

Neben dem Einfluss auf die genaue zeitliche Planung im Falle eines klinischen Einsatzes ist die Prozessdauer auch hinsichtlich der Herstellungskosten eines Implantates von Relevanz. Hier müssen neben dem zeitlichen Aspekt die verwendeten Ressourcen, der personelle Einsatz und die benötigte Infrastruktur berücksichtigt werden. Insbesondere beim in-vitro Ansatz sind daher neben der genannten, langen Produktionszeit auch die benötigte, zum Teil sehr spezifische Infrastruktur und teure Ressourcen (z.B. Zellkulturmedien) für hohe Kosten verantwortlich. Beim in-situ Ansatz hingegen kann durch spezielle Modifikationen mit Wachstumsfaktoren und Adhäsionsmolekülen (Chokoza et al., 2019) oder durch den Einsatz von Enzymen im DZ-Prozess (Koenig et al., 2019) ein relevanter Kostenpunkt entstehen. Ansatzpunkte für eine mögliche Kostenreduktion im Herstellungsprozess regenerativer Implantate sind die Prozessautomatisierung oder auch die Verwendung von innovativen und kostengünstigen Produktionsmethoden wie dem 3D-Druck (Carbonaro et al., 2020). Dies konnte im Rahmen der Habilitationsarbeit durch die Verwendung von 3D-Druck zur Produktion von Bioreaktoren bestätigt werden (Grab et al., 2021).

## 4.2 Sicherheitsrelevante und regulatorische Aspekte

Jedes potenzielle Medizinprodukt muss vor einer kommerziellen Nutzung von einer „benannten Stelle“ geprüft und zertifiziert werden. Im Verlauf dieses Prozesses, der in Deutschland durch die europäische Medizinprodukteverordnung („medical device regulation“ = MDR) definiert ist, wird die Sicherheit eines jeden Medizinproduktes evaluiert (Europ.Rat“, 2020). Auch alle im Rahmen der Habilitationsarbeit gefertigten Implantate wären von dieser regulatorischen Maßnahme betroffen und fallen dabei sogar unter die „Hochrisikoklasse“ III, da sie zu einer Anwendung im zentralen kardiovaskulären System entwickelt wurden. Der zentrale Aspekt des Zertifizierungsprozesses ist die Gewährleistung der Patientensicherheit. Dies soll unter anderem durch die Verwendung sicherer (ggf. bewährter) Materialien mit gleichbleibender Güte, der Anwendung eines definierten Produktionsprozesses zur Gewährleistung einer hohen Reproduzierbarkeit und einer stringenten Qualitätssicherung sowie der Vermeidung einer Pathogenübertragung erreicht werden.

In unterschiedlichen, hier dargestellten Studien konnte nachgewiesen werden, dass die verwendeten biologischen Rohstoffe eine natürliche und zum Teil signifikante Varianz zeigen (Stieglmeier et al., 2021, Grefen et al., 2018). Dies macht im Produktionsprozess von biologischen Implantaten eine genaue Materialelektion und akribische Qualitätskontrolle zwingend notwendig. Am Beispiel von Perikard lassen sich zum aktuellen Zeitpunkt jedoch erstaunlicherweise nur sehr wenige und alte Daten zur Charakterisierung des Materials finden (Braile et al., 1998, Simionescu et al., 1993, Sacks et al., 1994). Daher ist eine Studie zur Kartografie von bovinem Perikard durchgeführt worden und es kann ein Bereich mit Projektion auf den linken Ventrikel zur Verwendung empfohlen werden (Stieglmeier et al., 2021).

Neben einer akribischen Materialelektion ist auch eine strenge Qualitätssicherung im Herstellungsprozess regenerativer kardiovaskulärer Implantate zwingend notwendig. Im Verlauf des Habilitationsprojektes konnten diesbezüglich mehrere relevante Punkte adressiert werden. So war es möglich, mit Hilfe nicht-invasiver  $\mu$ -CT-Aufnahmen unterschiedliche Schritte im Produktionsprozess anhand von Dickenänderungen nachzuvollziehen und so auch die erfolgreiche Zellularisierung der Scaffolds zu belegen (Haller et al., 2013). Üblicherweise werden für diesen Nachweis bisher histologische und damit zerstörende Verfahren herangezogen (Zuncheddu et al., 2021). In einer weiteren Studie konnte außerdem nachgewiesen werden, dass eine multimodale Qualitätssicherung unter Verwendung von histologischen und molekulargenetischen Methoden bei der Herstellung von dezellulierten Implantaten essenziell ist (Koenig et al., 2019). In diesem Zusammenhang findet sich auch eine mögliche Erklärung für das kontroverse klinische Outcome bisheriger Implantate (Ruffer et al., 2010, Horke et al., 2020). So wird berichtet, dass mit hoher Wahrscheinlichkeit eine unzureichende Dezellularisation zu frühzeitigem Versagen bestimmter Implantate geführt hat (Simon et al., 2003,

Kasimir et al., 2005). Unter Berücksichtigung der gewonnenen Erkenntnisse kann somit die Hypothese aufgestellt werden, dass die dort verwendeten Methoden keine ausreichende Reproduzierbarkeit hatten und in der Qualitätssicherung der Implantatherstellung unzureichende Methoden zum Nachweis der vollständigen DZ herangezogen worden sind.

Im Allgemeinen lässt sich konstatieren, dass bei höherer Prozesskontrolle eine bessere Reproduzierbarkeit erreicht und damit einheitlichere Implantate hergestellt werden können. Unter dieser Prämisse zeichnet sich die Verwendung von synthetischen Scaffolds des in-situ-Ansatzes besonders aus. Wie erfolgreich gezeigt wurde, konnten durch die Entwicklung zweier komplett neuartiger Produktionstechniken genaue Materialeigenschaften (Chokoza et al., 2019) ebenso wie eine spezifische Scaffoldarchitektur (Freystetter et al., 2022) definiert und erreicht werden. Bisher sind nur wenige Studien publiziert, die beispielsweise bei der Herstellung von Herzklappensegeln eine vergleichbare Prozesskontrolle gewährleisten (Jana et al., 2019b, Masoumi et al., 2014).

Ein weiterer sicherheitsrelevanter Aspekt bei allen Medizinprodukten und damit auch bei tissue-engineerten Implantaten ist die Gewährleistung ihrer Sterilität vor dem Einsatz im Lebewesen (Tipnis and Burgess, 2018). In diesem Zusammenhang sind insbesondere biologische Materialien risikobehaftet, da sie einerseits bereits verunreinigt in den Produktionsprozess gelangen können (cave Zoonosen (Kim et al., 2016b)) und auch bei einer späteren Kontamination meist ideale Bedingungen für die Vermehrung von Mikroorganismen bieten. Andererseits können solche Materialien nicht jedem bekannten Sterilisationsverfahren ausgesetzt werden, da die Gefahr einer starken Veränderung oder Zerstörung des Gewebes besteht (Harrell et al., 2018, Gosztyla et al., 2020). Für biologische Materialien finden daher, wie in einer der Habilitationsstudien gezeigt (Grefen et al., 2018), meist bestimmte chemische Sterilisationsverfahren Anwendung. Dabei werden die Materialien oft in schwache, organische Säuren (z.B. Peressigsäure (Farrington et al., 2002)) oder quervernetzende Substanzen (z.B. Glutaraldehyd (Lim et al., 2015)) eingelegt. Das in diesem Zusammenhang unzureichende Sterilisationsergebnis von Glutaraldehyd in der Habilitationsstudie könnte durch glutaraldehydresistente (Myko-)Bakterien (Serry et al., 2003, Fisher et al., 2012) oder in einer, im Vergleich mit anderen Studien, zu geringen Konzentration oder zu kurzen Einwirkdauer der Chemikalie zu erklären sein (Ozalp et al., 2006).

### 4.3 Einsatz tissue-engineerter Implantate

Für den klinischen Anwender sind neben der in-vivo Langzeitfunktion – die außerhalb der wissenschaftlichen Fragestellung dieser Arbeit lag – insbesondere die Handhabung und die Verfügbarkeit eines medizinischen Implantates relevant. Es zeigte sich, dass besonders lebende tissue-

engineerte Implantate sehr vulnerabel sind und dass allein durch die Implantationsprozedur ein signifikanter Teil der Zellen absterben kann (Koenig et al., 2016). In diesem Zusammenhang wurde auch eine relevante Inflammationsreaktion hervorgerufen, wobei zu postulieren ist, dass dies für die Haltbarkeit des jeweiligen Implantates prognostisch ungünstig ist.

Hinsichtlich des für den klinischen Anwender ebenso relevanten Aspektes der Verfügbarkeit medizinischer Implantate kann zwischen „of-the-shelf“ und „on demand“ unterschieden werden (Shahverdyan et al., 2016, Farber et al., 2014). Die allermeisten Produkte sind normalerweise in der jeweiligen Einrichtung auf Lager („of-the-shelf“) und können damit direkt, d.h. auch in einem Notfall, zum Einsatz kommen. An dieser Stelle disqualifiziert sich der in-vitro TE-Ansatz durch die bereits genannten langen Produktionszeiten. Eine weitere Limitation dieses Ansatzes zeigt sich bei der Größenwahl einer Prothese, die nicht immer prä-operativ oder -interventionell so möglich ist, wie es aktuell beispielsweise in der TAVI-Planung durchgeführt wird (Lalys et al., 2019). So muss jedoch für ein lebendes Implantat des in-vitro Ansatzes bereits Wochen vorher, d.h. zu Beginn des Produktionsprozesses die genaue Prothesengröße klar sein. Azelluläre Implantate zur in-situ Regeneration können hingegen in verschiedensten Größen vorproduziert, in der Klinik gelagert und dann bei Bedarf entsprechend ausgewählt werden.

#### 4.4 Zusammenfassung

Im Verlauf des Habitationsprojektes war es in Übereinstimmung mit früheren Publikationen möglich, Perikardpatches (Grefen et al., 2018), biologische (Thierfelder et al., 2013) und synthetische (Aleksieva et al., 2012) Herzklappen, sowie Hydrogele (Chokoza et al., 2019) unter präklinischen Rahmenbedingungen zu produzieren und zu evaluieren. Auch die Implementierung neuer Trends konnte durch die Fertigung einer minimalinvasiven Herzklappe (Koenig et al., 2016), die Etablierung einer neuen Zellquelle (von Nathusius et al., 2017), den Einsatz von  $\mu$ -CT-Aufnahmen (Haller et al., 2013) und 3D-Druck (Grab et al., 2021) oder auch die Entwicklung eines Verfahrens zur Herstellung individualisierter Implantate (Freystetter et al., 2022) erfolgreich vollzogen werden. Dies bestätigt den allgemeinen Konsensus, dass es möglich ist, mit Hilfe von TE eine breite und für den klinischen Anwender interessante Produktpalette an kardiovaskulären Implantaten herzustellen (Fioretta et al., 2021). Unter Berücksichtigung der individuellen Vor- und Nachteile der regenerativen Implantate des Habitationsprojektes zeichnet sich insbesondere das in-situ TE auf Basis synthetischer Scaffolds aus und sollte im Sinne eines translationalen Ansatzes weiterverfolgt werden, um es in den klinischen Einsatz zu bringen.



## 5 Schlussfolgerung und Ausblick

Nach erfolgreicher Durchführung von 12 experimentellen Studien im Bereich des kardiovaskulären TE und in Zusammenschau ihrer Ergebnisse können aus präklinischer Sicht mögliche Erklärungen zum bisher geringen klinischen Einsatz regenerativer Implantate, aber auch Innovationen und potenzielle Lösungsansätze aufgezeigt werden. Es ist erkennbar, dass die Anforderungen von Seiten eines Herstellers, unter Berücksichtigung der regulatorischen Aspekte, aber auch die Bedürfnisse der Anwender und Nutzer teilweise stark von den Eigenschaften der unterschiedlichen tissue-engineerten Produkte differieren (s. Tabelle 5).

**Tabelle 5: Soll-Anforderungen und gegebene Eigenschaften tissue-engineerter Implantate**

uws = unwahrscheinlich; \*: ggf. Schädigung der Zellen

Rubrik	Soll-Anforderungen	In-vitro TE	In-situ TE		
			Dezellularisation	Synthetische Scaffolds	
Herstellung	Rohstoff-verfügbarkeit	gut	schwierig	<u>gut</u>	<u>gut</u>
	Komplexität des Prozesses	gering	hoch	<u>gering</u>	intermediär
	Produktionszeit	kurz	lang	intermediär	<u>kurz</u>
	Kosten	gering	hoch	<u>gering</u>	intermediär
Zertifizierung	Qualität	hoch	schwankend	schwankend	<u>hoch</u>
	Reproduzierbarkeit	gut	schwierig	intermediär	<u>gut</u>
	Pathogenübertragung	uws	<u>uws</u>	möglich	<u>uws</u>
Anwendung	Handling	einfach	schwierig*	<u>einfach</u>	<u>einfach</u>
	Verfügbarkeit	direkt	Vorlauf notwendig	<u>direkt</u>	<u>direkt</u>
<b>Ist-/Soll-Anforderungen</b>			<b>1/9</b>	<b>5/9</b>	<b>7/9</b>

So finden sich beispielsweise anhand der generierten Ergebnisse für den „ursprünglichen“ in-vitro Ansatz so gut wie keine Überschneidungspunkte mit den Idealanforderungen. Selbst für

dezellularisierte Produkte (in-situ Ansatz), welche stellenweise bereits in der klinischen Anwendung zu finden sind, liegen keine idealen Voraussetzungen vor. Einzig synthetische Scaffolds im in-situ Ansatz offenbaren aufgrund ihrer vergleichsweise ökonomischen Herstellung, guter regulatorischer Voraussetzungen und einer praktischen Anwendung das größte Potential für einen längerfristig erfolgreichen Einsatz in der kardiovaskulären Medizin. Alle Ansätze werden zwar auch in Zukunft mit großer Wahrscheinlichkeit durch Innovationen, so wie bereits im Rahmen dieser Habilitationsarbeit aufgezeigt, Limitationen überwinden, neue Entwicklungsstufen erreichen und weitere Einsatzgebiete erschließen. Letztendlich wird ihr Erfolg aber auch dann noch von den klinischen Anwendungsergebnissen abhängen.

Diese Habilitationsarbeit offenbart nach der Durchführung von in-vitro und in-vivo Studien eine Erklärungsmöglichkeit für den bisher fehlenden klinischen Erfolg des kardiovaskulären TE durch die Diskrepanz zwischen den Anforderungen an ein tissue-engineertes Implantat und dessen gegebenen Eigenschaften. Ferner werden Möglichkeiten aufgezeigt, die bisher verfolgten TE-Ansätze durch Weiterentwicklung und Innovation voranzutreiben, um sie wettbewerbs- und zukunftsfähig zu machen.

## 6 Quellenverzeichnis

- A. M. SCHNELL, S. P. H., G. ZUND, S. KOLB, R. SODIAN, J. F. VISJAGER, J. GRUNENFELDER, A. SUTER, AND M. TURINA 2001. Optimal Cell Source for Cardiovascular Tissue Engineering: Venous vs. Aortic Human Myofibroblasts. *Thorac Cardiovasc Surg*, 49, 221-225.
- AGUIARI, P., FIORESE, M., IOP, L., GEROSA, G. & BAGNO, A. 2016. Mechanical testing of pericardium for manufacturing prosthetic heart valves. *Interact Cardiovasc Thorac Surg*, 22, 72-84.
- ALEKSIEVA, G., HOLLWECK, T., THIERFELDER, N., HAAS, U., KOENIG, F., FANO, C., DAUNER, M., WINTERMANTEL, E., REICHART, B., SCHMITZ, C. & AKRA, B. 2012. Use of a special bioreactor for the cultivation of a new flexible polyurethane scaffold for aortic valve tissue engineering. *Biomed Eng Online*, 11, 92.
- AREFIN, A., HUANG, J. H., PLATTS, D., HYPES, V. D., HARRIS, J. F., IYER, R. & NATH, P. 2017. Fabrication of flexible thin polyurethane membrane for tissue engineering applications. *Biomed Microdevices*, 19, 98.
- ATTIA, R. Q. & RAJA, S. G. 2021. Surgical pericardial heart valves: 50 Years of evolution. *Int J Surg*, 94, 106121.
- AZHIM, A., SYAZWANI, N., MORIMOTO, Y., FURUKAWA, K. & USHIDA, T. 2014. The use of sonication treatment to decellularize aortic tissues for preparation of bioscaffolds. *Journal of Biomaterials Applications*, 29, 130-141.
- BAIRD, C. W., MARATHE, S. P. & DEL NIDO, P. J. 2020. Aortic valve neo-cuspidation using the Ozaki technique for acquired and congenital disease: where does this procedure currently stand? *Indian J Thorac Cardiovasc Surg*, 36, 113-122.
- BLOOMFIELD, P. 2002. Choice of heart valve prosthesis. *Heart (British Cardiac Society)*, 87, 583-589.
- BOROUMAND, S., ASADPOUR, S., AKBARZADEH, A., FARIDI-MAJIDI, R. & GHANBARI, H. 2018. Heart valve tissue engineering: an overview of heart valve decellularization processes. *Regen Med*, 13, 41-54.
- BOURANTAS, C. V. & SERRUYS, P. W. 2014. Evolution of transcatheter aortic valve replacement. *Circ Res*, 114, 1037-51.
- BRAILE, D. M., SOARES, M. J., SOUZA, D. R., RAMIREZ, V. D., SUZIGAN, S. & GODOY, M. F. 1998. Mapping of bovine pericardium: physical and histopathologic tests. *J Heart Valve Dis*, 7, 202-6.
- BUCHANAN, R. M. & SACKS, M. S. 2014. Interlayer micromechanics of the aortic heart valve leaflet. *Biomechanics and modeling in mechanobiology*, 13, 813-826.
- BYRNE, R. A. 2019. Medical device regulation in Europe - what is changing and how can I become more involved? *EuroIntervention*, 15, 647-649.

- CAO, Y., VACANTI, J. P., PAIGE, K. T., UPTON, J. & VACANTI, C. A. 1997. Transplantation of chondrocytes utilizing a polymer-cell construct to produce tissue-engineered cartilage in the shape of a human ear. *Plast Reconstr Surg*, 100, 297-302; discussion 303-4.
- CARBONARO, D., PUTAME, G., CASTALDO, C., MEGLIO, F. D., SICILIANO, K., BELVISO, I., ROMANO, V., SACCO, A. M., SCHONAUER, F., MONTAGNANI, S., AUDENINO, A. L., MORBIDUCCI, U., GALLO, D. & MASSAI, D. 2020. A low-cost scalable 3D-printed sample-holder for agitation-based decellularization of biological tissues. *Med Eng Phys*, 85, 7-15.
- CEBOTARI, S., TUDORACHE, I., JAEKEL, T., HILFIKER, A., DORFMAN, S., TERNES, W., HAVERICH, A. & LICHTENBERG, A. 2010. Detergent decellularization of heart valves for tissue engineering: toxicological effects of residual detergents on human endothelial cells. *Artif Organs*, 34, 206-10.
- CHAUDHURI, R., RAMACHANDRAN, M., MOHARIL, P., HARUMALANI, M. & JAISWAL, A. K. 2017. Biomaterials and cells for cardiac tissue engineering: Current choices. *Mater Sci Eng C Mater Biol Appl*, 79, 950-957.
- CHEN, Q., BRUYNEEL, A., CARR, C. & CZERNUSZKA, J. 2020. Trilayer scaffold with cardiosphere-derived cells for heart valve tissue engineering. *J Biomed Mater Res B Appl Biomater*, 108, 729-737.
- CHENG, J., WANG, C. & GU, Y. 2019. Combination of freeze-thaw with detergents: A promising approach to the decellularization of porcine carotid arteries. *Biomed Mater Eng*, 30, 191-205.
- CHIRCOV, C., GRUMEZESCU, A. M. & BEJENARU, L. E. 2018. Hyaluronic acid-based scaffolds for tissue engineering. *Rom J Morphol Embryol*, 59, 71-76.
- CHOI, W. S., BAE, J. W., LIM, H. R., JOUNG, Y. K., PARK, J. C., KWON, I. K. & PARK, K. D. 2008. RGD peptide-immobilized electrospun matrix of polyurethane for enhanced endothelial cell affinity. *Biomed Mater*, 3, 044104.
- CHOKOZA, C., GUSTAFSSON, C. A., GOETSCH, K. P., ZILLA, P., THIERFELDER, N., PISANO, F., MURA, M., GNECCHI, M., BEZUIDENHOUT, D. & DAVIES, N. H. 2019. Tuning Tissue Ingrowth into Proangiogenic Hydrogels via Dual Modality Degradation. *ACS Biomaterials Science & Engineering*, 5, 5430-5438.
- CHOUDHURY, D., YEE, M., SHENG, Z. L. J., AMIRUL, A. & NAING, M. W. 2020. Decellularization systems and devices: State-of-the-art. *Acta Biomater*, 115, 51-59.
- CHUNG, J. J., IM, H., KIM, S. H., PARK, J. W. & JUNG, Y. 2020. Toward Biomimetic Scaffolds for Tissue Engineering: 3D Printing Techniques in Regenerative Medicine. *Front Bioeng Biotechnol*, 8, 586406.
- CRAPO, P. M., GILBERT, T. W. & BADYLAK, S. F. 2011. An overview of tissue and whole organ decellularization processes. *Biomaterials*, 32, 3233-43.
- DA COSTA, F. D., COSTA, A. C., PRESTES, R., DOMANSKI, A. C., BALBI, E. M., FERREIRA, A. D. & LOPES, S. V. 2010. The early and midterm function of decellularized aortic valve allografts. *Ann Thorac Surg*, 90, 1854-60.

- DAVIES, N. H., SCHMIDT, C., BEZUIDENHOUT, D. & ZILLA, P. 2012. Sustaining neovascularization of a scaffold through staged release of vascular endothelial growth factor-A and platelet-derived growth factor-BB. *Tissue Eng Part A*, 18, 26-34.
- ELASSAL, A. A., AL-RADI, O. O., ZAHER, Z. F., DOHAIN, A. M., ABDELMOHSEN, G. A., MOHAMED, R. S., FATANI, M. A., ABDELMOTALEB, M. E., NOAMAN, N. A., ELMELIGY, M. A. & ELDIB, O. S. 2021. Equine pericardium: a versatile alternative reconstructive material in congenital cardiac surgery. *J Cardiothorac Surg*, 16, 110.
- EMMERT, M. Y., WEBER, B., WOLINT, P., BEHR, L., SAMMUT, S., FRAUENFELDER, T., FRESE, L., SCHERMAN, J., BROKOPP, C. E., TEMPLIN, C., GRUNENFELDER, J., ZUND, G., FALK, V. & HOERSTRUP, S. P. 2012. Stem cell-based transcatheter aortic valve implantation: first experiences in a pre-clinical model. *JACC Cardiovasc Interv*, 5, 874-83.
- EUROP.RAT“, E. P. U. 2020. VERORDNUNG (EU) 2017/745 DES EUROPÄISCHEN PARLAMENTS UND DES RATES vom 5. April 2017 über Medizinprodukte, zur Änderung der Richtlinie 2001/83/EG, der Verordnung (EG) Nr. 178/2002 und der Verordnung (EG) Nr. 1223/2009 und zur Aufhebung der Richtlinien 90/385/EWG und 93/42/EWG des Rates. *In: UNION, E. (ed.)*.
- FARBER, M. A., VALLABHANENI, R. & MARSTON, W. A. 2014. "Off-the-shelf" devices for complex aortic aneurysm repair. *J Vasc Surg*, 60, 579-84.
- FARRINGTON, M., WREGHITT, T., MATTHEWS, I., SCARR, D., SUTEHALL, G., HUNT, C. J., SANTIAGO, T., GRUYS, E., VOORHOUT, W., RAMOS, T. & PEGG, D. E. 2002. Processing of cardiac valve allografts: 2. Effects of antimicrobial treatment on sterility, structure and mechanical properties. *Cell Tissue Bank*, 3, 91-103.
- FIDALGO, C., IOP, L., SCIRO, M., HARDER, M., MAVRILAS, D., KOROSSIS, S., BAGNO, A., PALÙ, G., AGUIARI, P. & GEROSA, G. 2018. A sterilization method for decellularized xenogeneic cardiovascular scaffolds. *Acta Biomater*, 67, 282-294.
- FIORETTA, E. S., DIJKMAN, P. E., EMMERT, M. Y. & HOERSTRUP, S. P. 2018. The future of heart valve replacement: recent developments and translational challenges for heart valve tissue engineering. *J Tissue Eng Regen Med*, 12, e323-e335.
- FIORETTA, E. S., MOTTA, S. E., LINTAS, V., LOERAKKER, S., PARKER, K. K., BAAIJENS, F. P. T., FALK, V., HOERSTRUP, S. P. & EMMERT, M. Y. 2021. Next-generation tissue-engineered heart valves with repair, remodelling and regeneration capacity. *Nat Rev Cardiol*, 18, 92-116.
- FISHER, C. W., FIORELLO, A., SHAFFER, D., JACKSON, M. & MCDONNELL, G. E. 2012. Aldehyde-resistant mycobacteria bacteria associated with the use of endoscope reprocessing systems. *Am J Infect Control*, 40, 880-2.
- FUCHS, J. R., NASSERI, B. A. & VACANTI, J. P. 2001. Tissue engineering: a 21st century solution to surgical reconstruction. *Ann Thorac Surg*, 72, 577-91.
- GALGON, R. E. 2016. Understanding medical device regulation. *Curr Opin Anaesthesiol*, 29, 703-710.

- GENSLER, M., LEIKEIM, A., MÖLLMANN, M., KOMMA, M., HEID, S., MÜLLER, C., BOCCACCINI, A. R., SALEHI, S., GROEBER-BECKER, F. & HANSMANN, J. 2020. 3D printing of bioreactors in tissue engineering: A generalised approach. *PLOS ONE*, 15, e0242615.
- GHASSEMI, T., SAGHATOLESLAMI, N., MAHDAVI-SHAHRI, N., MATIN, M. M., GHESHLAGHI, R. & MORADI, A. 2019. A comparison study of different decellularization treatments on bovine articular cartilage. *J Tissue Eng Regen Med*, 13, 1861-1871.
- GILBERT, T. W., SELLARO, T. L. & BADYLAK, S. F. 2006. Decellularization of tissues and organs. *Biomaterials*, 27, 3675-83.
- GILPIN, S. E., GUYETTE, J. P., GONZALEZ, G., REN, X., ASARA, J. M., MATHISEN, D. J., VACANTI, J. P. & OTT, H. C. 2014. Perfusion decellularization of human and porcine lungs: bringing the matrix to clinical scale. *J Heart Lung Transplant*, 33, 298-308.
- GOMEZ-FLORIT, M., PARDO, A., DOMINGUES, R. M. A., GRAÇA, A. L., BABO, P. S., REIS, R. L. & GOMES, M. E. 2020. Natural-Based Hydrogels for Tissue Engineering Applications. *Molecules*, 25.
- GONZÁLEZ-ANDRADES, M., CARRIEL, V., RIVERA-IZQUIERDO, M., GARZÓN, I., GONZÁLEZ-ANDRADES, E., MEDIALDEA, S., ALAMINOS, M. & CAMPOS, A. 2015. Effects of Detergent-Based Protocols on Decellularization of Corneas With Sclerocorneal Limbus. Evaluation of Regional Differences. *Transl Vis Sci Technol*, 4, 13.
- GORMAN, D. E., WU, T., GILPIN, S. E. & OTT, H. C. 2018. A Fully Automated High-Throughput Bioreactor System for Lung Regeneration. *Tissue Eng Part C Methods*, 24, 671-678.
- GOSZTYLA, C., LADD, M. R., WERTS, A., FULTON, W., JOHNSON, B., SODHI, C. & HACKAM, D. J. 2020. A Comparison of Sterilization Techniques for Production of Decellularized Intestine in Mice. *Tissue Eng Part C Methods*, 26, 67-79.
- GRAB, M., STIEGLMEIER, F., EMRICH, J., GREFEN, L., LEONE, A., KÖNIG, F., HAGL, C. & THIERFELDER, N. 2021. Customized 3D printed bioreactors for decellularization-High efficiency and quality on a budget. *Artif Organs*, 45, 1477-1490.
- GREFEN, L., KONIG, F., GRAB, M., HAGL, C. & THIERFELDER, N. 2018. Pericardial tissue for cardiovascular application: an in-vitro evaluation of established and advanced production processes. *J Mater Sci Mater Med*, 29, 172.
- GUALANDI, C., BLOISE, N., MAURO, N., FERRUTI, P., MANFREDI, A., SAMPAOLES, M., LIGUORI, A., LAURITA, R., GHERARDI, M., COLOMBO, V., VISAI, L., FOCARETE, M. L. & RANUCCI, E. 2016. Poly-L-Lactic Acid Nanofiber-Polyamidoamine Hydrogel Composites: Preparation, Properties, and Preliminary Evaluation as Scaffolds for Human Pluripotent Stem Cell Culturing. *Macromol Biosci*, 16, 1533-1544.
- GUPTA, S. K. & MISHRA, N. C. Decellularization Methods for Scaffold Fabrication. Totowa, NJ: Humana Press.
- GURUSWAMY DAMODARAN, R. & VERMETTE, P. 2018. Tissue and organ decellularization in regenerative medicine. *Biotechnol Prog*, 34, 1494-1505.

- HALLER, N., HOLLWECK, T., THIERFELDER, N., SCHULTE, J., HAUSHERR, J. M., DAUNER, M. & AKRA, B. 2013. Noninvasive analysis of synthetic and decellularized scaffolds for heart valve tissue engineering. *ASAIO J*, 59, 169-77.
- HARRELL, C. R., DJONOV, V., FELLABAUM, C. & VOLAREVIC, V. 2018. Risks of Using Sterilization by Gamma Radiation: The Other Side of the Coin. *Int J Med Sci*, 15, 274-279.
- HASHIMOTO, Y., FUNAMOTO, S., SASAKI, S., NEGISHI, J., HONDA, T., HATTORI, S., NAM, K., KIMURA, T., MOCHIZUKI, M., KOBAYASHI, H. & KISHIDA, A. 2015. Corneal Regeneration by Deep Anterior Lamellar Keratoplasty (DALK) Using Decellularized Corneal Matrix. *PLoS One*, 10, e0131989.
- HE, M., CALLANAN, A., LAGARAS, K., STEELE, J. A. M. & STEVENS, M. M. 2017. Optimization of SDS exposure on preservation of ECM characteristics in whole organ decellularization of rat kidneys. *J Biomed Mater Res B Appl Biomater*, 105, 1352-1360.
- HERSEL, U., DAHMEN, C. & KESSLER, H. 2003. RGD modified polymers: biomaterials for stimulated cell adhesion and beyond. *Biomaterials*, 24, 4385-415.
- HEUSCHKEL, M. A., LEITOLIS, A., RODERJAN, J. G., SUSS, P. H., LUZIA, C. A. O., DA COSTA, F. D. A., CORREA, A. & STIMAMIGLIO, M. A. 2019. In vitro evaluation of bovine pericardium after a soft decellularization approach for use in tissue engineering. *Xenotransplantation*, 26, e12464.
- HILFIKER, A., KASPER, C., HASS, R. & HAVERICH, A. 2011. Mesenchymal stem cells and progenitor cells in connective tissue engineering and regenerative medicine: is there a future for transplantation? *Langenbecks Arch Surg*, 396, 489-97.
- HINDERER, S., SEIFERT, J., VOTTELER, M., SHEN, N., RHEINLAENDER, J., SCHAFFER, T. E. & SCHENKEL-LAYLAND, K. 2014. Engineering of a bio-functionalized hybrid off-the-shelf heart valve. *Biomaterials*, 35, 2130-9.
- HOERSTRUP, S. P., KADNER, A., MELNITCHOUK, S., TROJAN, A., EID, K., TRACY, J., SODIAN, R., VISJAGER, J. F., KOLB, S. A., GRUNENFELDER, J., ZUND, G. & TURINA, M. I. 2002. Tissue engineering of functional trileaflet heart valves from human marrow stromal cells. *Circulation*, 106, I143-50.
- HOF, A., RASCHKE, S., BAIER, K., NEHRENHEIM, L., SELIG, J. I., SCHOMAKER, M., LICHTENBERG, A., MEYER, H. & AKHYARI, P. 2016. Challenges in developing a reseeded, tissue-engineered aortic valve prosthesis. *Eur J Cardiothorac Surg*, 50, 446-55.
- HOFFMANN, G., LUTTER, G. & CREMER, J. 2008. Durability of bioprosthetic cardiac valves. *Dtsch Arztebl Int*, 105, 143-8.
- HORKE, A., BOBYLEV, D., AVSAR, M., MEYNS, B., REGA, F., HAZEKAMP, M., HUEBLER, M., SCHMIADY, M., TZANAVAROS, I., CESNJEVAR, R., CIUBOTARU, A., LAUFER, G., ZIMPFER, D., JASHARI, R., BOETHIG, D., CEBOTARI, S., BEERBAUM, P., TUDORACHE, I., HAVERICH, A. & SARIKOUCH, S. 2020. Paediatric aortic valve replacement using decellularized allografts. *Eur J Cardiothorac Surg*, 58, 817-824.
- JANA, S., BHAGIA, A. & LERMAN, A. 2019a. Optimization of polycaprolactone fibrous scaffold for heart valve tissue engineering. *Biomed Mater*, 14, 065014.

- JANA, S., FRANCHI, F. & LERMAN, A. 2019b. Trilayered tissue structure with leaflet-like orientations developed through in vivo tissue engineering. *Biomedical Materials*, 15, 015004.
- JANA, S., TEFFT, B. J., SPOON, D. B. & SIMARI, R. D. 2014. Scaffolds for tissue engineering of cardiac valves. *Acta Biomater*, 10, 2877-93.
- JANA, S., TRANQUILLO, R. T. & LERMAN, A. 2016. Cells for tissue engineering of cardiac valves. *J Tissue Eng Regen Med*, 10, 804-824.
- JIN, G., YANG, G.-H. & KIM, G. 2015a. Tissue engineering bioreactor systems for applying physical and electrical stimulations to cells. *Journal of Biomedical Materials Research Part B: Applied Biomaterials*, 103, 935-948.
- JIN, G., YANG, G. H. & KIM, G. 2015b. Tissue engineering bioreactor systems for applying physical and electrical stimulations to cells. *J Biomed Mater Res B Appl Biomater*, 103, 935-48.
- JOCKENHOEVEL, S., ZUND, G., HOERSTRUP, S. P., CHALABI, K., SACHWEH, J. S., DEMIRCAN, L., MESSMER, B. J. & TURINA, M. 2001. Fibrin gel -- advantages of a new scaffold in cardiovascular tissue engineering. *Eur J Cardiothorac Surg*, 19, 424-30.
- KASIMIR, M. T., RIEDER, E., SEEBACHER, G., WOLNER, E., WEIGEL, G. & SIMON, P. 2005. Presence and elimination of the xenoantigen gal ( $\alpha$ 1, 3) gal in tissue-engineered heart valves. *Tissue Eng*, 11, 1274-80.
- KAWECKI, M., ŁABUŚ, W., KLAMA-BARYLA, A., KITALA, D., KRAUT, M., GLIK, J., MISIUGA, M., NOWAK, M., BIELECKI, T. & KASPERCZYK, A. 2017. A review of decellurization methods caused by an urgent need for quality control of cell-free extracellular matrix' scaffolds and their role in regenerative medicine. *Journal of Biomedical Materials Research Part B: Applied Biomaterials*, n/a-n/a.
- KHALPEY, Z., QU, N., HEMPHILL, C., LOUIS, A. V., FERNG, A. S., SON, T. G., STAVOE, K., PENICK, K., TRAN, P. L., KONHILAS, J., LAGRAND, D. S. & GARCIA, J. G. N. 2015. Rapid Porcine Lung Decellularization Using a Novel Organ Regenerative Control Acquisition Bioreactor. *ASAIO Journal*, 61, 71-77.
- KIM, M. S., LIM, H. G. & KIM, Y. J. 2016a. Calcification of decellularized and alpha-galactosidase-treated bovine pericardial tissue in an alpha-Gal knock-out mouse implantation model: comparison with primate pericardial tissue. *Eur J Cardiothorac Surg*, 49, 894-900.
- KIM, N., CHOI, J., KIM, S., GWON, Y. D., CHO, Y., YANG, J. M., OH, Y. K. & KIM, Y. B. 2016b. Transmission of Porcine Endogenous Retrovirus Produced from Different Recipient Cells In Vivo. *PLoS One*, 11, e0165156.
- KISIEL, M. A. & KLAR, A. S. 2019. Isolation and Culture of Human Dermal Fibroblasts. *Methods Mol Biol*, 1993, 71-78.
- KLUIN, J., TALACUA, H., SMITS, A. I. P. M., EMMERT, M. Y., BRUGMANS, M. C. P., FIORETTA, E. S., DIJKMAN, P. E., SÖNTJENS, S. H. M., DUIJVELSHOFF, R., DEKKER, S., JANSSEN-VAN DEN BROEK, M. W. J. T., LINTAS, V., VINK, A., HOERSTRUP, S. P., JANSSEN, H. M., DANKERS, P. Y. W.,



- BAAIJENS, F. P. T. & BOUTEN, C. V. C. 2017. In situ heart valve tissue engineering using a bioresorbable elastomeric implant – From material design to 12 months follow-up in sheep. *Biomaterials*, 125, 101-117.
- KOENIG, F., KILZER, M., HAGL, C. & THIERFELDER, N. 2019. Successful decellularization of thick-walled tissue: Highlighting pitfalls and the need for a multifactorial approach. *Int J Artif Organs*, 42, 17-24.
- KOENIG, F., LEE, J. S., AKRA, B., HOLLWECK, T., WINTERMANTEL, E., HAGL, C. & THIERFELDER, N. 2016. Is Transcatheter Aortic Valve Implantation of Living Tissue-Engineered Valves Feasible? An In Vitro Evaluation Utilizing a Decellularized and Reseeded Biohybrid Valve. *Artif Organs*, 40, 727-37.
- LALYS, F., ESNEAULT, S., CASTRO, M., ROYER, L., HAIGRON, P., AUFFRET, V. & TOMASI, J. 2019. Automatic aortic root segmentation and anatomical landmarks detection for TAVI procedure planning. *Minim Invasive Ther Allied Technol*, 28, 157-164.
- LANGER, R. & VACANTI, J. P. 1993. Tissue engineering. *Science*, 260, 920-6.
- LAUER, M., BARKER, J. P., SOLANO, M. & DUBIN, J. 2017. FDA Device Regulation. *Mo Med*, 114, 283-288.
- LI, J., ZILZ, C., FLOERCHINGER, B., HOLZAMER, A., CAMBONI, D., SCHACH, C., SCHMID, C. & RUPPRECHT, L. 2020. Long-Term Results of Patch Repair in Destructive Valve Endocarditis. *Thorac Cardiovasc Surg*.
- LI, X., GUO, Y., ZIEGLER, K. R., MODEL, L. S., EGHBALIEH, S. D., BRENES, R. A., KIM, S. T., SHU, C. & DARDIK, A. 2011. Current usage and future directions for the bovine pericardial patch. *Ann Vasc Surg*, 25, 561-8.
- LIM, H. G., KIM, G. B., JEONG, S. & KIM, Y. J. 2015. Development of a next-generation tissue valve using a glutaraldehyde-fixed porcine aortic valve treated with decellularization,  $\alpha$ -galactosidase, space filler, organic solvent and detoxification. *Eur J Cardiothorac Surg*, 48, 104-13.
- MASOUMI, N., ANNABI, N., ASSMANN, A., LARSON, B. L., HJORTNAES, J., ALEMDAR, N., KHARAZIHA, M., MANNING, K. B., MAYER, J. E., JR. & KHADEMHOSSEINI, A. 2014. Tri-layered elastomeric scaffolds for engineering heart valve leaflets. *Biomaterials*, 35, 7774-85.
- MAURMANN, N., SPERLING, L. E. & PRANKE, P. 2018. Electrospun and Electrospayed Scaffolds for Tissue Engineering. *Adv Exp Med Biol*, 1078, 79-100.
- MEWHORT, H. E. M., SVYSTONYUK, D. A., TURNBULL, J. D., TENG, G., BELKE, D. D., GUZZARDI, D. G., PARK, D. S., KANG, S., HOLLENBERG, M. D. & FEDAK, P. W. M. 2017. Bioactive Extracellular Matrix Scaffold Promotes Adaptive Cardiac Remodeling and Repair. *JACC Basic Transl Sci*, 2, 450-464.
- MIRDAMADI, E. S., KALHORI, D., ZAKERI, N., AZARPIRA, N. & SOLATI-HASHJIN, M. 2020. Liver Tissue Engineering as an Emerging Alternative for Liver Disease Treatment. *Tissue Eng Part B Rev*, 26, 145-163.

- MOREIRA, R., GESCHE, V. N., HURTADO-AGUILAR, L. G., SCHMITZ-RODE, T., FRESE, J., JOCKENHOEVEL, S. & MELA, P. 2014. TexMi: Development of Tissue-Engineered Textile-Reinforced Mitral Valve Prosthesis. *Tissue Engineering. Part C, Methods*, 20, 741-748.
- NASO, F. & GANDAGLIA, A. 2017. Different approaches to heart valve decellularization: A comprehensive overview of the past 30 years. *Xenotransplantation*.
- NATHUSIUS, S. V., KÖNIG, F., SODIAN, R., BORN, F., HAGL, C. & THIERFELDER, N. 2018. The cardiomy reservoir – a preliminary evaluation of a new cell source for cardiovascular tissue engineering. *The International Journal of Artificial Organs*, 41, 115-123.
- O'CONNOR MOONEY, R., DAVIS, N. F., HOEY, D., HOGAN, L., MCGLOUGHLIN, T. M. & WALSH, M. T. 2015. On the Automatic Decellularisation of Porcine Aortae: A Repeatability Study Using a Non-Enzymatic Approach. *Cells Tissues Organs*, 201, 299-318.
- OHNUKI, M. & TAKAHASHI, K. 2015. Present and future challenges of induced pluripotent stem cells. *Philos Trans R Soc Lond B Biol Sci*, 370, 20140367.
- OTTO, C. M., KUMBHANI, D. J., ALEXANDER, K. P., CALHOON, J. H., DESAI, M. Y., KAUL, S., LEE, J. C., RUIZ, C. E. & VASSILEVA, C. M. 2017. 2017 ACC Expert Consensus Decision Pathway for Transcatheter Aortic Valve Replacement in the Management of Adults With Aortic Stenosis: A Report of the American College of Cardiology Task Force on Clinical Expert Consensus Documents. *J Am Coll Cardiol*, 69, 1313-1346.
- OZALP, N., OKTE, Z. & OZCELIK, B. 2006. The rapid sterilization of gutta-percha cones with sodium hypochlorite and glutaraldehyde. *J Endod*, 32, 1202-4.
- PANIAGUA GUTIERREZ, J. R., BERRY, H., KOROSSIS, S., MIRSADRAEE, S., LOPES, S. V., DA COSTA, F., KEARNEY, J., WATTERSON, K., FISHER, J. & INGHAM, E. 2015. Regenerative potential of low-concentration SDS-decellularized porcine aortic valved conduits in vivo. *Tissue Eng Part A*, 21, 332-42.
- PERRI, G., POLITO, A., ESPOSITO, C., ALBANESE, S. B., FRANCALANCI, P., PONGIGLIONE, G. & CAROTTI, A. 2012. Early and late failure of tissue-engineered pulmonary valve conduits used for right ventricular outflow tract reconstruction in patients with congenital heart disease. *Eur J Cardiothorac Surg*, 41, 1320-5.
- PUPERI, D. S., O'CONNELL, R. W., PUNSKE, Z. E., WU, Y., WEST, J. L. & GRANDE-ALLEN, K. J. 2016. Hyaluronan Hydrogels for a Biomimetic Spongiosa Layer of Tissue Engineered Heart Valve Scaffolds. *Biomacromolecules*, 17, 1766-75.
- RAHHAB, Z., EL FAQUIR, N., TCHETCHE, D., DELGADO, V., KODALI, S., MARA VOLLEMA, E., BAX, J., LEON, M. B. & VAN MIEGHEM, N. M. 2020. Expanding the indications for transcatheter aortic valve implantation. *Nat Rev Cardiol*, 17, 75-84.
- RJ, I. J., DUCHATEAU, S. D. R., SCHOUTEN, R. M., SLIEKER, M. G., HAZEKAMP, M. G. & SCHOOF, P. H. 2020. Long-Term Follow-Up of Pericardium for the Ventricular Component in Atrioventricular Septal Defect Repair. *World J Pediatr Congenit Heart Surg*, 11, 742-747.

- ROOSENS, A., ASADIAN, M., DE GEYTER, N., SOMERS, P. & CORNELISSEN, R. 2017. Complete Static Repopulation of Decellularized Porcine Tissues for Heart Valve Engineering: An in vitro Study. *Cells Tissues Organs*, 204, 270-282.
- RUFFER, A., PURBOJO, A., CICHA, I., GLOCKLER, M., POTAPOV, S., DITTRICH, S. & CESNJEVAR, R. A. 2010. Early failure of xenogenous de-cellularised pulmonary valve conduits--a word of caution! *Eur J Cardiothorac Surg*, 38, 78-85.
- SACKS, M. S., CHUONG, C. J. & MORE, R. 1994. Collagen fiber architecture of bovine pericardium. *ASAIO J*, 40, M632-7.
- SAIDY, N. T., WOLF, F., BAS, O., KEIJDENER, H., HUTMACHER, D. W., MELA, P. & DE-JUAN-PARDO, E. M. 2019. Biologically Inspired Scaffolds for Heart Valve Tissue Engineering via Melt Electrowriting. *Small*, 15, e1900873.
- SCHEUER, M. H., T.; HAAS, U.; BARTOK, E.; BOMBIEN, R.; FANO, C.; DAUNER, M.; REICHART, B.; SCHMITZ, C.; AKRA, B. 2012. The Effect of Rolling and Crimping on Cell-Seeded Synthetic Scaffolds for the Development of Transcatheter Valves by Tissue Engineering. *Journal of Materials Science Research*, 1, 1-10.
- SCHOEN, F. J. & LEVY, R. J. 2005. Calcification of tissue heart valve substitutes: progress toward understanding and prevention. *Ann Thorac Surg*, 79, 1072-80.
- SELDEN, C. & FULLER, B. 2018. Role of Bioreactor Technology in Tissue Engineering for Clinical Use and Therapeutic Target Design. *Bioengineering (Basel)*, 5.
- SERRY, F. M., KADRY, A. A. & ABDELRAHMAN, A. A. 2003. Potential biological indicators for glutaraldehyde and formaldehyde sterilization processes. *J Ind Microbiol Biotechnol*, 30, 135-40.
- SHAHVERDYAN, R., GRAY, D., GAWENDA, M. & BRUNKWALL, J. 2016. Single Centre Results of Total Endovascular Repair of Complex Aortic Aneurysms with Custom Made Anaconda Fenestrated Stent Grafts. *Eur J Vasc Endovasc Surg*, 52, 500-508.
- SIERAD, L. N., SHAW, E. L., BINA, A., BRAZILE, B., RIERSON, N., PATNAIK, S. S., KENNAMER, A., ODUM, R., COTOI, O., TEREZIA, P., BRANZANIUC, K., SMALLWOOD, H., DEAC, R., EGYED, I., PAVAI, Z., SZANTO, A., HARCEAGA, L., SUCIU, H., RAICEA, V., OLAH, P., SIMIONESCU, A., LIAO, J., MOVILEANU, I., HARPA, M. & SIMIONESCU, D. T. 2015. Functional Heart Valve Scaffolds Obtained by Complete Decellularization of Porcine Aortic Roots in a Novel Differential Pressure Gradient Perfusion System. *Tissue Eng Part C Methods*, 21, 1284-96.
- SIMIONESCU, D., SIMIONESCU, A. & DEAC, R. 1993. Mapping of glutaraldehyde-treated bovine pericardium and tissue selection for bioprosthetic heart valves. *J Biomed Mater Res*, 27, 697-704.
- SIMON, P., KASIMIR, M. T., SEEBACHER, G., WEIGEL, G., ULLRICH, R., SALZER-MUHAR, U., RIEDER, E. & WOLNER, E. 2003. Early failure of the tissue engineered porcine heart valve SYNERGRAFT in pediatric patients. *Eur J Cardiothorac Surg*, 23, 1002-6; discussion 1006.

- SIMONINI, A., MOSCUCCI, M., MULLER, D. W., BATES, E. R., PAGANI, F. D., BURDICK, M. D. & STRIETER, R. M. 2000. IL-8 is an angiogenic factor in human coronary atherectomy tissue. *Circulation*, 101, 1519-26.
- SODIAN, R., HOERSTRUP, S. P., SPERLING, J. S., DAEBRITZ, S., MARTIN, D. P., MORAN, A. M., KIM, B. S., SCHOEN, F. J., VACANTI, J. P. & MAYER, J. E., JR. 2000. Early in vivo experience with tissue-engineered trileaflet heart valves. *Circulation*, 102, III22-9.
- SODIAN, R., LUEDERS, C., KRAEMER, L., KUEBLER, W., SHAKIBAEI, M., REICHART, B., DAEBRITZ, S. & HETZER, R. 2006. Tissue engineering of autologous human heart valves using cryopreserved vascular umbilical cord cells. *Ann Thorac Surg*, 81, 2207-16.
- STARNECKER, F., KONIG, F., HAGL, C. & THIERFELDER, N. 2018. Tissue-engineering acellular scaffolds- The significant influence of physical and procedural decellularization factors. *J Biomed Mater Res B Appl Biomater*, 106, 153-162.
- STIEGLMEIER, F., GRAB, M., KÖNIG, F., BÜCH, J., HAGL, C. & THIERFELDER, N. 2021. Mapping of bovine pericardium to enable a standardized acquirement of material for medical implants. *J Mech Behav Biomed Mater*, 118, 104432.
- TEXAKALIDIS, P., GIANNOPOULOS, S., CHARISIS, N., GIANNOPOULOS, S., KARASAVVIDIS, T., KOULLIAS, G. & JABBOUR, P. 2018. A meta-analysis of randomized trials comparing bovine pericardium and other patch materials for carotid endarterectomy. *J Vasc Surg*, 68, 1241-1256.e1.
- THIERFELDER, N., KOENIG, F., BOMBIEN, R., FANO, C., REICHART, B., WINTERMANTEL, E., SCHMITZ, C. & AKRA, B. 2013. In vitro comparison of novel polyurethane aortic valves and homografts after seeding and conditioning. *ASAIO J*, 59, 309-16.
- TIPNIS, N. P. & BURGESS, D. J. 2018. Sterilization of implantable polymer-based medical devices: A review. *Int J Pharm*, 544, 455-460.
- VAHANIAN, A., ALFIERI, O., ANDREOTTI, F., ANTUNES, M. J., BARÓN-ESQUIVIAS, G., BAUMGARTNER, H., BORGER, M. A., CARREL, T. P., DE BONIS, M., EVANGELISTA, A., FALK, V., LUNG, B., LANCELLOTTI, P., PIERARD, L., PRICE, S., SCHÄFFERS, H. J., SCHULER, G., STEPINSKA, J., SWEDBERG, K., TAKKENBERG, J., VON OPPELL, U. O., WINDECKER, S., ZAMORANO, J. L. & ZEMBALA, M. 2012. Guidelines on the management of valvular heart disease (version 2012): the Joint Task Force on the Management of Valvular Heart Disease of the European Society of Cardiology (ESC) and the European Association for Cardio-Thoracic Surgery (EACTS). *Eur J Cardiothorac Surg*, 42, S1-44.
- VAN DEN BOGAERDT, A. J., VAN ZUIJLEN, P. P., VAN GALEN, M., LAMME, E. N. & MIDDELKOOP, E. 2002. The suitability of cells from different tissues for use in tissue-engineered skin substitutes. *Arch Dermatol Res*, 294, 135-42.
- VAN VELTHOVEN, M. J. J., RAMADAN, R., ZÜGEL, F. S., KLOTZ, B. J., GAWLITTA, D., COSTA, P. F., MALDA, J., CASTILHO, M. D., DE KORT, L. M. O. & DE GRAAF, P. 2020. Gel Casting as an Approach for Tissue Engineering of Multilayered Tubular Structures. *Tissue Eng Part C Methods*, 26, 190-198.

- VAZ, C. M., VAN TUIJL, S., BOUTEN, C. V. & BAAIJENS, F. P. 2005. Design of scaffolds for blood vessel tissue engineering using a multi-layering electrospinning technique. *Acta Biomater*, 1, 575-82.
- VEDEPO, M. C., DETAMORE, M. S., HOPKINS, R. A. & CONVERSE, G. L. 2017. Recellularization of decellularized heart valves: Progress toward the tissue-engineered heart valve. *J Tissue Eng*, 8, 2041731417726327.
- VOLAREVIC, V., MARKOVIC, B. S., GAZDIC, M., VOLAREVIC, A., JOVICIC, N., ARSENIJEVIC, N., ARMSTRONG, L., DJONOV, V., LAKO, M. & STOJKOVIC, M. 2018. Ethical and Safety Issues of Stem Cell-Based Therapy. *Int J Med Sci*, 15, 36-45.
- VON NATHUSIUS, S., KONIG, F., SODIAN, R., BORN, F., HAGL, C. & THIERFELDER, N. 2017. The cardiotomy reservoir - a preliminary evaluation of a new cell source for cardiovascular tissue engineering. *Int J Artif Organs*, 0.
- VOORNEVELD, J., OOSTHUYSEN, A., FRANZ, T., ZILLA, P. & BEZUIDENHOUT, D. 2017. Dual electrospinning with sacrificial fibers for engineered porosity and enhancement of tissue ingrowth. *J Biomed Mater Res B Appl Biomater*, 105, 1559-1572.
- WALKER, S., DITTFELD, C., JAKOB, A., SCHÖNFELDER, J., KÖNIG, U. & TUGTEKIN, S. M. 2020. Sterilization and Cross-Linking Combined with Ultraviolet Irradiation and Low-Energy Electron Irradiation Procedure: New Perspectives for Bovine Pericardial Implants in Cardiac Surgery. *Thorac Cardiovasc Surg*.
- WANG, J., ZHANG, F., TSANG, W. P., WAN, C. & WU, C. 2017. Fabrication of injectable high strength hydrogel based on 4-arm star PEG for cartilage tissue engineering. *Biomaterials*, 120, 11-21.
- WEBER, B., DIJKMAN, P. E., SCHERMAN, J., SANDERS, B., EMMERT, M. Y., GRUNENFELDER, J., VERBEEK, R., BRACHER, M., BLACK, M., FRANZ, T., KORTSMIT, J., MODREGGER, P., PETER, S., STAMPANONI, M., ROBERT, J., KEHL, D., VAN DOESELAAR, M., SCHWEIGER, M., BROKOPP, C. E., WALCHLI, T., FALK, V., ZILLA, P., DRIESSEN-MOL, A., BAAIJENS, F. P. & HOERSTRUP, S. P. 2013. Off-the-shelf human decellularized tissue-engineered heart valves in a non-human primate model. *Biomaterials*, 34, 7269-80.
- WILCZEK, P., LESIAK, A., NIEMIEC-CYGANEK, A., KUBIN, B., SLOMSKI, R., NOZYNSKI, J., WILCZEK, G., MZYK, A. & GRAMATYKA, M. 2015. Biomechanical properties of hybrid heart valve prosthesis utilizing the pigs that do not express the galactose- $\alpha$ -1,3-galactose ( $\alpha$ -Gal) antigen derived tissue and tissue engineering technique. *J Mater Sci Mater Med*, 26, 5329.
- WILSON, S. L., SIDNEY, L. E., DUNPHY, S. E., DUA, H. S. & HOPKINSON, A. 2015. Corneal Decellularization: A Method of Recycling Unsuitable Donor Tissue for Clinical Translation? *Curr Eye Res*, 1-14.
- WILTZ, D., AREVALOS, C. A., BALAOING, L. R., BLANCAS, A. A., SAPP, M. C., ZHANG, X. & GRANDE-ALLEN, K. J. 2013. *Extracellular Matrix Organization, Structure, and Function*.
- XUE, Y., SANT, V., PHILLIPPI, J. & SANT, S. 2017. Biodegradable and biomimetic elastomeric scaffolds for tissue-engineered heart valves. *Acta Biomater*, 48, 2-19.

- YAMASHITA, H., OZAKI, S., IWASAKI, K., KAWASE, I., NOZAWA, Y. & UMEZU, M. 2012. Tensile strength of human pericardium treated with glutaraldehyde. *Ann Thorac Cardiovasc Surg*, 18, 434-7.
- YANG, J., SHEN, M., WEN, H., LUO, Y., HUANG, R., RONG, L. & XIE, J. 2020. Recent advance in delivery system and tissue engineering applications of chondroitin sulfate. *Carbohydr Polym*, 230, 115650.
- YANO, K., SPEIDEL, A. T. & YAMATO, M. 2018. Four Food and Drug Administration draft guidance documents and the REGROW Act: A litmus test for future changes in human cell- and tissue-based products regulatory policy in the United States? *J Tissue Eng Regen Med*, 12, 1579-1593.
- YAO, T., WIERINGA, P. A., CHEN, H., AMIT, C., SAMAL, P., GISELBRECHT, S., BAKER, M. B. & MORONI, L. 2020. Fabrication of a self-assembled honeycomb nanofibrous scaffold to guide endothelial morphogenesis. *Biofabrication*, 12, 045001.
- ZHANG, F. & KING, M. W. 2020. Biodegradable Polymers as the Pivotal Player in the Design of Tissue Engineering Scaffolds. *Adv Healthc Mater*, 9, e1901358.
- ZHU, J. 2010. Bioactive modification of poly(ethylene glycol) hydrogels for tissue engineering. *Biomaterials*, 31, 4639-56.
- ZUNCHEDDU, D., DELLA BELLA, E., SCHWAB, A., PETTA, D., ROCCHITTA, G., GENERELLI, S., KURTH, F., PARRILLI, A., VERRIER, S., RAU, J. V., FOSCA, M., MAIOLI, M., SERRA, P. A., ALINI, M., REDL, H., GRAD, S. & BASOLI, V. 2021. Quality control methods in musculoskeletal tissue engineering: from imaging to biosensors. *Bone Res*, 9, 46.
- ZUND, G., BREUER, C. K., SHINOKA, T., MA, P. X., LANGER, R., MAYER, J. E. & VACANTI, J. P. 1997. The in vitro construction of a tissue engineered bioprosthetic heart valve. *Eur J Cardiothorac Surg*, 11, 493-7.

## 7 Originalarbeiten

### 7.1 Use of a special bioreactor for the cultivation of a new flexible polyurethane scaffold for aortic valve tissue engineering (Aleksieva et al., 2012)

- Genoveva Aleksieva, Trixi Hollweck, Nikolaus Thierfelder, Ulrike Haas, Fabian König, Cornelia Fano, Martin Dauner, Erich Wintermantel, Bruno Reichart, Christoph Schmitz, Bassil Akra
- BioMedical Engineering OnLine Eng Online. 2012 Dec 4;11:92
- DOI: 10.1186/1475-925X-11-92

RESEARCH

Open Access

# Use of a special bioreactor for the cultivation of a new flexible polyurethane scaffold for aortic valve tissue engineering

Genoveva Aleksieva<sup>1†</sup>, Trixi Hollweck<sup>1†</sup>, Nikolaus Thierfelder<sup>1</sup>, Ulrike Haas<sup>1</sup>, Fabian Koenig<sup>3</sup>, Cornelia Fano<sup>2</sup>, Martin Dauner<sup>2</sup>, Erich Wintermantel<sup>3</sup>, Bruno Reichart<sup>1</sup>, Christoph Schmitz<sup>1</sup> and Bassil Akra<sup>1\*</sup>

\* Correspondence: [bassil.akra@med.uni-muenchen.de](mailto:bassil.akra@med.uni-muenchen.de)  
<sup>†</sup>Equal contributors  
<sup>1</sup>Department of Cardiac Surgery, Medical Center Munich University, Marchioninistraße 15, Munich 81377, Germany  
Full list of author information is available at the end of the article

## Abstract

**Background:** Tissue engineering represents a promising new method for treating heart valve diseases. The aim of this study was evaluate the importance of conditioning procedures of tissue engineered polyurethane heart valve prostheses by the comparison of static and dynamic cultivation methods.

**Methods:** Human vascular endothelial cells (ECs) and fibroblasts (FBs) were obtained from saphenous vein segments. Polyurethane scaffolds (n = 10) were primarily seeded with FBs and subsequently with ECs, followed by different cultivation methods of cell layers (A: static, B: dynamic). Group A was statically cultivated for 6 days. Group B was exposed to low flow conditions (t<sub>1</sub>= 3 days at 750 ml/min, t<sub>2</sub>= 2 days at 1100 ml/min) in a newly developed conditioning bioreactor. Samples were taken after static and dynamic cultivation and were analyzed by scanning electron microscopy (SEM), immunohistochemistry (IHC), and real time polymerase chain reaction (RT-PCR).

**Results:** SEM results showed a high density of adherent cells on the surface valves from both groups. However, better cell distribution and cell behavior was detected in Group B. IHC staining against CD31 and TE-7 revealed a positive reaction in both groups. Higher expression of extracellular matrix (ICAM, Collagen IV) was observed in Group B. RT-PCR demonstrated a higher expression of inflammatory Cytokines in Group B.

**Conclusion:** While conventional cultivation method can be used for the development of tissue engineered heart valves. Better results can be obtained by performing a conditioning step that may improve the tolerance of cells to shear stress. The novel pulsatile bioreactor offers an adequate tool for in vitro improvement of mechanical properties of tissue engineered cardiovascular prostheses.

**Keywords:** Tissue engineering, Heart valve, Polyurethane scaffold, Static cultivation, Dynamic cultivation

## Background

Valve replacement represents the most common surgical therapy for end staged valvular diseases with an estimated number of 275.000 procedures performed annually worldwide [1]. The commonly used artificial heart valves are mechanical or biological prostheses. According to the American Heart Association, mechanical heart valves are recommended for patient under 60 years of age [2]. However, the increased risk of postoperative hemorrhage, thromboembolism, and drug-drug interactions affect patients' quality of life



[2]. Biological valves are accompanied by a low risk for thromboembolism and endocarditis, and offer growth potential for pediatric patients [3,4]. However, biological valves are associated with different major complications such as deterioration of valve structure, graft calcification, limited durability, and affinity to immunological response [2]. Tissue engineered heart valves (TEHVs) are a promising approach to overcome the limitations of conventional heart valve prostheses. Tissue engineering generally aims for the *in-vitro* creation of viable neo-tissue indistinguishable from native tissue [5]. Biological and engineering challenges are focused on three principal components that comprise the “cell–scaffold–bioreactor system” [6]. An adequate combination of these components could be the ideal solution for heart valve grafting leading to biocompatibility, non-thrombogenicity, non-teratogenicity, long-term durability and growth potential of TEHVs [7]. The aim of this study was to compare static cultivation (SC) and dynamic cultivation (DC) of endothelial cells (ECs) and fibroblasts (FBs) seeded onto polyurethane heart valve scaffolds by evaluating cell confluency, extracellular matrix (ECM) formation and inflammatory response.

## Methods

### Cell isolation

Cells were isolated from human saphenous vein segments left over from cardiac surgery interventions. Tissue samples were only taken with the patients' informed consent and were further used in an anonymous fashion with no individual-related data. Veins were cannulated and rinsed with aliquots of 500 ml M199 (Biochrom AG, Berlin, Germany) supplemented with 1 ml Heparin (5000 i.E.; Ratiopharm GmbH, Ulm, Germany) and 5 ml Gentamycin (10 mg/ml; Invitrogen AG, Darmstadt, Germany). For EC isolation, segments were incubated with trypsin/EDTA-solution (10x; Sigma-Aldrich GmbH, Taufkirchen, Germany) for 25 min at 37°C / 5% CO<sub>2</sub>. For FBs isolation, veins were subsequently flushed with 2 mg/ml collagenase type II (Worthington Biochemical Corporation / CellSystems GmbH, St. Katharinen, Germany) in human serum albumin (200 g/l; Baxter GmbH, Unterschleißheim, Germany) and incubated for 30 min. Cell suspensions were centrifuged at 750 rpm for 10 min, and cultured in endothelial cell growth medium (Promocell GmbH, Heidelberg, Germany) supplemented with 6% FCS (Lonza GmbH, Köln, Germany) and 0.2% Penicillin/Streptomycin (Sigma Aldrich GmbH, Hamburg, Germany) and fibroblast growth medium (Promocell GmbH, Heidelberg, Germany) supplemented with 11% FCS and 0.2% Penicillin/Streptomycin, respectively. Medium was changed every second day. Cells were passaged at confluency.

### Phenotypic characterization of isolated cells

Morphological and immunocytological analysis were performed to characterize isolated cell types. ECs were identified by their typical cobblestone morphology. FBs were identified by a characteristic elongated spindle-shaped appearance with several extensions. For immunocytological verification of ECs and FBs, 35.000 cells/cm<sup>2</sup> were cultured in an 8-well culture slide (BD Bioscience, Bedford, USA) until confluency. Vascular cells were stained against EC-specific CD31 (0.14 µg/ml; Dianova GmbH, Hamburg, Germany) and FB-specific TE-7 (0.67 µg/ml, Millipore Corporation BioScience Division, Temecula, CA, USA), respectively according to manufacturer's protocol using EnVision™ + Dual Link System-HRP (Dako

Deutschland GmbH, Hamburg, Germany). Briefly, cells were fixed at  $-80^{\circ}\text{C}$  in 96% ethanol. The staining procedure was performed at room temperature (RT). After rinsing with phosphate buffered saline (PBS; Biochrom AG, Berlin, Germany) and blocking for endogenous peroxidase using 30%  $\text{H}_2\text{O}_2$ , cells were incubated with the primary antibody for 30 min. The procedure was completed by incubation with EnVision™ + Dual Link System- HRP (Dako Deutschland GmbH, Hamburg, Germany) for 30 min; and AEC- Peroxidase-Substrate (Vector Laboratories, Inc., Burlingame, CA, USA) incubation for 10 min. Counterstaining was performed using 25% Mayer's Haemalaun (Merck KGaA, Darmstadt, Germany) in PBS for 3 min at RT. Controls for non-specific binding of biotinylated link were performed by excluding the primary antibody. The stained cells were analyzed using bright field microscopy (Leica DMR microscope, Leica Microsystems GmbH, Wetzlar, Germany).

#### Fabrication of polyurethane heart valve prosthesis (PHVP)

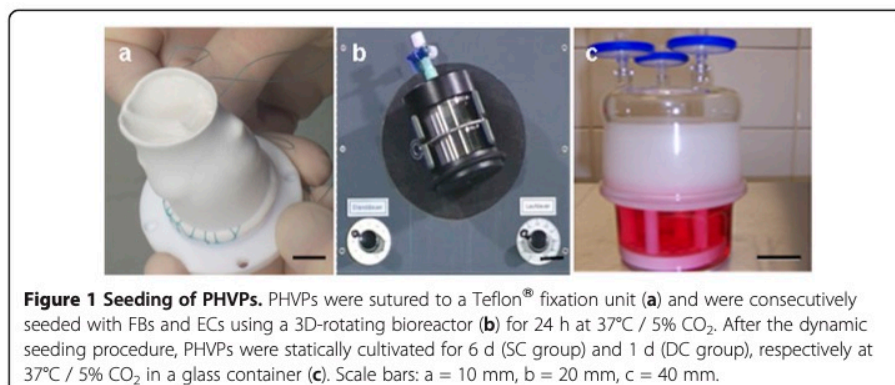
PHVPs (h = 55 mm, d = 18 mm) were manufactured by ITV-Denkendorf (Denkendorf, Germany) using a polyurethane spraying technique (patent DE 28 06 030 C2). Randomly oriented PU fibres formed a sheet with a thickness of 0.3 mm. For seeding purpose, PHVP was  $\gamma$ -sterilized at 10 kGy according to a certified sterilization procedure.

#### Seeding procedure

PHVPs were sutured to a Teflon® fixation unit (Figure 1a, manufactured in-house) and were seeded as previously described [8]. Briefly, PHVPs were initially seeded with FBs ( $1.5 \times 10^6$  cells/cm<sup>2</sup>) using a 3D- rotating seeding device (Figure 1b; manufactured in-house) for 24 h (running phase: 2.5 min; holding phase: 30 min), at  $37^{\circ}\text{C}$  / 5%  $\text{CO}_2$  followed by a stationary cultivation phase of 6 d (SC group) and 1 d (DC group), respectively at  $37^{\circ}\text{C}$  / 5%  $\text{CO}_2$  in a glass container (Figure 1c). Cell medium was changed every two days. Colonization of ECs was analogously performed.

#### Cultivation procedures

For SC, seeded PHVPs (n = 5) were cultured for 6 d at  $37^{\circ}\text{C}$  / 5%  $\text{CO}_2$  in a glass container. This procedure is analog the stationary cultivation phase of the seeding procedure shown in Figure 1c.

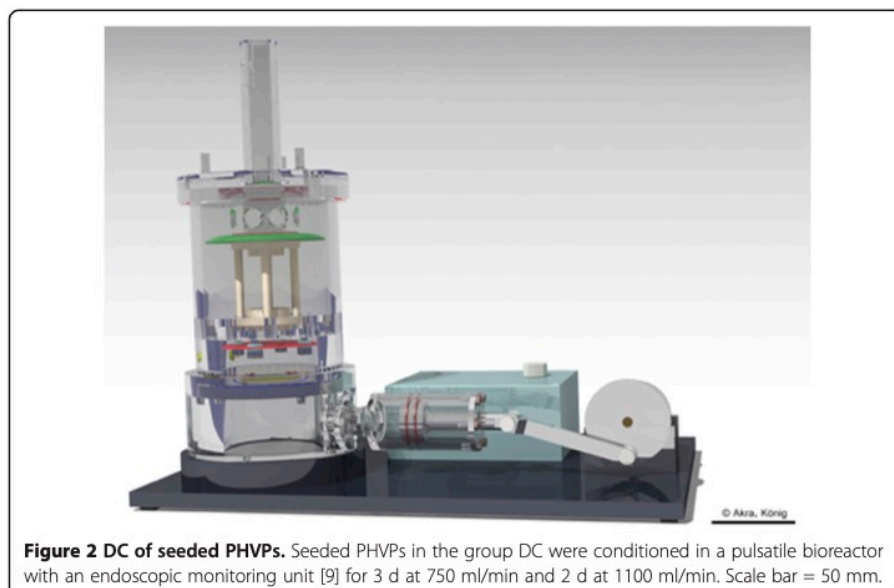




For DC, PHVPs ( $n = 5$ ) were conditioned in a novel pulsatile bioreactor with an endoscopic monitoring unit (Figure 2; EU-Patent pending EP10166094; manufactured in-house, [9]) for 3 d at 750 ml/min and 2 d at 1100 ml/min medium flow, after FB seeding and after EC seeding. For the conditioning of FB seeded PHVP, fibroblast growth medium supplemented with 11% FCS and 0.2% Penicillin/Streptomycin were used. FB +EC seeded PHVP were conditioned using endothelial cell growth supplemented with 6% FCS and 0.2% Penicillin/Streptomycin. The viscosity of the media was  $0.738 \text{ mPas} \pm 0.078 \text{ mPas}$ . Cell medium was partially changed every two days. For further analysis, samples were taken from native as well as from seeded PHVPs after SC and after DC. Samples were taken from the supra-avalvular, valvular and subvalvular region of the aortic wall as well as from the valvular leaflets.

#### Immunohistochemistry (IHC)

Immunohistochemical stainings were performed to differentiate between FB and EC layers on seeded PHVPs ( $n = 10$ ). Samples were fixed in 4% formalin (Microcos GmbH, Garching, Germany) for 10 d, embedded in paraffin and sectioned at  $10 \mu\text{m}$ . Specimen were deparaffinized in Xylene (Carl Roth GmbH + Co. KG, Karlsruhe, Germany), rehydrated by an descending ethanol (Merck KGaA, Darmstadt, Germany) series and permeabilized with 0.5% Triton-X (Sigma Aldrich Chemie GmbH, Taufkirchen, Germany) in PBS for 10 min at RT. Samples for staining against VE-Cadherin, Connexin-43, Fibronectin and Collagen IV were exposed to 10% Protease (Dako Deutschland GmbH, Hamburg, Germany) in distilled water (Ampuwa, Fresenius Kabi Deutschland GmbH, Bad Homburg v.d. H., Germany) for 10 min at RT. For proteolysis of Fibronectin, Collagen IV, and SMC-Myosin, specimens were boiled in 0.1 mM EDTA buffer ( $\text{pH} = 8.0$ , Sigma Aldrich Chemie GmbH, Taufkirchen, Germany) or in Target Retrieval solution ( $\text{pH} = 6.0$ , Dako Deutschland GmbH, Hamburg, Germany) for 15 min. For demasking of  $\alpha$ -Actin, samples were boiled in 10 mM Tris/1 mM EDTA solution ( $\text{pH} = 9.0$ , Sigma Aldrich Chemie



GmbH, Taufkirchen, Germany) for 15 min. After blocking for endogenous peroxidase using 0.4% H<sub>2</sub>O<sub>2</sub> in PBS, samples were incubated overnight at 4°C with primary antibodies against VCAM (200 µg/ml), ICAM, SMC-Myosin (0.954 mg/ml; Dako Deutschland GmbH, Hamburg, Germany), Fibronectin (0.6 mg/ml; Sigma Aldrich Chemie GmbH, Taufkirchen, Germany), TE-7 (0.1 mg/ml; Millipore GmbH, Schwalbach / Ts., Germany), Connexin- 43 (1 µg/ml; Millipore GmbH, Schwalbach/Ts., Germany), VE- Cadherin (0.2 mg/ml; Beckmann Coulter Inc., Marseille, France), Collagen IV (5.4 mg/ml; Sigma Aldrich Chemie GmbH, Taufkirchen, Germany), CD31 (0.2 mg/ml; Dako Deutschland GmbH, Hamburg, Germany) and α- Actin (44 µg/ml; Dako Deutschland GmbH, Hamburg, Germany). Specimens were incubated with EnVision™ + Dual Link System-HRP (Dako Deutschland GmbH, Hamburg, Germany), for 10 min, followed by AEC labelling using AEC-Peroxidase-Substrate Kit (Vector Laboratories, Inc., Burlingame, CA, USA) for 10 min at RT. Counterstaining was performed for 3 min at RT using Mayer's Hemalaun (Merck KGaA, Darmstadt, Germany). Controls for non-specific binding of biotinylated link were performed by excluding primary antibodies. Sections in duplicates of each region were qualitatively observed using bright field microscopy (Leica DMR microscope, Leica Microsystems GmbH, Wetzlar, Germany) in four fields of vision. The intensity of IHC staining was analyzed by a minimum of two experts without being blinded to intervention and were classified as high (+++), medium (++), low (+) and absent (0).

#### Scanning electron microscopy (SEM)

Samples were fixed in 456 ml aqua bidest supplemented with 0.75 ml 1 N hydrochloric acid (Titrisol, Merck KGaA, Darmstadt, Germany), 43.5 ml glutaraldehyd (Sigma-Aldrich Chemie GmbH, Steinheim, Germany) and 5.65 g sodium cocodylate trihydrate (Sigma-Aldrich Chemie GmbH, Steinheim, Germany) at 4°C for 48 h. Dehydration of fixed specimens was performed by an ascending ethanol series (30%, 50%, 70%, 96%) and after which the samples were placed in 100% acetone (Merck KGaA, Darmstadt, Germany). After sample drying at the critical point, specimens were coated with gold for 180 s at 10<sup>-5</sup> and examined under a scanning electron microscope (Carl Zeiss MikroImaging GmbH, Göttingen, Germany). Unseeded PHVP specimen served as negative controls.

#### Real time PCR (RT- PCR)

For detection of cytokine expression after SC and DC, RT-PCR was performed according to manufacturer's protocols. Briefly, RNA was isolated from samples stored in liquid nitrogen using RNAeasy Plus Mini Kit (Qiagen, GmbH, Hilden, Germany). RNA purity and quantity was photometrically (BioPhotometer, Eppendorf AG, Hamburg, Germany) assessed. QuantiTect Reverse Transcription Kit (Qiagen, GmbH, Hilden, Germany) was applied for reverse transcription. Rotor-Gene Q 2plex System (35 cycles; Qiagen GmbH, Hilden, Germany) and QuantiFast SYBR Green PCR Kit (Qiagen GmbH, Hilden, Germany) were used to determine IL-1a, IL-6, IL-8, MCP-1, VCAM and GAPDH (QuantiTect Primer Assay, Qiagen GmbH, Hilden, Germany) expression. A standard curve was generated to determine the primer-dilution. Negative controls without sample material were included for all PCR measurements. Resulting Ct-values were normalized to the housekeeping gene GAPDH. PCR-product specificity was verified by melt curve analysis and gel electrophoresis (FlashGel System, Lonza GmbH, Basel, Switzerland).



### Statistical analysis

All values are expressed as mean  $\pm$  standard deviation. Student's t-test was performed for comparison of data of unpaired samples. All tests are one-tailed; the probability value  $p < 0.05$  was considered significant.

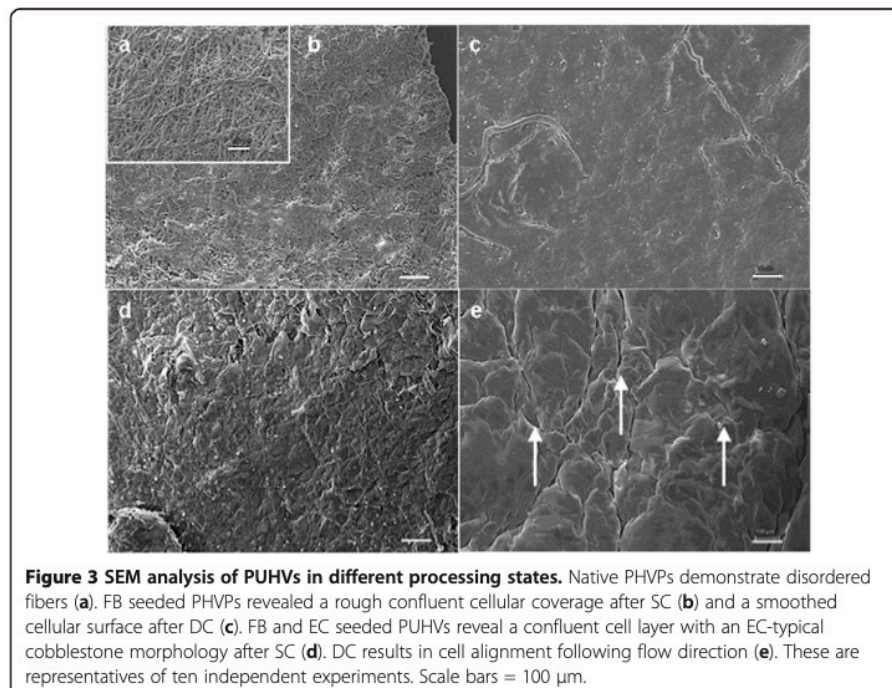
## Results

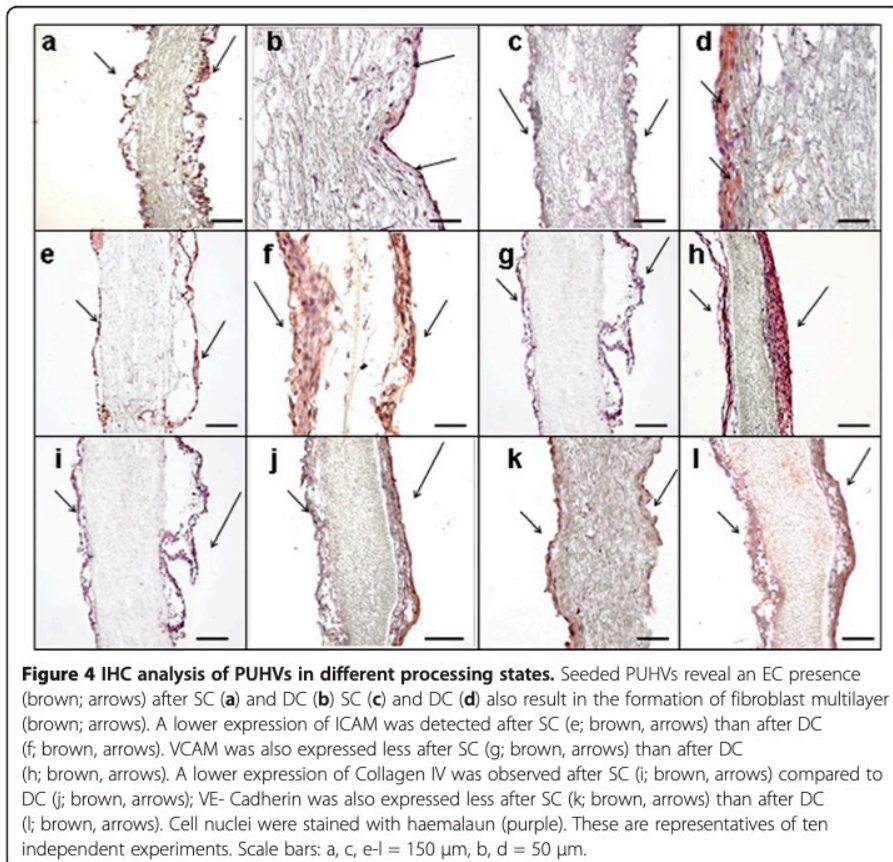
### Cell confluence

Seeding and cultivation of PHVPs were performed as described in materials and methods section. SEM analysis (Figure 3) of native samples (a) showed randomly orientated fibres. FB seeded PHVPs revealed a rough confluent cellular coverage after SC (b) and a smoothed cellular surface after DC (c). FB and EC seeded PHVPs showed a confluent cell layer after SC (d) and DC (e). In addition, the typical cobblestone morphology indicates an endothelial layer after SC and DC. Moreover, flow conditions ( $t_1 = 3$  d at 750 ml/min,  $t_2 = 2$  d at 1100 ml/min) influence cell alignment; ECs of the internal side of the PHVPs were orientated in flow direction (e).

### Protein expression

IHC examination was performed to compare cellular coverage and ECM formation after SC and DC. Cell nuclei were stained with haemalaun (purple). As shown in Figure 4, staining against CD31 (brown; arrows) revealed a positive reaction at both culture conditions (a: SC, b: DC), indicating EC presence. Fibroblasts were detected after SC (c) and DC (d) in a continuous multilayer by staining against TE-7 (brown, arrows). Comparison of cellular adhesion molecules demonstrated a lower expression of ICAM after SC (e; brown, arrows) than after DC (f; brown, arrows). VCAM was also expressed less after



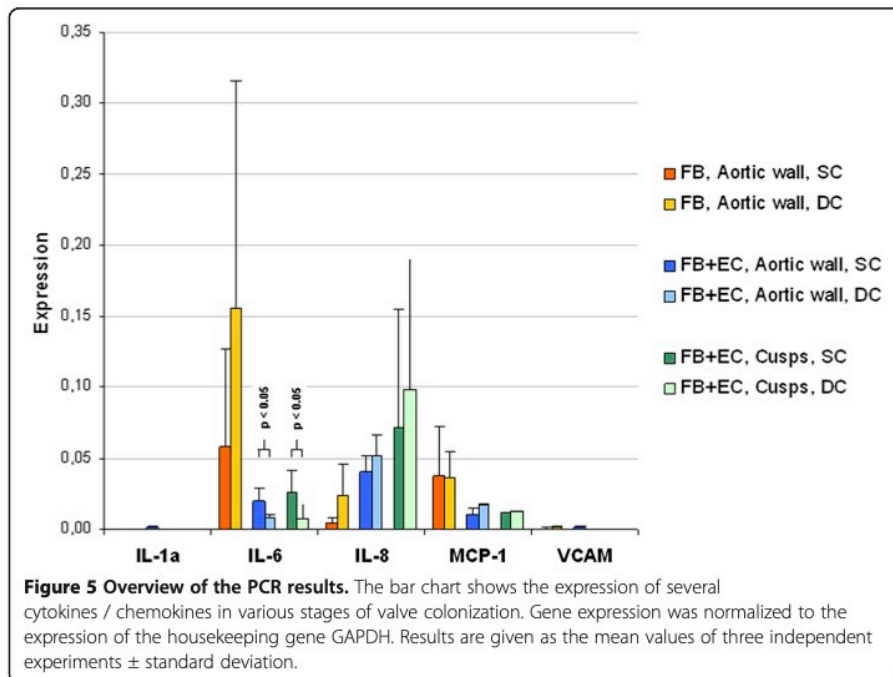


SC (g; brown, arrows) than after DC (h; brown, arrows). A lower expression of Collagen IV was observed after SC (i; brown, arrows) compared to DC (j; brown, arrows); VE- Cadherin was also expressed less after SC (k; brown, arrows) than after DC (l; brown, arrows). Controls for non-specific chromogen binding displayed negligible staining for antigens (data not shown).

#### Gene expression

Figure 5 illustrates the mean values of gene expression in the aortic wall and cusps after SC and DC. Gene expression was normalized to the expression of the housekeeping gene GAPDH. The analysis of the aortic wall segments and the cusps of the heart valves proportionately showed equivalent gene expressions after SC and DC for all cytokines. The analysis of IL-1a and VCAM revealed a negligible expression after SC and DC. In both cultivation procedures seeding of EC results in a decrease of IL-6 (SC: -66%, DC: -95%) and MCP-1 (SC: -71%, DC: -56%) expression while IL-8 (SC: + 868%, DC: + 123%) was expressed to a higher level. The comparison of the SC and DC of FB+EC seeded aortic wall showed a lower expression of IL-6 (- 59%) and an increase of IL-8 (+ 29%) and MCP-1 (+ 51%) expression after DC. FB+EC seeded cusps showed a lower expression of IL-6 (- 72%), an increase of IL-8 (+ 37%) expression and a comparable MCP-1 expression (+ 10%) after DC compared to SC.





## Discussion

Tissue engineering is an emerging field focused on the development of bioartificial substitutes to restore, maintain, or improve tissue function. These applications are the key for the future treatment of many diseases [10]. Currently, in tissue engineering are several scaffolds materials under investigation. Synthetic, non-degradable polymers like polyurethane are mainly characterized by their structural resistance, a three dimensional form with defined pore sizes, non-immunogenic and anti-thrombotic properties [11]. Within the monomeric unit, moieties could be substituted by different groups, resulting in versatile properties. Fabrication of hydrolytic stable PU already led to the development of different implants like vascular grafts, artificial heart valves and catheters [11,12]. Cells needed for the development of the tissue engineered heart valves can be obtained from a saphenous vein - vascular cells, be taken by a bone marrow biopsy - bone marrow stromal cells, from newborn patients, umbilical cord-derived cells or blood derived endothelial progenitor cells and chorionic villi-derived cells [13]. In our study, we obtained FBs and ECs from saphenous vein segments which were no longer required in coronary bypass operations. According to Schmidt et al., neither the proliferation in a monolayer nor the three-dimensional growth as tissue engineered constructs is influenced by the age of the cell donor [13], indicating that adult saphenous vein segments are an adequate cell source for tissue engineering applications. During the development of a cardiovascular tissue-engineered construct, a large challenge is the creation of a confluent and stable endothelial cell layer. Complications after the implantation of artificial grafts are caused in part by the lack of an intact endothelium [14]. The endothelial cell function has been described several times [15,16]. Consigny et al. showed a better adhesion and shear stress resistance of ECs on prosthetic vessels or heart valves pre-coated with different ECM proteins [16]. Although this coating improves cell adhesion, the integrity of the coating is compromised at high flow rates [17]. Another

strategy to enhance the adhesion of ECs is the pre-seeding of prosthesis with vascular FBs, mimicking conditions *in vivo* [8]. In addition, the fibrillar structure of PHVPs is similar to collagen, the main component of native ECM, and may support cell adhesion. Moreover, *In vivo*, cellular phenotype, morphology, and proliferation are affected by mechanical, electrical and chemical signals [18]. If these signals are inappropriate or absent, cells lose their ability to develop an ECM and to form organized tissues [19]. Thus, the simulation of physiological conditions, such as shear stress, plays an important role in the development of tissue engineered constructs [20,21]. For the fabrication of vascular grafts, Syedain *et al.* and Tschoeke *et al.* demonstrated the expression of ECM components by human dermal fibroblast and ovine arterial myofibroblasts in fibrin gel under dynamic culture conditions generated by a pulsed flow-stretch bioreactor and a pulsatile bioreactor, respectively [22,23].

In heart valve fabrication, bioreactors for tissue formation under dynamic culture conditions have been reported several times [24,25]. Ramaswamy *et al.* described a large collagen mass production after the use of simulated pulmonary artery conditions using an organ-level heart valve bioreactor [26]. The stimulation of human dermal fibroblasts seeded onto a decellularized porcine matrix by a pneumatic flow bioreactor, resulting in the synthesis of ECM proteins was shown by Zeltinger *et al.* [27]. Mol *et al.* demonstrated that dynamically strained leaflets reveal a more homogenous and denser cellular coverage than leaflets exposed to pre-strain only [25]. This is in line with results, generated in our study: SC and DC results in a confluent cell layer. In this context, numerous studies have reported the behaviour of ECs to flow shear stress *in-vitro*. ECs are constantly subjected to hemodynamic forces, including shear stresses that induce various functional changes in vascular endothelium. Initially, it was found that exposure of ECs to elevated shear stresses *in-vitro* caused them to align in the direction of flow [28]. In our study, after DC ECs were also orientated into flow direction after DC, indicating the adaption to shear stress. The higher expression of cellular adhesion molecules after DC illustrates the intensified formation of cell connecting molecules, due to the pulsatile conditioning process. Moreover, a higher expression of Collagen IV, VE-Cadherin and Fibronectin was observed after DC indicating the formation of an ECM, essential for tissue and organ morphogenesis, maintenance, and reconstruction following injury in association with constructive tissue remodeling [29]. However, shear stress as a result of the DC provoked a higher cytokine expression compared to SC [30]. EC are able to sense changes in the shear stress or flow forces and respond, for instance, by expression of pro-inflammatory cytokines [31]. These cytokines and/or chemokines play key roles in mediating inflammatory reactions [32]. Gerszten *et al.* already concluded that cytokines are important modulators of monocyte-endothelial interactions under flow conditions [33]. McGill *et al.* demonstrated that consecutive seeding of heart valve scaffolds with FB and EC results in a less inflammatory response after DC than singly seeding with EC [34]. Chiu *et al.* reported that a coculture of vascular ECs with vascular smooth muscle cells induces the expression of ICAM-1, VCAM-1, and E-selectin genes in ECs in the static condition, whereas the application of shear stress to ECs inhibits these coculture-induced gene expressions [35]. Our analysis of IL-1a and VCAM expression revealed a negligible expression after SC and DC of FB and EC seeded scaffolds. These findings are also described by McHale *et al.* and Murui *et al.*, indicate a lower risk of inflammatory response and arteriosclerosis [36,37]. While IL-1a and VCAM were expressed to a lower level after DC, the expression of IL-8 increased after DC. Several studies have shown a correlation between IL-8 expression, arteriosclerosis and coagulation which is thought to



be caused by monocyte activation, adhesion and transmigration across the endothelial barrier [34,38]. However, not only shear stress, but rather cell isolation from biopsies provokes stress symptoms. For example, the process of human islet isolation triggers a cascade of stressful events in the islets of Langerhans involving the production of proinflammatory molecules. Two of the major pathways responsible for cellular responses to stress, already occurs in pancreatic cells during the isolation procedure. The production and release of IL-6, IL-8 and MCP-1, were observed days after the isolation procedure in isolated purified islets [39]. Therefore, the next step will be long-term conditioning of our TEHV's for a better adaption of cells to shear stress after isolation and cultivation procedure and consequently to reduce inflammatory response.

### Conclusions

In conclusion, we demonstrate that DC is more effective than SC in generating TEHV's. DC supports ECM formation and homogeneity of the cellular coverage. The novel pulsatile bioreactor provides a strong tool for dynamic pre-conditioning of TEHV's.

### Abbreviations

AEC: 3-amino-9-ethylcarbazole; CD31: Cluster of differentiation 31; DC: Dynamic cultivation; ECs: Endothelial cells; ECM: Extracellular matrix; FBs: Fibroblasts; FCS: Fetal calf serum; GAPDH: Glyceraldehyde-3-phosphate dehydrogenase; HRP: Horseradish peroxidase; ICAM: Intracellular adhesion molecule; IHC: Immunohistochemistry; IL-1a: Interleukin-1a; IL-6: Interleukin-6; IL-8: Interleukin-8; MCP-1: Monocyte chemotactic protein-1; PBS: Phosphate buffered saline; PHVPs: Polyurethane heart valve prostheses; PU: Polyurethane; RNA: Ribonucleic acid; RT: Room temperature; RT-PCR: Real time polymerase chain reaction; SC: Static cultivation; SMC-Myosin: Smooth muscle cell myosin; TEHV's: Tissue engineered heart valves; VCAM: Vascular cell adhesion molecule.

### Competing interests

The authors declare that they have no competing interests.

### Authors' contributions

GA mainly conducted experiments. TH wrote the manuscript, performed data analyses and statistical evaluations. NT also conducted experiments. UH supported the data generation. FK constructed the pulsatile bioreactor. CF manufactured the polymer scaffolds by spraying. MD was supervising the PHVP development and was one of the inventors of the 3-dimensional scaffolds. EW supervised the technical construction done by FK. BR was one of the inventors of the 3-dimensional scaffolds. CS supported this study from the medical point of view and supervised GA. BA conceived the experimental study, was the project owner; the device inventor, the group leader and overall supervisor. All authors read and approved the final manuscript.

### Acknowledgments

We would like to thank Medtronic, Inc. for their support and ITV Denckendorf Produktservice GmbH for providing the polymers.

### Author details

<sup>1</sup>Department of Cardiac Surgery, Medical Center Munich University, Marchioninstraße 15, Munich 81377, Germany. <sup>2</sup>Institute of Textile Technology and Process Engineering, Körschtalstraße 26, Denckendorf 73770, Germany. <sup>3</sup>Chair of Medical Engineering, Technical University of Munich, Boltzmannstrasse 15, Garching 85748, Germany.

Received: 6 September 2012 Accepted: 30 November 2012

Published: 4 December 2012

### References

1. Schoen FJ, Levy RJ: Calcification of tissue heart valve substitutes: progress toward understanding and prevention. *Ann Thorac Surg* 2005, **79**:1072–1080.
2. Huang G, Rahimtoola SH: Prosthetic heart valve. *Circulation* 2011, **123**:2602–2605.
3. Sewell-Loftin MK, Chun YW, Khademhosseini A, Merryman WD: EMT-inducing biomaterials for heart valve engineering: taking cues from developmental biology. *J CardiovascTransl Res* 2011, **4**:658–671.
4. Cohen IS, Gaudette GR: *Regenerating the Heart*. New York: Springer; 2011.
5. Weber B, Emmert MY, Schoenauer R, Brokopp C, Baumgartner L, Hoerstrup SP: Tissue engineering on matrix: future of autologous tissue replacement. *Semin Immunopathol* 2011, **33**:307–315.
6. Meinel L, Fajardo R, Snyder B, Shinde-Patil V, Zichner L, Kaplan D, Langer R, Vunjak-Novakovic G: Bone tissue engineering using human mesenchymal stem cells: effects of scaffold material and medium flow. *Ann Biomed Eng* 2004, **32**:112–122.
7. Cebotari S, Tudorache I, Schilling T, Haverich A: Heart valve and myocardial tissue engineering. *Herz* 2010, **35**:334–341.

8. Gulbins H, Goldemund A, Anderson I, Haas U, Uhlig A, Meiser B, Reichart B: **Preseeding with autologous fibroblasts improves endothelialization of glutaraldehyde-fixed porcine aortic valves.** *J Thorac Cardiovasc Surg* 2003, **125**:592–601.
9. König F, Hollweck T, Pfeiffer S, Schmitz C, Reichart B, Wintermantel E, Akra B: **A pulsatile bioreactor for conditioning of tissue-engineered cardiovascular constructs under endoscopic visualization.** *J Funct Biomater* 2012, **3**:480–496.
10. Khait L, Hecker L, Blan NR, Cohan G, Migneco F, Huang YC, Birla RK: **Getting to the heart of tissue engineering.** *J Cardiovasc Transl Res* 2008, **1**:71–84.
11. Wintermantel E, Ha SW: *Medizintechnik: Life Science Engineering.* Berlin, Heidelberg, New York: Springer Verlag GmbH; 2008.
12. Wintermantel E, Ha SW: *Medizintechnik mit biokompatiblen Werkstoffen und Verfahren.* Berlin, Heidelberg, New York: Springer Verlag GmbH; 2002.
13. Schmidt D, Hoerstrup SP: **Tissue engineered heart valves based on human cells.** *Swiss Med Wkly* 2007, **3**:480–496.
14. Stachelek SJ, Alferiev I, Connolly JM, Sacks M, Hebbel RP, Bianco R, Levy RJ: **Cholesterol-modified polyurethane valve cusps demonstrate blood outgrowth endothelial cell adhesion post-seeding in vitro and in vivo.** *Ann Thorac Surg* 2006, **81**:47–55.
15. Rademacher A, Paulitschke M, Meyer R, Hetzer R: **Endothelialization of PTFE vascular grafts under flow induces significant cell changes.** *Int J Artif Organs* 2001, **24**:235–242.
16. Consigny PM, Vitali NJ: **Resistance of freshly adherent endothelial cells to detachment by shear stress is matrix and time dependent.** *J Vas Interv Radiol* 1998, **9**:479–485.
17. Kannan RY, Salacinski HJ, Butler PE, Hamilton G, Seifalian AM: **Current status of prosthetic bypass grafts: a review.** *J Biomed Mater Res B Appl Biomater* 2005, **74**:570–581.
18. Georges PC, Janmey PA: **Cell type-specific response to growth on soft materials.** *J Appl Physiol* 2005, **98**:1547–1553.
19. Barron V, Lyons E, Stenson-Cox C, McHugh PE, Pandit A: **Bioreactors for cardiovascular cell and tissue growth: a review.** *Ann Biomed Eng* 2003, **31**:1017–1030.
20. Yeung T, Georges PC, Flanagan LA, Marg B, Ortiz M, Funaki M, Zahir N, Ming W, Weaver V, Janmey PA: **Effects of substrate stiffness on cell morphology, cytoskeletal structure, and adhesion.** *Cell Motil Cytoskeleton* 2005, **60**:24–34.
21. Sheikh S, Rainger GE, Gale Z, Rahman M, Nash GB: **Exposure to fluid shear stress modulates the ability of endothelial cells to recruit neutrophils in response to tumor necrosis factor-alpha: a basis for local variations in vascular sensitivity to inflammation.** *Blood* 2003, **102**:2828–2834.
22. Syedain ZH, Meier LA, Bjork JW, Lee A, Tranquillo RT: **Implantable arterial grafts from human fibroblasts and fibrin using a multi-graft pulsed flow-stretch bioreactor with noninvasive strength monitoring.** *Biomaterials* 2011, **32**:714–722.
23. Tschoeke B, Flanagan TC, Cornelissen A, Koch S, Roehl A, Sriharwoko M, Sachweh JS, Gries T, Schmitz-Rode T, Jockenhoevel S: **Development of a composite degradable/nondegradable tissue-engineered vascular graft.** *Artif Organs* 2008, **32**:800–809.
24. Sierad LN, Simionescu A, Albers C, Chen J, Maivelett J, Tedder ME, Liao J, Simionescu DT: **Design and testing of a pulsatile conditioning system for dynamic endothelialization of polyphenol-stabilized tissue engineered heart valves.** *Cardiovasc Eng Technol* 2010, **1**:138–153.
25. Mol A, Driessen NJ, Rutten MC, Hoerstrup SP, Bouten CV, Baaijens FP: **Tissue engineering of human heart valve leaflets: a novel bioreactor for a strain-based conditioning approach.** *Ann Biomed Eng* 2005, **33**:1778–1788.
26. Ramaswamy S, Gottlieb D, Engelmayr GC, Aikawa E, Schmidt DE, Gaitan-Leon DM, Sales VL, Mayer JE, Sacks MS: **The role of organ level conditioning on the promotion of engineered heart valve tissue development in vitro using mesenchymal stem cells.** *Biomaterials* 2010, **31**:1114–1125.
27. Zeltinger J, Landeen LK, Alexander HG, Kidd ID, Sibanda B: **Development and characterization of tissue-engineered aortic valves.** *Tissue Eng* 2011, **7**:9–22.
28. Fuster V, Alexander RW, O'Rourke RA: *The Heart.* New York: The McGraw-Hill Companies, Inc; 2004.
29. Simionescu A, Schulte JB, Fercana G, Simionescu DT: **Inflammation in cardiovascular tissue engineering: the challenge to a promise: a minireview.** *Int J Inflamm* 2011, **2011**:1–11.
30. Montes-Worboys A, Rodriguez-Portal JA, Arellano-Orden E, Digon-Pereiras J, Rodriguez-Panadero F: **Interleukin-8 activates coagulation and correlates with survival after talc pleurodesis.** *Eur Respir J* 2010, **35**:160–166.
31. Nagel T, Resnick N, Atkinson WJ, Dewey CF Jr, Gimbrone MA Jr: **Shear stress selectively upregulates intercellular adhesion molecule-1 expression in cultured human vascular endothelial cells.** *J Clin Invest* 1994, **94**:885–891.
32. Feghali CA, Wright TM: **Cytokines in acute and chronic inflammation.** *Front Biosci* 1997, **2**:d12–d26.
33. Gerszten RE, Garcia-Zepeda EA, Lim YC, Yoshida M, Ding HA, Gimbrone MA Jr, Luster AD, Luscinskas FW, Rosenzweig A: **MCP-1 and IL-8 trigger firm adhesion of monocytes to vascular endothelium under flow conditions.** *Nature* 1999, **398**:718–723.
34. McGill SN, Ahmed NA, Christou NV: **Endothelial cells: role in Infection and Inflammation.** *World J Surg* 1998, **22**:171–178.
35. Chiu JJ, Chen LJ, Lee PL, Lee CI, Lo LW, Usami S, Chien S: **Shear stress inhibits adhesion molecule expression in vascular endothelial cells induced by coculture with smooth muscle cells.** *Blood* 2003, **101**:2667–2674.
36. McHale JF, Marshall D, Haskard DO: **TNF- $\alpha$  and IL-1 sequentially induce endothelial ICAM-1 and VCAM-1 expression in MRL/lpr lupus-prone mice.** *J Immunol* 1999, **7**:3993–4000.
37. Marui N, Offermann MK, Swerlick R, Kunsch C, Rosen CA, Ahmad M, Alexander RW, Medford RM: **Vascular cell adhesion molecule-1 (VCAM-1) gene transcription and expression are regulated through an antioxidant-sensitive mechanism in human vascular endothelial cells.** *J Clin Invest* 1993, **92**:1866–1874.
38. Rainwater DL, Shi Q, Mahaney MC, Hodara V, Vandenberg JL, Wang XL: **Genetic regulation of endothelial inflammatory responses in baboons.** *Arterioscler Thromb Vac Biol* 2010, **30**:1628–1633.
39. Bottino R, Balamurugan AN, Tse H, Thirunavukkarasu C, Ge X, Profozich J, Milton M, Ziegenfuss A, Trucco M, Piganelli JD: **Response of human islets to isolation stress and the effect of antioxidant treatment.** *Diabetes* 2004, **53**:2559–2568.

doi:10.1186/1475-925X-11-92

Cite this article as: Aleksieva et al.: Use of a special bioreactor for the cultivation of a new flexible polyurethane scaffold for aortic valve tissue engineering. *BioMedical Engineering OnLine* 2012 11:92.



## 7.2 In vitro comparison of novel polyurethane aortic valves and homografts after seeding and conditioning (Thierfelder et al., 2013)

- Nikolaus Thierfelder, Fabian König, René Bombien, Cornelia Fano, Bruno Reichart, Erich Wintermantel, Christoph Schmitz, Bassil Akra
- ASAIO Journal. 2013 May-Jun;59(3):309-16
- DOI: 10.1097/MAT.0b013e318289b95e

### **In Vitro Comparison of Novel Polyurethane Aortic Valves and Homografts After Seeding and Conditioning**

NIKOLAUS THIERFELDER,\* FABIAN KOENIG,\*† RENÉ BOMBIEN,\* CORNELIA FANO,‡ BRUNO REICHART,\* ERICH WINTERMANTEL,† CHRISTOPH SCHMITZ,\* AND BASSIL AKRA\*

The aim of the study was to compare the behavior of seeded cells on synthetic and natural aortic valve scaffolds during a low-flow conditioning period. Polyurethane (group A) and aortic homograft valves (group B) were consecutively seeded with human fibroblasts (FB), and endothelial cells (EC) using a rotating seeding device. Each seeding procedure was followed by an exposure to low pulsatile flow in a dynamic bioreactor for 5 days. For further analysis, samples were taken before and after conditioning. Scanning electron microscopy showed confluent cell layers in both groups. Immunohistochemical analysis showed the presence of EC and FB before and after conditioning as well as the establishment of an extracellular matrix (ECM) during conditioning. A higher expression of ECM was observed on the scaffolds' inner surface. Real-time polymerase chain reaction showed higher inflammatory response during the conditioning of homografts. Endothelialization caused a decrease in inflammatory gene expression. The efficient colonization, the establishment of an ECM, and the comparable inflammatory cell reaction to the scaffolds in both groups proved the biocompatibility of the synthetic scaffold. The newly developed bioreactor permits conditioning and cell adaption to shear stress. Therefore, polyurethane valve scaffolds may offer a new option for aortic valve replacement. *ASAIO Journal* 2013;59:309–316.

**Key Words:** tissue engineering, heart valve, homograft, cell conditioning, bioreactor, synthetic scaffold

Cardiovascular diseases are currently the major cause of death. With the growing global population and the increasing life expectancy, this problem will continue to grow. The number of patients requiring heart valve surgery will increase from 290,000 in 2003 to 850,000 in 2050.<sup>1</sup>

Currently, there are two different types of heart valve prostheses in use: mechanical and biological implants. Both types of implants offer the possibility to recover the normal valve-function, but unfortunately with a large number of limitations. On the one hand, mechanical prostheses require life-long oral anticoagulation therapy,<sup>2</sup> and on the other hand, the lifetime of the biological prostheses is limited.<sup>3</sup> Therefore, it is necessary to develop a new kind of heart valve whose properties do not include the most critical disadvantages of the currently available prostheses. The development of a tissue engineered heart valve seems to be the most promising way: "Advantages of an engineered tissue heart valve would likely include non-thrombogenicity, infection resistance, and cellular viability."<sup>4</sup>

The field of tissue engineering has the aim of restoring diseased organs or lost functions by a combination of cells with scaffolds.<sup>5</sup> Heart valve tissue engineering attempts, by an intelligent combination of these resources, to develop prostheses with a high durability and an inert surface, concerning coagulation. At the moment, three different approaches are used by research groups to achieve this aim. One possibility is the development of tissue engineered heart valves based on biodegradable scaffolds.<sup>6</sup> The application of decellularized biological valves presents the second possibility.<sup>7</sup> The development of a third cell-based option by using nondegradable scaffold materials is also under investigation.

The aim of the study was to compare new synthetic polyurethane (PU) scaffolds (group A) with conventional cryopreserved/thawed aortic homograft valves (group B) under analogous conditions in a newly developed bioreactor. Group B was used as a control group. The main interest was to study the reaction of seeded cells on variable materials to low flow shear stress after a short resting period of 24 hours.

#### **Material and Methods**

##### *Cell Isolation and Cultivation*

Saphenous vein segments, leftover from bypass operations, were used for vascular cell isolation. The study was approved by the Ethics Committee of Ludwig-Maximilian University Munich and before operation, patients gave their written informed consent for the use of their venous cells. Cells were isolated according to previously published methods.<sup>8</sup> However, collagenase was replaced with trypsin/ethylenediaminetetraacetic acid (EDTA) solution (10x; Sigma-Aldrich GmbH, Taufkirchen, Germany) to preserve the remaining fibroblast (FB) cell layer. First, the vein segments

From the \*Department of Cardiac Surgery, Laboratory for Tissue Engineering, Grosshadern Medical Center, Ludwig-Maximilian-University, Munich, Germany; †Institute of Textile Technology and Process Engineering, Denkendorf, Germany; and ‡Institute of Medical and Polymer Engineering, Technical University of Munich, Munich, Germany.

Submitted for consideration July 2012; accepted for publication in revised form January 2013.

Disclosure: The authors declare no conflicts of interest.

Reprint Requests: Dr. -Ing Bassil Akra, Department of Cardiac Surgery, Laboratory for Tissue Engineering, Grosshadern Medical Center, Ludwig-Maximilian-University of Munich; Marchioninistraße 15; 81377 Munich, Germany. Email: bassil.akra@med.uni-muenchen.de.

Copyright © 2013 by the American Society for Artificial Internal Organs

DOI: 10.1097/MAT.0b013e318289b95e



were cannulated and rinsed with 500ml M199 (Biochrom AG, Berlin, Germany) supplemented with 1 ml heparin (5000 i.E.; Ratiopharm GmbH, Ulm, Germany) and 5 ml gentamycin (10mg/ml; Invitrogen AG, Darmstadt, Germany). For endothelial cell (EC) isolation, the segments were filled with trypsin/EDTA solution and incubated for 25 minutes at 37°C. For FB isolation, the segments were incubated for 30 minutes at 37°C with 20mg collagenase solved in 10ml of human serum albumin (200g/L; Baxter GmbH, Unterschleißheim, Germany). The obtained cells were initially cultivated in 12.5 cm<sup>2</sup> culture flasks in EC growth medium (ECGM; Promocell GmbH, Heidelberg, Germany) supplemented with 6% fetal calf serum (Lonza GmbH, Köln, Germany) and 0.2% penicillin/streptomycin (Sigma-Aldrich GmbH, Hamburg, Germany) and FB growth medium (FGM; Promocell GmbH, Heidelberg, Germany) supplemented with 11% fetal calf serum and 0.2% penicillin/streptomycin, respectively. Medium was changed every 2–3 days. Cells were passaged at confluency.

#### Scaffolds

Polyurethane valves (group A, n = 4; **Figure 1A**) and homografts (group B, n = 4; **Figure 1B**) were used as scaffolds for the development of a new tissue engineered heart valve.

**Polyurethane scaffolds.** Polyurethane scaffolds with a diameter of 24 mm were manufactured by a spraying technique (patent DE 28 06 030 C2). Randomly oriented PU fibers were measured to have a median diameter of 1.55 µm (**Figure 3A**). The fibers formed a sheet with a thickness of 0.3 mm. Surface modification was not realized for the cell-seeding procedure. For seeding purpose, PU scaffolds were sent to a certified sterilization supplier and were γ-sterilized at 10 kGy. For safe handling, the scaffolds were fixed to a special Teflon (Sahlberg GmbH&Co. KG, Munich, Germany) mounting (**Figure 1C**) by a continuous circular suture using a surgical thread (Suprolene 3/0, Resorba GmbH, Nürnberg, Germany) prior to cell seeding. The mounting was designed for application in the seeding device and the conditioning bioreactor.

**Homografts.** Heart valve donors had an average age of 52.25 ± 5.74 years at the date of explantation. Exclusion criteria

for the experiment were any signs of insufficiency or any macroscopic damage. Average storage time was 7.33 ± 2.11 years. Cryopreservation of the homografts was performed according to previously published methods.<sup>9</sup> Scaffolds with a diameter of 27 mm were thawed in Ringer solution at 56°C and washed in Earle's M199 (Biochrom AG, Berlin, Germany) for 2 hours at room temperature (RT). Homografts were sutured to the Teflon mounting (**Figure 1C**) by single stitches using a surgical thread (Suprolene).

#### Cell Seeding and Conditioning

For better endothelialization results, the scaffolds were pre-seeded with FB, followed by colonization with EC. The seeding procedure using a 3D rotating seeding device (**Figure 2A**) was performed as previously described.<sup>9,10</sup> Briefly, 92.11 ± 11.08 × 10<sup>6</sup> FB (difference of counted cells in the suspension before and after seeding procedure) in 100ml supplemented FGM were dynamically seeded onto the native scaffolds for 24 hours (running phase: 2.5 minutes; holding phase: 30 minutes). Gas exchange was ensured by a silicone membrane. After FB seeding, the scaffolds were transferred to a glass bin containing 200ml fresh supplemented FGM and were cultured for 24 hours under static conditions. In the following 5 days, the valves were incubated in a novel self-made conditioning bioreactor (EU-Patent pending: EP10166094.2; **Figure 2B**).<sup>11</sup> During this period, the valves were perfused with 400ml supplemented FGM by an increasing sinusoidal pulsatile flow for 48 hours at 750ml/min (≈24 bpm) and 72 hours at 1100ml/min (≈35.5 bpm). Half of the supplemented FGM was exchanged after 2 days. The conditioning period was followed by a second seeding procedure for the EC (96.48 ± 8.05 × 10<sup>6</sup> cells). The EC seeding, the subsequent second resting period, and the final conditioning procedure were performed as described for FB; however, supplemented ECGM was used for cell nutrition. The performance of the valve leaflets was controlled and documented using an endoscope (**Figure 2B5**).

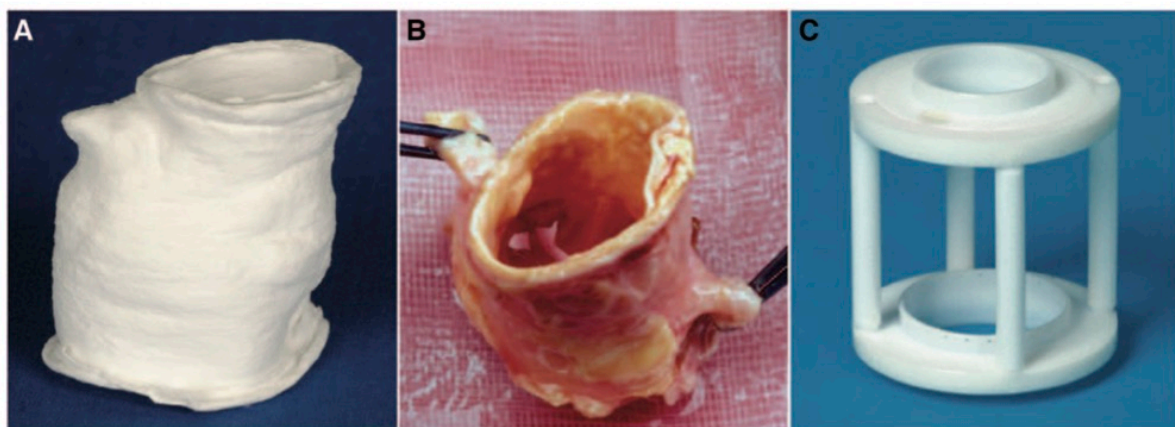


**Figure 1.** **A:** Sprayed polyurethane (PU) scaffold, diameter: 24 mm, group A (n = 4). **B:** Cryopreserved/thawed homograft, diameter: 27 mm, group B (n = 4). **C:** Teflon mounting for valve fixation in the seeding device and the conditioning bioreactor. Valves were fixed with a surgical thread in a continuous suture technique (polyurethane), respectively, single stitches (homograft).



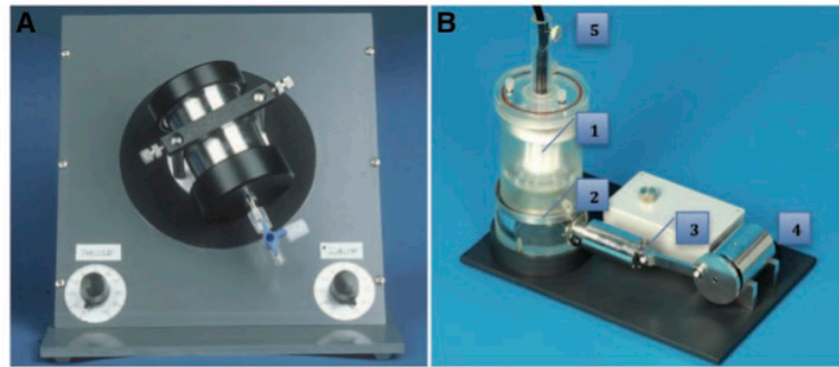


**Figure 2.** **A:** Bioreactor for 24 hours 3D cell seeding (running phase = 2.5 min, holding phase = 30 min).<sup>10</sup> **B:** Bioreactor for 5 day conditioning period<sup>11</sup> (750–1100 ml/min). **B1:** Mounting with polyurethane scaffold placed in the incubation chamber filled with 400 ml culture medium during the experiment. **B2:** Silicone membrane for conduction of pulsatile movement to the culture medium. **B3:** Piston for generation of pulsatile movements. **B4:** Electronic motor with eccentric piston rod. **B5:** Endoscope for the monitoring of valve performance.

#### Evaluation Methods

Scanning electron microscopy (SEM), immunohistochemistry (IHC), and real-time polymerase chain reaction (PCR) were used for evaluation. Samples were taken from veins, cell cultures, and native scaffolds, before and after each processing step. After the second conditioning period, samples were taken from the supra- and subvalvular, valvular, and subvalvular region of the aortic wall as well as from the valvular cusps.

**SEM evaluation.** For this procedure, the samples were fixed in a solution of 456 ml aqua bi-distilled (Ampuwa, Fresenius Kabi Deutschland GmbH, Bad Homburg v.d. H., Germany), 0.75 ml 1 N hydrochloric acid (Titrisol, Merck KGaA, Darmstadt, Germany), 43.5 ml glutaraldehyde, and 5.65 gm sodium cocodylate trihydrate (Sigma-Aldrich Chemie GmbH, Steinheim, Germany) at 4°C for a minimum of 48 hours. Subsequently, they were dehydrated by an ascending ethanol series (30, 50, 70, and 96%) and 100% acetone (Merck KGaA, Darmstadt, Germany), followed by critical point drying and gold sputtering (28 mA; 570V) of 180 s at 10<sup>-5</sup> mbar. A "Zeiss Evo LS 10" (Carl Zeiss AG, Oberkochen, Germany) scanning electron microscope was used for microscopy and documentation.

**IHC analysis.** In IHC evaluation, an indirect staining method was used. After at least 3 days of fixation time in a formalin solution (Roti-Histofix 4%, Carl Roth GmbH, Karlsruhe, Germany), the samples were embedded in paraffin and sectioned with a thickness of 10 µm. In a few interim stages, the paraffin was washed out, the cell membrane was permeabilized, and the antigens were unmasked. Samples were incubated for 16 hours at 4°C with monoclonal mouse antibodies (AB) against cluster of differentiation (CD)31 (dilution: 1:30; Dianova GmbH, Hamburg, Germany), Human Thymic Fibroblasts Antibody (TE)-7 (0,1 mg/ml; Chemicon-Millipore GmbH, Schwalbach, Germany), smooth muscle cell (SMC)-myosin (954 mg/L; DakoCytomation, Hamburg, Germany), -actin (44 mg/L; DakoCytomation), vascular endothelial (VE)-cadherin/CD144 (0.2 mg/ml; Beckman Coulter GmbH, Krefeld, Germany), connexin-43 (1 mg/ml; Chemicon-Millipore GmbH), fibronectin (0.6 mg/ml; Sigma-Aldrich GmbH), intercellular adhesion molecule (ICAM; clone: W-CAM-1; dilution: 1:20; Chemicon-Millipore GmbH), CD106 (200 µg/ml;

Thermo Fisher Scientific GmbH, Dreieich, Germany), and collagen IV (5.4 mg/ml; Sigma-Aldrich GmbH). In the following step, the samples were incubated for 30 minutes at RT with the second AB (Dual Link System-HRP, Dianova GmbH). This horseradish-peroxidase-linked AB allowed the visualization of the AB complexes. Furthermore, nuclear counter staining with Mayer's hemalum solution (Merck, Darmstadt, Germany) was performed.

**PCR evaluation.** Samples, stored in liquid nitrogen, were used for the RNA isolation using RNeasy Plus Mini kit (Qiagen GmbH, Hilden, Germany) according to the manufacturer's protocol. The purity and quantity of the RNA were measured by photometry (BioPhotometer, Eppendorf AG, Hamburg, Germany). Reverse transcription (QuantiTect Reverse Transcription kit, Qiagen GmbH) was performed according to Qiagen protocol. For PCR, a Rotor-Gene Q 2plex System (Qiagen GmbH) with SYBR Green detection was used. To determine the primer concentration, a dilution series (1:5, 1:10, 1:100, 1:1000, 1:10000) for standard curve graphing was compiled. During measurement, 35 replication cycles were performed, including, respectively, one negative control using water instead of the primer. Temperatures of 95°C (10 seconds) in the denaturation phase and 60°C (30 seconds) in the replication phase were used. The expressions of interleukin (IL)-1a (QuantiTect Primer Assay IL-1a, Qiagen GmbH), IL-6 (QuantiTect Primer Assay IL-6, Qiagen GmbH), IL-8 (QuantiTect Primer Assay IL-8, Qiagen GmbH), monocyte chemoattractant protein (MCP)-1 (QuantiTect Primer Assay CCL2, Qiagen GmbH), vascular cell adhesion molecule (VCAM; QuantiTect Primer Assay VCAM, Qiagen GmbH), and glyceraldehyde 3-phosphate dehydrogenase (GAPDH; QuantiTect Primer Assay GAPDH, Qiagen GmbH) were measured. The obtained Ct-values were normalized to the housekeeping gene GAPDH. The specificity of the PCR products was checked by melting curve analysis (from 60–90°C; +1°C/10sec) and gel electrophoresis (FlashGel System, Lonza GmbH, Cologne, Germany).

All values are expressed as means ± standard deviation. Student's t-test was performed for comparison of data; the probability value  $p < 0.05$  was considered significant.



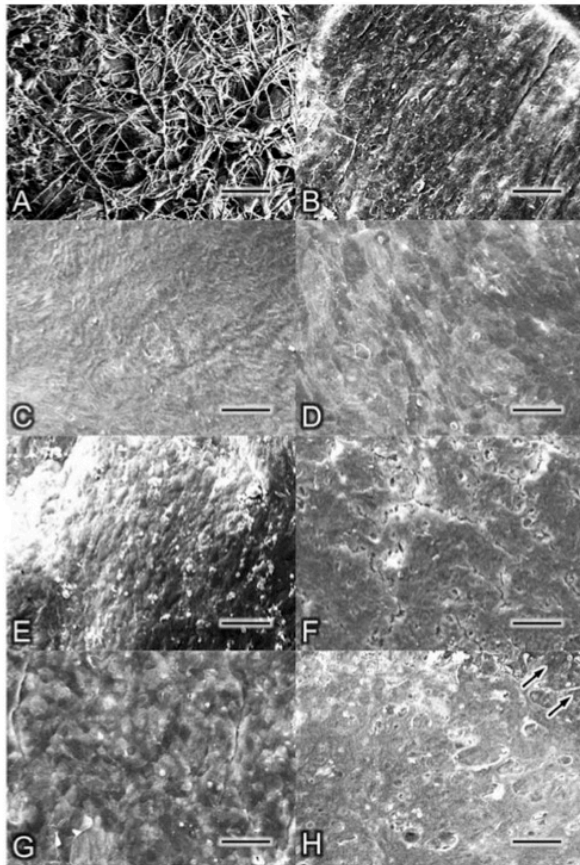


**Figure 3.** **A:** Native samples of polyurethane (PU) scaffolds demonstrated randomly orientated fibers with a median diameter of 1.55  $\mu\text{m}$ . **B:** Native samples of the homografts showed an abrasive surface with some cell fragments. **C:** Complete coverage of the PU fibers after fibroblasts (FB) seeding. The typical fusiform shape of FBs is recognizable. **D:** Smooth and homogenous surface after FB seeding due to a complete coverage of the scaffold. **E:** Endothelial cell (EC) seeding of PU scaffolds resulted in a confluent cellular coverage with the characteristic cobblestone pattern. **F:** EC seeding of the homografts also generated a confluent EC layer. The fissures found on the scaffold are dehydration artifacts. **G:** A cobblestone-like relief indicates a confluent endothelial lining of PU scaffolds after the second conditioning period. **H:** Homografts were also covered with EC after conditioning. A few areas revealed marginal damage (black arrows); samples **C**, **D**, **E**, and **F** were taken after the resting period (24h after conditioning). Samples **G** and **H** were taken directly after the second conditioning period; scale bars: **A** = 20  $\mu\text{m}$ , **B-H** = 150  $\mu\text{m}$ .

## Results

### Topography of the Scaffolds Surface

SEM analysis was performed to assess the topography of the cell layer. The recordings showed an uneven, abrasive but homogenous surface in the native samples of both groups (**Figure 3, A and B**). The structure of the sprayed randomly orientated PU fibers (group A) was clearly visible (**Figure 3A**).

After FB seeding procedure, a nearly confluent cell layer was visible in both groups. On homograft surfaces at few positions, the cells were not clearly identifiable. Overall, the surface

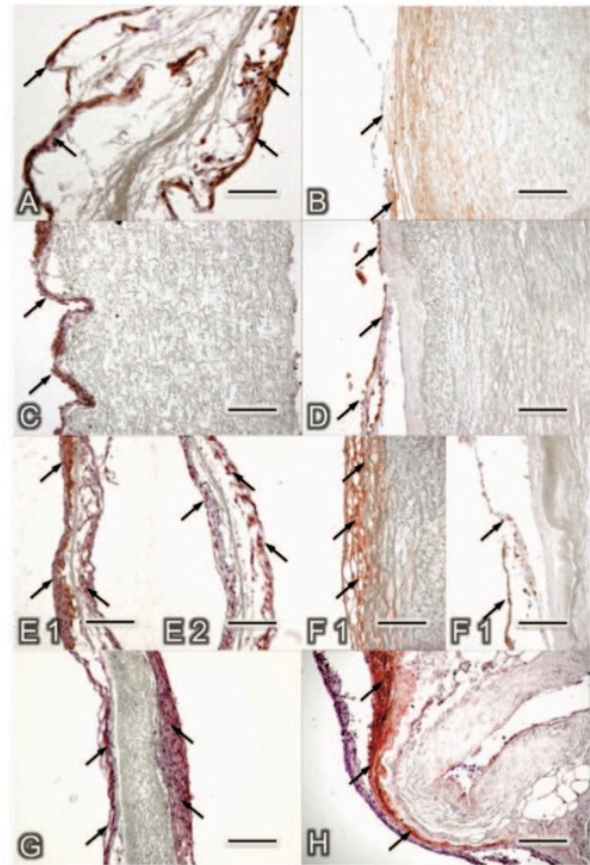


**Figure 4.** After fibroblasts (FB) seeding, TE-7 staining displayed a compact and confluent FB layer on polyurethane (PU) scaffolds (**A**; arrows) and a thin cell layer on homografts (**B**; arrows); staining against CD31 revealed successful endothelial cells (EC) seeding on PU scaffolds (**C**; arrows) and on homografts (**D**; arrows). After the final conditioning period, confluent cell layers of FB were detected on PU (**E1**; arrows) and on homografts (**F1**; arrows) by staining against TE-7. The presence of EC on the surface of the PU (**E2**; arrows) and of the homografts (**F2**; arrows) was demonstrated by CD31 staining. The establishment of a distinct extracellular matrix during the second conditioning period was found by positive staining against Collagen IV on polyurethanes (**G**; arrows) and homografts (**H**; arrows). Cell nuclei were stained with hemalaun (purple); scale bars: 300  $\mu\text{m}$ . CD, cluster of differentiation; TE, human thymic fibroblasts antibody.

appeared smoother and in group A, the PU fibers were completely covered with cells. Partially the fusiform shape of the FB was recognizable (**Figure 3, C and D**).

The structure of the surface in both groups seemed to be changed after cellularization with EC. The seeded endothelial layer appeared as a cobblestone surface. In group A, a totally confluent cell layer was visible (**Figure 3E**). In group B, a nearly confluent cell layer was observable; however, several small unseeded regions were noticeable (**Figure 3F**).

At the end of the second conditioning period, the samples showed a slightly different sight. On several spots the surface of the conditioned homografts seemed lacerated (**Figure 3H**, arrows). In group A, a few PU fibers were visible. However, nearly the entire surface was covered with a cobblestone-like



**Table 1. Pooled IHC Staining Results**

	Cell Culture		Nativ Scaffold	After FB Seeding	After EC Seeding	After EC Conditioning
	EC	FB				
<b>Group A</b>						
CD 31	+++	0	ND	0	+++	+++
TE-7	0	+++	ND	++	+	+++
SMC-myosin	ND	ND	ND	0	0	0
$\alpha$ -actin	ND	ND	ND	+	+	+++
VE-cadherin	ND	ND	ND	+	+	+++
Connexin-43	++	ND	ND	0	+	+
Fibronectin	ND	+++	ND	+	+	+++
ICAM	ND	ND	ND	+	++	+++
CD 106	ND	ND	ND	0	0	+
Collagen IV	ND	++	ND	+	++	+++
<b>Group B</b>						
CD 31	+++	0	0	0	++	++
TE-7	0	+++	0*	0*	+++	+++
SMC-myosin	ND	ND	0*	0*	0*	0*
$\alpha$ -actin	ND	ND	0*	+	+	+++
VE-cadherin	ND	ND	0	0	+	++
Connexin-43	++	ND	0	+	+	+
Fibronectin	ND	+++	0*	0*	+	+++
ICAM	ND	ND	0*	+	++	+++
CD 106	ND	ND	0	0	0*	0*
Collagen IV	ND	++	0*	0*	+	+++

0 denotes no staining visible; +, light staining; ++, moderate staining; +++, strong staining.

\*Positive reaction on scaffold material.

CD, cluster of differentiation; EC, endothelial cells; FB, fibroblasts; ICAM, intercellular adhesion molecule; IHC, immunohistochemistry; ND, not done; SMC, smooth muscle cell; TE, human thymic fibroblasts antibody; VE, vascular endothelial.

cell layer (**Figure 3G**). The cusps were completely coated with a continuous cell layer.

#### Protein Expression

The presence of EC and FB in the respective cell cultures was displayed by staining against CD31 (EC antibody) and TE-7 (FB antibody). Cell nuclei were stained with hemalaun (A–H purple). The native samples of group B showed no superficial cell layer stainable by hemalaun, but some positive reactions in the internal space of the scaffold wall. Additionally, staining against fibronectin and collagen IV (extracellular matrix [ECM] specific) evoked a strong reaction.

Staining of FB-seeded scaffolds displayed a moderately positive reaction of TE-7 AB, pointing to a successful FB seeding procedure (**Figure 4, A and B**; arrows). ICAM and  $\alpha$ -actin ABs also showed a lightly positive reaction (**Table 1**). The moderately positive reaction of CD31 AB (**Figure 4, C and D**; arrows) after the EC seeding procedure suggested successful seeding of EC in both groups. ICAM and collagen IV expression increased, as shown by a stronger staining reaction (**Table 1**). Strong positive peroxidase reactions in the staining against TE-7 and CD31 of both groups after the second conditioning procedure confirm the unchanged presence and integrity of the FB and EC layers, respectively (**Figure 4, E1, E2, F1, F2**; arrows). An enhancement of ECM and cellular adhesion after the EC conditioning period was detected by a strong, intensified positive reaction of  $\alpha$ -actin, VE-cadherin, fibronectin, ICAM, and collagen IV (**Figure 4, G and H**, arrows; **Table 1**). A higher expression of ECM was observed on the scaffold's inner surface.

#### Gene Expression

**Figure 5** demonstrates the mean values of gene expression before and after the conditioning period of FB-seeded as well as FB- and EC-seeded PU valves and homografts, respectively. Gene expression was normalized to the expression of the housekeeping gene GAPDH. The analysis of different segments of the heart valves (aortic wall and cusps) in both groups showed equivalent gene expressions for all cytokines and chemokines.

IL-1a and VCAM presented a negligible expression in both groups during the whole experiment. Negligible pro-inflammatory gene expression change of IL-6 (–1.12%) was detected while the seeded FB layer in Group A (**Figure 5A**) was conditioned, whereas the level of IL-8 gene expression decreased (–59.48%) and an increase of MCP-1 (+138.78%,  $p < 0.05$ ) was detected during the conditioning of FB in group A. An increase in the expression of most genes was observed (IL-6: +122.61%; IL-8: +454.38%; MCP-1: +45.39%) in group B (**Figure 5B**).

In both groups, the endothelialization caused a decrease in inflammatory cell response (group A, **Figure 5A**: IL-6: –78.82%; MCP-1: –68.71%; group B, **Figure 5B**: IL-6: –97.42%; IL-8: –67.01%; MCP-1: –89.44%,  $p < 0.05$ ). For IL-8 in group A only, an increase of +559.7% ( $p < 0.05$ ) was observed. Nonetheless, IL-8 expression after endothelialization is slightly lower than that in group B.

During the second conditioning step of the scaffold colonized with FB and EC, a slight decrease in IL-8 (group A, **Figure 5A**: –66.23%; group B, **Figure 5B**: –13.98%) was observed. IL-6- and MCP-1 expression was approximately on the same level in this period.

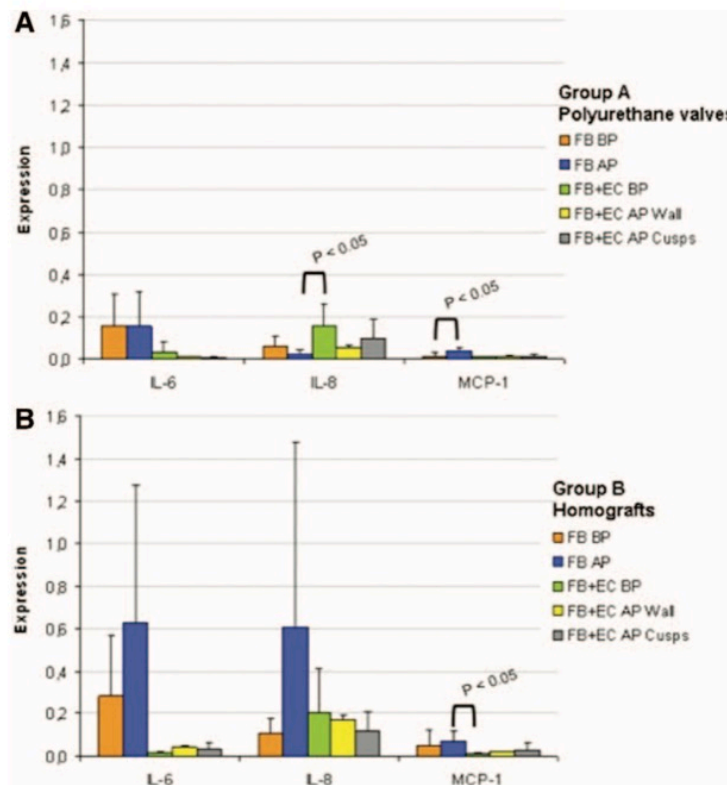


**Figure 5.** Cyto- and chemokine expressions of fibroblast and fibroblast-endothelial cell seeded scaffolds before (BC) and after conditioning (AC) **A:** Gene expression of interleukin (IL)-6, IL-8, and monocyte chemoattractant protein (MCP)-1 in cells seeded onto polyurethane valves: fibroblasts (FB) conditioning induced a decrease in IL-8 and an increase in MCP-1 expression. IL-6 expression remained at a constant level. The endothelialization step caused decrease in IL-6 and MCP-1 expression. Measured IL-8 increased in this step, which regresses in the following conditioning step. For IL-6 and MCP-1 no significant change was observed during endothelial cell (EC) conditioning. **B:** Gene expression of IL-6, IL-8, and MCP-1 in cells seeded on homografts: conditioning of FB causes an increase of the gene expression of IL-6, IL-8, and MCP-1, which is regressive after EC seeding. EC conditioning does not cause a significant change in gene expression. No significant difference was found between the gene expression of cells in aortic walls and cusps in either group; samples were taken directly BC and AC periods; values are normalized to glyceraldehyde 3-phosphate dehydrogenase (GAPDH).

### Discussion

The mean age of patients requiring cardiac valve replacement increases every year.<sup>12</sup> Therefore, the most beneficial form of therapy seems to be the extraction and the use of adult cells with good cultivation characteristics for the manufacturing of a tissue engineered heart valve. It has already been described that cells of aortic valvular origin appear as one of the most suitable cell types for aortic valve tissue engineering; however, there is no reasonable mode of autologous application.<sup>13</sup> On the other hand, cell source comparisons, also performed in our department,<sup>14</sup> have shown excellent results for cells isolated from saphenous vein segments.<sup>15,16</sup> Corresponding to these results, a specific isolation of EC and FB from saphenous vein segments was possible, a good replication rate in cell culture enabled a fast usage, and good conditioning attributes were observed. Considering these arguments, this cell source seems to be a good consensus concerning a practicable harvesting and the creation of a durable and viable tissue engineered aortic valve for an autologous application.

In the choice of the scaffold, several reasons militated for taking a nondegradable material, such as PU, for a tissue

engineered aortic heart valve. Polyurethane is known as one of the most bio- and hemocompatible materials used in the development of medical devices.<sup>17</sup> However, aging of PU has been found to be a possible drawback of this material in clinical studies. Nevertheless, its degradation rate is significantly lower than that of most degradable materials used for tissue engineering applications (e.g., polyglycolic acid and polylactic-coglycolic acid).<sup>18,19</sup> Another reason against degradable scaffolds is the high pressure stress in aortic position, meaning that proper function and a high life expectancy cannot be guaranteed.<sup>20,21</sup> Under these conditions, just decellularized homografts showed a promising *in vivo* short- and mid-term performance.<sup>22–24</sup> Baraki *et al.*<sup>23</sup> showed in their comparison between decellularized homografts and a native control group that the decellularized valves had even a better outcome concerning morphology and function after 9 months in systemic circulation. A drawback of this kind of scaffold is, however, the limited availability of homografts.<sup>25</sup> Up to now, synthetic degradable materials proved their qualification only in pulmonary arterial position.<sup>6</sup> The uncontrollable absorbability and the possible inflammatory reaction during the resorption time are additional arguments against biodegradable materials.<sup>4,26</sup>



The untreated cryoconserved/thawed homografts, which are established prostheses in modern heart surgery, were used as a control group in our study. In this way, it was possible to compare the behavior of seeded cells on native tissue and synthetic scaffold. The absence of endothelial and interstitial cells on native homografts surface, shown by negative CD31- and HE-staining results, could be explained by the cryopreservation process. Confirming these results, Lupinetti *et al.*<sup>27</sup> showed that cryopreservation of homografts can result in a severe loss of EC coverage.

In all experiments, both scaffold materials showed an adequate cell-seeding efficiency and presented a nearly completely confluent FB cell layer on the surface. The already described preseeding with FB resulted in a good subsurface for a confluent EC layer with good cell adherence.<sup>12</sup> The achieved intact endothelial surface plays a decisive role for the avoidance of the anticoagulation therapy in a following *in vivo* use.<sup>2</sup> Additionally, the endothelialization caused a desirable decrease in IL-6 and MCP-1 gene expression in both groups. Due to the known importance of these cytokines and IL-8 on inflammatory reaction, a downregulation in a target-cell-free surrounding is crucial.<sup>28,29</sup> A low inflammatory cell response plays *in vivo* a decisive role in the healing process after a heart valve implantation and the long-term functionality of a bio-prosthetic valve.<sup>30</sup> However, IL-8 is also known as a pro-proliferative, a pro-angiogenic, and anti-apoptotic cytokine.<sup>31,32</sup> This might explain the persistent expression after endothelialization and during the second conditioning period.

An essential component of each tissue is a specific ECM.<sup>33</sup> To provoke the establishment of an ECM by the seeded cells of a tissue engineering construct, an appropriate stimulus is necessary. In cardiovascular tissue engineering, Jockenhoevel *et al.*<sup>34</sup> and other research groups showed that flow-depending mechanical stress induces ECM formation.<sup>35</sup> In line with these results, the establishment of an ECM and the habituation of the cells were observed during the 5-day conditioning periods, demonstrated by positive staining against collagen IV and fibronectin. An increased ECM growth on scaffolds' inner/flow surface proved the flow dependence. The major construction of the ECM was observed during EC conditioning and due to the increased inflammatory influence, the first conditioning period did not appear to be beneficial. Additionally, the desired effect of downregulation of chemotactic factors, such as IL-8 and MCP-1,<sup>29</sup> was mainly observed after endothelialization. So, longer resting periods and longer EC conditioning for a further decrease in inflammatory cell reaction and less possible arteriosclerotic effects should be investigated.<sup>36</sup>

The PU scaffold showed a good cell-seeding efficiency and provoked no higher, or even a lower, inflammatory cell reaction during the whole experiment. The endothelialization results were similar in the control group (group B). In summary, the PU scaffolds proved their good biocompatibility. Our conditioning bioreactor allowed the cells to adapt to shear stress by establishing a strong ECM. At this point, these results cannot yet be transferred to the *in vivo* environment; however, the results have suggested that the polymer-based scaffold is a good candidate for this step. Thus this new tissue engineered heart valve may offer a new option for aortic valve replacement surgery.

### Acknowledgment

The authors thank the ITV-Denkendorf and especially Dr. -Ing. Martin Dauner for his support in manufacturing the synthetic scaffolds. Additionally, we thank Ulrike Haas and Antje Uhlig for their help in the evaluation of the experiments.

### References

1. Yacoub MH, Takkenberg JJ: Will heart valve tissue engineering change the world? *Nat Clin Pract Cardiovasc Med* 2: 60–61, 2005.
2. De Campos NL, de Andrade RR, Silva MA: Oral anticoagulation in carriers of mechanical heart valve prostheses: experience of ten years. *Rev Bras Cir Cardiovasc* 25: 457–465, 2010.
3. Hoffmann G, Lutter G, Cremer J: Durability of bioprosthetic cardiac valves. *Dtsch Arztebl Int* 105: 143–148, 2008.
4. Mendelson K, Schoen FJ: Heart valve tissue engineering: concepts, approaches, progress, and challenges. *Ann Biomed Eng* 34: 1799–1819, 2006.
5. Langer R, Vacanti JP: Tissue engineering. *Science* 260: 920–926, 1993.
6. Sodian R, Hoerstrup SP, Sperling JS, *et al*: Early *in vivo* experience with tissue-engineered trileaflet heart valves. *Circulation* 102(19 suppl 3): III22–III29, 2000.
7. Lichtenberg A, Cebotari S, Tudorache I, Hilfiker A, Haverich A: Biological scaffolds for heart valve tissue engineering. *Methods Mol Med* 140: 309–317, 2007.
8. Gulbins H, Dauner M, Petzold R, *et al*: Development of an artificial vessel lined with human vascular cells. *J Thorac Cardiovasc Surg* 128: 372–377, 2004.
9. Gulbins H, Pritisanac A, Uhlig A, *et al*: Seeding of human endothelial cells on valve containing aortic mini-roots: development of a seeding device and procedure. *Ann Thorac Surg* 79: 2119–2126, 2005.
10. Gulbins H, Goldemund A, Anderson I, *et al*: Preseeding with autologous fibroblasts improves endothelialization of glutaraldehyde-fixed porcine aortic valves. *J Thorac Cardiovasc Surg* 125: 592–601, 2003.
11. Koenig F, Hollweck T, Pfeifer S: A pulsatile bioreactor for conditioning of tissue-engineered cardiovascular constructs under endoscopic visualization. *J. Funct. Biomater.* 3, 480–496, 2012.
12. Yacoub MH, Cohn LH: Novel approaches to cardiac valve repair: From structure to function: Part I. *Circulation* 109: 942–950, 2004.
13. Butcher JT, Penrod AM, García AJ, Nerem RM: Unique morphology and focal adhesion development of valvular endothelial cells in static and fluid flow environments. *Arterioscler Thromb Vasc Biol* 24: 1429–1434, 2004.
14. Schaefermeier PK, Cabeza N, Besser JC, *et al*: Potential cell sources for tissue engineering of heart valves in comparison with human pulmonary valve cells. *ASAIO J* 55: 86–92, 2009.
15. Schnell AM, Hoerstrup SP, Zund G, *et al*: Optimal cell source for cardiovascular tissue engineering: venous vs. aortic human myofibroblasts. *Thorac Cardiovasc Surg* 49: 221–225, 2001.
16. Schmidt D, Hoerstrup SP: Tissue engineered heart valves based on human cells. *Swiss Med Wkly* 136: 618–623, 2006.
17. Zdrahala RJ, Zdrahala IJ: Biomedical applications of polyurethanes: A review of past promises, present realities, and a vibrant future. *J Biomater Appl* 14: 67–90, 1999.
18. Szycher M: Biostability of polyurethane elastomers: A critical review. *J Biomater Appl* 3: 297–402, 1988.
19. Kim MS, Kim JH, Min BH: Polymeric scaffolds for regenerative medicine. *Polymer Reviews* 51: 23–52, 2011.
20. Weston MW, LaBorde DV, Yoganathan AP: Estimation of the shear stress on the surface of an aortic valve leaflet. *Ann Biomed Eng* 27: 572–579, 1999.
21. Balachandran K, Sucusky P, Yoganathan AP: Hemodynamics and mechanobiology of aortic valve inflammation and calcification. *Int J Inflamm* 2011: 263870, 2011.
22. da Costa FD, Costa AC, Prestes R, *et al*: The early and midterm function of decellularized aortic valve allografts. *Ann Thorac Surg* 90: 1854–1860, 2010.

23. Baraki H, Tudorache I, Braun M, et al: Orthotopic replacement of the aortic valve with decellularized allograft in a sheep model. *Biomaterials* 30: 6240–6246, 2009.
24. Akhyari P, Kamiya H, Gwanmesia P, et al: *In vivo* functional performance and structural maturation of decellularised allogenic aortic valves in the subcoronary position. *Eur J Cardiothorac Surg* 38: 539–546, 2010.
25. Delmo Walter EM, de By TMMH, Meyer R, Hetzer R: The future of heart valve banking and of homografts: perspective from the Deutsches Herzzentrum Berlin. *HSR Proceedings in Intensive Care and Cardiovascular Anesthesia* 4: 97–108, 2012.
26. Filová E, Straka F, Mirejovský T, Masín J, Bacáková L: Tissue-engineered heart valves. *Physiol Res* 58 suppl 2: S141–S158, 2009.
27. Lupinetti FM, Tsai TT, Kneebone JM, Bove EL: Effect of cryopreservation on the presence of endothelial cells on human valve allografts. *J Thorac Cardiovasc Surg* 106: 912–917, 1993.
28. Van Snick J: Interleukin-6: an overview. *Annu Rev Immunol* 8: 253–278, 1990.
29. Mukaida N, Harada A, Matsushima K: Interleukin-8 (IL-8) and monocyte chemoattractant and activating factor (MCAF/MCP-1), chemokines essentially involved in inflammatory and immune reactions. *Cytokine Growth Factor Rev* 9: 9–23, 1998.
30. Simionescu A, Schulte JB, Fercana G, Simionescu DT: Inflammation in cardiovascular tissue engineering: the challenge to a promise: a minireview. *Int J Inflamm* 2011: 958247, 2011.
31. Li A, Dubey S, Varney ML, Dave BJ, Singh RK: IL-8 directly enhanced endothelial cell survival, proliferation, and matrix metalloproteinases production and regulated angiogenesis. *J Immunol* 170: 3369–3376, 2003.
32. Heidemann J, Ogawa H, Dwinell MB, et al: Angiogenic effects of interleukin 8 (CXCL8) in human intestinal microvascular endothelial cells are mediated by CXCR2. *J Biol Chem* 278: 8508–8515, 2003.
33. Bosman FT, Stamenkovic I: Functional structure and composition of the extracellular matrix. *J Pathol* 200: 423–428, 2003.
34. Jockenhoevel S, Zund G, Hoerstrup SP, Schnell A, Turina M: Cardiovascular tissue engineering: a new laminar flow chamber for *in vitro* improvement of mechanical tissue properties. *ASAIO J* 48: 8–11, 2002.
35. Sierad LN, Simionescu A, Albers C, et al: Design and testing of a pulsatile conditioning system for dynamic endothelialization of polyphenol-stabilized tissue engineered heart valves. *Cardiovasc Eng Technol* 1: 138–153, 2010.
36. Szmítko PE, Wang CH, Weisel RD, de Almeida JR, Anderson TJ, Verma S: New markers of inflammation and endothelial cell activation. *Circulation* 108: 1917–1923, 2002.

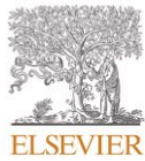
### 7.3 Is TAVI of living tissue engineered valves feasible? An in-vitro evaluation utilizing a decellularized and re-seeded biohybrid valve (Koenig et al., 2016)

- Fabian König\*, Jang-Sun Lee\*, Bassil Akra, Martin Dauner, Erich Wintermantel, Christian Hagl, Nikolaus Thierfelder
- *Artificial Organs*. 2016 Aug;40(8):727-37
- DOI: 10.1111/aor.12683
- *Die hier genannte, publizierte Originalarbeit ist zum Drucklegungszeitpunkt der vorliegenden Habilitationsschrift lizenzrechtlich geschützt und nicht frei veröffentlichungsfähig. Der Text kann unter der angegebenen Quelle kostenpflichtig angefordert oder mit entsprechenden Rechten eingesehen werden.*

### 7.4 Mapping of Bovine Pericardium to Enable a Standardized Acquisition of Material for Medical Implants (Stieglmeier et al., 2021)

- Felix Stieglmeier, Maximilian Grab, Fabian König, Joscha Büch, Christian Hagl, Nikolaus Thierfelder
- *Journal of the Mechanical Behavior of Biomedical Materials*. 2021 Jun;118 104432
- DOI: 10.1016/j.jmbbm.2021.104432





Contents lists available at ScienceDirect

Journal of the Mechanical Behavior of Biomedical Materials

journal homepage: <http://www.elsevier.com/locate/jmbbm>



## Mapping of bovine pericardium to enable a standardized acquirement of material for medical implants

Felix Stieglmeier<sup>\*</sup>, Maximilian Grab, Fabian König, Joscha Büch, Christian Hagl, Nikolaus Thierfelder

Laboratory for Cardiovascular Tissue Engineering, Department of Cardiac Surgery, Ludwig - Maximilian University Munich, Germany

### ARTICLE INFO

**Keywords:**  
Biomaterial  
Bovine pericardium  
Cartography  
Decellularization  
Durability testing  
Tissue engineering

### ABSTRACT

**Objectives:** Bovine pericardium - native, fixed as well as decellularized - is one of the most common implant materials in modern cardiovascular surgery. Although used in everyday procedures, there are no recommendations in regard to which part of the pericardium to prefer. It was the aim of this study, to identify areas of the pericardium with consistent properties and high durability.

**Methods:** Fresh bovine pericardia were collected from a local slaughterhouse. The native pericardia were analyzed at 140 spots in regard to thickness and fiber orientation. Based on these results, five promising areas were selected for further evaluation. The pericardia were decellularized with detergents (0.5% sodiumdesoxycholate/0.5% sodiumdodecylsulfate) and subsequently incubated in DNase. The two investigation groups native und DC consisted of 20 samples each. The efficiency of the decellularization was evaluated by DNA quantification, as well as DAPI and H&E staining. Biomechanical properties were determined using uniaxial tensile tests. To evaluate the microstructure, scanning electron microscopy, Picrosirius Red- and Movat's Pentachrome staining were utilized. To assess the long-term durability, patches were tested in a high-cycle system for a duration equaling the stress of three months in-vivo. Commercially available, fixed pericardium patches served as control group.

**Results:** Only a limited part of the pericardium showed a homogenous and usable thickness. The decellularization removed all cell nuclei, proven by negative DAPI and H&E staining, and also significantly reduced the DNA amount by 84%. The mechanical testing revealed that two investigated areas had an inconsistent tensile strength. Microscopical observations showed that the integrity of the extracellular matrix did not suffer by the decellularization procedure. During the long-term testing, most of the pericardia slowly lost tautness, though none of them got measurably damaged. Especially one area showed no decline of tensile strength after durability testing at all. Decellularized patches and fixed patches achieved comparable results in mechanical testing and microscopical evaluation after the durability testing.

**Conclusion:** We could clearly document significant, location-based differences within single pericardia. Only one area showed consistent properties and a high durability. We highly recommend taking this into account for future implant material selections.

### 1. Introduction

Bovine pericardium (BP) - native, fixed as well as decellularized (DC) - is one of the most common implant materials in modern cardiovascular surgery. Possible applications are manifold and reach from heart valve replacement to closure of septal defects and repair of pulmonary arteries

(Bell et al., 2019; Santibanez-Salgado et al., 2010; Shiraishi et al., 2019; Sheng et al., 2019). Although used in everyday surgical procedures, biological implants often come to failure after some period of time. There are many reported cases, in which fixed tissue was susceptible to calcification, probably caused by the glutaraldehyde treatment (Braile-Sternieri et al., 2020; Kiesendahl et al., 2020).

**Abbreviations:** BP, bovine pericardium; DC, decellularization; HC, high cycle system; IA, investigation area; LD, longitudinal direction; CD, circumferential direction; CP, commercial patch; HF, heart-facing side; HA, heart-averted side.

<sup>\*</sup> Corresponding author.

**E-mail address:** [F.Stieglmeier@campus.lmu.de](mailto:F.Stieglmeier@campus.lmu.de) (F. Stieglmeier).

<https://doi.org/10.1016/j.jmbbm.2021.104432>

Received 2 September 2020; Received in revised form 21 February 2021; Accepted 26 February 2021

Available online 11 March 2021

1751-6161/© 2021 The Authors. Published by Elsevier Ltd. This is an open access article under the CC BY license (<http://creativecommons.org/licenses/by/4.0/>).

An additional reason for the failure of implanted pericardia is the development of tears and structural weakening during the continuing exposure in vivo (Siddiqui et al., 2009; Johnston et al., 2015). While this may be caused by the natural vulnerability of the biological tissue, it also might indicate an insufficient choice of implant material.

Following our hypothesis, certain characteristics such as thickness, fiber orientation or mechanical behavior vary extremely from one area of BP to another. Bovine pericardia are an extremely heterogeneous tissue, which raises the question of whether some parts of the BP are better suited for implantation than others. The study of Whelan et al. even pointed out, that they preferred a patch of BP with mixed collagen fiber orientation but had to realize, that there is a lack of investigation of the whole pericardial sack, to locate suitable areas (Whelan et al., 2020).

These differences in typical location-based characteristics should definitely be considered. However, there are no recommendations regarding which parts of the pericardium should be preferred.

There have been studies with the aim to evaluate the whole pericardium, but none of them achieved conclusive results. Simionescu et al. investigated fixed tissue (n = 6) for their investigation (Simionescu et al., 1993). Another research by Sacks et al. came to the conclusion that the area above the left anterior ventricle has very suitable characteristics regarding the mechanical strength (Sacks et al., 1994). However, as a substantial limitation, they only investigated two large areas of BP and just used fiber orientation and mechanical testing as reference points for their recommendation. Moreover, Braile et al. even suggested that there were not enough significant differences at all, to prioritize just one specific area (Braile et al., 1998).

Consequently, the specific characteristics of a certain area of BP are currently not considered. The preselection process of most research groups is mainly reduced to macroscopic criteria, such as searching for areas without vascularization (Rassoli et al., 2018) or to avoid parts with tendon insertions (Sacks and Chuong, 1998). In many other cases, there is no reference at all, which part of BP had been used for the investigation (Li et al., 2018; Laker et al., 2020; Collatusso et al., 2019). Any differing characteristics between sectors of one single BP might have an impact on these research results that cannot be neglected. Therefore, it was the aim of this study, to identify defined areas of BP with a high durability and consistent properties.

## 2. Methods and material

### 2.1. Procurement of pericardia and preparation

Whole bovine hearts including the surrounding pericardium and fat tissue were collected from a local slaughterhouse. Only young bulls (ø age:  $19.5 \pm 1.4$  months) were chosen as donors. Between the collection and the preparation passed a maximum of 3 h. The fat tissue was carefully removed from the pericardium using a scalpel and gauze sheets. Thereafter, pericardia were separated from the hearts by performing an axial incision above the center of the left ventricle from the base to the apex of the heart and a circular incision near the base of the heart (Fig. 1). By reproducing these standardized incisions for every BP, the same shape of pericardium could be obtained every time. Afterwards, the pericardia were spread on an illumination plate. By using bright backlight, the fiber orientation was visualized and documented. Each of the two investigation groups, native und DC, consisted of 20 samples each.

### 2.2. Thickness measurement

The thickness of whole native pericardia (n = 20) was measured at 140 spots using a stamp measuring device (ID-C112XB, Mitutoyo, Neuss, GER). The standardized measuring spots were spaced in proportion to the whole surface of each pericardium, to make them comparable. Therefore, the size of the whole BP was measured using the ImageJ software (National Institutes of Health, USA) and subsequently, the measuring spots were distributed as in a coordinate system.

### 2.3. Defining of investigation areas

Based on the thickness measurements, areas with homogeneous thickness were identified. To form an average thickness of certain areas, up to 16 measuring spots were merged into one investigation area (IA) and compared to the corresponding DC area. Every IA had to be large enough, to obtain a patch of sufficient size after DC to provide sufficient investigation material. Consequently, IAs had a minimum size of  $8 \times 8$  cm which also fits most requirements for implantation material. Based on these results, five IAs could be defined (Fig. 1). Samples for the investigation were collected from these areas before and after DC.

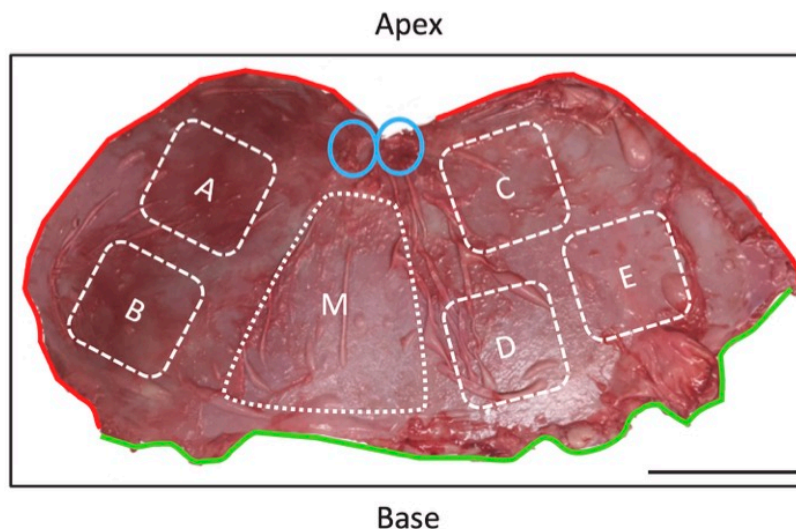


**Fig. 1.** Native pericardium  
Whole native flattened BP with heart averted side on top. The circular incision shows where the pericardium was loosened from the vessels surrounding the heart (green line). The incision in axial direction was made above the middle of the left ventricle (red lines). Also marked are tendon insertions of *Ligg. Sternopericardica* (blue circles). "A" to "E" symbolize investigation areas, "M" indicates an unsuitable area. Scale bar: 10 cm.



#### 2.4. Decellularization

For the DC process, a protocol developed and successfully tested by our research group was used. Thus, we utilized 0.5% sodiumdesoxycholate (SD, Sigma-Aldrich Chemie GmbH, Steinheim, GER) and 0.5% sodiumdodecylsulfate (SDS, Carl Roth GmbH, Karlsruhe, GER) and incubated the tissue under constant flow. Therefore, all IAs were sewed into frames, which then were placed in a 3D printed chamber, designed and manufactured by our research group. Inside the chamber, the frames were aligned parallel to each other and to the flow of detergents. Detergents continuously circulated through the chamber for 24 h in total. After the first 12 h of this procedure, the detergents were replaced. Subsequently, the IAs were washed with phosphate-buffered saline (PBS, Biochrom GmbH, Berlin, GER) in ten cycles of 15 min. After DC, the IAs were treated with 1% DNase (Desoxyribonuclease I, Worthington, Lakewood, USA) with an activity of 30 u/ml for 24 h. Finally, BP were washed again with PBS in three cycles of 30 min.

#### 2.5. DNA quantification

Native and DC samples (each n = 20) were frozen in liquid nitrogen and afterwards stored at -80 °C until further processing. For the DNA quantification, an Isolate II Genomic DNA Kit (Bioline GmbH, Luckenwalde, GER) was used. 25 mg of tissue were dissolved by a proteinase and processed according to the manufacturer's manual. The amount of DNA was measured with a spectrophotometer (BioPhotometer, Eppendorf AG, Hamburg, GER) at a wavelength of 260 nm. The results were converted to ng DNA/mg tissue.

#### 2.6. Histology

For histological investigations, samples were taken from every IA before and after DC (each n = 20) and stored in 4% formalin solution (Carl Roth GmbH) at 4 °C. Afterwards, they were dehydrated by an ascending alcohol series and then embedded into paraffin. The paraffin blocks were cut into slices of 5 µm, collected on standard microscope slides and dewaxed.

To evaluate the efficiency of DC, H&E staining (Merck KGaA, Darmstadt, GER) and DAPI staining (4',6-diamidino-2-phenylindole, Sigma-Aldrich Chemie GmbH) were used. Picrosirius Red (PSR) staining (Morphisto® GmbH, Frankfurt a. M., GER) and Movat's Pentachrome (MPC) staining (Morphisto® GmbH) were used to investigate the composition of tissue and the structure of extracellular matrix (ECM). All stainings were performed according to the manufacturer's manual.

A fluorescence microscope and the corresponding software AxioObserver (Carl Zeiss AG, Oberkochen, GER) were utilized to take pictures of DAPI staining. The same exposure time of 500 ms was used for every picture. For bright field microscopy of H&E, PSR and MPC staining, a Leica DM R (Leica Microsystems GmbH, Wetzlar, GER) was used. Pictures were taken with LAS EZ software (V.3.4, Leica GmbH).

#### 2.7. Scanning electron microscopy (SEM)

For SEM, samples were taken from every IA before and after DC (each n = 20) and stored in a glutaraldehyde fixative solution at 4 °C until further processing. For preparation, the samples were dehydrated by an ascending alcohol series and dried within a critical point dryer (Baltec CPD 030, BalTec, Schalksmühle, GER). Afterwards, samples were covered with a gold layer in a sputter device (Coater SCD 50, BalTec). SEM pictures were taken at different magnifications (100x, 1000x and 5000x) by an EVO LS 10 (Carl Zeiss AG). Both sides of the samples were evaluated.

#### 2.8. Biomechanical properties

Biomechanical properties were determined using a uniaxial tensile

testing machine (zwickiLine, 2.5 kN, ZwickRoell GmbH & Co. KG, Ulm, GER) and tensile test software (testXpert V12.3, ZwickRoell GmbH & Co. KG). The extension speed during the test procedure was set to 40 mm/min. Tests were done before and after DC for each BP. For each IA, two samples in perpendicular position were tested. One of them was aligned in longitudinal direction (LD) from base to apex of the heart, the second respectively in circumferential direction (CD) of the heart. The samples were taken in a standardized dogbone shape (DIN 53504 - S3A) with a length of 50 mm and a width of 4 mm. The maximal force (=absolute load) every sample was able to withstand was measured in Newton. By using the total force (Newton), a most realistic prediction on the actual clinical performance of the patch should be given. Since in some other studies also the unit Pascal is used, we additionally added results quoted in Pascal. Therefore, the measured force in Newton was normalized to the individual width and thickness (= cross section) of every sample. Additionally, the elongation in percentage of the samples' length, while maximal force was applied, was documented.

#### 2.9. Durability testing

To investigate the long-term durability, patches were tested in a modified high-cycle (HC) system (HiCycle Durability Tester; ViVITro Labs Inc., Victoria, CAN). A 3D printed, tube shaped mounting was designed, in which the patches were arranged perpendicular to the lumen. This way, a patch could be clamped circularly, while its middle part was able to bulge freely (Fig. 2). The whole mounting with clamped patches was placed in the device's water column, where it was able to move upwards and downwards. With a set frequency of 10 Hz, patches cycled for 9.5 ± 0.5 million cycles in 10.5 days. The mean peak pressure working on the patches was set to approximately 120 mmHg, to simulate arterial pressure. This way, we simulated the estimated stress of three months "arterial stress" in vivo on the IAs in a short time. The solution inside the system consisted of 98% PBS and 2% antibiotic/antimycotic solution (AntiAnti; gibco® by Life Technologies GmbH, Darmstadt, GER). After five days, the amount of antibiotic/antimycotic solution was refreshed. The device was able to test six patches at the same time. In each run, one DC patch from every IA of the same BP (n = 5) was tested.

Additionally, commercial, fixed bovine pericardium patches (CP, n

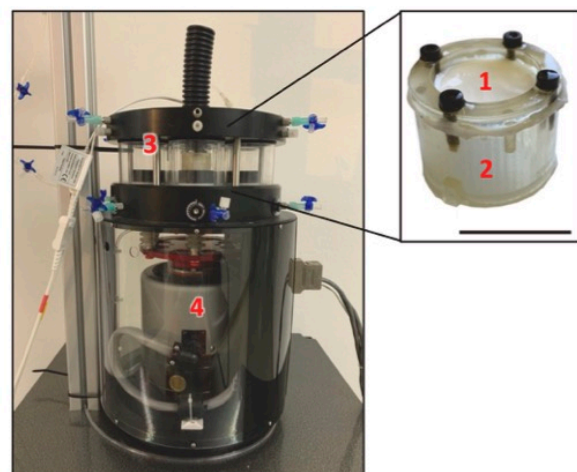


Fig. 2. Modified High Cycle System

The mounting with an attached patch (black box on the right) placed in the modified device for the durability testing. Inside the device, the mounting was surrounded by solution, in which it cycled upwards and downwards with a frequency of 10 Hz. (1) Decellularized BP patch; (2) Mounting with an attached patch; (3) One of the six waterfilled chambers, equipped with a mounting; (4) Motor for driving the cycling units. Scale bar: 3 cm.

= 5) of  $4 \times 4$  cm (Supple Peri-Guard; Synovis, St. Paul, USA) served as a control in each procedure. Native patches were not tested, due to sterility problems, related to an incubation at room temperature for 10.5 days. During the testing period, the mean pressures acting on the patches were measured in constant intervals. To investigate the outcome of durability testing, tensile tests, SEM and histological stainings such as MPC and PSR were performed as described above (2.6–2.8).

### 2.10. Statistical analysis

All results were indicated as mean value  $\pm$  standard deviation. Data were tested for normality using the Kolmogorov-Smirnov test. To test for significance, Student's t-test was used for normally distributed data, Mann-Whitney U test for nonparametric distributed data and one-way analysis of variance (ANOVA) to compare more than two groups.  $P < 0.05$  was specified as significant,  $p < 0.01$  as highly significant and  $p < 0.001$  as extremely significant.

## 3. Results

### 3.1. Mapping of thickness

The size measurement showed that pericardia had an average size of  $920 \pm 135$  cm<sup>2</sup>, after they were flattened.

The thickness remarkably varied across the native pericardia. There was one area "M" in the middle of the pericardium (Fig. 3 (A&B)), where the thickness changed from  $984 \pm 147$   $\mu$ m to  $681 \pm 141$   $\mu$ m in very short distance. Consequently, it was not possible to define IAs with

homogenous thicknesses there. On both sides of this unusable area, two bigger areas were located, where thickness only varied barely between neighboring measuring spots. These areas had a thickness range from  $453 \pm 77$   $\mu$ m to  $682 \pm 72$   $\mu$ m.

Every IA was thinner and more homogenous than the average of the whole pericardium ( $\phi$  native:  $657 \mu\text{m} \pm 181$ ) (Table 1). While IA-"C" showed the highest homogeneity (standard deviation: 16% of the thickness), areas "A", "D" and "E" still achieved similar results (each 18% of the thickness). IA-"B" had an extraordinary high variance within some single measuring spots between different individuals ( $565 \pm 166$   $\mu$ m)

**Table 1**

Results of the thickness measurement

The average thickness of every IA compared before and after DC. Area "B" was the least homogenous area. The DC significantly increased the thickness of every IA except area "B". The mean value in the last row represents the average of the five IAs.  $n = 20$ .

	Thickness		
	$\phi$ native in $\mu$ m	$\phi$ DC in $\mu$ m	p
A	$566 \pm 104$	$630 \pm 140$	*** <0.001
B	$538 \pm 135$	$544 \pm 192$	0.354
C	$607 \pm 95$	$694 \pm 143$	*** <0.001
D	$525 \pm 94$	$566 \pm 129$	*** <0.001
E	$612 \pm 111$	$810 \pm 179$	*** <0.001
$\bar{\phi}$	$567 \pm 114$	$648 \pm 185$	*** <0.001

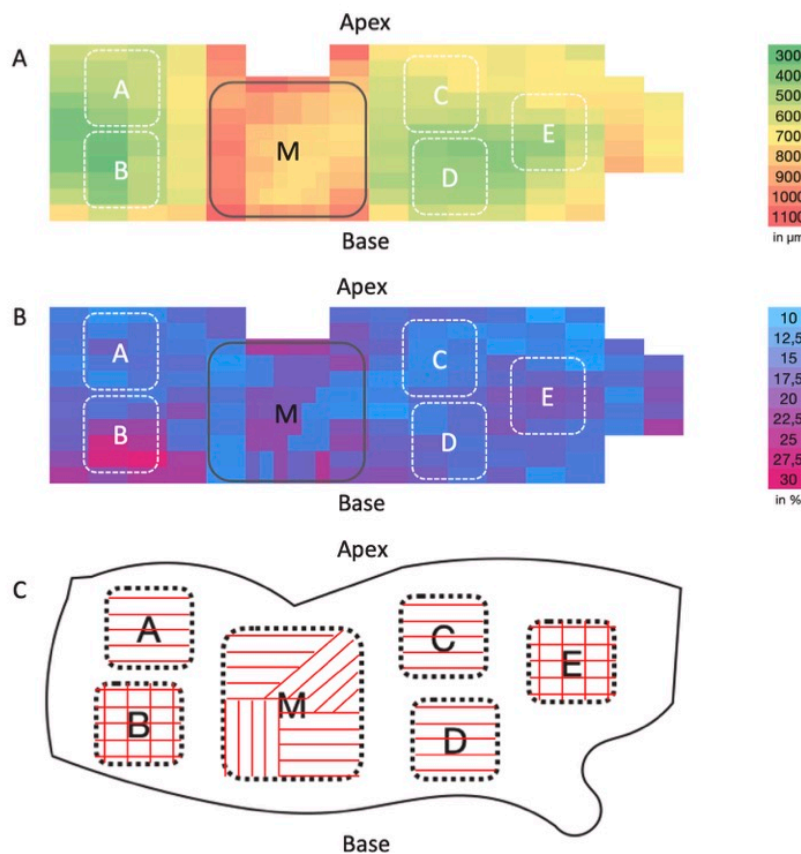


**Fig. 3.** Visualization of thickness measurement and fiber orientation

(A) Thickness mapping in  $\mu$ m. "M" indicates an area with high thickness up to  $984 \pm 147$   $\mu$ m in some spots. IAs "A-E" were spread over the thinner parts of BP, where thickness was between 300 and 700  $\mu$ m  $n = 20$ (B) Mapping of the intersample standard deviation in percent of the thickness. Especially IA-"B" showed a very high variation up to 30%.  $n = 20$  (C) Fiber orientation was mainly aligned in circumferential direction for IA "A", "C" and "D". IAs "B" and "E" consisted of fibers aligned in crossed direction.  $n = 20$ .



(Fig. 3 (B)).

The average thickness of most IAs was significantly increased after DC (Table 1). After DC, IA- "C" still was the most homogenous area (standard deviation: 21% of the thickness), followed by IAs "A" and "E" (standard deviation: each 22% of the thickness).

### 3.2. Fiber orientation

The occurrence of the three fiber orientations longitudinal, circumferential and transversal were documented (Fig. 3 (C)). Noteworthy, only areas "B" and "E" had a balanced amount in the appearance of all three directions. Areas "A", "C" and "D" mainly showed fibers aligned in circumferential direction. The area "M" in the middle (Fig. 3 (C)) had no clearly classifiable fiber directions, except for a small part with mixed fibers near the base.

### 3.3. Decellularization efficiency assessment

The DNA isolation was able to show the efficiency of DC for every investigated pericardium. On average, there was an extremely significant reduction of the DNA amount from  $72.14 \pm 34.63$  ng/mg to  $11.59 \pm 4.39$  ng/mg ( $p < 0.001$ ), resulting in an average decrease of 84% (Fig. 4 (A)). Also, for every IA on its own, the decrease was significant in comparison of native to DC samples.

Evidence for the success of DC was provided by DAPI and H&E staining, which highlighted cell nuclei all over the native pericardium, while no nuclei could be detected in any sample after DC (Fig. 4 (B&C)).

### 3.4. Mechanical testing

The tensile strength varied across BP, depending on the direction of tensile stress. Areas "A" and "C" showed significantly differing results between LD and CD (Table 2).

The tensile strength did not decrease significantly due to DC for any

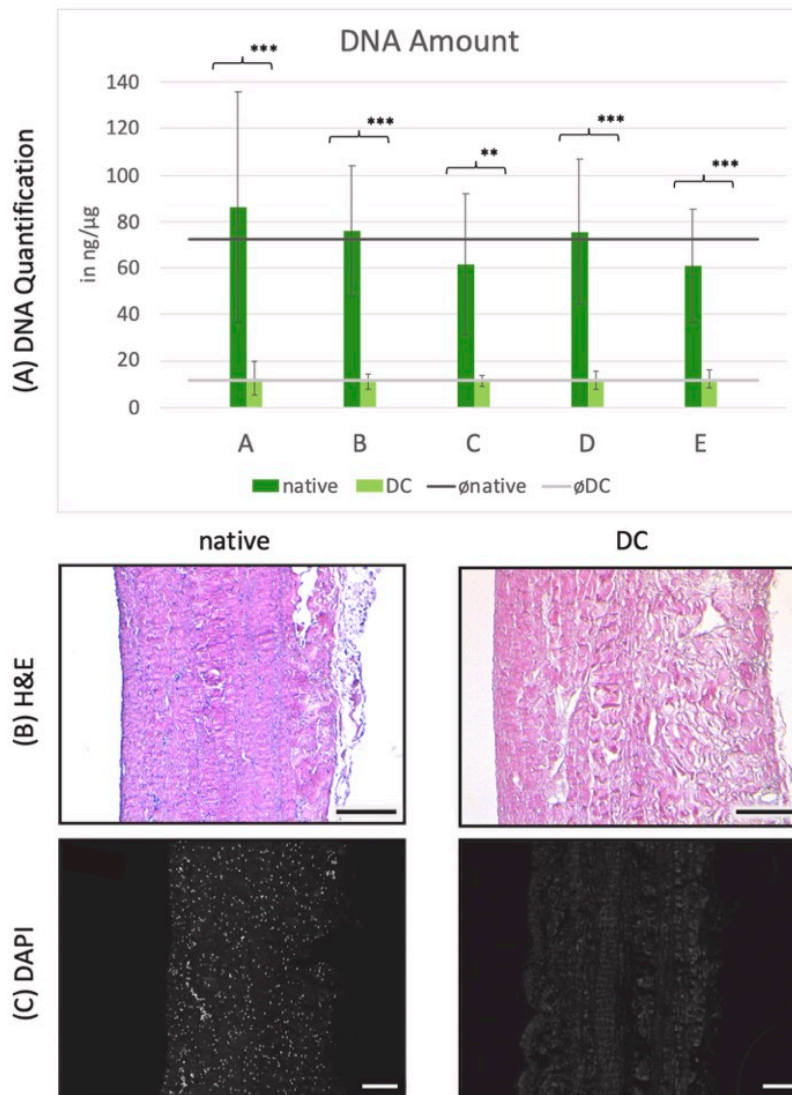


**Fig. 4. DNA Measurement**

(A) DNA amount before and after DC in ng/mg. For every IA a significant reduction of  $\approx 84\%$  was achieved.  $n = 20$ ;  $**p < 0.01$ ;  $***p < 0.001$  (B) H&E staining, native and DC sample in comparison. While the native samples showed many blue stained cell nuclei, no nuclei were visible in the DC samples. (C) DAPI staining, native and DC sample in comparison. The DC samples showed no remaining fluorescent cell nuclei, which were clearly visible in the native samples. All images in Fig. 4 are representative. Scale bars (B&C): 200  $\mu\text{m}$ .

**Table 2**

Tensile strength and elongation of native and DC pericardia

The results of the tensile tests are presented depending on force applied in longitudinal direction (LD) or circumferential direction (CD). Areas "A", "C" and "D" showed significant differences between both perpendicular directions of tensile stress. Results are expressed as total force (Newton) and normalized to the respective pericardial thickness (MPa).

The testing for elongation showed, that DC did not reduce the average elongation at all. Especially IAs "A" and "E" even showed a higher extensibility after the DC. n = 20; \*p < 0.05; \*\*p < 0.01; \*\*\*p < 0.001.

	Tensile strength native			p	DC			p
	LD in N LD in MPa	CD in N CD in MPa			LD in N LD in MPa	CD in N CD in MPa		
A	13.34 ± 6.79 5.99 ± 2.74	34.29 ± 16.01 16.59 ± 6.55	* 0.040 0.780	12.99 ± 9.93 5.20 ± 3.74	32.70 ± 14.27 15.09 ± 5.46	* 0.040 * 0.044		
B	25.17 ± 11.31 14.41 ± 6.82	38.52 ± 17.97 21.79 ± 10.22	0.054 0.165	25.77 ± 12.44 13.40 ± 6.35	27.64 ± 8.38 15.96 ± 6.63	0.096 0.465		
C	13.31 ± 8.66 5.87 ± 3.37	39.40 ± 15.46 18.75 ± 6.73	** 0.002 * 0.018	11.31 ± 14.81 4.52 ± 5.00	34.42 ± 13.97 14.83 ± 5.48	*** <0.001 0.317		
D	31.33 ± 13.05 15.37 ± 6.02	50.62 ± 22.98 27.30 ± 10.73	0.054 0.184	21.87 ± 8.47 11.46 ± 5.09	44.81 ± 22.84 21.77 ± 6.96	1.489 *** <0.001		
E	24.33 ± 15.58 9.02 ± 5.29	35.79 ± 22.76 14.15 ± 8.50	0.284 0.728	22.09 ± 15.44 8.35 ± 6.87	34.76 ± 22.56 12.22 ± 7.54	0.366 0.682		
∅		30.61 ± 19.15 14.92 ± 9.51			26.84 ± 17.73 12.28 ± 7.69	0.134 0.226		
	Elongation native			p	DC			p
	LD in %	CD in %			LD in %	CD in %		
A	42.68 ± 13.22	48.20 ± 11.91	0.425	58.05 ± 23.54	52.17 ± 16.29	0.335		
B	47.60 ± 16.16	53.52 ± 16.79	0.433	48.63 ± 10.39	45.90 ± 10.51	0.120		
C	38.87 ± 12.30	53.69 ± 16.80	0.058	48.36 ± 16.49	52.09 ± 13.49	0.242		
D	48.49 ± 14.28	52.69 ± 10.06	0.264	46.69 ± 11.47	49.81 ± 8.98	0.487		
E	54.82 ± 15.67	62.66 ± 20.75	0.259	58.35 ± 16.45	63.38 ± 16.23	* 0.011		
∅		50.32 ± 16.05			52.34 ± 15.61	0.312		

IA (∅ native: 30.61 ± 19.15 N, ∅ DC: 26.84 ± 17.73 N; p = 1.33). The highest absolute tensile strength showed IA-"D" (IA-"D" native: 40.98 ± 20.87 N, IA-"D" DC: 33.34 ± 20.59 N), still areas "B" and "E" had comparable results.

Regarding the tensile strength normalized to the individual thickness of a sample, it was noticeable that area "D" showed the highest relative tensile strength (Table 2 MPa). In general, the results normalized to thickness supported the absolute measured results, as for example IAs "A" and "C" still had significant differing results depending on direction of applied force. Additionally, area "D" also showed a significant inhomogeneity regarding the direction of applied force in decellularized samples.

Tensile tests showed that the pericardia clearly behaved elastic against the tensile stress, until maximal resistible force was reached. The average elongation of native samples was 50.32 ± 16.06% (∅ native) of their length, at the moment of maximal resisted force. In average the elongation remained constant during the whole investigation and showed almost no difference between native and DC samples (∅ DC: 52.34 ± 15.61%). Nevertheless, IA-"E" constantly achieved a higher extensibility than any other IA (∅ IA-"E" native: 58.74 ± 18.58%, ∅ IA-"E" DC: 60.86 ± 16.33%).

### 3.5. Histology

MPC staining was primarily used to highlight collagen (yellow) and elastic fibers (red). It showed that BP consisted of a compact structure, mainly made of collagen (Fig. 5 (A)).

While samples of areas "C" and "D" showed a very compact composition of tissue, areas "A" and "B" often consisted of a looser composition. IA "E" showed a higher quantity of elastic fibers in many samples, compared to other IAs. Especially areas "A" "B" and "C" very clearly showed the characteristic wavy structure of collagen fibers. In comparison of DC samples to native samples, no remarkable loosening of the compact structure was recognized after DC. The wavy structure of

the collagen fibers was flattened, but still intact after DC. Overall, histology showed that the microscopic appearance of ECM did not change due to DC.

PSR staining enabled the differentiation between collagen type I (yellow) and type III (green). Also in this staining, a differentiation in three layers was visible, while the middle layer clearly represented the bulk of the tissue. In the middle layer, both types of collagen approximately appeared in equal amounts. In the two outer layers, collagen I and III were almost equally common, but still the amount of collagen type I prevailed (Fig. 5 (B)). No destruction of collagen fibers was detected after DC.

### 3.6. SEM

The heart-facing (HF) side of most of the native samples showed a covered surface, which had the appearance of mesothelium. DC samples in comparison contained almost no coverage so that collagen fibers were clearly visible after DC. In most samples, the fibers did not have any clear alignment. The HF surface of native and DC samples was furrowed in general.

On the heart-averted side (HA), extracellular fibers were spread disordered and loose over the surface. However, neighboring fibers often ran parallel (Fig. 5 (C)). Some of the fibers twisted with other surrounding fibers and formed stronger main fibers together. In none of the observations, any damage to the ECM was perceptible. Furthermore, no remarkable differences between the IAs were recorded during SEM. There were no significant differences visible on the HA side in comparison of native and DC samples.

### 3.7. Durability testing

The CPs from the control group had an average thickness of 503 ± 65 µm, which made them 27% thinner than DC patches.

The average peak pressure on the patches rose from 113 ± 16 mmHg



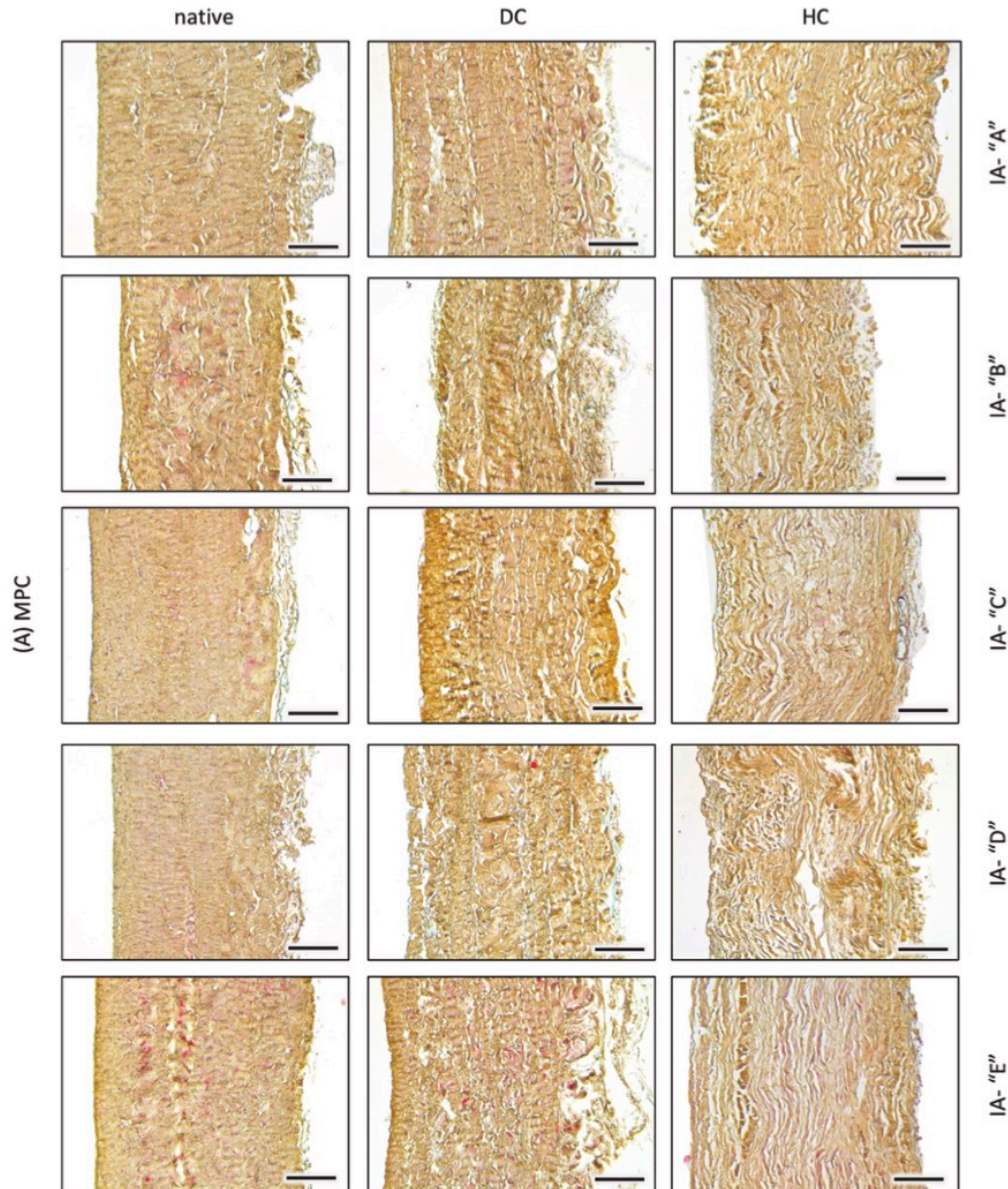


**Fig. 5.** Histological stainings and SEM

(A) MPC staining. Collagen was stained yellow, elastic fibers appeared red. All IAs in comparison before and after DC as well as after HC. The wavy structure of collagen remained intact after DC in most of the samples. Especially IA "E" showed a compact structure of tissue after DC as well as HC. All images in Fig. 5 are representative. Scale bars (A): 200  $\mu\text{m}$  Fig. 5 Histological stainings and SEM. (B) PSR staining, native and DC sample in comparison. Collagen type I colored yellow, collagen type III colored green. Scale bars (B): 200  $\mu\text{m}$  (C) Both sides of the pericardium in comparison before and after DC, as well as after HC. While HA side did not change significantly, HF side appeared more flattened after HC. Scale bars (C) HF side: 10  $\mu\text{m}$ ; HA side: 40  $\mu\text{m}$ . All images in Fig. 5 are representative.

in the beginning to  $135 \pm 15$  mmHg at the end of the testing period, resulting in an average pressure of  $127 \pm 21$  mmHg.

During the long-term testing, none of the patches got visibly damaged. Most of the DC patches appeared macroscopically stretched after HC. Additionally, the tensile strength was decreased by  $\approx 29\%$  in comparison to DC samples ( $\sigma$  DC:  $26.84 \pm 17.73$  N,  $\sigma$  HC:  $19.30 \pm 10.44$  N), still for no IA this decrease was significant ( $p = 0.113$ ). However, the

tensile strength was significantly lower after HC in comparison to native samples ( $\sigma$  native:  $30.61 \pm 19.15$  N;  $p = 0.028$ ) (Table 3).

It is noteworthy that tensile strength of IA-"E" did not decline at all and reached a higher resilience after durability testing than any other IA (IA "E" DC:  $28.42 \pm 20.13$  N, IA-"E" HC:  $28.86 \pm 10.54$  N). There were also no significant differences in tensile strength between unfixed patches compared to the CPs after HC ( $\sigma$  CP:  $17.71 \pm 11.70$  N).



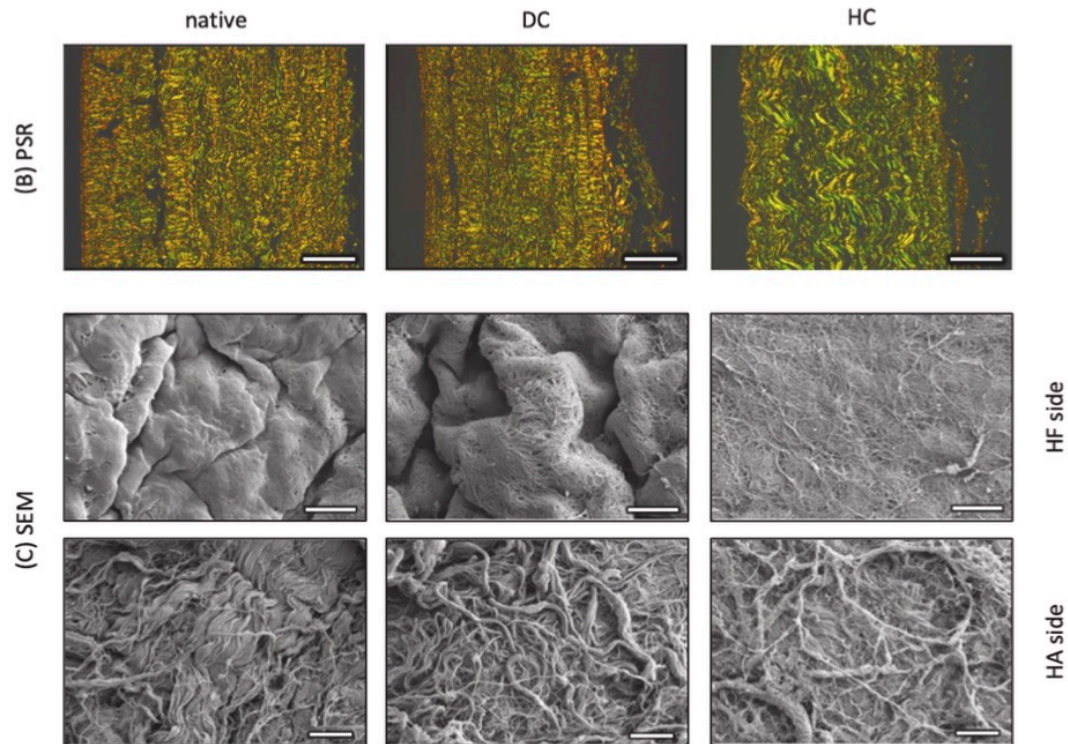


Fig. 5. (continued).

While pericardia could be stretched by  $50.32 \pm 16.06\%$  (native) and  $52.34 \pm 15.61\%$  (DC) of the samples' length, HC samples only reached  $36.60 \pm 13.30\%$  elongation until the maximal resistible force was applied (Table 3). According to that, the elongation was significantly reduced after HC, compared to native and DC samples (both:  $p < 0.001$ ). Additionally, areas "D" and "E" had a significantly decreased elasticity on their own ("D":  $p < 0.001$ ; "E":  $p = 0.039$ ). In comparison of CPs to DC and HC patches, no significant differences in elongation were measured ( $\phi$  CP:  $41.81 \pm 10.31\%$ ). However, CPs had a significantly lower elongation than native samples ( $p = 0.037$ ).

SEM showed that the structure of the ECM was still intact after HC. The HF side showed comparable characteristics to the DC samples and showed only ECM without cellular coverage (Fig. 5 (C)). Also, HC samples were not furrowed on the HF side. In comparison of native to fixed samples, no cellular coverage was visible on the HF side of CP samples (Fig. 6 (C)). The HA side widely consisted of ECM as well, matching the observation of DC HA sides. In contrast to the HA side, where some bacteria stuck to the surface of ECM after HC in a part of the samples, no adherence of bacteria was visible on HF sides. However, there was no destruction of fibers visible during the investigation. MPC and PSR staining showed that the composition of the tissue of unfixed and fixed HC samples got looser and collagen fibers appeared less wavy (Fig. 5 (A&B) & Fig. 6 (C)).

#### 4. Discussion

Until now, almost no research group or commercial company clearly indicated, from which part of the BP their patches for investigations or medical implementations were taken. In most of the studies, there are only brief descriptions of the selection of investigation material or even no reference on the selection at all (Rassoli et al., 2018; Sacks and Chuong, 1998; Li et al., 2018; Laker et al., 2020; Collatusso et al., 2019).

Furthermore, to our knowledge, there is no usable recommendation, which part of the BP is most suitable as material for implantation. Since BP are much bigger ( $920 \pm 135 \text{ cm}^2$ ) than the size of an average patch, qualified areas have to be preselected. We assume that the selection of a certain area has a high impact on every investigation involving BP and can even significantly affect the durability of a medical implant.

In order to define specific location-based characteristics of BP, we investigated the thickness. Regarding the respective results, we recommend not to use the large area "M" in the middle of the pericardium (Fig. 3 (A&B)), since we were not able to define an IA with a homogenous thickness in this part. The thickness varied strongly here, from  $681 \pm 141 \mu\text{m}$  up to  $984 \pm 147 \mu\text{m}$ . Also, the thickness in this area was higher than the thickness of commonly used patches in other studies. While Bielli et al. used pericardia with a thickness range from  $400 \mu\text{m}$  to  $700 \mu\text{m}$ , Sulejmani et al. measured an average thickness of  $430 \mu\text{m}$  (Bielli et al., 2018; Sulejmani et al., 2019). Noteworthy, the IA-"B" had a variation of up to 30% of its thickness within the same measuring spots on interindividual pericardia, which makes the area not recommendable as well. The remaining areas "A", "C", "D" and "E" showed homogenous thicknesses.

There was a significant increase of the average thickness of the BP through DC, which also was published before (Hulsmann et al., 2012), and could not be evaluated as a disadvantage. After DC, microscopical observations, as well as biomechanical testing did not detect any loosening of structure or a significant decline of mechanical strength, which could be traced back to thickness.

During the microscopical investigation, we could clearly document a wavy appearance of collagen fibers. This structure was also described before and was evaluated as a positive impact on BP's stability (Rassoli et al., 2019). Especially in the middle-layer of the tissue, the wavy structure of collagen was clearly visible. Through the DC process, fibers appeared flatter, which might lead back to a wear out effect. Also, we

**Table 3**

**Tensile strength and elongation after HC**

Native, DC and HC samples in comparison. Especially IA-“E” showed consistent results during the durability testing. On average, the tensile strength of native samples was significantly higher than the tensile strength of HC samples. Results are presented as total force (Newton) and normalized to the respective pericardial thickness (MPa). Elongation quoted in percentage of the samples' length after HC. The elongation of areas “D” and “E” significantly decreased due to HC. On average, HC also significantly reduced the extensibility of BP. CPs reached a significantly lower elongation than native BP patches. n = 20 for “native” and “DC”, n = 5 for “HC” and “CP”; \*p < 0.05; \*\*\*p < 0.001.

Tensile strength: Comparison after HC						
		σ native in N φ native in MPa	σ DC in N φ DC in MPa	σ HC in N φ HC in MPa	p HC vs native p HC vs native	p HC vs DC p HC vs DC
HC	A	23.82 ± 16.12	22.84 ± 15.71	17.85 ± 12.54	0.478	0.370
		11.29 ± 7.31	10.15 ± 6.81	8.47 ± 4.48	0.670	0.667
	B	31.85 ± 16.29	26.70 ± 10.51	16.57 ± 9.77	0.287	0.474
		18.10 ± 9.35	14.68 ± 6.54	10.17 ± 4.47	0.453	0.303
	C	26.36 ± 18.09	22.87 ± 18.41	17.62 ± 8.55	0.106	0.327
		12.31 ± 8.37	9.68 ± 7.35	8.06 ± 4.78	0.184	0.697
	D	40.98 ± 20.87	33.34 ± 20.59	15.58 ± 5.08	0.207	0.306
		21.33 ± 10.50	16.61 ± 7.97	9.51 ± 2.53	0.075	0.407
	E	30.06 ± 20.10	28.42 ± 20.13	28.86 ± 10.54	0.456	0.405
		11.59 ± 7.46	10.29 ± 7.38	10.88 ± 4.54	0.779	0.667
σ	30.61 ± 19.15	26.84 ± 17.73	19.30 ± 10.44	* 0.028	0.113	
	14.92 ± 9.51	12.28 ± 7.69	9.42 ± 4.20	0.094	0.395	
CP			17.71 ± 11.70	-	-	
			9.52 ± 6.17			
		p native vs CP	p DC vs CP	p HC vs CP		
		0.159	0.236	0.409		
		0.631	0.841	0.826		
Elongation: Comparison after HC						
		σ native in %	σ DC in %	σ HC in %	p HC vs native	p HC vs DC
HC	A	45.44 ± 12.73	55.11 ± 20.20	37.76 ± 14.49	0.092	0.120
	B	50.56 ± 16.54	47.27 ± 10.41	33.17 ± 7.12	0.183	0.320
	C	46.28 ± 16.35	50.23 ± 14.99	40.60 ± 16.83	0.162	0.132
	D	50.59 ± 12.38	48.25 ± 10.29	31.20 ± 9.34	*** <0.001	*** <0.001
	E	58.74 ± 18.58	60.87 ± 16.33	40.27 ± 15.88	* 0.020	* 0.039
	σ	50.32 ± 16.06	52.34 ± 15.61	36.60 ± 13.30	*** <0.001	*** <0.001
CP			41.81 ± 10.31	-	-	
		p native vs CP	p DC vs CP	p HC vs CP		
		* 0.037	0.063	0.352		

could not measure a correlation between flattened fibers and a reduced mechanical strength or elongation. Thus, the mentioned optical effect is deceptive and should be neglected. Compared to the remaining methods, it was not possible to clearly define differing characteristics between the IAs through histology. According to our hypothesis, this similarity in histology could be the reason why there are almost no studies, which investigated location-based characteristics.

Regarding the fiber alignment, clear differences between the IAs could be recorded indeed. As shown before, the tensile strength is higher, when tensile stress is applied in the direction of fiber orientation (Sacks et al., 1994). Patches with mixed fiber orientation are therefore more suitable for use as a medical implant, where stress is very likely, to operate in many directions (Alavi et al., 2013). Especially areas “B” and “E” showed fibers in mixed orientation, which makes them more recommendable. Areas “A”, “C” and “D” mainly showed fibers orientated in CD, which results in a possible weakness against tensile strength in LD.

These observations match the results from the tensile tests. Areas “A”, “C” and “D” achieved remarkably lower results in LD than in CD. Since this difference in tensile strength even was significant for area “A” and area “C”, we highly dissuade from using these both areas. Inhomogeneity can be a sensitive vulnerability, if stress operates in the direction of weak tensile strength. Otherwise, there might be requirements, where a patch with high tensile strength in only one direction might be a fitting choice. For example, Oeverhaus et al. used BP to perform a tendon elongation of the medial rectus muscle in order to fix strong strabismus (Oeverhaus et al., 2018; Hedergott et al., 2020). For cases like this, the quality of IA “D” could also be appropriate, since it has a high total tensile strength.

However, areas “B” and “E” equally resisted tensile stress from any applied direction, which makes them suitable for a large field of applications. Area “E” additionally showed its potential regarding the elongation, since it constantly achieved the highest elasticity. As a result, we highly recommend using IA “E”, to benefit the most from its homogenic and suitable mechanical properties. Apart from this, there might be special situations like the repair of an abdominal wall defect, which require a patch of a larger size (Limpert et al., 2009). In this case a combination of areas “D” and “E” would be the best choice.

The durability testing showed that through HC, the mechanical strength was reduced in general. While most IAs showed a clear decline after HC, IA “E” was the only one with consistent tensile strength in comparison of native, DC and HC samples.

Also, the average extensibility of all areas was significantly decreased after durability testing. This might be an indication that the scaffolds became irreversibly stretched during the long-term testing. Although IA “E” also had a significantly decreased elongation compared to the native and DC elongation, its elasticity was still equal to the remaining areas.

Concerning tensile tests, some other studies quote results of tensile tests only in the unit F/mm<sup>2</sup> or MPa (Mendoza-Novelo et al., 2011; Gauvin et al., 2013). From a “materials science point-of-view”, this is plausible and gives a good comparability to other tissues. However, there might be the scenario in which a biomaterial area has a high relative tensile strength (MPa), but only achieves a low absolute tensile strength (N) in comparison to another area. In a clinical setting implant failure occurs when the acting force exceeds the absolute tensile strength of the material. Therefore, the absolute tensile strength of biological implant materials is of high importance to make a reliable prediction on



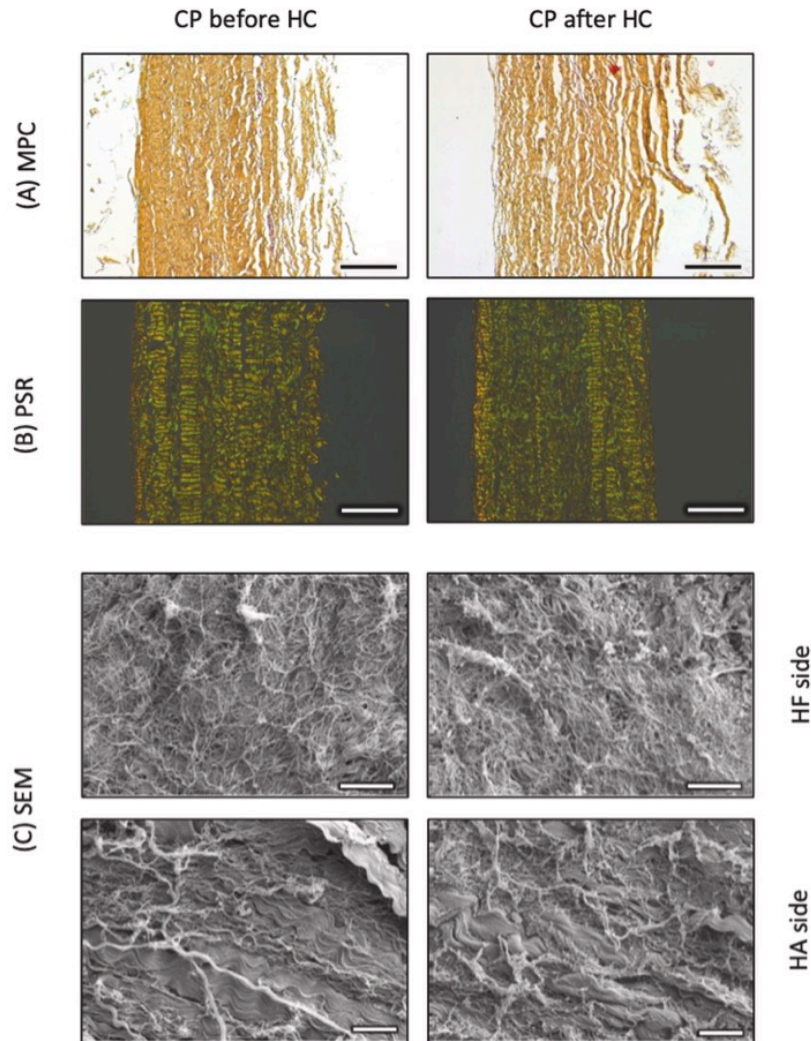


**Fig. 6.** Histological and SEM results of the CP (A&B) Histology of the CP. MPC (A) and PSR staining (B) showed a similar composition of tissue in comparison to unfixed patches. The main component of the tissue was collagen besides from some elastic fibers. The fixed pericardium remained in a compact structure, although the ECM appeared loosened up after HC. Scale bars (A&B): 200  $\mu\text{m}$  (C) SEM of the CP. Unlike unfixed samples, SEM showed no cellular covering of the surface on native samples. After HC, no destruction of the ECM was visible in the fixed samples. Scale bars (C): HF side 10  $\mu\text{m}$ ; HA side 40  $\mu\text{m}$ .

the clinical behavior.

Durability testing also highlighted that the commercial, fixed patches did not perform noticeably better than DC patches. Neither in tensile tests nor in microscopical observations, significant advantages could be recorded. Similar results were documented by Hülsmann et al. who also pointed out that decellularized BP had an equal mechanical strength as fixed BP (Hülsmann et al., 2012). Immense disadvantages of fixation are correlations to an increased calcification, as well as a difficult recellularization (Umashankar et al., 2012; Huang-Lee et al., 1990). DC patches still provide this possibility (Yang et al., 2012; Ferroni et al., 2019), which may increase their durability in vivo. Since we have proven that DC patches can be able to withstand the same stress as fixed patches do, these results should not be neglected in further investigation. In this study we wanted to highlight the advantages of decellularized tissue and thus we did not include fixed patches into our evaluation. Even though, the combination of decellularization and fixation represents an approach with high potential and should be the subject of further investigations.

We also compared our results to the earlier approach of mapping BP by Simionescu et al. (1993). Similar to our results, they also measured a

comparable thickness for IA-E and also noticed a mixed fiber orientation in this area. In contrast to our results, they measured a higher tensile strength in other parts of BP so that a different area was recommended, than in this study. As a limitation, Simionescu et al. only used a few fixed BP ( $n = 6$ ) for their research instead of native and DC pericardium.

The conclusions made by Sacks et al. on the other hand are too generalized, since BPs characteristics vary too much, to only compare two areas (Sacks et al., 1994). As an example, Sacks et al. published that the left anterior side of BP mainly showed circumferential aligned fibers. Compared to IA "A" and "B", which approximately refer to this area, we could recognize that IA "A" indeed showed fibers in CD, but IA "B" mainly showed randomly oriented fibers.

Braile et al. also attempted mapping BP and prioritized an area close to IA "C" from our study, but were not able to prove these results with significant data (Braile et al., 1998). Since in that study samples for mechanical testing were aligned randomly, significant differences in mechanical strength depending on direction were not considered.

Comparing the utilized methods and outcome from our research to other studies, some relevant aspects have been noticed. Regarding the DC method, the protocol established by our research group can be



described as very reliable and efficient. For DC success, there are minimum standards. Crapo et al. published in particular a DNA amount <50 ng/mg and the absence of nuclear material in H&E and DAPI staining as criteria (Crapo et al., 2011). We were able to satisfy these standards and also preserved the desired characteristics of BP, like the mechanical resistance and the compact collagen fiber composition. While our DC protocol only required 2.5 days, other approaches took approximately 13 days (Heuschkel et al., 2019). Although their protocol was more time-consuming, they only achieved 77% reduction of the DNA amount. Furthermore, they detected a decline of the samples' elongation by 20%, while our DC samples remained equally tensile as native samples. In another study, Li et al. still recognized DNA fragments with a H&E staining after DC, which did not appear in our study (Li et al., 2018). Since all mentioned researches used SDS and SD for DC, this might be an indicator for the advantage of the constant flow system used in this study.

## 5. Conclusion

We could clearly document significant differences within single BP. Consequently, the selection of a certain part of BP has a high influence on the characteristics of a patch. Only one area achieved consistently satisfying results. A homogeneous thickness, mixed fiber orientation, high extensibility, high and consistent tensile strength and resilient properties after durability testing can only be found in IA-“E”. The best way to find this area is performing the axial incision of the BP above the middle of the left ventricle and subsequently flattening the BP as shown above with the HA side on top. We highly recommend taking this into account for future implant material selection. We also recommend research groups and companies, who are working with BP, to precisely describe which areas were used in their research. This way, studies become more comparable and reproducible.

## 6. Ethical statement

During investigation no human or animals were used so that no institutional or national ethical committee approval had to be consulted.

## CRedit authorship contribution statement

**Felix Stieglmeier:** Conceptualization, Investigation, Methodology, Formal analysis, Writing – original draft, Visualization. **Maximilian Grab:** Conceptualization, Methodology, Validation, Resources, Writing – review & editing, Funding acquisition. **Fabian König:** Methodology, Writing – review & editing. **Joscha Büch:** Validation, Writing – review & editing. **Christian Hagl:** Conceptualization, Project administration, Funding acquisition. **Nikolaus Thierfelder:** Conceptualization, Methodology, Validation, Writing – review & editing, Project administration, Supervision.

## Declaration of competing interest

The authors declare that they have no known competing financial interests or personal relationships that could have appeared to influence the work reported in this paper.

## Acknowledgments

The authors would like to thank *Lamed GmbH* (Oberhaching; GER) for supplying us with fixed BP material (Supple Peri-Guard; Synovis).

## References

Alavi, S.H., et al., 2013. Characterizing the collagen fiber orientation in pericardial leaflets under mechanical loading conditions. *Ann. Biomed. Eng.* 41 (3), 547–561.

- Bell, D., et al., 2019. Durability of tissue-engineered bovine pericardium (CardioCel(R)) for a minimum of 24 months when used for the repair of congenital heart defects. *Interact. Cardiovasc. Thorac. Surg.* 28 (2), 284–290.
- Bielli, A., et al., 2018. Characterization of a new decellularized bovine pericardial biological mesh: structural and mechanical properties. *J. Mech. Behav. Biomed. Mater.* 78, 420–426.
- Braile, D.M., et al., 1998. Mapping of bovine pericardium: physical and histopathologic tests. *J. Heart Valve Dis.* 7 (2), 202–206.
- Braile-Sternieri, M., et al., 2020. In Vivo Evaluation of Vivere Bovine Pericardium Valvular Bioprosthesis with a New Anti-calcifying Treatment. *Artif. Organs.*
- Collatusso, C., et al., 2019. Decellularization as a Method to Reduce Calcification in Bovine Pericardium Bioprosthetic Valves. *Interact. Cardiovasc. Thorac. Surg.*
- Crapo, P.M., Gilbert, T.W., Badylak, S.F., 2011. An overview of tissue and whole organ decellularization processes. *Biomaterials* 32 (12), 3233–3243.
- Ferroni, L., et al., 2019. Bovine pericardium membrane as new tool for mesenchymal stem cells commitment. *J. Tissue Eng. Regen. Med.* 13 (10), 1805–1814.
- Gauvin, R., et al., 2013. A comparative study of bovine and porcine pericardium to highlight their potential advantages to manufacture percutaneous cardiovascular implants. *J. Biomater. Appl.* 28 (4), 552–565.
- Hedergott, A., et al., 2020. Tendon elongation with bovine pericardium in strabismus surgery-indications beyond Graves' orbitopathy. *Graefes Arch. Clin. Exp. Ophthalmol.* 259 (1), 145–155. <https://doi.org/10.1007/s00417-020-04939-7>. Epub 2020 Sep 19.
- Heuschkel, M.A., et al., 2019. In vitro evaluation of bovine pericardium after a soft decellularization approach for use in tissue engineering. *Xenotransplantation* 26 (2), e12464.
- Huang-Lee, L.L., Cheung, D.T., Nimni, M.E., 1990. Biochemical changes and cytotoxicity associated with the degradation of polymeric glutaraldehyde derived crosslinks. *J. Biomed. Mater. Res.* 24 (9), 1185–1201.
- Hulsmann, J., et al., 2012. Transplantation material bovine pericardium: biomechanical and immunogenic characteristics after decellularization vs. glutaraldehyde-fixing. *Xenotransplantation* 19 (5), 286–297.
- Johnston, D.R., et al., 2015. Long-term durability of bioprosthetic aortic valves: implications from 12,569 implants. *Ann. Thorac. Surg.* 99 (4), 1239–1247.
- Kiesendahl, N., et al., 2020. In Vitro Calcification of Bioprosthetic Heart Valves: Test Fluid Validation on Prosthetic Material Samples. *Ann. Biomed. Eng.*
- Laker, L., Dohmen, P.M., Smit, F.E., 2020. Synergy in a detergent combination results in superior decellularized bovine pericardial extracellular matrix scaffolds. *J. Biomed. Mater. Res. B Appl. Biomater.* 108 (6), 2571–2578. <https://doi.org/10.1002/jbmb.34588>. Epub 2020 Feb 12.
- Li, N., et al., 2018. Efficient decellularization for bovine pericardium with extracellular matrix preservation and good biocompatibility. *Interact. Cardiovasc. Thorac. Surg.* 26 (5), 768–776.
- Limpert, J.N., et al., 2009. Repair of abdominal wall defects with bovine pericardium. *Am. J. Surg.* 198 (5), e60–e65.
- Mendoza-Novelo, B., et al., 2011. Decellularization of pericardial tissue and its impact on tensile viscoelasticity and glycosaminoglycan content. *Acta Biomater.* 7 (3), 1241–1248.
- Oeverhaus, M., et al., 2018. Tendon elongation with bovine pericardium in patients with severe esotropia after decompression in graves' orbitopathy-efficacy and long-term stability. *Strabismus* 26 (2), 62–70.
- Rassoli, A., Fatourae, N., Guidoin, R., 2018. Structural model for viscoelastic properties of pericardial bioprosthetic valves. *Artif. Organs* 42 (6), 630–639.
- Rassoli, A., et al., 2019. Comparison of Tensile Properties of Xenopericardium from Three Animal Species and Finite Element Analysis for Bioprosthetic Heart Valve Tissue. *Artif. Organs.*
- Sacks, M.S., Chuong, C.J., 1998. Orthotropic mechanical properties of chemically treated bovine pericardium. *Ann. Biomed. Eng.* 26 (5), 892–902.
- Sacks, M.S., Chuong, C.J., More, R., 1994. Collagen fiber architecture of bovine pericardium. *Am. Soc. Artif. Intern. Organs J.* 40 (3), M632–M637.
- Santibanez-Salgado, J.A., et al., 2010. Lyophilized glutaraldehyde-preserved bovine pericardium for experimental atrial septal defect closure. *Eur. Cell. Mater.* 19, 158–165.
- Sheng, W., et al., 2019. Aortic valve replacement with bovine pericardium in patients with aortic valve regurgitation. *Int. Heart J.* 60 (6), 1344–1349.
- Shiraishi, T., et al., 2019. Pulmonary Artery “conduit” Reconstruction Using Bovine Pericardium Following Long-Segment Sleeve Resection: a Unique “in Situ Tailor-Made” Sewing Method. *Gen. Thorac. Cardiovasc. Surg.*
- Siddiqui, R.F., Abraham, J.R., Butany, J., 2009. Bioprosthetic heart valves: modes of failure. *Histopathology* 55 (2), 135–144.
- Simionescu, D., Simionescu, A., Deac, R., 1993. Mapping of glutaraldehyde-treated bovine pericardium and tissue selection for bioprosthetic heart valves. *J. Biomed. Mater. Res.* 27 (6), 697–704.
- Sulejmani, F., et al., 2019. Evaluation of transcatheter heart valve biomaterials: computational modeling using bovine and porcine pericardium. *J. Mech. Behav. Biomed. Mater.* 97, 159–170.
- Umashankar, P.R., Mohanan, P.V., Kumari, T.V., 2012. Glutaraldehyde treatment elicits toxic response compared to decellularization in bovine pericardium. *Toxicol. Int.* 19 (1), 51–58.
- Whelan, A., et al., 2020. In: Bovine Pericardium of High Fibre Dispersion Has High Fatigue Life and Increased Collagen Content; Potentially an Untapped Source of Heart Valve Leaflet Tissue. *Ann. Biomed. Eng.*
- Yang, M., et al., 2012. Preseeding of human vascular cells in decellularized bovine pericardium scaffold for tissue-engineered heart valve: an in vitro and in vivo feasibility study. *J. Biomed. Mater. Res. B Appl. Biomater.* 100 (6), 1654–1661.

#### 7.5 Pericardial tissue for cardiovascular application: an in-vitro evaluation of established and advanced production processes (Grefen et al., 2018)

- Linda Grefen, Fabian König, Maximilian Grab, Christian Hagl, Nikolaus Thierfelder
- Journal of Materials Science: Materials in Medicine. 2018 Nov 3;29(11):172
- DOI: 10.1007/s10856-018-6186-6
- *Die hier genannte, publizierte Originalarbeit ist zum Drucklegungszeitpunkt der vorliegenden Habilitationsschrift lizenrechtlich geschützt und nicht frei veröffentlichungsfähig. Der Text kann unter der angegebenen Quelle kostenpflichtig angefordert oder mit entsprechenden Rechten eingesehen werden.*


#### 7.6 Tissue-engineering acellular scaffolds – The significant influence of physical and procedural decellularization factors (Starnecker et al., 2018)

- Fabian Starnecker, Fabian König, Christian Hagl, Nikolaus Thierfelder
- Journal of Biomedical Materials Research Part B: Applied Biomaterials. 2018 Jan;106(1):153-162
- DOI: 10.1002/jbm.b.33816
- *Die hier genannte, publizierte Originalarbeit ist zum Drucklegungszeitpunkt der vorliegenden Habilitationsschrift lizenrechtlich geschützt und nicht frei veröffentlichungsfähig. Der Text kann unter der angegebenen Quelle kostenpflichtig angefordert oder mit entsprechenden Rechten eingesehen werden.*

#### 7.7 Successful decellularization of thick-walled tissue: Highlighting pitfalls and the need for a multifactorial approach (Koenig et al., 2019)

- Fabian König, Marie Kilzer, Christian Hagl, Nikolaus Thierfelder
- The International Journal of Artificial Organs, 2019 Jan;42(1):17-24
- DOI: 10.1177/0391398818805624

# Successful decellularization of thick-walled tissue: Highlighting pitfalls and the need for a multifactorial approach

The International Journal of Artificial  
Organs  
2019, Vol. 42(1) 17–24  
© The Author(s) 2018  
Article reuse guidelines:  
sagepub.com/journals-permissions  
DOI: 10.1177/0391398818805624  
journals.sagepub.com/home/ijao  


Fabian Koenig, Marie Kilzer, Christian Hagl  
and Nikolaus Thierfelder

## Abstract

**Introduction:** Decellularization of thick tissue is challenging and varying. Therefore, we tried to establish a multifactorial approach for reliable aortic wall decellularization.

**Methods:** Porcine aortic walls were decellularized according to different procedures. Decellularization was performed for 24 (G1), 48 (G2), and 72 h (G3) with a solution of 0.5% desoxycholate and 0.5% dodecyl sulfate. The procedure was characterized using intermittent washing steps, the inclusion of sonication as well as DNase and  $\alpha$ -galactosidase treatment. The decellularization efficiency was measured by the evaluation of 4',6-diamidino-2-phenylindole and hematoxylin and eosin staining and quantitative DNA assays. Pentachrome and picosirius red staining, scanning electron microscopy as well as glycosaminoglycan assays were performed to evaluate the effect of the procedure on the extracellular matrix.

**Results:** 4',6-Diamidino-2-phenylindole and hematoxylin and eosin staining revealed a large amount of remaining nuclei in all groups. However, consecutive DNase treatment had a significant effect. While the remaining DNA was detected in some samples of G1 and G2, samples of G3 were fully decellularized. Glycosaminoglycan content was significantly reduced to 50% after 24 h (G1) but remained constant for G2 and G3. Picosirius red staining revealed an intact and stable collagen network without any visible defects. Pentachrome staining substantiated these results. Nonetheless, the fiber network remains intact, which could be confirmed by reflection electron microscopy analysis.

**Conclusion:** In this study, we developed a procedure that grants successful decellularization of porcine aortic wall while maintaining the fibrous microstructure. We highlighted the significant effect of DNase and  $\alpha$ -galactosidase treatment. In addition, we could show the need for a multifactorial treatment and comprehensive evaluation protocols for thick tissue decellularization.

## Keywords

Decellularization, aorta, thick tissue, galactose- $\alpha$ -1,3-galactose, DNA

Date received: 12 April 2018; accepted: 4 July 2018

## Introduction

Up to now, countless and varying decellularization (DC) protocols and methods are published.<sup>1</sup> Usually, DC is performed by incubation of the specific tissue with chemical (e.g. detergents) and/or biological (e.g. nucleases) reagents.<sup>2</sup> This process is normally supported by physical (e.g. shear stress) and procedural factors (e.g. washing steps).<sup>3</sup> As biological tissues are subject to physiologic variations, a comprehensive quality control has to be done after each DC procedure.

Successful DC can be defined as preservation of the native extracellular matrix (ECM), while removing all cellular and immunogenic components.<sup>4</sup> In this context, DNA

and the immunogenic carbohydrate galactose- $\alpha$ -1,3-galactose ( $\alpha$ -Gal) are described as the major immunogenic residues.<sup>5,6</sup> There is a bundle of publications available, reporting severe complications or failure of decellularized implants.<sup>7–10</sup> Clinical problems with

Department of Cardiac Surgery, Laboratory for Tissue Engineering, Grosshadern Medical Centre, Ludwig-Maximilians-University, Munich, Germany

### Corresponding author:

Nikolaus Thierfelder, Department of Cardiac Surgery, Laboratory for Tissue Engineering, Grosshadern Medical Centre, Ludwig-Maximilians-University, Marchioninistrasse 15, 81377 Munich, Germany.  
Email: Nikolaus.Thierfelder@med.uni-muenchen.de



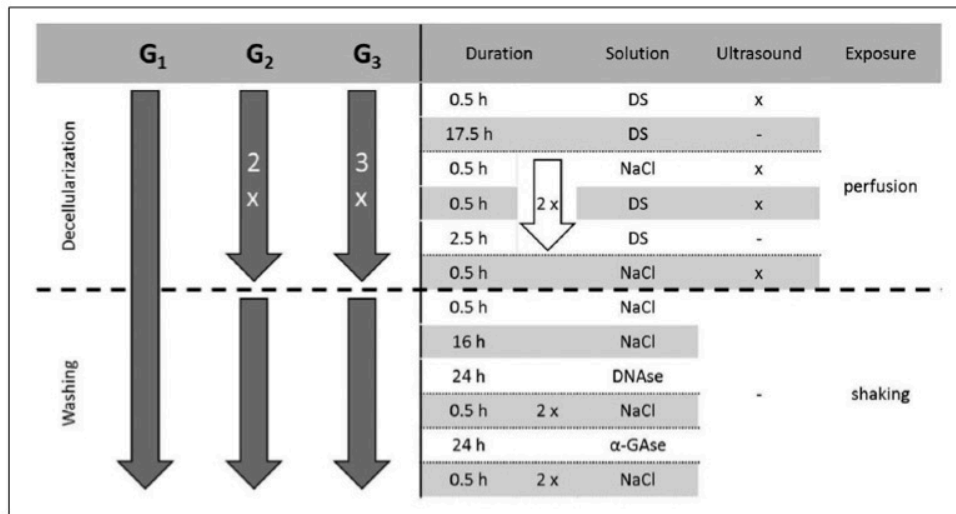


**Figure 1.** Experimental setup.

DS: decellularization solution (0.5% deoxycholate/0.5% dodecyl sulfate); NaCl: 0.9% sodium chloride solution supplemented with 1% Anti-Anti; DNase: 30 U/mL solution; αGAse: 0.1 U/mL α-galactosidase solution.

decellularized implants can originate from inflammatory responses due to incomplete DC.<sup>11,12</sup>

Even though it is possible to successfully decellularize vascularized and thin tissue, for thick and less vascularized tissues contradictory results are published.<sup>13,14</sup> Especially, fibrous human materials like cartilage, cornea, or aortic/aortic heart valves are described as resistant to DC.<sup>15–18</sup> For example, Sierad et al.<sup>16</sup> and Da Costa et al.<sup>19</sup> reported that durations for complete aortic wall (AW) DC strongly vary from 24h to 16days. DC should be as short as possible, due to the known temporal impairment of the ECM - on the other hand, it should last as long as needed to grant a complete cell removal.<sup>20</sup> In a previous publication, we could show that DC efficiency can be significantly enhanced by procedural and physical modifications of established protocols.<sup>21</sup> Based on these findings, we developed a stable, safe, and reproducible protocol for successful aortic DC with a multifactorial approach.

## Methods

### Sample preparation

Fresh porcine hearts (n=20) were obtained from a local slaughterhouse. Segments of 4 cm length were cut from the ascending part of each aorta, directly above the sinus aortae. Prior to DC, each aorta was longitudinally segmented in three parts and each segment was assigned randomly to one of the three treatment groups (G<sub>1</sub>, G<sub>2</sub>, and G<sub>3</sub>).

### DC

DC was performed by incubation in a 0.5% sodium desoxycholate/0.5% sodium dodecyl sulfate (Sigma-Aldrich GmbH, Darmstadt, Germany) solution (phosphate-buffered

saline (PBS) based). Samples were treated once (G<sub>1</sub>), twice (G<sub>2</sub>), or thrice (G<sub>3</sub>) by a specific DC sequence (Figure 1), resulting in 24-, 48-, or 72-h detergent exposure. Ultrasonic exposure, cyclic treatments with intermittent washing steps, and enforced whirling were used to generate an effective DC sequence. During and after DC, the samples were exposed to different washing steps with 0.9% sodium chloride solution (supplemented with amphotericin B, penicillin, and streptomycin; 1% Anti-Anti 100×; Gibco®; Life Technologies GmbH, Darmstadt, Germany). Furthermore, each sample was incubated with DNase (30U/mL, Worthington Biochemical Corporation, Lakewood, CA, USA) and α-galactosidase (0.1U/mL; Sigma-Aldrich). Samples were taken from native tissues as well as after treatment in the respective groups.

### 4',6-Diamidino-2-phenylindole staining

Defining the absence of DNA as one criterion of successful DC, double-stranded DNA binding 4',6-diamidino-2-phenylindole (DAPI) was chosen to evaluate the DC efficiency. Tissue sections were permeabilized with methanol–acetone (1:1) for 2 min before incubating with DAPI solution (c=0.1 μg/mL; Sigma-Aldrich) for 5 min. In order to minimize background fluorescence, the sections were counterstained with 0.3% Sudan Black in 70% ethanol for 2 min. The samples were analyzed by fluorescence microscopy using identical exposure times (Axio Observer; Carl Zeiss AG, Oberkochen, Germany).

### Histology

Hematoxylin and eosin (H&E), picosirius red (PSR) as well as Movat's pentachrome (MPC) staining were used to



assess the overall histologic appearance of the samples, AW architecture, and ECM constitution. For preparation, the samples were fixed in formalin solution (Roti®-Histofix 4.5%; Carl Roth GmbH, Karlsruhe, Germany) before being embedded in paraffin. Transversal sections (6 µm layer thickness) were cut, dewaxed, and stained. H&E (hemalum from Merck KGaA, Darmstadt, Germany; Eosin from Sigma-Aldrich), MPC (Morphisto GmbH, Frankfurt am Main, Germany), and PSR (Morphisto) staining were performed according to the manufacturer's protocols. Images of the stained sections were taken with a transversal light microscope (DMR; Leica Mikrosysteme Vertrieb GmbH, Wetzlar, Germany). PSR staining further allowed the examination of collagen (rhodamine channel) and autofluorescent substances (fluorescein channel) including elastic fibers by fluorescence microscopy.<sup>22,23</sup> For comparability, all images were taken with equal exposure times.

### *α-Gal immunohistochemistry*

Fixed and sectioned samples were used and further processed for immunohistochemical (IHC) staining. After antigen unmasking, the sections were incubated with the primary antibody ( $\alpha$ -galactosidase ( $\alpha$ -Gal) epitope (Gal $\alpha$ 1-3Gal $\beta$ 1-4GlcNAc-R) monoclonal antibody; Enzo Life Sciences GmbH, Lörrach, Germany) overnight. Finally, antigen-antibody complexes were visualized (CytoScan™ HRP Detection System; Cell Marque, Merck). Images were taken with an optical microscope.

### *DNA quantification*

DNA was isolated according to the manufacturer's instructions (Isolate II Genomic DNA Kit; Bioline, Luckenwalde, Germany). For DNA quantification, the isolated DNA solution was diluted by Tris-HCl buffer and measured at 260/280 nm using a photometer (BioPhotometer; Eppendorf GmbH, Hamburg, Germany). Values were normalized in regard to tissue weight.

### *Scanning electron microscopy*

Scanning electron microscopy (SEM) was used for topographic analysis of the inner and outer surfaces of the AW. Samples were fixed with glutaraldehyde, dehydrated, critical point dried (Leica) with CO<sub>2</sub>, and gold sputtered (Leica). A scanning electron microscope (Zeiss Evo LS10; Carl Zeiss AG) with secondary electron detection was used for image acquisition.

### *Glycosaminoglycan quantification*

The effect of the DC procedure on the glycosaminoglycan (GAG) content of the ECM was quantified by colorimetric

assessment of the samples. Samples were processed according to the manufacturer's protocol (Glycosaminoglycan Assay Blyscan; Biocolor, Carrickfergus, UK). The GAG measurements were normalized to native samples.

### *Statistical analysis*

The Anderson-Darling test was applied to evaluate if the measured data were adequately described by the normal distribution. Differences between the groups were detected by performing the unpaired student's t-test. Values were considered significant if  $p < 0.05$ , very significant if  $p < 0.01$  and extremely significant if  $p < 0.001$ . Data are reported as mean  $\pm$  standard deviation (SD).

## **Results**

### *DC efficiency*

**DAPI staining.** Staining of native samples showed a strong fluorescence of homogeneously distributed nuclei all over the AW in all specimens (Figure 2, A1). DC without DNase treatment led to a fading of the nuclei, especially at the sub-surficial areas. Furthermore, nuclei were not sharply delineated anymore. Only the surface layers of the AW were not stained, indicating complete removal of DNA (Figure 2, B1). DC with additional DNase incubation resulted in a significant loss of fluorescence in all groups. However, after 24-h DC (G<sub>1</sub>), the results were extremely inhomogeneous and half of the samples appeared completely decellularized, whereas other samples still showed the remaining nuclei. These nuclei were localized in a ribbon-like shape at the middle of the samples (Figure 2, C1). Even after 48-h DC (G<sub>2</sub>), some samples still showed fluorescence in the middle layers, indicating remaining nuclei (Figure 2, D1). Only after 72-h DC, no sample was stained positive, indicating a complete and successful DC of all specimens (Figure 2, E1).

**H&E staining.** Native H&E-stained samples showed similar results as those obtained with DAPI staining. Cytoplasmic and ECM components were observed in a homogeneous pattern, indicated by the pinkish-red basophilic eosin stain (Figure 2, A2). Staining of the decellularized samples without DNase treatment substantiated DAPI findings. Eosinophilic background appeared unchanged compared to the native samples (Figure 2, B2). All H&E-stained samples of G<sub>1</sub>, G<sub>2</sub>, and G<sub>3</sub> did not match with the DAPI observations. Decellularized and DNase-treated samples showed no remaining nuclei in the sections of all protocols. The pinkish-red stain appeared weakened and loosened, indicating a loss of stained substance. This was especially observable for the areas in between the fibrous bundles, which were still stained reddish (Figure 2, C2 + D2 + E2).

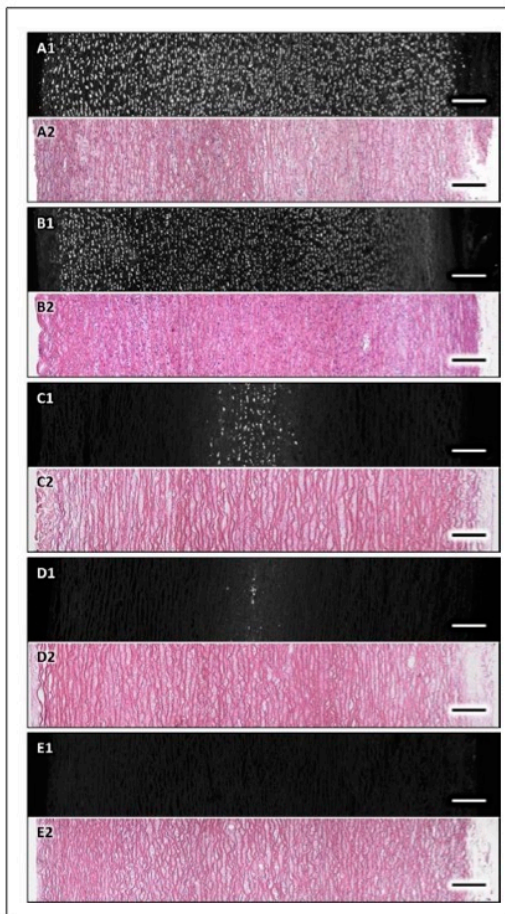


**Figure 2.** DAPI fluorescence (1) and H&E staining (2): Native (A) and “decellularized” (B) samples showed strong nucleic staining. DNase treatment reduced staining reactions significantly. However, G1 (C) and G2 (D) were not completely decellularized. Only G3 (E) showed no nucleic staining; scale bars: 200  $\mu$ m.

### DNA quantification

Native AW revealed a mean amount of  $453.39 \pm 83.96$  ng DNA/mg tissue. After 24-h DC and without DNase treatment, DNA was extremely significantly ( $p < 0.001$ ) reduced to  $366.13 \pm 102.51$  ng DNA/mg tissue. Assessment of the different groups after DC and DNase incubation also showed an extremely significant DNA reduction of 91.91% ( $G_1$ ), 93.32% ( $G_2$ ), and 94.08% ( $G_3$ ) compared to the respective native samples. The final amounts of DNA were  $38.07 \pm 18.24$  ( $G_1$ ),  $31.53 \pm 27.49$  ( $G_2$ ) and  $27.43 \pm 18.53$  ng DNA/mg tissue ( $G_3$ ), respectively (Figure 3(a)).

### ECM preservation

**MPC staining.** The typical three-layered structure of AW (tunica intima, media, and adventitia) was shown by all

native samples (Figure 4, A1). Cell nuclei (black stained in MPC) were detected all over the native AW. Elastic (stained red in MPC) and collagen (stained yellow in MPC) fibers were the dominating components of the specimen.

In all treatment groups, a preservation of the three-layered structure was possible. Evaluation of decellularized scaffolds revealed the unchanged presence of collagen and elastic fibers for all groups (Figure 4, B1–D1). Microscopic evaluation did not reveal any alterations or losses of ECM components during the DC procedure. Overall the AW appeared brighter after the DC process, indicating a loss of cellular substance.

**Picosirius red staining.** Evaluation of the native samples revealed that collagen (red colored) spread over the entire AW with an accumulation in the internal and external layers. Green autofluorescence showed a homogeneous spread over the cross section. Wriggle-shaped filaments, resembling elastic fibers, were detectable (Figure 4, A2).

PSR staining showed preservation of collagen in all treated samples. No influence of treatment duration on the integrity of the collagen network was observed (Figure 4, B2–D2). A general loosening, as observed by MPC staining, was confirmed by the decreased intensity of green autofluorescence, which indicates the loss of cellular substances.

**GAG quantification.** Measurements revealed an extremely significant GAG reduction of  $48.63\% \pm 37.7\%$  ( $p < 0.001$ ) after 24-h DC. Among the  $G_1$ ,  $G_2$  (native  $\rightarrow G_2$ :  $-56.38\% \pm 18.12\%$ ,  $p < 0.001$ ), and  $G_3$  (native  $\rightarrow G_3$ :  $-50.01\% \pm 37.44\%$ ,  $p < 0.001$ ) groups, no significant variations were detected (Figure 3(b)).

### Surface topography

Native samples showed a homogeneous surface topography with a regular pattern on the aortic luminal side (Figure 4, A4). A confluent cellular coverage was observable across the whole surface. Images of the outer surface revealed inhomogeneously orientated fiber bundles, some cell clusters, detritus, and residual fat. After 24-h DC ( $G_1$ ), major areas of the surface showed no cellular coverage and revealed distinct fibers. However, individual sections were still covered by a layer of cellular material and the overall impression was not homogeneous. No damages to the fibers were detectable and the samples showed a stable and unimpaired fiber network (Figure 4, B4). A distinct and filigree fiber network was observable after 48 h of DC ( $G_2$ ) on the inner and outer surfaces of the samples. No damages to the bundles or single fibers were detectable. The luminal surface was free from cellular coverage and revealed a homogeneous fiber distribution (Figure 4, C4). The longest treatment time (72h,  $G_3$ ) led to a complete and



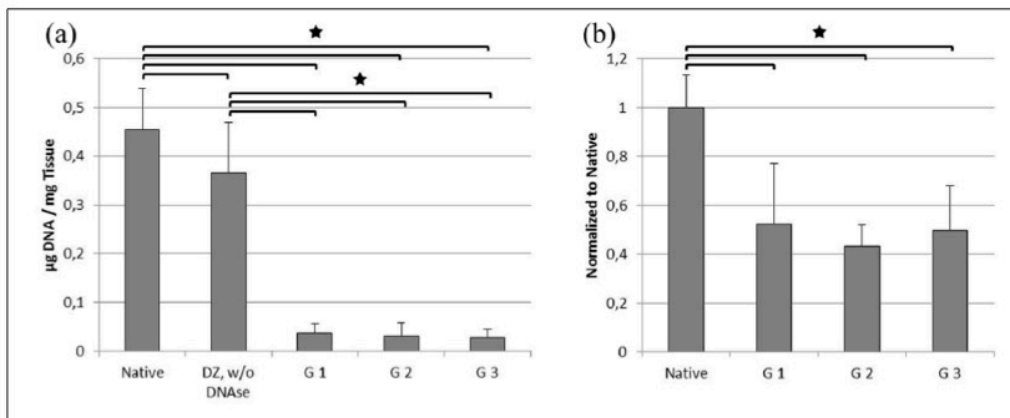


**Figure 3.** Quantitative DNA (a) and GAG (b) evaluation; stars indicate extremely significant differences.

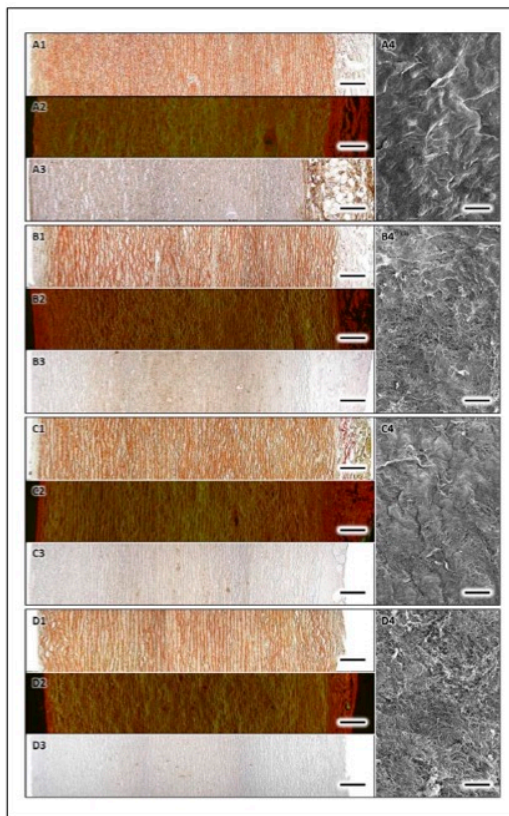


**Figure 4.** ECM status and  $\alpha$ -Gal presence of native (A) and treated samples (G<sub>1</sub> = B, G<sub>2</sub> = C, G<sub>3</sub> = D): MPC (1) and fluorescent PSR imaging (2) showed a preserved ECM after all treatment protocols. Immunohistochemical staining (3; brown color) against  $\alpha$ -Gal revealed the decreasing (A  $\rightarrow$  D<sub>3</sub>) presence of this antigen with longer treatment durations. Only a few positive spots at the aortic vasa vasorum in G<sub>3</sub> showed the presence of  $\alpha$ -Gal (D<sub>3</sub>). SEM imaging showed the removal of the superficial cell layer (A<sub>4</sub>) and the uncovering of the underlying fiber network (B–D); scale bars: 1–3 = 200  $\mu$ m, 4 = 15  $\mu$ m.

homogeneous DC, observable on the samples' inner and outer surfaces. No damages of the fiber network were detectable (Figure 4, D<sub>4</sub>).

#### $\alpha$ -Gal epitope

IHC staining against  $\alpha$ -Gal revealed the presence of the immunogenic disaccharide in all native samples. Besides a discreet overall staining shade of the samples, three major accumulation sites were recognizable: the endothelial layer of the aortae, the external part, and finally all microvascular structures (vasa vasorum) of the AW showed highly positive staining reactions (Figure 4, A<sub>3</sub>). Samples of G<sub>1</sub> (24 h) showed an obvious reduction of the  $\alpha$ -Gal epitope by reduced staining. Previously, highly positive inner and outer layers of the AW showed no positive reactions after treatment. However, microvascular structures all over the AW were still strongly positive for  $\alpha$ -Gal (Figure 4, B<sub>3</sub>). Negative staining results of the endothelial and the outer layer against  $\alpha$ -Gal were confirmed after 48-h treatment (G<sub>2</sub>). However, the microvascular network was still stained positive for the antigen. The overall stain was further reduced and was only detectable in the middle layers of the AW tissue (Figure 4, C<sub>3</sub>). Samples of 72-h DC (G<sub>3</sub>) showed the highest reduction of the  $\alpha$ -Gal epitope. The inner and outer surfaces revealed no staining reactions. However, some vasa vasorum of the AW still showed a demarcated and distinct positive staining (Figure 4, D<sub>3</sub>).

#### Discussion

During our study, we recognized a few general particularities and pitfalls in the DC process.

#### DNA detection

Usually, DNA measurements and quantifications are used to prove success and efficiency of DC protocols.<sup>3,24</sup> As a

guideline, it is recommended to use a quantitative measurement of the DNA content as well as histological nuclei staining, either with H&E or with DAPI.<sup>4</sup> In this study, we used quantitative proof as well as two different nucleic staining methods (DAPI and H&E). Interestingly, we were not able to recognize nuclei with H&E stain in many samples, whereas the respective DAPI stain of the same specimens showed a lot of remaining nucleic acid. Roosens et al.<sup>25</sup> observed the same results after DC of porcine aortic leaflets. This confirmed the insensitivity of H&E staining and shows the inadequacy to use it as a sole proof of DC.<sup>24</sup> In addition, it was also possible to observe inconsistencies between DAPI staining and quantitative measurements. In general, tissues with <50 ng DNA/mg tissue are considered successfully decellularized.<sup>4</sup> Conversely, in our study, some samples showed a high amount of remaining nuclei after 24 h, while quantitative measurements indicated a successful DC. It is known that even a few remaining cells can lead to focal inflammatory reactions after implantation.<sup>12</sup> To exclude focal nucleic remnants, we highly recommend a multiprocedural analysis with DAPI staining and a quantitative measurement for a safe and reliable DNA detection. As H&E is not sensitive enough, this method can be neglected. Interestingly, many publications are not matching these requirements and are using H&E staining and photometric DNA quantification as sole means for DC assessment.<sup>19,26-34</sup>

### DC efficiency

Assessment of the decellularized specimen revealed significant differences in DC efficiency. While the majority of the treated samples showed no DNA remains after 24 h of DC, other AWs were not completely decellularized after 48 h. These intragroup differences are surprising as the specimen originated from the same source and were treated equally. However, the fibrous nature of the AW could provoke differences in the DC efficiency. These findings could be a possible explanation for the high variations in published DC durations.<sup>16,19</sup> Furthermore, it also highlights the need for precise and strict quality management at the end of every DC process. This is also of highest importance if these tissues are translated to clinical application in order to provide a secure and reliable implant and to prevent severe complications.<sup>11</sup>

### $\alpha$ -Gal removal

Besides DNA,  $\alpha$ -Gal is considered as one of the most critical antigens in xenogeneic tissue DC.<sup>35</sup> Therefore, an effective and reliable method to remove this immunogenic disaccharide is essential. In this study, we could show that the implementation of  $\alpha$ -Gal actosidase is reducing the amount of  $\alpha$ -Gal significantly. However, even after complete DC and enzymatic incubation with  $\alpha$ -Gal actosidase, IHC staining revealed the remaining antigens. According to

the published results, the remaining antigens are localized at the vasa vasorum of the AW.<sup>11</sup> It is proved that even small amounts of  $\alpha$ -Gal can induce strong immunogenic reactions after implantation. To overcome this problem, the use of  $\alpha$ -Gal-knock-out animals for tissue donation should be considered.<sup>36</sup> The success of this approach was already demonstrated for glutaraldehyde-fixed heart valves.<sup>37</sup>

We postulate that the consideration of the abovementioned particularities and pitfalls should help prevent a major part of clinical, implant-related complications.<sup>11,12</sup>

In order to provide a DC protocol for thick and resistant AW, we evaluated the results of our study. A safe and reproducible removal of nuclei was only possible after 72 h of DC. We cannot support publications where a complete DC of AW within 24 h was successful.<sup>19</sup> Histology and quantitative DNA measurements further demonstrated the need of an additional DNase treatment. This is in line with the previous publications.<sup>38</sup> As ECM preservation is the second major criterion for successful DC, ECM status was assessed after treatment.<sup>24</sup> Microscopy showed a maintained delicate fibrous network after all DC durations. Histologic assessment revealed no observable changes or aging phenomena of the ECM. As published previously, no negative effects were induced by sonication treatment.<sup>21,34</sup> The slight loosening (higher transparency) of the tissue could be explained by the removal of cellular components and GAGs. It is known that DC normally affects and reduces the GAG content of tissue.<sup>25,39</sup> Quantitative measurements in our study confirmed these claims by a 48.6% reduction after 24-h DC. Interestingly, the remaining amount of GAGs stayed at a comparable level for longer DC durations. This is in contrast to the previously published results, where a continuous reduction of the GAG amount was observed with increased treatment times.<sup>32</sup>

In this study, we established a new protocol for DC of thick and fibrous tissue. By applying a multifactorial method to AW, a significant reduction of DC time from 16 days to 72 h was possible.<sup>16</sup> However, the complete removal of  $\alpha$ -Gal epitope remains a challenging task and the use of  $\alpha$ -Gal-knock-out tissue should be considered in the future. As the duration of the total DC is strongly varying strongly, a precise quality management to prove acellularity is essential for each treated sample. In this context, we could show that H&E staining is not suitable for this assessment. Furthermore, a multi-methodological approach including DAPI staining and quantitative measurements is required. These measures are essential for a safe and reliable clinical application of decellularized implants.

### Acknowledgements

F.K. and M.K. have contributed equally to this article.

### Declaration of conflicting interests

The author(s) declared no potential conflicts of interest with respect to the research, authorship, and/or publication of this article.

## Funding

The author(s) received no financial support for the research, authorship, and/or publication of this article.

## References

1. Gupta SK and Mishra NC. *Decellularization methods for scaffold fabrication*. Totowa, NJ: Humana Press, 2017, pp. 1–10.
2. Gilbert TW, Sellaro TL and Badylak SF. Decellularization of tissues and organs. *Biomaterials* 2006; 27: 3675–3683.
3. Keane TJ, Swinehart IT and Badylak SF. Methods of tissue decellularization used for preparation of biologic scaffolds and in vivo relevance. *Methods* 2015; 84: 25–34.
4. Crapo PM, Gilbert TW and Badylak SF. An overview of tissue and whole organ decellularization processes. *Biomaterials* 2011; 32: 3233–3243.
5. Gilbert TW, Freund J and Badylak SF. Quantification of DNA in biologic scaffold materials. *J Surg Res* 2009; 152: 135–139.
6. Mathapati S, Verma RS, Cherian KM, et al. Inflammatory responses of tissue-engineered xenografts in a clinical scenario. *Interact Cardiovasc Thorac Surg* 2011; 12: 360–365.
7. Johnson CC, Johnson DJ, Garcia GH, et al. High short-term failure rate associated with decellularized osteochondral allograft for treatment of knee cartilage lesions. *Arthroscopy* 2017; 33: 2219–2227.
8. Dobrilovic N, Soukas P, Sadiq I, et al. Early complications of biologic extracellular matrix patch after use for femoral artery repair. *J Vasc Surg* 2017; 65: 705–710.
9. Perri G, Polito A, Esposito C, et al. Early and late failure of tissue-engineered pulmonary valve conduits used for right ventricular outflow tract reconstruction in patients with congenital heart disease. *Eur J Cardiothorac Surg* 2012; 41: 1320–1325.
10. Simon P, Kasimir MT, Seebacher G, et al. Early failure of the tissue engineered porcine heart valve SYNERGRAFT in pediatric patients. *Eur J Cardiothorac Surg* 2003; 23: 1002–1006.
11. Kasimir MT, Rieder E, Seebacher G, et al. Presence and elimination of the xenoantigen gal (alpha1, 3) gal in tissue-engineered heart valves. *Tissue Eng* 2005; 11: 1274–1280.
12. Zheng MH, Chen J, Kirilak Y, et al. Porcine small intestine submucosa (SIS) is not an acellular collagenous matrix and contains porcine DNA: possible implications in human implantation. *J Biomed Mater Res B Appl Biomater* 2005; 73: 61–67.
13. Syed O, Walters NJ, Day RM, et al. Evaluation of decellularization protocols for production of tubular small intestine submucosa scaffolds for use in oesophageal tissue engineering. *Acta Biomater* 2014; 10: 5043–5054.
14. Hillebrandt K, Polenz D, Butter A, et al. Procedure for decellularization of rat livers in an oscillating-pressure perfusion device. *J Vis Exp* 2015; 10: e53029.
15. González-Andrades M, Carriel V, Rivera-Izquierdo M, et al. Effects of detergent-based protocols on decellularization of corneas with sclerocorneal limbus. Evaluation of regional differences. *Transl Vis Sci Technol* 2015; 4: 13.
16. Sierad LN, Shaw EL, Bina A, et al. Functional heart valve scaffolds obtained by complete decellularization of porcine aortic roots in a novel differential pressure gradient perfusion system. *Tissue Eng Part C Methods* 2015; 21: 1284–1296.
17. Cheng CW, Solorio LD and Alsberg E. Decellularized tissue and cell-derived extracellular matrices as scaffolds for orthopaedic tissue engineering. *Biotechnol Adv* 2014; 32: 462–484.
18. O'Connor Mooney R, Davis NF, Hoey D, et al. On the automatic decellularisation of porcine aortae: a repeatability study using a non-enzymatic approach. *Cells Tissues Organs* 2016; 201: 299–318.
19. Da Costa FD, Costa AC, Prestes R, et al. The early and mid-term function of decellularized aortic valve allografts. *Ann Thorac Surg* 2010; 90: 1854–1860.
20. Conconi MT, De Coppi P, Di Liddo R, et al. Tracheal matrices, obtained by a detergent-enzymatic method, support in vitro the adhesion of chondrocytes and tracheal epithelial cells. *Transpl Int* 2005; 18: 727–734.
21. Starnecker F, Köenig F, Hagl C, et al. Tissue-engineering acellular scaffolds—the significant influence of physical and procedural decellularization factors. *J Biomed Mater Res B Appl Biomater* 2018; 106: 153–162.
22. Borges LF, Taboga SR and Gutierrez PS. Simultaneous observation of collagen and elastin in normal and pathological tissues: analysis of Sirius-red-stained sections by fluorescence microscopy. *Cell Tissue Res* 2005; 320: 551–552.
23. Vogel B, Siebert H, Hofmann U, et al. Determination of collagen content within picrosirius red stained paraffin-embedded tissue sections using fluorescence microscopy. *MethodsX* 2015; 2: 124–134.
24. Kaweckı M, Łabuś W, Klama-Baryla A, et al. A review of decellularization methods caused by an urgent need for quality control of cell-free extracellular matrix scaffolds and their role in regenerative medicine. *J Biomed Mater Res B Appl Biomater* 2018; 106: 909–923.
25. Roosens A, Somers P, De Somer F, et al. Impact of detergent-based decellularization methods on porcine tissues for heart valve engineering. *Ann of Biomed Eng* 2016; 44: 2827–2839.
26. Grauss RW, Hazekamp MG, van Vliet S, et al. Decellularization of rat aortic valve allografts reduces leaflet destruction and extracellular matrix remodeling. *J Thorac Cardiovasc Surg* 2003; 126: 2003–2010.
27. Khalpey Z, Qu N, Hemphill C, et al. Rapid porcine lung decellularization using a novel organ regenerative control acquisition bioreactor. *ASAIO J* 2015; 61: 71–77.
28. Liao J, Joyce EM and Sacks MS. Effects of decellularization on the mechanical and structural properties of the porcine aortic valve leaflet. *Biomaterials* 2008; 29: 1065–1074.
29. Numata S, Fujisato T, Niwaya K, et al. Immunological and histological evaluation of decellularized allograft in a pig model: comparison with cryopreserved allograft. *J Heart Valve Dis* 2004; 13: 984–990.
30. Paniagua Gutierrez JR, Berry H, Korossis S, et al. Regenerative potential of low-concentration SDS-decellularized porcine aortic valved conduits in vivo. *Tissue Eng Part A* 2015; 21: 332–342.
31. Rosario DJ, Reilly GC, Ali Salah E, et al. Decellularization and sterilization of porcine urinary bladder matrix for tissue

- engineering in the lower urinary tract. *Regen Med* 2008; 3: 145–156.
32. Wu L-C, Kuo YJ, Sun FW, et al. Optimized decellularization protocol including  $\alpha$ -Gal epitope reduction for fabrication of an acellular porcine annulus fibrosus scaffold. *Cell Tissue Bank* 2017; 18: 383–396.
33. Schenke-Layland K, Vasilevski O, Opitz F, et al. Impact of decellularization of xenogeneic tissue on extracellular matrix integrity for tissue engineering of heart valves. *J Struct Biol* 2003; 143: 201–208.
34. Azhim A, Syazwani N, Morimoto Y, et al. The use of sonication treatment to decellularize aortic tissues for preparation of bioscaffolds. *J Biomater Appl* 2014; 29: 130–141.
35. Konakci KZ, Bohle B, Blumer R, et al. Alpha-Gal on bioprostheses: xenograft immune response in cardiac surgery. *Eur J Clin Invest* 2005; 35: 17–23.
36. Puga Yung GL, Li Y, Borsig L, et al. Complete absence of the  $\alpha$ Gal xenoantigen and isoglobotrihexosylceramide in  $\alpha$ 1,3galactosyltransferase knock-out pigs. *Xenotransplantation* 2012; 19: 196–206.
37. McGregor CG, Kogelberg H, Vlasin M, et al. Gal-knockout bioprostheses exhibit less immune stimulation compared to standard biological heart valves. *J Heart Valve Dis* 2013; 22: 383–390.
38. Iablonskii P, Cebotari S, Tudorache I, et al. Tissue-engineered mitral valve: morphology and biomechanics. *Interact Cardiovasc and Thorac Surg* 2015; 20: 712–719.
39. Uygun BE, Soto-Gutierrez A, Yagi H, et al. Organ reengineering through development of a transplantable recellularized liver graft using decellularized liver matrix. *Nat Med* 2010; 16: 814–820.

## 7.8 The cardiotomy reservoir – a preliminary evaluation of a new cell source for cardiovascular tissue engineering (von Nathusius et al., 2017)

- Sophie von Nathusius, Fabian König, Ralf Sodian, Frank Born, Christian Hagl, Nikolaus Thierfelder
- The International Journal of Artificial Organs. 2018 Feb; 41(2):115-123
- DOI: 10.5301/ijao.5000653
- *Die hier genannte, publizierte Originalarbeit ist zum Drucklegungszeitpunkt der vorliegenden Habilitationsschrift lizenrechtlich geschützt und nicht frei veröffentlichungsfähig. Der Text kann unter der angegebenen Quelle kostenpflichtig angefordert oder mit entsprechenden Rechten eingesehen werden.*

## 7.9 Noninvasive analysis of synthetic and decellularized scaffolds for heart valve tissue engineering (Haller et al., 2013)

- Haller N., Hollweck T., **Thierfelder N.**, Schulte J., Hausherr J.M., Dauner M., Akra B.;
- ASAIO Journal. 2013 Mar-Apr;59(2):169-77
- DOI: 10.1097/MAT.0b013e31827db6b6



## Noninvasive Analysis of Synthetic and Decellularized Scaffolds for Heart Valve Tissue Engineering

NICOLE HALLER,\* TRIXI HOLLWECK,\* NIKOLAUS THIERFELDER,\* JULIA SCHULTE,\* JAN-MARCEL HAUSHERR,†  
MARTIN DAUNER,‡ AND BASSIL AKRA\*

**Microcomputed tomography ( $\mu$ -CT) is a nondestructive, high-resolution, three-dimensional method of analyzing objects. The aim of this study was to evaluate the feasibility of using  $\mu$ -CT as a noninvasive method of evaluation for tissue-engineering applications. The polyurethane aortic heart valve scaffold was produced using a spraying technique. Cryopreserved/thawed homograft and biological heart valve were decellularized using a detergent mixture. Human endothelial cells and fibroblasts were derived from saphenous vein segments and were verified by immunocytochemistry. Heart valves were initially seeded with fibroblasts followed by colonization with endothelial cells. Scaffolds were scanned by a  $\mu$ -CT scanner before and after decellularization as well as after cell seeding. Successful colonization was additionally determined by scanning electron microscopy (SEM) and immunohistochemistry (IHC). Microcomputed tomography accurately visualized the complex geometry of heart valves. Moreover, an increase in the total volume and wall thickness as well as a decrease in total surface was demonstrated after seeding. A confluent cell distribution on the heart valves after seeding was confirmed by SEM and IHC. We conclude that  $\mu$ -CT is a new promising noninvasive method for qualitative and quantitative analysis of tissue-engineering processes. *ASAIO Journal* 2013;59:169–177.**

**Key Words:** tissue engineering, biological heart valve, polyurethane heart valve, homograft, microcomputerized tomography

Heart valve replacement is one of the most common surgical interventions in cardiac health care.<sup>1–3</sup> The implantation of mechanical or biological prostheses is currently state of the art in this field.<sup>4</sup> However, both types of implants have several limitations that affect the patient's quality of life.<sup>5</sup> Biological

substitutes tend to degenerate resulting in loss of function, thus indicating reoperation. Mechanical heart valves require a life-long oral anticoagulation therapy and can be accompanied by severe complications.<sup>6–10</sup> The field of tissue engineering gives hope to solve the deficiencies of recent heart valve prostheses. The variety of approaches to develop tissue-engineered heart valve prostheses is large. The promising approaches are the seeding of decellularized porcine or human heart valves and the application of synthetic materials such as polyurethane as scaffold materials.<sup>11–13</sup> Seeding is most frequently achieved using vascular or stem cells<sup>14,15</sup> Seeding scaffolds with autologous cells has the advantage of thrombogenicity and immunogenicity when implanted.<sup>16</sup> Decellularization success and seeding efficiency must be visualized in an attempt to develop quality control in tissue engineering. Usual techniques for validating cell adhesion to constructs are scanning electron microscopy (SEM) and immunohistochemistry (IHC). However, these procedures require invasive sampling and are, therefore, useless for later clinical application.

We suggest microcomputed tomography ( $\mu$ -CT) as a new high-resolution, noninvasive method for feasibility testing of seeded heart valve.<sup>17</sup> Computed tomography was introduced into clinical practice in 1972.<sup>18</sup> This imaging technology enables the generation of three-dimensional images by computer-based stacking of two-dimensional x-ray scans after axial rotation around a sample.<sup>19</sup> Today CT is used in material testing destruction-free examination of archeological troves, in veterinary medicine, and most of all in human medical diagnostics.<sup>17,20–23</sup> The spatial resolution of  $\mu$ -CT is 5–50  $\mu$ m; this is up to 66-fold more precise than the resolution achieved by conventional CT in the clinical setting implementation (330  $\mu$ m).<sup>24</sup> Therefore, the aim of this study was to evaluate the feasibility of using  $\mu$ -CT scanning as a noninvasive evaluation method for tissue-engineering applications, especially pertaining to heart valve constructs.

### Materials and Methods

#### Heart Valve Fixation

The aortic walls of the heart valves were sutured (Supolene suture, Resorba Wundversorgung GmbH & Co. KG, Nürnberg, Germany) to the base ring of special Teflon fixation units (manufactured in-house). The units consisted of two circular plates (outer diameter  $d_o = 4.8$  cm, inner diameter  $d_i = 2.0$  cm) connected by four struts (height  $h = 4.9$  cm,  $d = 0.6$  cm) to avoid heart valve deformation during further processing.

From the \*Department of Cardiac Surgery, Medical Center Munich University, Munich, Germany; †Chair of Ceramic Materials Engineering, University of Bayreuth, Bayreuth, Germany; and ‡Institute of Textile Technology and Process Engineering, Denkendorf, Germany.

Submitted for consideration February, 2012; accepted for publication in revised form November, 2012.

Disclosure: The authors have no conflicts of interest to report.

Reprint Requests: Bassil Akra, University of Munich Hospital, Department of Cardiac Surgery, Laboratory for Tissue Engineering, Marchioninstr. 15, 81377 Munich, Germany. Email: bassil.akra@med.uni-muenchen.de.

Copyright © 2013 by the American Society for Artificial Internal Organs

DOI: 10.1097/MAT.0b013e31827db6b6



### Heart Valve Types and Preparation

**Polyurethane heart valve.** Aortic polyurethane heart valves (PUHVs) (h = 55 mm, d = 18 mm) were manufactured by ITV-Denkendorf using a polyurethane spraying technique (patent DE 28 06 030 C2). Randomly oriented polyurethane (PU) fibers were measured to have diameters between 100 nm and 550 nm. The fibers formed a sheet with a thickness of 0.3 mm. For seeding purpose, PUHV was  $\gamma$ -sterilized at 10 kGy according to a certified sterilization procedure.

**Homograft.** After aortic homograft (h = 50 mm, d = 19 mm) thawing in 56°C warm phosphate-buffered saline (PBS) (Biochrom AG, Berlin, Germany), cryoprotectiva were removed by washing once with PBS and once with M199 (Biochrom AG) at 56°C. The homograft was stored for 24 hours in M199 and was decellularized by treatment of the valve with 0.5% sodium dodecyl sulfate and 0.5% sodium deoxycholate (Sigma-Aldrich Chemie GmbH, Steinheim, Germany) dissolved in PBS for 24 hours at room temperature (RT). This was followed by six 24-hour washing steps in which the valves were washed in PBS at RT to remove cellular remnants and chemicals to which the valves were previously exposed. The homograft was incubated for 24 hours in M199 medium at RT before cell seeding.

**Biological heart valve.** Glutaraldehyde fixation of porcine heart valve (h = 45 mm, d = 19 mm, Medtronic GmbH, Meerbusch, Germany) was neutralized by 10% citric acid (Merck KGaA, Darmstadt, Germany) in distilled water for 5 minutes at RT. For a neutral pH, biological heart valve (BHV) was washed thrice with PBS for 15 minutes. The heart valve was stored in endothelial cell growth medium (Promocell GmbH, Heidelberg, Germany) containing 20% fetal calf serum (FCS, Lonza AG, Verviers, Belgium) for 1 week at 37°C/5% CO<sub>2</sub>. Decellularization of BHV was analogously performed as described for homograft decellularization.

### Cell Isolation and Cell Culture

Endothelial cells (ECs) and fibroblasts (FBs) were isolated from left-over human saphenous vein segments harvested for coronary artery bypass grafting. Samples were taken from the patients only after their informed consent. Veins were stored in M199 medium at 4°C for a maximum of 5 days until further processing. The vein segments were cannulated and washed with M199 medium containing 0.2% heparin (5000 I.E., Ratiopharm GmbH, Ulm, Germany) and 0.5% gentamycin (10 mg/ml, Biochrom AG). For EC isolation, veins were filled with 1 mg/ml collagenase II (280 u, Worthington Biochemical Corporation, NJ) and incubated for 30 minutes at 37°C/5% CO<sub>2</sub>. After EC isolation, veins were incubated with 2 mg/ml collagenase II for 40 minutes at the same conditions for FB isolation. After each incubation step, collagenase cell solutions were rinsed out of the vein, centrifuged for 7 minutes at 500 rpm, and cultivated in the respective growth media (endothelial cell growth medium: ECGM; fibroblast growth medium: FGM; PromoCell GmbH, Heidelberg, Germany) in culture flasks (12.5 cm<sup>2</sup>, Becton Dickinson GmbH, Heidelberg, Germany) at 37°C/5% CO<sub>2</sub>. The medium was partially or completely exchanged every 2–3 days. Cells were passaged at confluency.

### Heart Valve Seeding and Cultivation

Heart valve scaffolds were first seeded with FBs, followed by colonization with ECs. For both cell types, a seeding density

of  $1.5 \times 10^6$  cells/cm<sup>2</sup> was used. To ensure a uniform cell distribution, the seeding procedure was performed in a specially designed rotating seeding device (running phase: 2.5 minutes, holding phase: 30 minutes) for 24 hours at 37°C/5% CO<sub>2</sub>. After FB seeding, the seeded heart valves were cultivated for 7 days at 37°C/5% CO<sub>2</sub> under static conditions. Medium was exchanged every 2–3 days. After this initial cultivation period, FB-seeded heart valves were analogously seeded with ECs. For further analysis, samples were taken from the supravalvular region of the aortic wall as well as from the valvular leaflets. Samples were taken from native, decellularized, and reseeded valves. The samples from the reseeded valves were taken upon completion of EC seeding.

### Phenotypic Cell Characterization

Phenotypic determination of FBs and ECs was performed by morphologic classification using phase contrast microscopy (Carl Zeiss Mikrolmaging GmbH, Göttingen, Germany). Fibroblasts were recognized by their elongated spindle-like appearance.<sup>25</sup> Endothelial cells were identified by their typical cobblestone morphology.<sup>26</sup> Additionally, the cell types were verified by immunocytochemistry. Cells were seeded and cultured on culture slides (eight-chamber; BD Biosciences, Bedford). At confluency cells were fixed and stored in 96% ethanol (Merck KGaA) at –80°C for a minimum of 48 hours. Slides were washed three times with PBS (Biochrom AG) and endogenous peroxidase activity was subsequently blocked via treatment with hydrogen peroxide (Merck KGaA). Primary antibodies for CD31 (ECs; 0.14 µg/ml, Dianova GmbH, Hamburg, Germany) and TE-7 (FBs; 0.67 µg/ml, Millipore Corp., BioScience Division, Temecula, CA) were applied, respectively, and the slides were incubated for 30 minutes. After washing, the slides were covered with biotinylated link (HRP Detection System, Biozol GmbH, Eching, Germany) according to manufacturer's protocol and were incubated for 10 minutes. Cells were labeled with HRP streptavidin for 10 minutes and subsequently incubated with AEC-peroxidase substrate (Vector Laboratories, Inc., Burlingame, CA) for another 10 minutes. All steps were performed at RT. Cell nuclei were stained with hemalaun (1:4 in PBS; Merck KGaA). A bright field microscope (Carl Zeiss Mikrolmaging GmbH) was used for microscopical evaluation.

### Microcomputerized Tomography

**Scanning procedure.** For transport and  $\mu$ -CT scanning, heart valve scaffolds were sutured to Teflon units and placed in a custom-fit glass container. Microcomputed tomography scanning of BHV was performed at RT before incubating the biological valve in cell medium by using the original glutaraldehyde-fixation solution, after decellularization and incubation in M199 medium, and finally after seeding and incubation in ECGM. The homograft was scanned at RT after thawing in M199 medium, after decellularization and incubation in M199 medium, and finally after seeding and incubation in ECGM. In the case of PU, scans were performed at RT on a dry scaffold, after seeding and incubating the scaffold for 7 days in FGM, and finally after seeding and incubating the scaffold for 7 days in ECGM. To obtain the necessary high-contrast images, approximately 90% of the medium was drained from the glass container, and 10% was left to avoid dehydration of the heart valve scaffolds during scanning.



Microcomputed tomography analysis allowed a noninvasive analysis of several positions of the scaffold heart valve types. The tomographic investigations were performed using a  $\mu$ -CT machine of the type HR-150-03. The reconstructed complete volume of the heart valve consisted of  $2048^3$  voxels with an edge length of  $35\ \mu\text{m}$  and was reconstructed from 1,600 individual x-ray radiography images. The detector used was a Perkin-Elmer flat panel detector type XRD 1621-CT3 consisting of  $2048^2$  pixels. The x-ray source used a tungsten target and was powered at 120 kV with a current of  $150\ \mu\text{A}$ , generating a polychromatic x-ray spectrum. The total exposure time was 35 minutes. In addition, a set of region of interest (ROI) measurements were performed to determine the thickness of the cellular coverage. The ROI procedure analyzes a specific small volume of a sample at very high resolution, ignoring the remaining volume. The procedure consists of an off-center measurement, with a focus on one specific region of the volume. A  $360^\circ$  rotation was performed around the ROI, resulting in high-resolution, high-contrast volumetric images of  $9\ \mu\text{m}$ , allowing the detection of thin cell layers.

For x-ray observation, heart valves do not need to be removed from the sterile container, offering an analysis under sterile conditions.

**Image generation.** The reconstruction of cross-sections was performed using a reconstruction algorithm developed by the Fraunhofer Institute EZRT, Fürth, Germany. Structural analysis and three-dimensional visualization were carried out using the visualization software VG-Studio Max, version 2.1, with an adapted wall-thickness algorithm developed by the University of Bayreuth. The algorithms used to determine the wall thickness are based on topographic algorithms. The algorithm first determines the exact surfaces of the valve (based on gray-scale gradients of voxels), resulting in two topographic data sets (e.g., inside and outside). For determining the actual thickness at a certain position, both topographic data sets are compared and used to calculate a local minimal distance vector at each position. The vector provides information on the direction as well as the local wall thickness. This approach is applied for each individual CT measurement. Geometric changes in the object are automatically correlated by applying the minimum distance method—any changes in the overall geometry result in a new set of vectors that include the geometric information and the new wall thickness, allowing for a direct comparison of different CT measurements.

The used x-ray tension was adjusted to 120 kV at  $150\ \mu\text{A}$ . The high resolution achieved ( $35\ \mu\text{m}$ ) resulted in commendable accuracies of  $0.02\ \text{mm}^2$  for the determination of total surface area and  $0.1\ \text{mm}^3$  for the determination of total volume. For our application, total volume was defined as the volume of the complete tissue-engineered structure itself, the lumen of the valve was excluded from this calculation. To determine the thickness of the cellular coverage, regions of the heart valve scaffolds were additionally subjected to an ROI analysis with a resolution of  $9\ \mu\text{m}$ .

#### Scanning Electron Microscopy

To detect surface topography of synthetic, biological, and human heart valve scaffolds in native, decellularized, and seeded status, the samples were analyzed by SEM. Specimens were fixed in a solution of 456 ml aqua bidistilled (Ampuwa, Fresenius Kabi Deutschland GmbH, Bad Homburg v.d. H.,

Germany), 0.75 ml 1 N hydrochloric acid (Titrisol, Merck KGaA), 43.5 ml glutaraldehyde, and 5.65 g sodium cocodylate trihydrate (Sigma-Aldrich Chemie GmbH) at  $4^\circ\text{C}$  for a minimum of 48 hours. The samples were dehydrated in an ascending ethanol series (30%, 50%, 70%, and 95%) and subsequently in 100% acetone. The specimens were dried by critical point drying, sputtered with gold for 180 seconds at  $10^{-5}$  mbar, and analyzed using SEM (EVO LS 10; Carl Zeiss MicroImaging GmbH).

#### Immunohistochemistry

Immunohistochemical analysis was performed to detect ECs and FBs after seeding as well as to evaluate the native and decellularized biological valves. Samples from native, decellularized, and seeded heart valves were fixed in 4% formaldehyde (Microcos GmbH, Garching, Germany) for 10 days at  $4^\circ\text{C}$ . Fixed samples were paraffin-embedded and sectioned at  $10\ \mu\text{m}$ . Slices were stained for CD31 (ECs;  $0.09\ \mu\text{g}/\text{ml}$ ; Dianova GmbH) and TE-7 (FBs;  $2\ \mu\text{g}/\text{ml}$ , Millipore Corp., BioScience Division). Endogenous peroxidase activity was blocked by treatment with hydrogen peroxide and then the samples were incubated with primary antibody overnight at  $4^\circ\text{C}$ . All the following steps were performed at RT. After washing with PBS, the samples were covered with biotinylated link for 10 minutes, and HRP Streptavidin label for 10 minutes according to the manufacturer's protocol (HRP Detection kit, Biozol GmbH), followed by chromogen labeling for 10 minutes using AEC peroxidase substrate kit (Vector Laboratories, Inc.). Cell nuclei were stained with hemalaun (1:4 in PBS; Merck KGaA). Controls for nonspecific binding of the chromogen label were performed by excluding the primary antibody. Samples were observed using bright field microscopy (Carl Zeiss MicroImaging GmbH).

#### Results

The evaluation of aortic heart valve in different states (native, decellularized, and seeded) was successfully achieved via  $\mu$ -CT scanning. To this end, BHV, homograft, and PUHV were tested by  $\mu$ -CT, with special focus on the effect of seeding on values calculated from  $\mu$ -CT data. Microcomputed tomography analysis of homograft aortic heart valves was performed analogously and showed similar results (data not shown).

#### Topology and Seeding Analysis of BHV and Homograft

Scanning electron microscopy analysis (Figure 1A–C) of native (A) and in particular of the decellularized (Figure 1B) BHV samples showed randomly orientated fibers resulting in a rough surface. Decellularized BHV demonstrated a confluent cell layer after seeding procedure (Figure 1C). Moreover, typical cobblestone morphology indicated an EC layer. Immunohistochemistry analysis (Figure 1D–F) of decellularized homograft (Figure 1D) did not show the presence of vascular cells. In contrast, reseeded homograft revealed a positive staining for CD31 and TE-7, indicating a confluent coverage with FBs (Figure 1E, brown) and ECs (Figure 1F, brown). Cell nuclei were stained with hemalaun (Figure 1D–F, purple).

#### Total Volume and Surface Area of BHV

Microcomputed tomography scanning of heart valve scaffolds was performed as described in the Materials and Methods

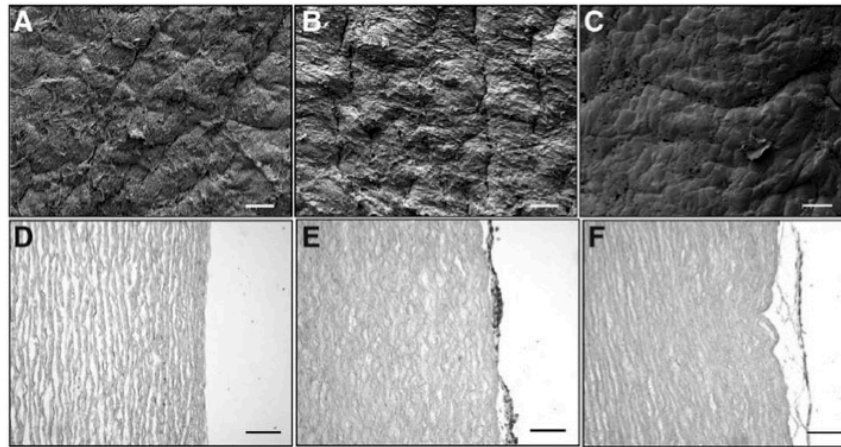


**Figure 1.** Scanning electron microscopy (SEM) and immunohistochemistry (IHC) analysis of biological heart valve (BHV) and homograft in different states of processing. SEM analysis of native (A) and decellularized (B) samples of BHV showed disordered fibers resulting in a rough surface. In contrast, reseeded samples (C) revealed a confluent endothelial layer. The acellularity of decellularized homograft samples was confirmed by IHC (D). In contrast, stainings reveal various layers of fibroblasts (FBs) (E; TE-7, brown) and endothelial cells (ECs) (F; CD31, brown) after seeding of the homograft. Cell nuclei were stained with hemalaun (D–F, purple). These are representative images of three independent experiments. Scale bars: A, C = 30  $\mu\text{m}$ ; B = 40  $\mu\text{m}$ ; D–F = 100  $\mu\text{m}$ .

section. Microcomputed tomography analysis allowed a numerical determination as well as a graphical representation of total volume and surface area. Microcomputed tomography images in **Figure 2** show cross- (A–C) and longitudinal (D–F) of native, decellularized, and reseeded BHV. A closer look revealed an intense thickening of the valvular leaflets (**Figure 2C**, arrows) and the aortic wall (**Figure 2F**, arrows) in the reseeded state.

Quantitative analysis revealed a 0.5% decrease in total volume and 0.2% increase in surface area after decellularization of BHV. In contrast, the analysis of seeded BHV after successful decellularization revealed an 8.6% increase in volume and a 0.3% decrease in surface area. Single values are summarized in **Table 1**.

#### Thickness Alteration of BHV

Changes in thickness during BHV processing were determined by the comparison of reconstructed cross-sections of

the same valve and the same section plane in different states. **Figure 3** demonstrates the native (A), decellularized (B), and reseeded (C) states of BHV. The four circular areas represent the Teflon struts of the heart valve fixation unit. At four positions, thicknesses are exemplary determined. The native state of BHV (**Figure 3A**) revealed a decrease in thickness compared with the decellularized state (**Figure 3B**). The analysis of the reseeded state (**Figure 3C**) compared with the decellularized and native state shows an increase in thickness at corresponding positions.

#### Wall Thicknesses of BHV

Wall thicknesses were volumetrically determined by using tangential analysis of the raw data. The thicknesses of the leaflets (**Figure 4A–C**) and of the aortic regions (**Figure 4D–F**) in native, decellularized, and reseeded status are color coded. Different

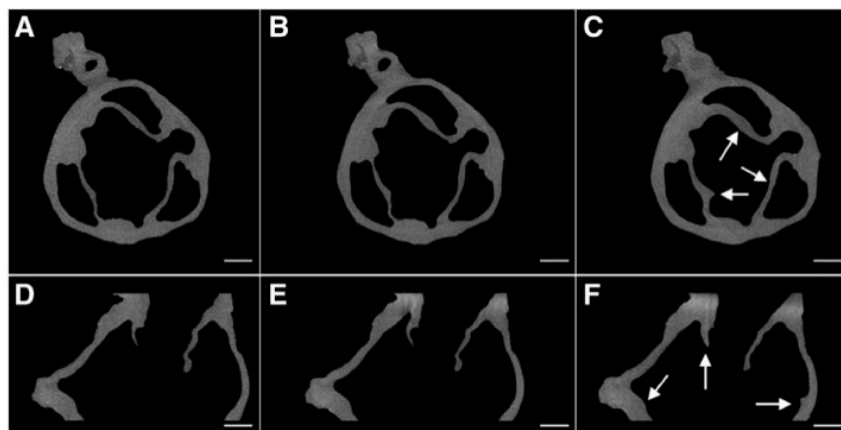


**Figure 2.** Cross- (A–C) and longitudinal (D–F) sections of native, decellularized, and reseeded biological heart valve from micro-computed tomography scan. Reseeded samples showed a distinct increase in the thickness of the valvular leaflets (C, arrows) and the aortic wall (F, arrows). These are representative images of three independent experiments. Scale bars: A–C = 5 mm; D–F = 10 mm.



**Table 1. Total Volume and Surface Area of BHV in Different States of Processing\***

BHV State	Total Volume (mm <sup>3</sup> )		Total Surface (mm <sup>2</sup> )	
Native	2197		4813	
Decellularized	2185	-0.5%	4904	+0.2%
Reseeded	2360	+8.6%	4775	-0.3%

Quantitative microcomputed tomography analysis demonstrated a decrease in volume and simultaneous increase in surface area after decellularization. Reseeding of decellularized BHV resulted in an expansion of volume accompanied with reduction of surface area. These are representative results of three independent experiments. BHV, biological heart valve.

levels of magnification are used for displaying the leaflets than for displaying the aortic regions to improve the visualization of changes in thickness. Increasing levels of thickness are indicated by red, green then blue coloring. Native (Figure 4A) and decellularized leaflets (Figure 4B) as well as native (Figure 4D) and decellularized aortic regions (Figure 4E) showed comparable wall thicknesses between states of processing (region specific). In contrast, after seeding a distinct thickening of the leaflet (Figure 4C) and the aortic regions (Figure 4F) was observed.

#### Thickness Variance of PUHV

As described in the Materials and Methods section, the algorithms used to determine the wall thickness are based on topographic algorithms. Changes in thickness of seeded PUHV compared with native status are demonstrated in three-dimensional graphics (Figure 5). Thickness variances are color coded; increasing levels of thickness are indicated by green, yellow, and then pink coloring. Decreasing levels of thickness are by turquoise and then blue coloring. In a vascular view (Figure

5A), a ventricular view (Figure 5B), and a coronal view (Figure 5C), leaflets showed a thickening of up to 0.40 mm (pink). Analysis of the aortic wall revealed a thickening up to 0.16 mm after seeding (green), with several regions having thickened by up to 0.32 mm (red) variance.

In addition, Figure 6 demonstrates the cumulated variance distribution of seeded PUHV compared with native PUHV. The histogram correlates the absolute deviation to the surface area and revealed a thickening of up to 0.210 mm at 90% of the surface. Ten percentage of the surface showed a thickening between 0.210 mm and 0.400 mm, proving colonization at every position of the PUHV.

Furthermore, Figure 7 shows ROI measurements of FB-seeded (A) and FB- and EC-seeded (B) PU scaffolds. At eight positions in each case, thicknesses are exemplary determined. The different contrast of the scaffold and the cellular coverage clearly demonstrate that a cell layer is available. Moreover, the FB- and EC-seeded (Figure 7B) scaffold revealed a thicker cellular coverage than the FB-seeded (Figure 7A) scaffold, explainable by the presence of EC. Immunohistochemistry analyses support this declaration as well. Staining for TE-7 of FB-seeded (Figure 7C) and staining for CD31 of FB- and EC-seeded (Figure 7D) scaffolds demonstrated the presence of FB (Figure 7C; brown) and a thin endothelial lining (Figure 7D; brown), respectively. Cell nuclei were stained with hemalaun (Figure 7C–D; purple).

#### Discussion

Conventional heart valve replacement using synthetic materials or unseeded biological valves is limited by viability, durability, and thrombogenicity. Tissue-engineered heart valves seeded with autologous cells constitute a promising alternative because of their potential antithromobogenicity effect and

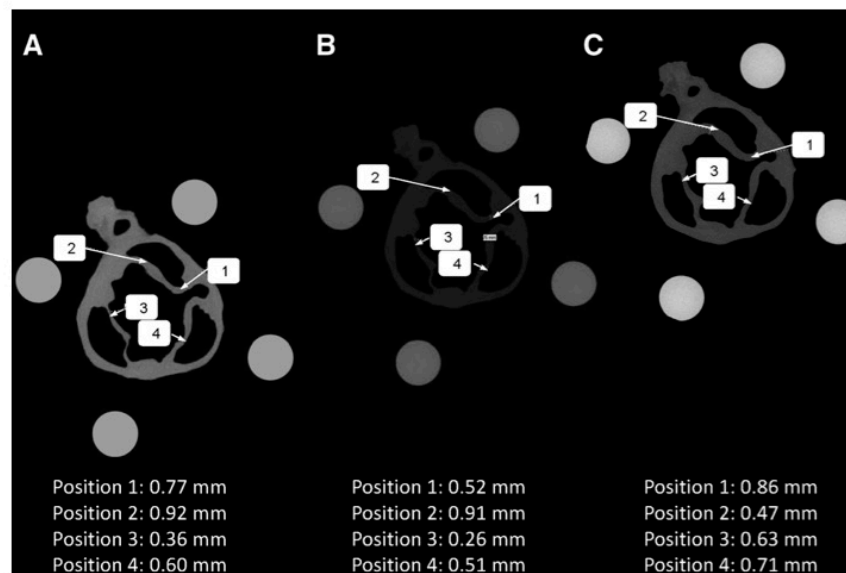


**Figure 3.** Thickness alteration of biological heart valve (BHV) in different processing states. The comparison of the native (A) and the decellularized (B) state of BHV shows a decrease in thickness at four exemplary positions. In contrast, the analysis in the reseeded state (C) compared with the decellularized and native state revealed an increase in thickness.

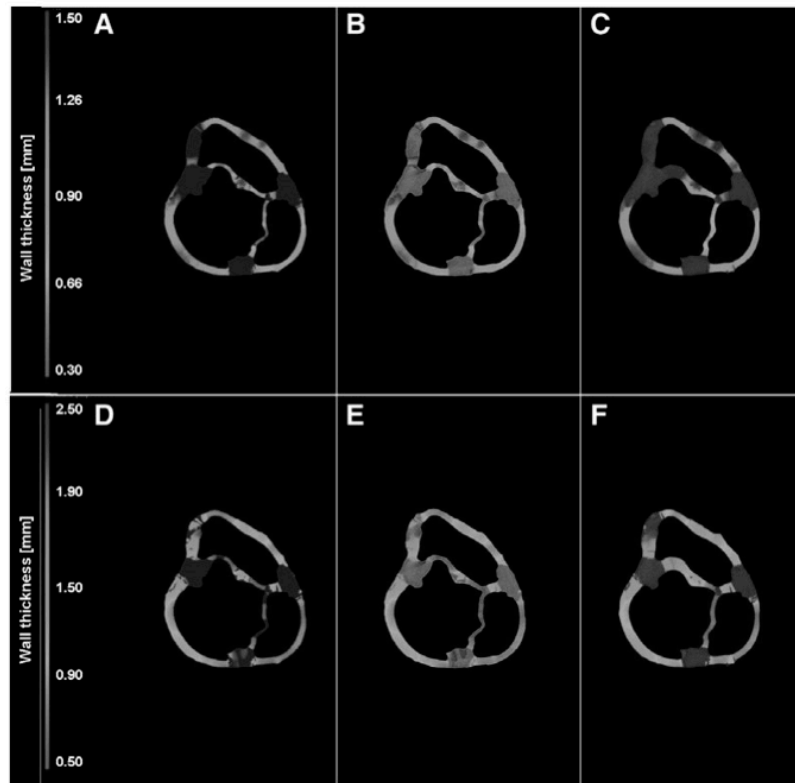


**Figure 4.** Wall thicknesses of biological heart valve (BHV) in different processing states. Micro-computed tomography analysis virtually generated cross-sections of BHV, illustrating the wall thickness in a color-coded manner. Different levels of magnification are used for displaying the valvular leaflets than for displaying the aortic wall regions to improve the visualization of changes in thickness in the different regions. Native (A) and decellularized leaflets (B) as well as native (D) and decellularized aortic regions (E) showed comparable wall thicknesses between states of processing (region specific). In contrast, reseeded results in a thickening of leaflets (C) and aortic wall regions (F). These are representative images of three independent experiments.

good immunocompatibility. An effective quality control of heart valve implants is indispensable for the preoperative evaluation of tissue-engineered valves planned for implantation.

Despite the successful application of SEM and IHC for the assessment of seeding efficiency, these procedures are inappropriate for quality control of valves produced for implantation

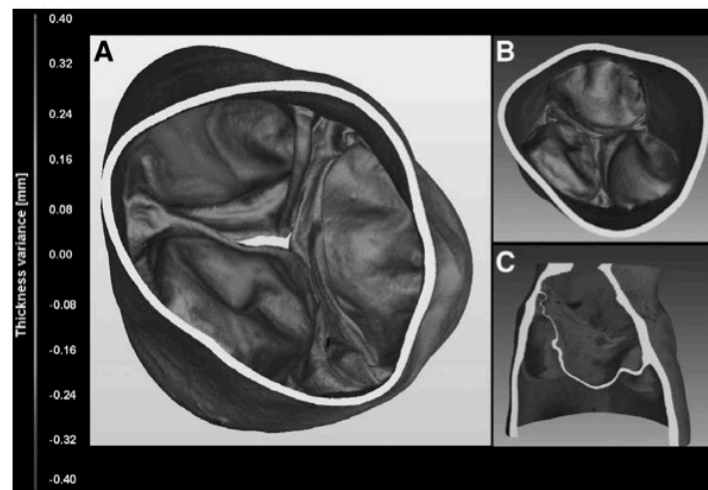


**Figure 5.** Thickness changes of polyurethane heart valve (PUHV) after seeding. Three-dimensional graphics represent changes in thickness of seeded PUHV compared with native PUHV by color coding. The vascular view (A), the ventricular view (B), and the coronal view (C) reveal a clear thickening of the valvular leaflets and of the aortic wall (0.40 mm: pink; 0.32 mm: red,  $\leq 0.16$  mm: green). These are representative images of three independent experiments.



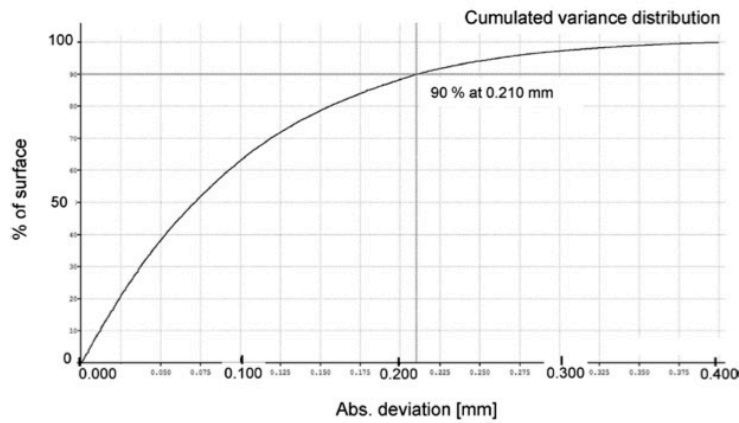


**Figure 6.** Cumulated variance distribution of seeded polyurethane heart valve (PUHV) compared to native PUHV. Ninety percent of the surface revealed a thickening of up to 0.210mm. Ten percent of the surface showed a thickening between 0.210mm and 0.400mm, indicating a total colonization of the PUHV. This is a representative histogram of three independent experiments.

because of the invasive nature of this method. Here, we provided evidence that  $\mu$ -CT scanning is an attractive method for the non-invasive evaluation of tissue-engineered heart valve constructs.

Microcomputed tomography as a modern imaging modality enables the visualization of tissue constructs with highly complex geometries, for example, the meniscus of a knee.<sup>27</sup>

In fact for several years,  $\mu$ -CT has been a standard tool for bio-mechanical evaluation and optimization in orthopedic surgery. Jacques *et al.*<sup>28</sup> even examined the postimplantation adaptation of bone tissue by  $\mu$ -CT. The ability of  $\mu$ -CT to visualize complex geometries precisely as tested in orthopedics is in line with results generated in this study. We successfully imaged

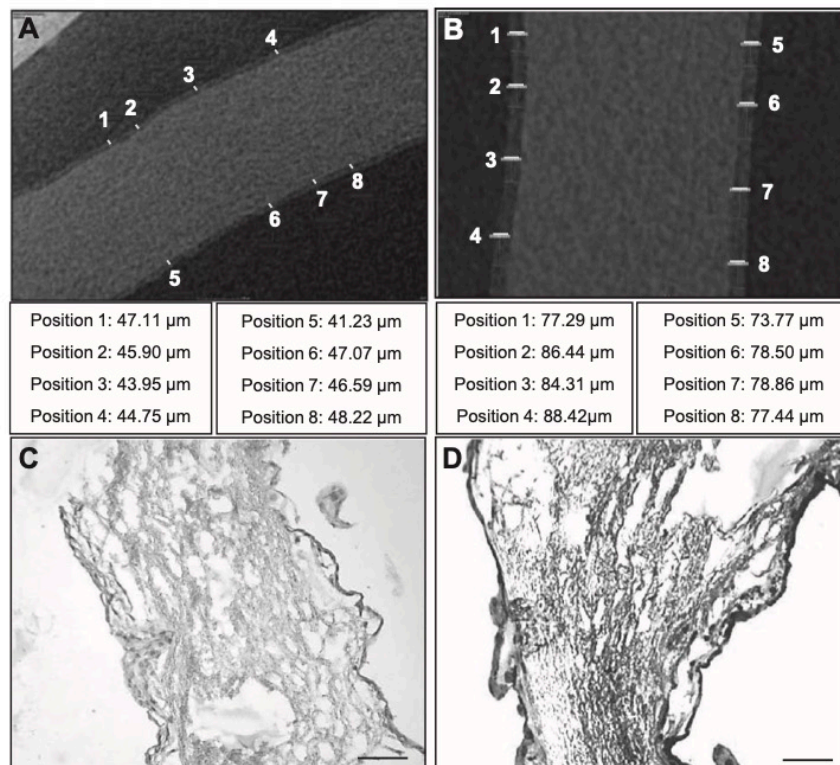


**Figure 7.** Region of interest measurements of seeded polyurethane (PU) scaffolds. The thickness of the cellular coverage of fibroblasts (FB)-seeded (A) as well as FB- and endothelial cells (EC)-seeded (B) PU scaffolds were exemplary compared at eight positions. The FB- and EC-seeded (B) scaffold revealed a thicker cell layer than the FB-seeded (A) scaffold, indicating EC presence. Immunohistochemistry analyses also demonstrated a FB layer (C; TE-7, brown) with a thin endothelial lining (D; CD31, brown). Cell nuclei were stained with hemalaun (C–D; purple). Scale bars: C = 125  $\mu$ m; D = 350  $\mu$ m.

the complex structure of our tissue-engineered heart valves. Further studies regarding the effect of  $\mu$ -CT on the cell viability should be carried out. Seeded heart valves were not maintained under physiological conditions such as 37°C and 5% CO<sub>2</sub> during scanning. These conditions were classified as not required because of the short evaluation time in sterile containers. However, 10% of media was left in the glass container to avoid dehydration of the heart valve scaffolds during scanning.

We determined that there are many aspects that can be evaluated by  $\mu$ -CT scanning. Besides the calculation of surface area and total volume, overlaying cross-sections of the valve at different states of processing provides important information about region-specific alterations of the valves' thickness. A deviation of cell layer thickness has been specially detected on the upper side of the cusps of the scaffold. This deviation is probably related to the seeding procedure. Cells are normally added into a seeding cylinder containing the scaffold. This process leads probably to the formation of a cell clump on the upper side of the cusps. It is clearly not a deviation because the three-dimensional images are based on approximately 1,300 images/side and valves were primarily fixed on Teflon support system for stabilization.

The results of REM analysis showed a confluent EC layer on the surface of the BHV. Moreover, the quantitative calculation enabled the definition of the minimum and maximum thickness of the seeded cell layer. This is applicable to decellularized BHV, decellularized homograft, and PUHV, and facilitates the verification of the success of different tissue engineering processes.

Other common methods for precise imaging are high-frequency ultrasound (HFU) and magnetic resonance imaging (MRI) of ferrumoxide-labeled cells.<sup>29,30</sup> However, HFU and MRI only achieve a maximum resolution of 100  $\mu$ m.<sup>30,31</sup> In contrast, current  $\mu$ -CT scanners provide a resolution of 35  $\mu$ m, thus making  $\mu$ -CT nearly three times more accurate than HFU and MRI.<sup>32</sup> The algorithm used in this study to determine the surface topography includes a large number of neighboring voxels, resulting in topographic surface information with improved resolution. Typically, the topographic data gained from a 35- $\mu$ m voxel resolution are accurate to at least a factor of four, providing an accurate topographic resolution of less than 10  $\mu$ m. Using ROI technique resulted in very highly detailed images with a 9- $\mu$ m voxel resolution *a priori* and *a posteriori*, allowing the detection of thin cell layers. An even higher detailed volume using ROI measurement (2- $\mu$ m voxel resolution) is possible using a tailored glass container for sterile  $\mu$ -CT scanning. This would be necessary to reduce the distance between the x-ray tube and the container to the minimum.

Furthermore, HFU is more adequate for use in the imaging of fine tissue structures,<sup>29</sup> than for creating virtual three-dimensional models. Magnetic resonance imaging has several drawbacks. For example, the possibility of the dissolution of ferrum particles after implantation of an imaged construct could put patients at medical risk.<sup>33</sup> A further disadvantage pertains to the labeling of the cells for imaging. For MRI visualization, cells of tissue constructs must be labeled with magnetic particles such as ferrumoxide.<sup>33</sup> These foreign molecules may potentially affect cell morphology, viability, and proliferation. If used as a method for preoperative valve evaluation, altering these cellular characteristics could negate the benefit aimed for by implanting a tissue-engineered heart valve. The

mentioned MRI linking system furthermore typically makes genetic manipulation of the cells necessary, to provide a counterpart for linking of ferrumoxide particles. Immunoprecipitation labeling systems are alternatives that do not necessitate genetic engineering.<sup>34</sup> However, such labeling systems result in the distortion of cell morphology and in the alteration of intracellular processes, making this an unattractive approach.

In conclusion, we have demonstrated that  $\mu$ -CT enables a quantitative calculation and quality control of seeding steps for tissue-engineered heart valve creation. Therefore, we are convinced that  $\mu$ -CT represents an effective, noninvasive imaging modality for the preoperative evaluation of tissue-engineering constructs.

#### Author Contributions

N.H. and T.H. have contributed equally to this study.

#### Acknowledgments

The authors thank Medtronic, Inc. for all their support. They also thank Kamil D. Szeplanski for the microcomputer tomography measurements and analyses.

#### References

1. Goodney PP, O'Connor GT, Wennberg DE, Birkmeyer JD: Do hospitals with low mortality rates in coronary artery bypass also perform well in valve replacement? *Ann Thorac Surg* 76: 1131–6; discussion 1136, 2003.
2. Prager RL, Fischer CR, Kong B, et al: The aortic homograft: Evolution of indications, techniques, and results in 107 patients. *Ann Thorac Surg* 64: 659–63; discussion 663, 1997.
3. Belcher P, Ross D: Aortic root replacement—20 years experience of the use of homografts. *Thorac Cardiovasc Surg* 39: 117–122, 1991.
4. Filová E, Straka F, Mirejovský T, Masín J, Bacáková L: Tissue-engineered heart valves. *Physiol Res* 58 Suppl 2: S141–S158, 2009.
5. Sacks MS, Schoen FJ, Mayer JE: Bioengineering challenges for heart valve tissue engineering. *Annu Rev Biomed Eng* 11: 289–313, 2009.
6. Chen RDJ, Nihill MD, Denton A, Cooley MD: Early degeneration of porcine xenograft valve in pediatric patients who have undergone apico-aortic bypass. *Tex Heart Inst J* 9: 41–47, 1982.
7. Hoffmann G, Lutter G, Cremer J: Durability of bioprosthetic cardiac valves. *Dtsch Arztebl Int* 105: 143–148, 2008.
8. Flanagan TC, Pandit A: Living artificial heart valve alternatives: A review. *Eur Cell Mater* 6: 28–45; discussion 45, 2003.
9. Rahimtoola SH: Choice of prosthetic heart valve for adult patients. *J Am Coll Cardiol* 41: 893–904, 2003.
10. Campos NL, Andrade RR, Silva MA: Oral anticoagulation in carriers of mechanical heart valve prostheses: experience of ten years. *Rev Bras Cir Cardiovasc* 25: 457–465, 2010.
11. Knight RL, Booth C, Wilcox HE, Fisher J, Ingham E: Tissue engineering of cardiac valves: re-seeding of acellular porcine aortic valve matrices with human mesenchymal progenitor cells. *J Heart Valve Dis* 14: 806–813, 2005.
12. Elkins RC DP, Goldstein S, Walsh SP, Black KS: Decellularized human valve allografts. *Cardiac Bioprostheses* 71: 428–432, 2001.
13. Mackay TG, Wheatley DJ, Bernacca GM, Fisher AC, Hindle CS: New polyurethane heart valve prosthesis: Design, manufacture and evaluation. *Biomaterials* 17: 1857–1863, 1996.
14. Lichtenberg AT, Cebotari S, Ringes-Lichtenberg S, et al: In vitro re-endothelialization of detergent decellularized heart valves under simulated physiological dynamic conditions. *Biomaterials* 27: 4221–4229, 2006.



15. Wu K, Liu YL, Cui B, Han Z: Application of stem cells for cardiovascular grafts tissue engineering. *Transpl Immunol* 16: 1–7, 2006.
16. Schmidt D, Stock UA, Hoerstrup SP: Tissue engineering of heart valves using decellularized xenogeneic or polymeric starter matrices. *Philos Trans R Soc Lond, B, Biol Sci* 362: 1505–1512, 2007.
17. Ritman EL: Current status of developments and applications of micro-CT. *Annu Rev Biomed Eng* 13: 531–552, 2011.
18. Kalender WA: X-ray computed tomography. *Phys Med Biol* 51: R29–43, 2006.
19. Herman GT (ed): *Fundamentals of Computerized Tomography: Image Reconstruction from Projection*. London, Springer, 2009.
20. Steinhäuser-Andresen S, Detterbeck A, Funk C, et al: Pilot study on accuracy and dimensional stability of impression materials using industrial CT technology. *J Orofac Orthop* 72: 111–124, 2011.
21. Morigi MP, Casali F, Bettuzzi M, Brancaccio R, D’Errico V: Application of X-ray Computed Tomography to Cultural Heritage diagnostics. *Applied Physics A: Materials Science & Processing* 100: 653–661, 2010.
22. Holdsworth DW, Thornton MM: Micro-CT in small animal and specimen imaging. *Trends in Biotechnology* 20: 34–39, 2002.
23. Kline TL, Zamir M, Ritman EL: Relating function to branching geometry: A micro-CT study of the hepatic artery, portal vein, and biliary tree. *Cells Tissues Organs (Print)* 194: 431–442, 2011.
24. Mollet NR, Cademartiri F, van Mieghem CA, et al: High-resolution spiral computed tomography coronary angiography in patients referred for diagnostic conventional coronary angiography. *Circulation* 112: 2318–2323, 2005.
25. Mauch C, Hatamochi A, Scharffetter K, Krieg T: Regulation of collagen synthesis in fibroblasts within a three-dimensional collagen gel. *Exp Cell Res* 178: 493–503, 1988.
26. Kubota Y, Kleinman HK, Martin GR, Lawley TJ: Role of laminin and basement membrane in the morphological differentiation of human endothelial cells into capillary-like structures. *J Cell Biol* 107: 1589–1598, 1988.
27. Ballyns JJ, Gleghorn JP, Niebrzydowski V, et al: Image-guided tissue engineering of anatomically shaped implants via MRI and micro-CT using injection molding. *Tissue Eng Part A* 14: 1195–1202, 2008.
28. Jaecques SV, Van Oosterwyck H, Muraru L, et al: Individualised, micro CT-based finite element modelling as a tool for bio-mechanical analysis related to tissue engineering of bone. *Biomaterials* 25: 1683–1696, 2004.
29. Hanwoo L: *High Frequency Ultrasound for Imaging and Characterization of Tissue Engineered Heart Valves*. University of Minnesota, Faculty of the graduate school, 2005.
30. Terrovitis JV, Bulte JW, Sarvananthan S, et al: Magnetic resonance imaging of ferumoxide-labeled mesenchymal stem cells seeded on collagen scaffolds-relevance to tissue engineering. *Tissue Eng* 12: 2765–2775, 2006.
31. Graham KC, Wirtzfeld LA, MacKenzie LT, et al: Three-dimensional high-frequency ultrasound imaging for longitudinal evaluation of liver metastases in preclinical models. *Cancer Res* 65: 5231–5237, 2005.
32. Engelke K, Karolczak M, Lutz A, Seibert U, Schaller S, Kalender W: [Micro-CT. Technology and application for assessing bone structure]. *Radiologe* 39: 203–212, 1999.
33. Terrovitis J, Stuber M, Youssef A, et al: Magnetic resonance imaging overestimates ferumoxide-labeled stem cell survival after transplantation in the heart. *Circulation* 117: 1555–1562, 2008.
34. Perea-Saveedra H: *Magnetic Vascular Engineering: Development And Validation*. Herzogenrath, Germany, Shaker, 2008.

## 7.10 Customized 3D-Printed Bioreactors for Decellularization – High Efficiency and Quality on a Budget (Grab et al., 2021)

- Maximilian Grab, Felix Stieglmeier, Jessica Emrich, Linda Grefen, Ariane Leone, Fabian König, Christian Hagl, Nikolaus Thierfelder



# Customized 3D printed bioreactors for decellularization—High efficiency and quality on a budget

Maximilian Grab<sup>1,2</sup> | Felix Stieglmeier<sup>1</sup> | Jessica Emrich<sup>1</sup> | Linda Grefen<sup>1</sup> |  
Ariane Leone<sup>1</sup> | Fabian König<sup>1,2</sup> | Christian Hagl<sup>1</sup> | Nikolaus Thierfelder<sup>1</sup>

<sup>1</sup>Department of Cardiac Surgery, Ludwig-Maximilian University, Munich, Germany

<sup>2</sup>Chair of Medical Materials and Implants, Technical University, Munich, Germany

## Correspondence

Maximilian Grab, Department of Cardiac Surgery, Ludwig-Maximilian University, Marchioninstr. 15, 81377 Munich, Germany.

Email: maximilian.grab@med.uni-muenchen.de

## Abstract

Decellularization (DC) of biomaterials with bioreactors is widely used to produce scaffolds for tissue engineering. This study uses 3D printing to develop efficient but low-cost DC bioreactors. Two bioreactors were developed to decellularize pericardial patches and vascular grafts. Flow profiles and pressure distribution inside the bioreactors were optimized by steady-state computational fluid dynamics (CFD) analysis. Printing materials were evaluated by cytotoxicity assessment. Following evaluation, all parts of the bioreactors were 3D printed in a commercial fused deposition modeling printer. Samples of bovine pericardium and porcine aortae were decellularized using established protocols. An immersion and agitation setup was used as a control. With histological assessment, DNA quantification and biomechanical testing treatment effects were evaluated. CFD analysis of the pericardial bioreactor revealed even flow and pressure distribution in between all pericardium. The CFD analysis of the vessel bioreactor showed increased intraluminal flow rate and pressure compared to the vessel's outside. Cytotoxicity assessment of the used printing material revealed no adverse effect on the tissue. Complete DC was achieved for all samples using the 3D printed bioreactors while DAPI staining revealed residual cells in aortic vessels of the control group. Histological analysis showed no structural changes in the decellularized samples. Additionally, biomechanical properties exhibited no significant change compared to native samples. This study presents a novel approach to manufacturing highly efficient and low budget 3D printed bioreactors for the DC of biomaterials. When compared to standard protocols, the bioreactors offer a cost effective, fast, and reproducible approach, which vastly improves the DC results.

## KEYWORDS

3D printing, bioreactor, cardiovascular, decellularization, pericardium, porcine aorta

This is an open access article under the terms of the Creative Commons Attribution-NonCommercial-NoDerivs License, which permits use and distribution in any medium, provided the original work is properly cited, the use is non-commercial and no modifications or adaptations are made.

© 2021 The Authors. Artificial Organs published by International Center for Artificial Organ and Transplantation (ICAOT) and Wiley Periodicals LLC.



## 1 | INTRODUCTION

Xenogeneic biomaterials are commonly used as implants in adult and pediatric cardiac surgery.<sup>1-3</sup> While in most cases the implant is chemically fixed prior to implantation, a growing number of decellularized biomatrices is available.<sup>1,4,5</sup> Decellularization (DC) aims to remove antigens while preserving the biomechanical properties of the extracellular matrix (ECM).<sup>6</sup> Due to the high amount of manual labor in traditional manufacturing techniques, the development of customized bioreactors for an effective DC often comes at a high cost. With the commercial rise of affordable 3D-printers paired with the ever-increasing number of printable materials and open-source files, the high manufacturing costs can be significantly reduced.<sup>7,8</sup> Additionally, the use of 3D printing allows for a greater freedom in the bioreactors' designing process since the stringent design rules for traditional manufacturing only partly apply.<sup>9,10</sup> The freedom provided by 3D printing allows for individual goals to be set, for example, to keep the price of the final bioreactor as low as possible, to make it a feasible option for every laboratory budget, all while still delivering reliable DC results.

Especially the DC of vessel grafts presents a great challenge due to the high thickness of the material.<sup>11</sup> Furthermore, the freedom in design enables the creation of a bioreactor that simultaneously decellularizes multiple tissue samples while preserving the structural integrity of the ECM. Based on these goals, this study aims to develop a novel DC system for pericardial patches and vessels. The use of 3D printing technology in the manufacturing process will be utilized to keep the overall costs low while sustaining a high quality of efficiently decellularized samples. For the analysis of the system's effectiveness, DC results for bovine and porcine biomaterials will be compared to results of samples decellularized with a standard immersion and agitation setup that constituted as a control group.

## 2 | MATERIALS AND METHODS

### 2.1 | Bioreactor design

To maximize the feasible output for both the pericardial matrix DC bioreactor (PDB) and the vascular graft DC bioreactor (VDB) a simultaneous DC of 10 pericardial patches and 5 vascular grafts, respectively, was determined. Therefore, overall dimensions of the bioreactors were designed to fit on a benchtop while holding ten 10 × 10 cm pericardial patches or five 10 cm long vessel grafts.

All parts of the bioreactors were designed using commercial computer-aided design (CAD) software Solidworks 2018 (Dassault Systèmes, Vélizy-Villacoublay, FRA). Part development followed common design rules with an emphasis on

avoiding overhang to reduce or eliminate the need for additional support structures in the 3D printing process.

The design of the inner chamber of the PDB includes two perforated plates at the bottom to equally distribute the detergent solution from the single inlet to every pericardial patch. The lower plate consists of 36 equally spaced holes with a diameter of 10 mm (Perforated plate #1; Figure 1A: 4). The top plate includes 88 holes with a diameter of 3 mm, organized in an 8 × 11 pattern (Perforated plate #2; Figure 1A: 3). The patches are spread out and placed in removable frames ( $n = 10$ ) with mounts for attaching the material with surgical sutures to prevent folding (Figure 1C). The detergent is introduced into the bioreactor at the bottom (Figure 1A: 1) and exits the bioreactor through a nozzle at the top (Figure 1A: 7). The frames containing the specimen are placed in the bioreactor dividing the holes in the perforated plate so on each side of a pericardial frame there are eight openings, with an equal distance of 12 mm.

In contrast, the VDB only includes one plate at the bottom with five openings for bayonet locks (Figure 1D: 3,4). Vessel grafts were clamped onto a removable nozzle, which in turn was placed inside the bayonet lock and subsequently turned 45° to secure the nozzle. The nozzle is surrounded by eight equally spaced holes with a diameter of 3 mm (Figure 1F). Additionally, a cube with five circular openings (Ø 50 mm) is placed inside the bioreactor to create five tubular chambers around the nozzles (Figure 1D: 5). This design was chosen to utilize the previously published improved efficacy of perfusion DC on thick-walled vessels, by allowing a high intraluminal flow while still retaining some extraluminal fluid pressure.<sup>12</sup>

Both bioreactors were fit with a gasket at the top and sealed with a fitting lid, which has one outlet that connects to a 3/8" hose. The lid is fixated with eight M4 screws and wing nuts for ease of handling during closing and opening. (Figure 1B,E).

### 2.2 | Computational fluid dynamics (CFD)

Both bioreactors were designed to offer equal DC conditions for all samples. To further investigate and ensure an equal distribution of the detergent between the samples, bioreactors were analyzed using CFD. Steady-state three-dimensional CFD analyses, were performed using Ansys CFX (Ansys Workbench 2019 R2, Ansys Inc, Canonsburg PA, USA). Perforated plates were investigated to establish comparable flow rates for every specimen chamber, to ensure equal flow and pressure distribution. Analysis of the specimen chambers allows a better understanding of the flow distribution between samples in the PDB, as well as the difference in intra- and extraluminal flow for the VDB. The inlet boundary condition was set as mass flow inlet with a flow rate of



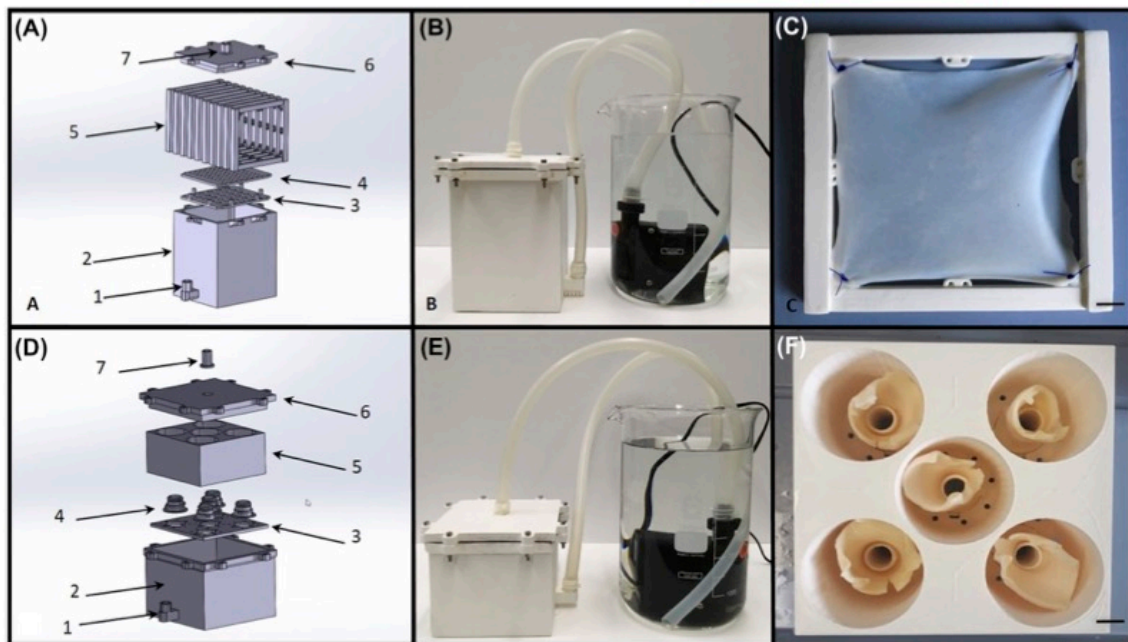


**FIGURE 1** Design of 3D printed DC bioreactors; A, CAD design of the PDB in exploded view; 1: inlet; 2: bioreactor box, 3: perforated plate #1, 4: perforated plate #2, 5: specimen frame (10×), 6: bioreactor lid, 7: lid adapter (outlet); B, Experimental setup of the PDB with aquaristic pump, detergent reservoir and tubing; C, Specimen frame with sutured pericardial patch after DC; D, CAD design of the VDB in exploded view; 1: inlet; 2: bioreactor box, 3: perforated plate, 4: specimen adapter (5×), 5: box inlay, 6: bioreactor lid, 7: lid adapter (outlet); E, Experimental setup of the VDB with aquaristic pump, detergent reservoir and tubing; F, Top-down view of the box inlay with 5 porcine aortae clamped to the specimen adapters; Scale bars: 10 mm. [Color figure can be viewed at [wileyonlinelibrary.com](http://wileyonlinelibrary.com)]

1.17 kg/s of water, which is the maximum rate of the aquaristic pump used in the experimental setup. The wall boundary was set as no-slip, while the outlet was set as an opening with atmospheric pressure.

### 2.3 | Material selection and budgeting

The printing technologies evaluated for the manufacturing of the bioreactors were standard fused deposition modeling (FDM) and the Polyjet printing technique. These technologies present different ends of the printing spectrum, where one is relatively inexpensive with limited accuracy (FDM), while the other offers highly accurate printing results at a higher overall cost (Polyjet). Two rigid materials Poly(lactic acid) (PLA, Ultimaker, Utrecht, NL) and AR-M2 (Keyence Corp., Osaka, JP) were chosen for further investigation. To print the materials, an Ultimaker 3 Extended (Ultimaker) for FDM and an Agilista 3200W (Keyence Corp.) for Polyjet were utilized.

Materials were analyzed and compared regarding their chemical resistance, cytotoxicity, and economic efficiency. To determine the chemical resistance and therefore usability in surface modification, the materials were exposed to chloroform (Sigma-Aldrich Chemie GmbH, Steinheim,

GER). Furthermore, material samples were exposed to ethanol (70%) and Bacillol AF (Bode Chemie GmbH, Hamburg, GER) to determine the adverse effects of the disinfection medium on the bioreactor. Sample chips (Ø11 mm, thickness: 3 mm) were submerged in chloroform for 10 minutes and subsequently analyzed using scanning electron microscopy (SEM).

While the bioreactors were not primarily designed for reseeding of the decellularized biomaterials, an adverse effect of the bioreactors' material on the tissue has to be evaluated. In case of cytotoxic effects, the printing material should be avoided to prevent complications once the biomaterial is used in subsequent processes, that is, *in vivo* testing. Therefore, a cytotoxicity test for both PLA and AR-M2 was conducted using human endothelial cells. Endothelial cells were isolated enzymatically from segments of the great saphenous vein as previously described.<sup>13</sup> To assess cytotoxicity, 30 000 cells were seeded in every well of a 24-well plate (Sarstedt AG & Co. KG, Nümbrecht, GER) and material chips (Ø11 mm, thickness: 3 mm) were placed in custom inlets to allow for an indirect exposition of the cells via the exposed cell medium. Subsequently, according to ISO 10993-5, a WST-1 analysis (Roche Diagnostics Deutschland GmbH, Mannheim, GER) was performed after 24, 48, and 72 hours of

exposure. Cell proliferation was measured using spectrophotometric quantification.

Since a budget friendly approach to the bioreactors' design was a main goal, the weight of the individual parts and support structures was recorded and multiplied by the wholesale price of the printing material to determine the overall manufacturing costs (Tables 1 and 2). Furthermore, essential components, such as the aquaristic pump and silicone hoses were added to the budgeting to offer a comprehensive cost estimate for creating a complete DC setup.

## 2.4 | 3D-printer settings

All CAD designed parts were converted into stereolithography file format (.stl) and imported into commercial slicing software Ultimaker Cura 4.2.0 (Ultimaker) for FDM or Modeling Studio (Keyence Corp.) for Polyjet, respectively. All parts were printed using a standard FDM 3D-printer

(Ultimaker 3 Extended, Ultimaker). Printing temperatures were set at 200°C at the nozzle and 60°C at the print bed. Commercial PLA material (2.85 mm, Ultimaker) was extruded through a 0.4 mm nozzle directly onto the print bed. Both boxes were printed using a raft to improve the stability of necessary support structures and prevent warping of the edges. All other parts were printed directly onto the glass surface of the print bed. Printing speed was set at 70 mm/s. Requirements of additional support structures, infill percentages, wall thickness, and layer height varied between parts due to differing mechanical loads (Tables 1 and 2). Data on printing time and amount of material used were taken directly from the slicing software.

After printing, the support structures were removed and all parts of the two bioreactors were coated with chloroform to remove grooves between individual layers and reduce surface roughness. Subsequently, the parts were placed in a flow hood for 24 hours to allow the chloroform to volatilize before assembly.

TABLE 1 Manufacturing metrics for the PDB

Part no	Part name	Quantity	Manufacturing metrics			Additional printing instructions
			Printing time [h:min]	Estimated weight [g]	Estimated costs [€]	
1	Bioreactor body	1	41:30	360	8.64	a,b,c,d,e
2	Perforated plate	1	04:30	40	0.96	b,c,e
3	Specimen adapter	5	05:00	40	0.96	b,c,e,f
4	Box inlay	1	22:50	249	5.97	c,d
5	Bioreactor lid	1	13:30	145	3.48	b,c,d,e
6	Lid adapter	1	00:30	5	0.12	b,c
	Total	10	87:50	839	20.13	

Note: a: Support structure required, b: High infill > 40% recommended, c: Increased wall thickness recommended, d: Raft recommended, e: Additional post processing required.

TABLE 2 Manufacturing metrics for the VDB

Part no	Part name	Quantity	Manufacturing metrics			Additional printing instructions
			Printing time [h:min]	Estimated weight [g]	Estimated costs [€]	
1	Bioreactor body	1	48:30	411	9.86	a,b,c,d,e
2	Perforated plate #1	1	05:10	44	1.06	b,c,e
3	Perforated plate #2	1	04:40	40	0.96	b,c,e
4	Specimen frame	10	33:40	290	6.96	b,c
5	Bioreactor lid	1	15:30	135	3.24	b,c,d,e
6	Lid adapter	1	00:30	5	0.12	b,c
	Total	15	108:00	925	22.07	

Note: a: Support structure required, b: High infill > 40% recommended, c: Higher wall thickness recommended, d: Raft recommended, e: Additional post processing required, f: multi-part print possible.



## 2.5 | Bioreactor validation

### 2.5.1 | DC setup

To determine the functionality and effectiveness of the bioreactors, an experimental setup was designed to compare the PDB and VDB's performance to standard DC protocols using immersion and agitation on an orbital shaker. In the following, the immersion and agitation group is referred to as control group. For the control group, the biomaterial samples were individually placed in 100 mL containers (Schott Duran GL45 100 mL, Schott AG) and filled with the detergent. Subsequently, the containers were placed in a shaking incubator (KS 15, Edmund Bühler GmbH, Bodelshausen, GER) at 150 motions per min to allow for constant movement of the detergent. The setup for the bioreactors consists of the closed bioreactor, which is connected to an aquaristic rotary pump (Eden 155, PfG GmbH, Hoerstel, GER) with a maximum output of 4200 L/h. The aquaristic pump is subsequently submerged in a 5 L reservoir (Schott Duran Super Duty 5000 mL, Schott AG, Mainz, GER) holding the detergent solution. To close the circuit, another tubing is connected to the top of the bioreactor to serve as a return. Once the experiment was started, the detergent entered the bioreactor at the bottom and recirculated to the reservoir from the top of the bioreactor.

### 2.5.2 | Treatment protocols

Native bovine pericardia ( $n = 10$ ) and porcine hearts ( $n = 10$ ) were obtained at a local slaughterhouse, transported in a refrigerated container to the laboratory, and processed within 3 hours after slaughtering. Adipose tissue was carefully removed with gauze wipes. Native samples were taken and stored in phosphate-buffered saline (PBS, Biochrom GmbH, Berlin, GER) at 4°C until further evaluation.

Different treatment protocols were applied for each tissue type. A 10 × 10 cm patch was cut from every pericardium. Areas with macroscopic surface damage or areas with heterogeneous fiber orientation were excluded. The thickness of the pericardial patches was measured at 20 spots equally spaced across the pericardium to ensure an even thickness of the biomaterial. For the aortic roots, the aorta was removed from the whole porcine heart just above the aortic valve. A sample area measuring 6 cm in total was determined to be between the aortic valve and the beginning curvature of the aortic arch to later ensure a vessel graft with minimal curvature and only moderate change in diameter. The wall thickness of all aortic root samples was measured at 20 points.

The DC of bovine pericardia was based on a previously described protocol.<sup>14</sup> The pericardia were decellularized using a solution of 0.5% sodium deoxycholate (SD, Sigma-Aldrich Chemie GmbH) and 0.5% sodium dodecyl sulfate (SDS, Carl

Roth GmbH, Karlsruhe, GER) in PBS at room temperature. The DC protocol consisted of two cycles á 12 hours with an exchange of the DC solution in between, resulting in a total DC time of 24 hours.

Aortic roots were decellularized using an adaptation of a published protocol.<sup>11</sup> Similar to the protocol for pericardial patches a solution of 0.5% SD and 0.5% SDS was used. The protocol consisted of two identical subsequently performed cycles starting with an 18 hours DC using the detergent solution, followed by a 30-minute washing step using PBS. Afterward, two DC steps each lasting 3 hours were performed. This cycle was repeated, which lead to an overall DC time of 51 hours for the aortic root protocol.

As a control group, pericardial and aortic samples (each  $n = 10$ ) were decellularized using standard immersion and agitation techniques following the above presented protocols for pericardial and aortic samples, respectively. Samples were decellularized in individual containers and the detergent exchange as well as the washing steps were performed manually.

Following detergent exposition, thorough rinsing of the samples was performed by 10 washing cycles with PBS for 15 minutes each. Pericardial patches and aortic roots were stored in a 1% DNase I (Activity: 3000 U/mg, LS002138, Worthington Corp, Lakewood NJ, USA) solution for 24 hours to further improve the DC effect. The DNase immersion was followed by three washing cycles with PBS for 30 minutes each.

## 2.6 | Scanning electron microscopy

For surface and structure evaluation, decellularized tissue samples were analyzed with SEM. Furthermore, specimen of 3D printing materials treated with chloroform for surface modification was also analyzed with SEM. Decellularized samples were fixed in a solution consisting of 912 mL aqua bidistilled (Ampuwa, Fresenius Kabi Deutschland GmbH, Bad Homburg v. d. H., GER), 86 mL of 25% glutaraldehyde (Sigma-Aldrich Chemie GmbH), 11.3 g of sodium cacodylate trihydrate (Merck KGaA), and 1.5 mL of 1N-hydrochloric acid (Titrisol, Merck KGaA). Thereafter, specimen was dehydrated by an ascending ethanol series and dried by critical point drying (CPD 030, BalTec, Schalksmühle, GER). Samples were sputtered with gold for 180 seconds at 10<sup>-5</sup> mbar (SCD 50, BalTec) and analyzed by SEM (Zeiss EVO LS 10, Carl Zeiss AG).

## 2.7 | Histology

For histological analysis, decellularized samples were fixed in 4% formaline (Carl Roth GmbH) for 24 hours and dehydrated



by an ascending ethanol series and xylene (Carl Roth GmbH). Tissue samples were embedded in paraffin and cut into sections (thickness: 5  $\mu\text{m}$ ) and deparaffinized. Subsequently, sections were used for staining hematoxylin/eosin (HE, Merck KGaA, Darmstadt, GER), picosirius red (PR, Morphisto GmbH, Frankfurt a. M., GER), and Movat's pentachrome (PC, Morphisto GmbH) according to the manufacturers' protocol. Images were taken with a Leica DM R (Leica Microsystems Wetzlar GmbH, Wetzlar, GER) and LAS EZ software (V.3.4., Leica GmbH). PR staining was analyzed using polarized light. For the analysis of remaining cell nuclei, sections were stained with a 1:1000 ratio of DAPI (4',6-diamidino-2-phenylindole, Sigma-Aldrich Chemie GmbH) in PBS for 5 minutes. Images were taken and analyzed by fluorescence microscopy (AxioObserver, Carl Zeiss AG, Oberkochen, GER). Images of all DAPI samples were taken with equal exposure times.

## 2.8 | Mechanical evaluation

For the biomechanical assessment, pericardial samples were observed using a backlight table to determine the main fiber orientation. Samples were then taken perpendicularly with a manual cutting press (ZCP020, Zwick GmbH & Co. KG, Ulm, GER) resulting in a dogbone-shaped specimen (ISO 53504 S3A) for testing of longitudinal and transverse fiber orientations. Vessel samples were taken in circumferential orientation with specimen cut as described above. Each specimen's thickness was measured using a thickness gauge (Mitutoyo ID-C112XB, Mitutoyo, Neuss, GER). Tensile testing was performed using a tensile testing system (zwick-iLine, 2.5kN, Zwick GmbH). Testing was recorded with the corresponding software (testXpert V2.3, Zwick) and results were normalized to tissue thickness.

## 2.9 | DNA analysis

Samples of 25 mg weight were minced and DNA extraction was performed according to the manufacturer's protocol utilizing the Isolate II Genomic DNA Kit (Bioline GmbH, Luckenwalde, GER). Dissolved DNA was analyzed using a spectrophotometer (BioPhotometer, Eppendorf AG, Hamburg, GER) at a wavelength of 260 nm. For quality assurance, only values within the ratio of 1,7-2,0  $E_{260}/E_{280}$  were included in the results. Measurements were performed in triplicates. Final DNA concentration was expressed in ng/mg tissue weight.

## 2.10 | Statistical analysis

If possible, results are presented as mean  $\pm$  standard deviation. Normal distribution was tested by Kolmogorov-Smirnov

test. Student's *t* test was used for Gaussian distributed data while Mann-Whitney *U* test was used for nonparametric distributed datasets. Groups were compared using one-way ANOVA analyses. A *P* value  $< .05$  was considered to be statistically significant, while  $P < .01$  was considered to be highly significant and  $P < .001$  extremely significant, respectively. Statistical analyses were performed with GraphPad Prism v9.0.0 (GraphPad Software, La Jolla, CA, USA).

## 3 | RESULTS

### 3.1 | CFD

Steady-state CFD analysis of the PDB revealed an even flow distribution between every pericardium, leading to a mean velocity of  $1.784 \pm 0.064$  m/s with no significant differences (Figure 2A). In a preliminary setting where only one perforated plate was placed at the bottom of the PDB, uneven flow distribution with a higher flowrate on the sides of the bioreactor was observed. Introducing a second perforated plate at the bottom helped improving the even distribution of the DC detergent coming into the bioreactor through one inlet (Figure 2B). At the top's outlet some turbulences occurred which have no influence on the pericardial samples. The VDB showed a different, yet desirable flow behavior for the DC of vessels (Figure 2C). The intraluminal flow velocity was significantly higher ( $5.547 \pm 0.200$  m/s) compared to the outside of the vessel ( $0.540 \pm 0.152$  m/s;  $P < .001$ ). All eight extraluminal openings showed comparable flow patterns (Figure 2D). Based on the CFD results, no further design improvements had to be made to the inlet or perforated plate. At the top, the same turbulences occurred as in the PDB, which can be accounted to the single center outlet of the box.

### 3.2 | Printing material properties and surface modification

Both printing materials available for the manufacturing of the bioreactors have similar maximum tensile strength (PLA: 49.5 MPa; AR-M2: 40-55 MPa), while PLA requires a higher amount of post-processing and offers a lower printing accuracy compared to the Polyjet-printed AR-M2. AR-M2 also comes at a significantly higher price of 449.33 €/kg compared to 53.27 €/kg for PLA. The tested materials showed differing behavior regarding their chemical resistance. While the use of ethanol 70% and surface cleaners (BacilloI) had no visible effect on the materials' surface, treatment with chloroform for 10 minutes showed signs of dissolution by clouding the solvent on both AR-M2 and PLA.

Cytotoxicity analysis of both materials showed a relative cell proliferation rate after 24 hours of  $-22.7 \pm 18.7\%$  for PLA and

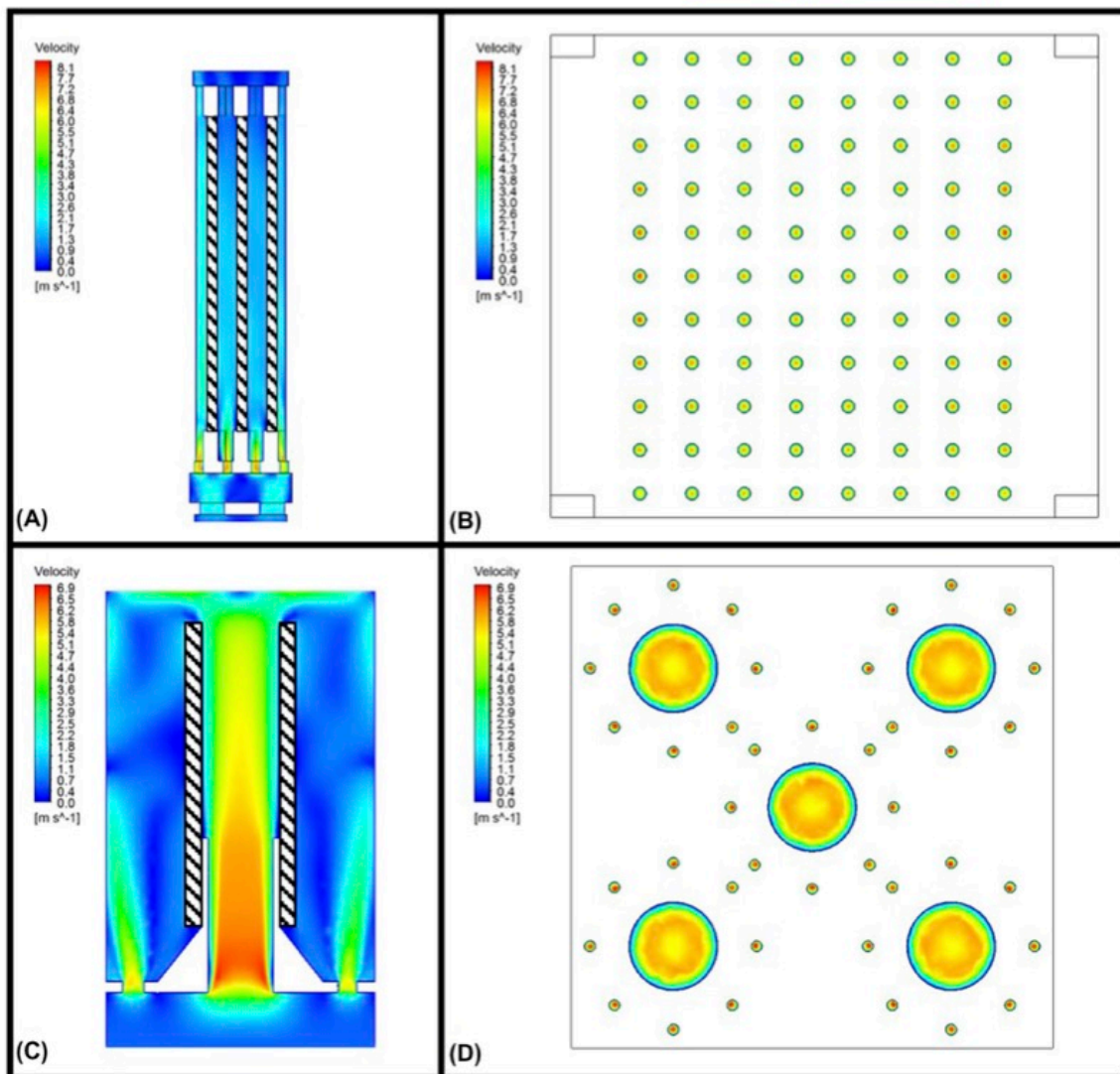


**FIGURE 2** Partial CFD analysis of the PDB and VDB; A, Visualization of the flow pattern between three pericardial sample frames. Fluid enters the chamber at the bottom, passes through two perforated plates and flows along the samples (striped boxes); B, Top down view of the flow pattern through the upper perforated plate, visualizing the flow distribution between the individual specimen rows; C, Flow visualization of one chamber in the VDB. The vessel sample (striped boxes) is clamped to the specimen adapter. The detergent enters at the bottom and has a higher intraluminal flow, compared to the outside of the vessel; D, Top down view of the perforated plate in the VDB without specimen adapters, visualizing the equal flow distribution between the five chambers. [Color figure can be viewed at [wileyonlinelibrary.com](http://wileyonlinelibrary.com)]

$-42.3 \pm 17.4\%$  for AR-M2 compared to control. For PLA, the relative proliferation rate changed only slightly after 48 hours ( $10.7 \pm 8.9\%$ ) and 72 hours ( $-23.3 \pm 15.8\%$ ) (Figure 3A). The cytotoxicity analysis of the AR-M2 material revealed a highly toxic effect on the endothelial cells resulting in a low relative proliferation rate after 48 hours ( $-85.6 \pm 25.7\%$ ) and almost no cell viability after 72 hours ( $-99.8 \pm 6.0\%$ ). Based on these results, PLA was chosen as printing material for the bioreactor parts due to its lower price and the potentially adverse effect of the AR-M2 material on the DC scaffolds.

Overall, the PDB consists of 15 3D-printable parts while the VDB is made up of 10 printable parts (Tables 1 and 2). Some post-processing had to be performed on the final printed parts, especially in areas where support structures were attached.

The PLA used in the printing process proved to be very durable and easy to handle. After completion of 10 DC experiments with each bioreactor, there was no leakage, deformation, or macroscopic damage to the printed parts. Based on the previous tests, disinfection of the bioreactors with ethanol 70% was



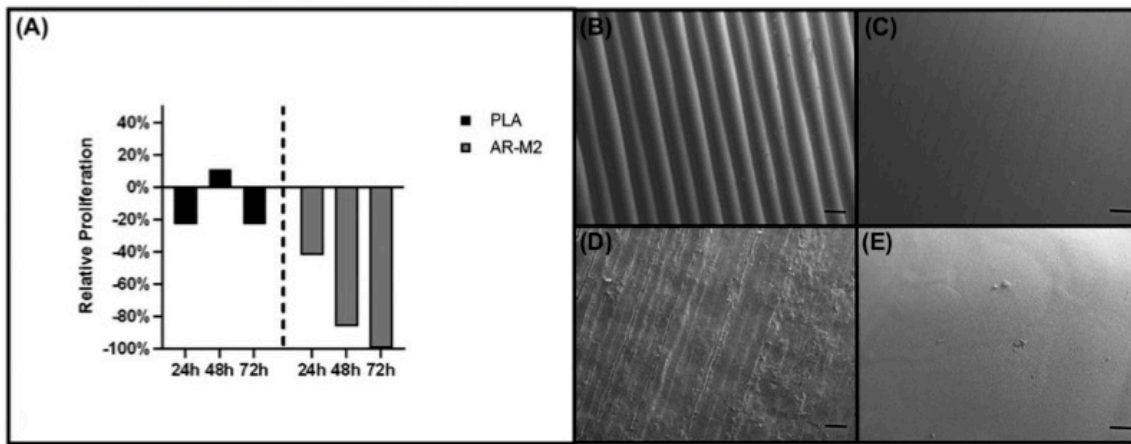


**FIGURE 3** Cytotoxicity assessment and analysis of surface modification; A, Relative cell proliferation for endothelial cells exposed to PLA and AR-M2 3D printing materials. Proliferation rates are normalized to a control of endothelial cells; B, SEM image of PLA material after printing process showing characteristic grooves caused by the layering; C, SEM image of PLA material after surface treatment with chloroform showing a relevant reduction in surface roughness; D, SEM image of AR-M2 material after printing process. The surface appears flakey with manufacturing lines caused by the print head; E, SEM image of AR-M2 material after treatment with chloroform. The surface appears smoother with a visible reduction of manufacturing marks; Scale bars: 200  $\mu$ m

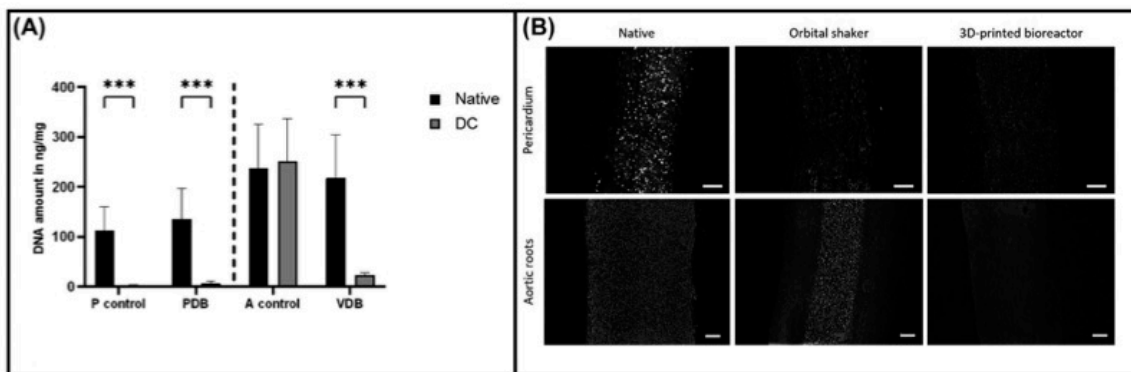


**FIGURE 4** Quantification of the DC efficiency; A, DNA quantification in ng/mg for all samples. Native DNA amounts are presented as black bars, the DNA amounts after the DC are presented as grey bars; B, Representative fluoroscopic DAPI fluoroscopic images of the native and DC samples. Cell nuclei are clearly visible in both native samples and the aortic root sample decellularized in the orbital shaker. All other samples showed no residual cell nuclei; Scale bars: 200  $\mu$ m

possible without damaging the printed parts. The treatment of the surface with chloroform proved to be an effective way of removing imperfections on the bioreactor's inner surfaces caused by the printing process. Especially, the characteristic grooves caused by the printer's nozzle (in *x* and *y* direction) and the layering (in *z* direction) were reduced drastically in the treated samples analyzed with SEM and microscopy (Figure 3B,C).

### 3.3 | Validation

The validation of the bioreactors compared to control group focused on the efficient removal of all cells and the amount

of residual DNA as well as the preservation of the tissue's structural integrity and biomechanical properties.

DNA quantification revealed a significant reduction of residual DNA in the bioreactor samples compared to native specimen. The DC with the PDB reduced the DNA amount from  $135.2 \pm 62.7$  ng/ $\mu$ g (native sample) to  $6.35 \pm 4.4$  ng/ $\mu$ g ( $P < .001$ ). The control group for the bovine pericardium reached a comparable result to the DC performed with the use of the PDB (DNA:  $1.5 \pm 1.8$  ng/ $\mu$ g;  $P < .001$ ). For the DC with the VDB the residual DNA in the decellularized aortic roots showed an extremely significant reduction from  $217.6 \pm 86.5$  ng/ $\mu$ g in the native sample to  $23.8 \pm 4.2$  ng/ $\mu$ g ( $P < .001$ ) (Figure 4A).

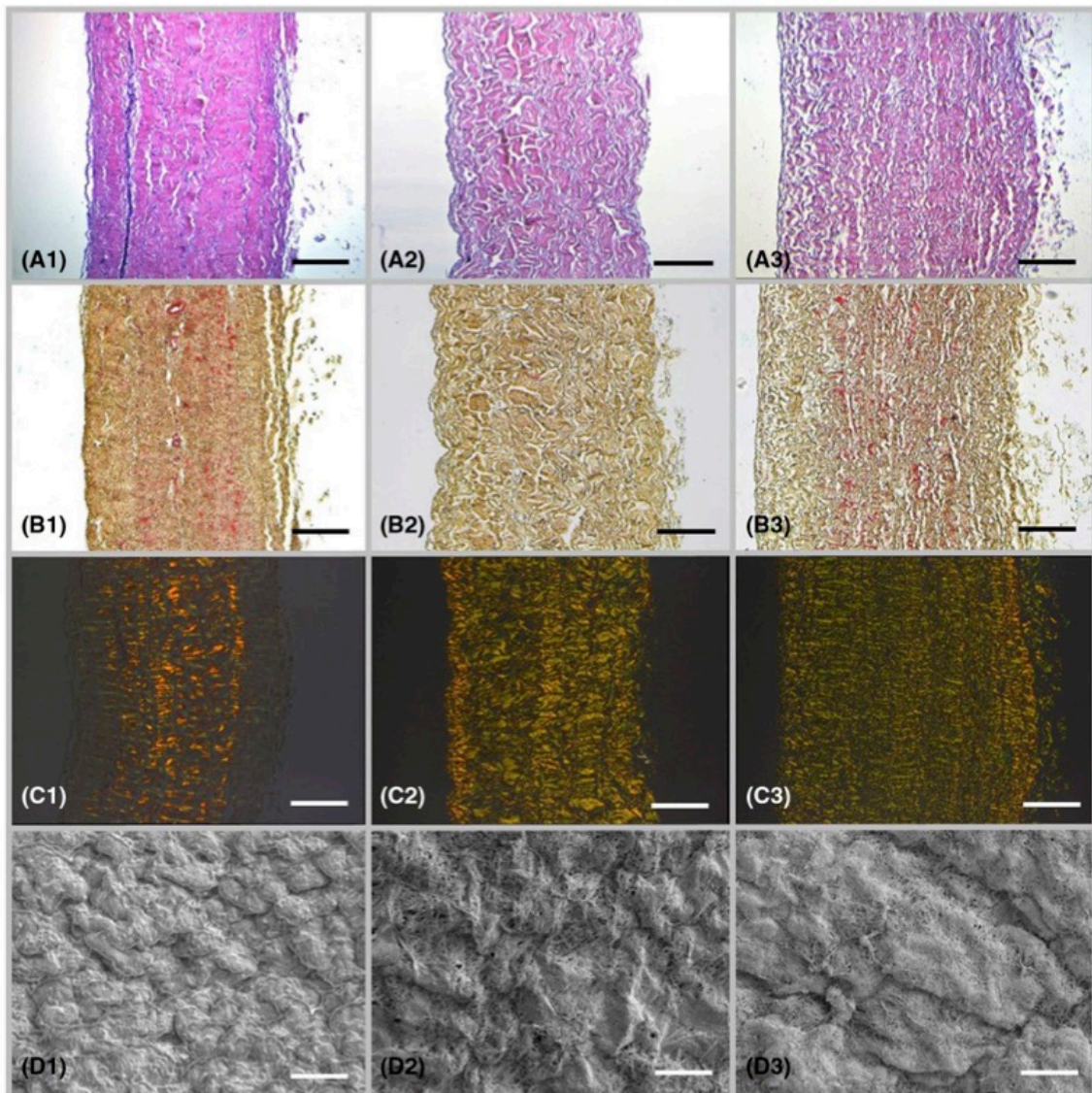


**FIGURE 5** Histological analysis of the pericardial samples; In HE staining cell nuclei are clearly visible (blue) in the native sample while no cell nuclei are present for both DC samples. In the PC staining elastic fibers (red) are visible before and after DC. The PR staining showed the appearance of collagen type I (yellow) and type III (green). Additionally, the compact structure of the tissue was highlighted, even after DC. SEM imaging revealed the removal of cell covering while fibers being more prominently displayed in both DC samples compared to the native images; Scale bars: 200  $\mu\text{m}$ . [Color figure can be viewed at [wileyonlinelibrary.com](http://wileyonlinelibrary.com)]

The control group for the aortic root DC, in contrast, showed a high amount of residual DNA ( $251.1 \pm 86.4 \text{ ng}/\mu\text{g}$ ;  $P = .684$ ). The appearance of cell nuclei was highlighted by DAPI staining in native pericardia as well as in the aortic samples. While the PDB and VDB were able to remove all of the cell nuclei after the DC, only insufficient results were achieved by the orbital shaker (Figure 4B). Aortic root specimen decellularized by immersion and agitation showed a cellular layer at the center of the section during DAPI analysis,

which is in accordance with the high residual DNA. All other decellularized samples showed no DAPI signal (Figure 4B).

Histological analysis of the native and decellularized samples revealed an overall preservation of the structural integrity. The HE staining showed a compact structure of tissue, mainly consisting of ECM (colored purple) and cell nuclei (colored blue). For the pericardia, both the orbital shaker and the PDB revealed no residual cell nuclei (Figure 5A2,A3). However, only the VDB was able to consistently remove the



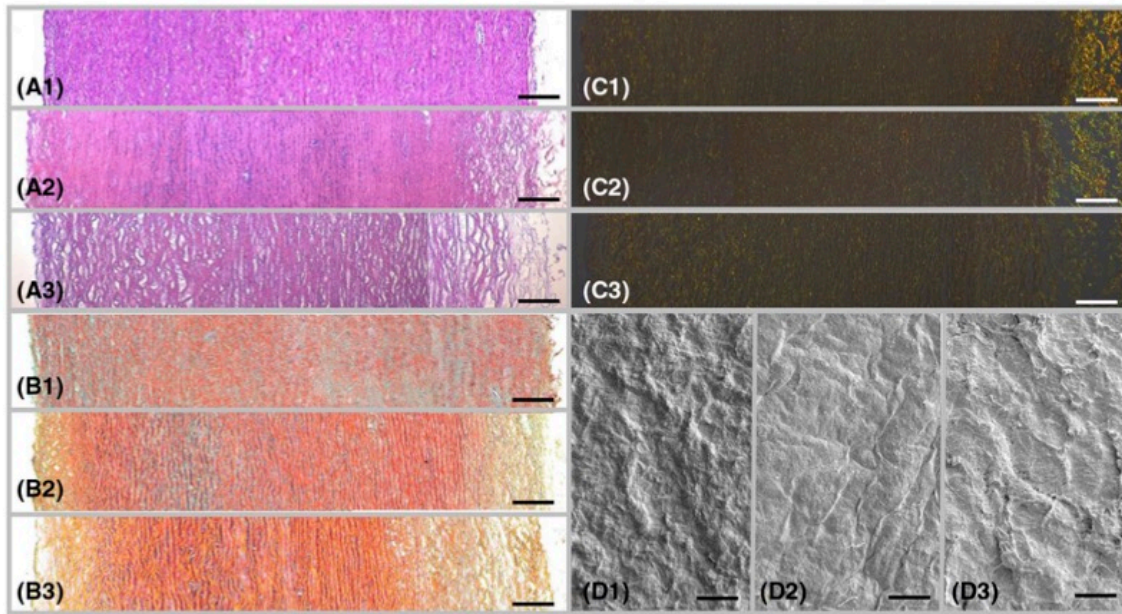


**FIGURE 6** Histological analysis of the aortic root samples: A, HE: Cell nuclei are clearly visible in the native (1) sample with a broad strip of cell nuclei being present in the control group (2). HE staining of the sample DC in the VDB showed no residual cell nuclei (3). B, PC: PC staining revealed the appearance of elastic fibers (red) in the full width of the aortas, although the highest amount was found in the middle layers. The DC process did not reduce the occurrence or structure of the elastic fibers. C, PR: Collagen type I (yellow) and collagen type III (green) both occurred in aortic tissue. Neither the orbital shaker nor the CDB reduced the visible amount of collagen fibers; D, SEM: In SEM imaging native samples (1) revealed a dense cover across which is still prevalent in the control group (2). Samples decellularized by using the VDB showed a noncontinuous cell layer with fibers being more prominently visible (3); Scale bars: 100  $\mu$ m. [Color figure can be viewed at [wileyonlinelibrary.com](http://wileyonlinelibrary.com)]

cell nuclei in aortic samples, while the orbital shaker did not remove cells from the inner layers (Figure 6A2). In the PR staining, collagen type I (yellow) and type III (green) were visible in both native and DC samples (Figures 5 and 6C). Furthermore, the staining revealed the compact structure of the tissue which was loosened slightly by the DC. PC staining additionally confirmed the presence of collagen (yellow) and elastin (red) fibers. After DC, there were more visible fibers in samples from the PDB than in samples from the control group. The composition of the tissue, for both pericardium and aortic root did not change visibly due to the DC process (Figures 5 and 6B).

SEM imaging of native pericardial samples showed a tightly covered surface on the heart-facing side, while presenting disorganized fiber bundles on heart-averted side (Figures 5 and 6D). After completion of the DC, the heart-facing side showed less cell coverage with visible collagen fibers. The frayed nature of the heart-averted side did not change after the DC process. Furthermore, there was no damage to the ECM observable on decellularized pericardial samples. Native aortic roots presented with a smooth and intraluminal surface, while the outer surface, similar to the pericardial samples, showed highly disorganized fiber bundles. After DC, the intraluminal surface showed no continuous

coverage, but rather individual fibers and fiber bundles were clearly visible.

Mechanical testing of native and decellularized samples revealed no significant change in both tensile strength and extensibility for the pericardial samples (Figure 7A). Native pericardial samples reached a maximum tensile strength of  $19.57 \pm 8.37$  N/mm<sup>2</sup> in longitudinal direction and  $12.43 \pm 6.35$  N/mm<sup>2</sup> in transversal direction ( $P = .089$ ). The elongation at break was  $43.80 \pm 8.35\%$  in longitudinal direction and  $44.30 \pm 11.72\%$  in transversal direction ( $P = .913$ ). After the DC using the bioreactor, the maximum tensile strength was slightly, yet not statistically significant, reduced (longitudinal:  $16.02 \pm 7.37$  N/mm<sup>2</sup>;  $P = .680$ ; transversal:  $12.22 \pm 7.94$  N/mm<sup>2</sup>;  $P > .99$ ) with the elongation at break staying on a similar level compared to native samples (longitudinal:  $39.50 \pm 7.59\%$ ;  $P = .569$ ; transversal:  $49.30 \pm 9.17\%$ ;  $P = .467$ ). These results are consistent with the mechanical properties of the pericardial samples of the control group. Neither maximum tensile strength (longitudinal:  $20.19 \pm 9.56$  N/mm<sup>2</sup>;  $P = .988$ ; transversal:  $9.13 \pm 5.12$  N/mm<sup>2</sup>;  $P = .717$ ) nor elongation at break (longitudinal:  $48.40 \pm 14.82\%$ ;  $P = .525$ ; transversal:  $45.70 \pm 12.80\%$ ;  $P = .942$ ) differed greatly from the native samples. Aortic root samples showed no significant change



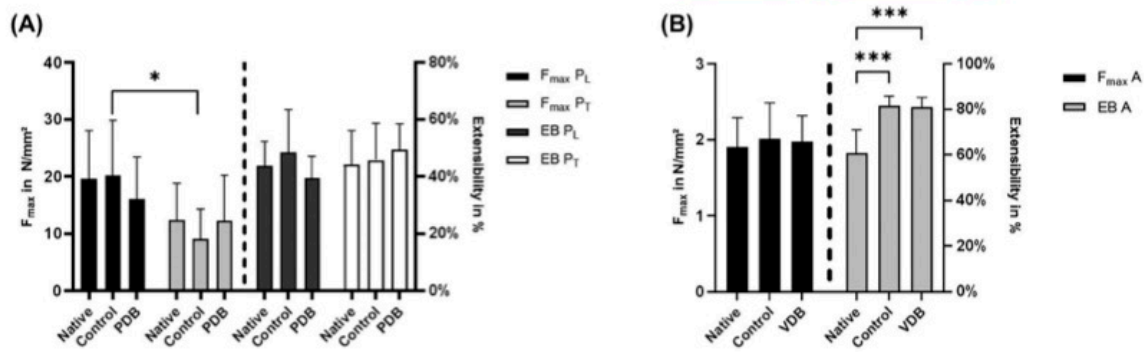


**FIGURE 7** Biomechanical properties of native and decellularized samples; A, Tensile test results for pericardial samples. Maximum tensile strength in longitudinal ( $F_{max}$  PL) and transversal ( $F_{max}$  PT) directions displayed on the left and elongation at break in both directions (EB PL, EB PT) displayed on the right for native, control and samples decellularized in the PDB; B, Tensile test results for aortic samples: Maximum tensile strength in circumferential direction ( $F_{max}$  A) displayed on the left and elongation at break (EB A) displayed on the right

in maximum tensile strength for both the 3D printed bioreactor ( $1.98 \pm 0.37$  N/mm<sup>2</sup>;  $P > .99$ ) and the control group ( $2.01 \pm 0.47$  N/mm<sup>2</sup>;  $P > .99$ ) compared to native samples ( $1.90 \pm 0.39$  N/mm<sup>2</sup>). Elongation at break showed a significant change in both the vessel grafts decellularized with the 3D printed bioreactor ( $80.90 \pm 4.07\%$ ;  $P < .001$ ) and the control group ( $81.40 \pm 4.40\%$ ;  $P < .001$ ) compared to native samples ( $60.90 \pm 10.04\%$ ).

#### 4 | DISCUSSION

In this study, we manufactured and evaluated two low-cost 3D-printable bioreactors for the DC of biomaterials for cardiovascular application. This setup proved to successfully decellularize porcine aortic roots and bovine pericardia in a stringent validation setting compared to conventional methods.

The development of individualized bioreactors has been an essential part of tissue engineering for a long time.<sup>15-17</sup> Especially the development of perfusion-based DC bioreactors increased the need for individually manufactured components drastically. In the past, those parts had to be created by classic machining production, which came with high costs, for both material and labor, as well as moderately long waiting times. The introduction of 3D printing allows bypassing most of these issues by enabling a research group to independently create and modify bioreactors at a fraction of the cost of traditional manufacturing techniques.<sup>10,18</sup> This was also proven in this study, as the raw material costs for the bioreactors did not exceed a total printing material value of 25 €. Furthermore, the total production time of 108 hours and 88 hours, respectively, allowed for a fast development cycle and integration of the bioreactors into a DC process. Costs and printing time are comparable to the 3D printed bioreactor described by Janvier et al, who describe a printing time of

5-6 days and overall costs of 40-50 £.<sup>19</sup> Toume et al described the creation of cost-efficient bioreactors using 3D printing for less than 100 \$.<sup>20</sup> This further confirms that it is possible to manufacture low-cost bioreactors using 3D printing technology.

Additionally, CFD analysis of the designed bioreactors revealed an even distribution of the detergents among all specimen, which is a crucial feature to ensure constant quality and reproducibility of the treated patches or vessel grafts. The results derived from the CFD simulation matched the results from the validation experiments very closely since there was no measurable difference between the different specimens, especially when looking at the low standard deviation between the bioreactor groups. Improvements in computing power make CFD analyses more available, which makes it a more common feature in designing bioreactors for tissue engineering.<sup>21,22</sup> Overall, CFD analysis of flow characteristics in bioreactors for tissue engineering is recommended prior to manufacturing, since it allows for early improvements in the design process. In DC, this will lead to a further improvement in quality of the final tissue product.

The evaluation of the 3D printing materials PLA and AR-M2 prior to printing led to the choice of using PLA for this specific setup. The cytotoxicity assessment conducted with human endothelial cells revealed a highly toxic effect of AR-M2 on the cell viability and relative cell proliferation rate as described in the results. Hence, we cannot confirm previous studies for AR-M2 to be biocompatible or suitable for the use in cardiovascular tissue engineering, at least not for direct or indirect contact with cells or tissues.<sup>23</sup> The findings presented in this study regarding the biocompatibility of PLA are in accordance with already published data<sup>24,25</sup> and reveal PLA to be the more favorable material to use for biological tissue. Cell viability test revealed only a discrete and acceptable reduction of cell proliferation rate after 72 hours, which



constitutes an even longer exposition to the material than in the originally performed DC protocol.

The prime goal for the DC of xenogeneic tissue is the removal of residual DNA to prevent an immune reaction or even rejection of the tissue after implantation in patients.<sup>26</sup> The experiments conducted in this study revealed the high effectiveness of the bioreactors in combination with the applied DC protocols. All samples that were decellularized in the bioreactors showed a significant reduction of residual DNA. While the amount of DNA in native samples widely differs in the literature, a reduction of residual DNA below 50 ng/ $\mu$ g in combination with an absence of cell nuclei in HE and DAPI staining is considered a successful DC.<sup>27-29</sup> In both, aortic roots and pericardial patches, the residual DNA was reduced below this threshold, which further reiterates the effectiveness of the presented bioreactors.

While this work focuses on the establishment of a cost-effective DC bioreactor, additional quality control steps have to be taken in order to ensure total removal of xenogeneic components. In addition to reduction in residual DNA below the mentioned threshold and a lack of visible nuclear material in tissue sections, Crapo et al recommend to analyze the DNA fragment length by electrophoresis with the limit being set at 200 base pairs.<sup>27</sup> Alternatively, PCR of genomic DNA was described as being an effective method in confirming the absence of DNA and used to further validate developed bioreactors.<sup>30</sup> After establishing the herein described reproducible DC setup, it is a further research focus of our research group to develop a standard protocol for quality control of decellularized xenogeneic tissue. This is a limitation in the presented work, which has to be resolved before transferring the created DC biomaterials to in vivo studies.

The biomechanical properties of decellularized patches and vessels are an important indicator to determine the altering effects of the DC process on the tissue's ECM. The slight reduction in mechanical strength of both pericardial patches and vessel grafts after DC is in accordance with previously published articles.<sup>31-34</sup> The effect of the DC on the structural integrity of the samples can be considered mild, since the loss in mechanical strength was not significant and there was no visible damage to the ECM in neither histology nor SEM analysis. Li et al described a significantly higher reduction in mechanical strength from 15.9 MPa to only 6.15 MPa in bovine pericardium, despite using a classic immersion DC setup.<sup>31</sup> Thus it can be postulated, that the presented DC method offers a more gentle DC treatment of the tissue while preserving the structural and biomechanical integrity of the tissue's ECM. Furthermore, it confirms the superiority of perfusion-based DC in cardiovascular vessels compared to standard immersion and agitation techniques.<sup>35,36</sup>

Since the presented bioreactors are designed to be cost-efficient and easy to manufacture, naturally they come with some limitations. Both current versions of the bioreactors are fully enclosed. Therefore, it is not possible to observe the DC

samples during the process, preventing the user to swiftly intervene in case of any malfunction. This could be easily fixed by including space for an acrylic glass window on the sides or the lid, or printing parts of the bioreactor using transparent materials. Both methods would slightly increase the manufacturing costs and time but could yield more control over the process.

We consider the presented bioreactors to be a great basis for further research and individualized improvements in the field of cardiovascular tissue engineering. 3D printing offers a multitude of possibilities in the design of novel bioreactors. Due to its accessibility and wide range of printable materials, it will become a staple in modern research groups trying to develop their own lab equipment. Similar to multiple research groups, we consider 3D printing to be a great tool for creating open source solutions in tissue engineering, which is why all .stl-files, including printing instructions are attached as supplement to this publication.<sup>36,37</sup>

## 5 | CONCLUSION

The presented bioreactors offer a novel and affordable way to effectively and reliably decellularize multiple xenogeneic tissue samples simultaneously. All parts, except pump and tubing were created using a commercial low-cost 3D-printer. This keeps the production costs low while pertaining the freedom to design, adapt, and replace individual parts quickly. The conducted experiments show that both bioreactors can reliably decellularize multiple tissue samples at the same time, while protecting the structural integrity of the ECM. Furthermore, in comparison to a standard immersion and agitation control group, both bioreactors proved to be superior regarding DC efficiency.

### CONFLICT OF INTEREST

The authors declare that they have no conflicts of interest with the contents of this article.

### AUTHOR CONTRIBUTIONS

*Engineering design, drafting article, and data analysis:* Maximilian Grab

*Data collection and drafting article:* Felix Stieglmeier

*Data collection:* Jessica Emrich

*Statistics and data analysis:* Linda Grefen

*Data collection:* Ariane Leone

*Engineering design:* Fabian König

*Funding and approval of article:* Christian Hagl

*Experimental design and drafting article:* Nikolaus Thierfelder

### ETHICAL APPROVAL STATEMENT

Ethical approval was waived by the ethics committee of the Ludwig-Maximilians-University, Munich, because no human





tissue was processed in this study. Porcine and bovine tissue samples were collected as waste from a local slaughterhouse after receiving municipal permission.

## ORCID

Maximilian Grab  <https://orcid.org/0000-0002-3158-9095>

Nikolaus Thierfelder  <https://orcid.org/0000-0003-1103-3775>

## REFERENCES

- Nordmeyer S, Murin P, Schulz A, Danne F, Nordmeyer J, Kretzschmar J, et al. Results of aortic valve repair using decellularized bovine pericardium in congenital surgery. *Eur J Cardiothorac Surg*. 2018;54:986–92.
- Parmaksiz M, Dogan A, Odabas S, Elçin AE, Elçin YM. Clinical applications of decellularized extracellular matrices for tissue engineering and regenerative medicine. *Biomed Mater*. 2016;11:022003.
- Umashankar PR, Sabareeswaran A, Shenoy SJ. Long-term healing of mildly cross-linked decellularized bovine pericardial aortic patch. *J Biomed Mater Res B Appl Biomater*. 2017;105:2145–52.
- Choe JA, Jana S, Tefft BJ, Hennessy RS, Go J, Morse D, et al. Biomaterial characterization of off-the-shelf decellularized porcine pericardial tissue for use in prosthetic valvular applications. *J Tissue Eng Regen Med*. 2018;12:1608–20.
- Collatusso C, Roderjan JG, de Noronha L, Klosowski A, Suss PH, Guarita-Souza LC, et al. Decellularization as a method to reduce calcification in bovine pericardium bioprosthetic valves. *Interact Cardiovasc Thorac Surg*. 2019;29:302–11.
- Hussein KH, Park K-M, Kang K-S, Woo H-M. Biocompatibility evaluation of tissue-engineered decellularized scaffolds for biomedical application. *Mater Sci Eng C Mater Biol Appl*. 2016;67:766–78.
- Richards DJ, Tan YU, Jia J, Yao H, Mei Y. 3D printing for tissue engineering. *Isr J Chem*. 2013;53:805–14.
- Wang P, Sun Y, Shi X, Shen H, Ning H, Liu H. 3D printing of tissue engineering scaffolds: a focus on vascular regeneration. *Biores Manuf*. 2021;4:344–78. <https://doi.org/10.1007/s42242-020-00109-0>
- Liaw CY, Guvendiren M. Current and emerging applications of 3D printing in medicine. *Biofabrication*. 2017;9:024102.
- Coakley M, Hurt DE. 3D printing in the laboratory: maximize time and funds with customized and Open-Source Labware. *J Lab Autom*. 2016;21:489–95.
- Starnecker F, König F, Hagl C, Thierfelder N. Tissue-engineering acellular scaffolds—the significant influence of physical and procedural decellularization factors. *J Biomed Mater Res B Appl Biomater*. 2018;106:153–62.
- Montoya CV, McFetridge PS. Preparation of ex vivo-based biomaterials using convective flow decellularization. *Tissue Eng Part C Methods*. 2009;15:191–200.
- Thierfelder N, Koenig F, Bombien R, Fano C, Reichart B, Wintermantel E, et al. In vitro comparison of novel polyurethane aortic valves and homografts after seeding and conditioning. *ASAIO J*. 2013;59:309–16.
- Grefen L, König F, Grab M, Hagl C, Thierfelder N. Pericardial tissue for cardiovascular application: an in-vitro evaluation of established and advanced production processes. *J Mater Sci Mater Med*. 2018;29:172.
- Martin I, Simmons PJ, Williams DF. Manufacturing challenges in regenerative medicine. *Sci Transl Med*. 2014;6:232fs16.
- Martin I, Wendt D, Heberer M. The role of bioreactors in tissue engineering. *Trends Biotechnol*. 2004;22:80–6.
- Schuerlein S, Schwarz T, Krzimirski S, Gätzner S, Hoppensack A, Schwedhelm I, et al. A versatile modular bioreactor platform for tissue engineering. *Biotechnol J*. 2017;12:1600326.
- Wolf F, Rojas González DM, Steinseifer U, Obdenbusch M, Herfs W, Brecher C, et al. VasuTrainer: a mobile and disposable bioreactor system for the conditioning of tissue-engineered vascular grafts. *Ann Biomed Eng*. 2018;46:616–26.
- Janvier AJ, Canty-Laird E, Henstock JR. A universal multi-platform 3D printed bioreactor chamber for tendon tissue engineering. *J Tissue Eng*. 2020;11:2041731420942462.
- Toume S, Gefen A, Weihs D. Printable low-cost, sustained and dynamic cell stretching apparatus. *J Biomech*. 2016;49:1336–9.
- Singh H, Huttmacher DW. Bioreactor studies and computational fluid dynamics. *Adv Biochem Eng Biotechnol*. 2009;112:231–49.
- Lee H, Marin-Araujo AE, Aoki FG, Haykal S, Waddell TK, Amon CH, et al. Computational fluid dynamics for enhanced tracheal bioreactor design and long-segment graft recellularization. *Sci Rep*. 2021;11:1187.
- Siller IG, Enders A, Gellermann P, Winkler S, Lavrentieva A, Scheper T, et al. Characterization of a customized 3D-printed cell culture system using clear, translucent acrylate that enables optical online monitoring. *Biomed Mater*. 2020;15:055007.
- Carvalho JRG, Conde G, Antonioli ML, Dias PP, Vasconcelos RO, Taboga SR, et al. Biocompatibility and biodegradation of poly(lactic acid) (PLA) and an immiscible PLA/poly(ε-caprolactone) (PCL) blend compatibilized by poly(ε-caprolactone-b-tetrahydrofuran) implanted in horses. *Polym J*. 2020;52:629–43.
- Diez-Escudero A, Harlin H, Isaksson P, Persson C. Porous polylactic acid scaffolds for bone regeneration: A study of additively manufactured triply periodic minimal surfaces and their osteogenic potential. *J Tissue Eng*. 2020;11:2041731420956541.
- Aamodt JM, Grainger DW. Extracellular matrix-based biomaterial scaffolds and the host response. *Biomaterials*. 2016;86:68–82.
- Crapo PM, Gilbert TW, Badylak SF. An overview of tissue and whole organ decellularization processes. *Biomaterials*. 2011;32:3233–43.
- Aguiari P, Iop L, Favaretto F, Fidalgo CM, Naso F, Milan G, et al. In vitro comparative assessment of decellularized bovine pericardial patches and commercial bioprosthetic heart valves. *Biomed Mater*. 2017;12:015021.
- Gardin C, Ricci S, Ferroni L, Guazzo R, Sbricoli L, De Benedictis G, et al. Decellularization and delipidation protocols of bovine bone and pericardium for bone grafting and guided bone regeneration procedures. *PLoS One*. 2015;10:e0132344.
- Price AP, England KA, Matson AM, Blazar BR, Panoskaltsis-Mortari A, et al. Development of a decellularized lung bioreactor system for bioengineering the lung: the matrix reloaded. *Tissue Eng Part A*. 2010;16:2581–91.
- Li N, Li Y, Gong D, Xia C, Liu X, Xu Z, et al. Efficient decellularization for bovine pericardium with extracellular matrix preservation and good biocompatibility. *Interact Cardiovasc Thorac Surg*. 2018;26:768–76.
- Vinci MC, Tessitore G, Castiglioni L, Prandi F, Soncini M, Santoro R, et al. Mechanical compliance and immunological compatibility





- of fixative-free decellularized/cryopreserved human pericardium. PLoS One. 2013;8:e64769.
33. Mirsadraee S, Wilcox HE, Korossis SA, Kearney JN, Watterson KG, Fisher J, et al. Development and characterization of an acellular human pericardial matrix for tissue engineering. Tissue Eng. 2006;12:763–73.
34. Stieglmeier F, Grab M, König F, Büch J, Hagl C, Thierfelder N. Mapping of bovine pericardium to enable a standardized acquirement of material for medical implants. J Mech Behav Biomed Mater. 2021;118:104432.
35. Guyette JP, Gilpin SE, Charest JM, Tapias LF, Ren XI, Ott HC, et al. Perfusion decellularization of whole organs. Nat Protoc. 2014;9:1451–68.
36. Schilling BK, Lamberti KK, Snowden MJ, Baker JS, Byrd K, Komatsu C, et al. Design and fabrication of an automatable, 3D printed perfusion device for tissue infusion and perfusion engineering. Tissue Eng Part A. 2020;26:253–64.
37. Pearce JM. Building research equipment with free, open-source hardware. Science 2012;337:1303–4.

#### SUPPORTING INFORMATION

Additional Supporting Information may be found online in the Supporting Information section.

**How to cite this article:** Grab M, Stieglmeier F, Emrich J, Grefen L, Leone A, König F, et al. Customized 3D printed bioreactors for decellularization—High efficiency and quality on a budget. Artif Organs. 2021;00:1–14. <https://doi.org/10.1111/aor.14034>

### 7.11 Tuning Tissue Ingrowth into Proangiogenic Hydrogels via Dual Modality Degradation (Chokoza et al., 2019)

- Cindy Chokoza, Carla A. Gustafsson, Kyle P. Goetsch, Peter Zilla, Nikolaus Thierfelder, Federica Pisano, Manuela Mura, Massimiliano Gnechi, Deon Bezuidenhout, Neil H. Davies
- ACS Biomaterials Science & Engineering. 2019, 5, 10, 5430-5438
- DOI: 10.1021/acsbmaterials.9b01220
- *Die hier genannte, publizierte Originalarbeit ist zum Drucklegungszeitpunkt der vorliegenden Habilitationsschrift lizenzrechtlich geschützt und nicht frei veröffentlichungsfähig. Der Text kann unter der angegebenen Quelle kostenpflichtig angefordert oder mit entsprechenden Rechten eingesehen werden.*

### 7.12 Combining 3D-Printing and Electrospinning to Manufacture Biomimetic Heart Valve Leaflets (Freystetter et al., 2022)

- Benedikt Freystetter, Maximilian Grab, Linda Grefen, Lara Bischof, Lorenz Isert, Deon Bezuidenhout, Petra Mela, Christian Hagl, Nikolaus Thierfelder
- JOVE Journal of Visualized Experiments; Zur Publikation angenommen am 02.02.2022

## 8 Danksagung

Mein großer Dank gilt Herrn Prof. Dr. med. Christian Hagl, Direktor der Herzchirurgischen Klinik und Poliklinik der LMU München, der mir die Durchführung der hier vorgestellten Forschung in seiner Klinik ermöglichte. Ferner stand er mir zusammen mit Herrn Prof. Dr. med. Nikolaus Haas, Direktor der Klinik für Kinderkardiologie und Pädiatrische Intensivmedizin der LMU München, und Herrn Prof. Dr. med. Christian Stief, Direktor der Urologischen Klinik und Poliklinik der LMU München, als Mentor und Betreuer der Habilitationsarbeit zur Seite.

Meinen ganz besonderen Dank möchte ich Herrn Dipl.-Ing. Fabian König ausdrücken. Er hat als Kollege meine gesamte wissenschaftliche Karriere seit Beginn an begleitet und ist mir in dieser Zeit auch ein besonders enger und ganz wichtiger Freund geworden. Lieber Fabian, herzlichen Dank für die vielen tollen, wissenschaftlichen Diskussionen, die bereichernden persönliche Gespräche und deine ganze Unterstützung - ohne dich wäre diese Arbeit so nicht entstanden!

Bei Herrn Maximilian Grab, M.Sc., möchte ich mich ganz besonders für die Arbeit und Unterstützung im Forschungslabor bedanken. Es gibt nicht viele Menschen mit seinem Organisationstalent sowie seiner sympathischen und immer hilfsbereiten Art (egal in welcher Situation!). So hat er mir jederzeit den „Rücken freigehalten“ und mich unterstützt, wenn es in der Klinik mal wieder turbulent zugeht.

Einen ganz besonderen Beitrag zur Entstehung dieser Arbeit haben alle meine Kolleginnen und Kollegen aus dem „Labor für Tissue Engineering und kardiovaskuläre Medizintechnik“ geleistet. Dafür möchte ich mich bei Frau Bettina Wimmer, Frau Barbara Steinl, Frau Ulrike Haas und Frau Eike Petersen, aber auch bei allen meinen Doktorand\*innen und Student\*innen bedanken. Alle zusammen haben einen Teil zum Entstehen dieser Arbeit beigetragen.

Ich möchte mich außerdem bei Herrn Prof. Deon Bezuidenhout, Ph.D., Direktor der „Cardiovascular Research Unit“ der Universität Kapstadt, bedanken. Während meiner Forschungszeit in Südafrika habe ich ihn kennen und als Mentor schätzen gelernt. Dear Deon, many thanks for your support and the great (scientific) discussions!

Einen ganz speziellen Dank möchte ich an dieser Stelle an meine Eltern richten. Sie haben mich, seit ich denken kann, in meiner Neugier gefördert und damit den „kleinen Wissenschaftler in meinem Inneren“ wachsen lassen.